

การศึกษาการกระเจิงรังสีเอกซ์ด้วยแสงซินโครตรอน ในสารละลายเอนไซม์
Glucose Oxidase และฟิล์มบางพอลิเมอร์กลุ่ม PHIC-PCL₁₋₃ และ
PHIC-PLLA₁₋₃



นายรามย์ พิณเจริญพันธุ์

วิทยานิพนธ์นี้เป็นส่วนหนึ่งของการศึกษาตามหลักสูตรปริญญาวิทยาศาสตรดุษฎีบัณฑิต
สาขาวิชาฟิสิกส์
มหาวิทยาลัยเทคโนโลยีสุรนารี
ปีการศึกษา 2557

**SYNCHROTRON X-RAY SCATTERING STUDIES OF
GLUCOSE OXIDASE IN SOLUTIONS AND PHIC-PCL₁₋₃
AND PHIC-PLLA₁₋₃ IN THIN FILMS**

Rarm Phinjaroenphan



**A Thesis Submitted in Partial Fulfillment of the Requirements for the
Degree of Doctor of Philosophy in Physics
Suranaree University of Technology
Academic Year 2014**

**SYNCHROTRON X-RAY SCATTERING STUDIES OF GLUCOSE
OXIDASE IN SOLUTIONS AND PHIC-PCL₁₋₃ AND PHIC-PLLA₁₋₃
IN THIN FILMS**

Suranaree University of Technology has approved this thesis submitted in partial fulfillment of the requirements for the Degree of Doctor of Philosophy.

Thesis Examining Committee

(Assoc. Prof. Dr. Prayoon Songsiriritthigul)

Chairperson

(Prof. Dr. Santi Maensiri)

Member (Thesis Advisor)

(Prof. Dr. Moonhor Ree)

Member

(Asst. Prof. Dr. Supagorn Rugmai)

Member

(Asst. Prof. Dr. Worawat Meevasana)

Member

(Dr. Siritwat Soontaranon)

Member

(Prof. Dr. Sukit Limpijumnong)

Vice Rector for Academic Affairs
and Innovation

(Assoc. Prof. Dr. Prapun Manyum)

Dean of Institute of Science

รามย์ พิณเจริญพันธุ์ : การศึกษาการกระเจิงรังสีเอกซ์ด้วยแสงซินโครตรอน ในสารละลาย
เอนไซม์ Glucose Oxidase และฟิล์มบางพอลิเมอร์กลุ่ม PHIC-PCL₁₋₃ และ PHIC-PLLA₁₋₃
(SYNCHROTRON X-RAY SCATTERING STUDIES OF GLUCOSE OXIDASE IN
SOLUTIONS AND PHIC-PCL₁₋₃ AND PHIC-PLLA₁₋₃ IN THIN FILMS) อาจารย์ที่ปรึกษา
: ศาสตราจารย์ ดร.สันติ แม่นศิริ, 216 หน้า.

โครงสร้างโมเลกุลของเอนไซม์ glucose oxidase (GOD) ถูกศึกษาโดยใช้วิธีการกระเจิงของ
รังสีเอกซ์ที่มุมเล็กด้วยแสงซินโครตรอน (SAXS) ผลกระทบเนื่องจากความเป็นกรดและด่างต่อ
โครงสร้างของเอนไซม์ GOD ถูกตรวจสอบโดยทำการวัดสารละลายเอนไซม์ GOD ที่มีค่า pH จาก
1 ถึง 10 ด้วยเทคนิค SAXS จากผลลัพธ์ที่ได้แสดงให้เห็นว่า โครงสร้างโมเลกุลของ GOD มีลักษณะ
รูปร่างคล้ายทรงกลมที่รวมตัวกันแน่น เมื่อมีค่า pH สูงกว่า 4 โครงสร้างโมเลกุลเกิดการเกาะกลุ่มกัน
เล็กน้อยเมื่อค่าความเป็นกรดสูงขึ้น และเกิดการสูญเสียโครงสร้างภายใต้ความเป็นกรดที่สูงมากที่ค่า
pH เป็น 1 และ 2 นอกจากนี้โครงสร้างโมเลกุลของสารละลายเอนไซม์ GOD ที่วัดด้วยเทคนิค
SAXS ถูกเปรียบเทียบกับโครงสร้างอะตอมสามมิติของ GOD ที่วัดมาจากเทคนิค Crystallography
โดยพบว่าโมเลกุลของเอนไซม์ GOD ในรูปแบบสารละลายมีปริมาตรสูงกว่า ซึ่งอาจเกิดมาจากการ
สูญเสียคาร์โบไฮเดรตของ GOD ในรูปแบบผลึก

ฟิล์มบางพอลิเมอร์รูปดาวแบบ rod-coil 2 กลุ่ม ถูกศึกษาโดยใช้วิธีการการกระเจิงของรังสี
เอกซ์มุมตกระทบแบบเกรซิ่งด้วยแสงซินโครตรอน (GIXS) กลุ่มแรกคือ poly(n-hexyl
isocyanate)-*block*-poly(ϵ -caprolactone) (PHIC-PCL₁₋₃) ซึ่งมีความแตกต่างของน้ำหนักโมเลกุล
เฉลี่ย คือ PHIC (5,000 กรัมต่อ โมล)-PCL₁₋₃ (17,000 กรัมต่อ โมล) และ PHIC (10,000 กรัมต่อ โมล)-
PCL₁₋₃ (10,000 กรัมต่อ โมล) ประกอบด้วยแขนพอลิเมอร์ poly(n-hexyl isocyanate) (PHIC) และ 1
ถึง 3 แขนพอลิเมอร์ poly(ϵ -caprolactone) (PCL_n; n = 1-3) และอีกกลุ่ม คือ poly(n-hexyl
isocyanate)-*block*-poly(L-lactid acid) (PHIC-PLLA₁₋₃) โดยมีน้ำหนักโมเลกุลเฉลี่ยเป็น PHIC
(10,000 กรัมต่อ โมล)-PLLA₁₋₃ (10,000 กรัมต่อ โมล) และมีแขนพอลิเมอร์ตัวสุดท้าย คือ 1 ถึง 3
แขนพอลิเมอร์ poly(L-lactid acid) (PLLA_n; n = 1-3) รวมทั้งฟิล์มบางไฮโม่พอลิเมอร์ เช่น PHIC
(5,400 กรัมต่อ โมล และ 10,400 กรัมต่อ โมล) และ PCL (15,000 กรัมต่อ โมล และ 10,500 กรัมต่อ
โมล) และ PLLA (10,200 กรัมต่อ โมล)

โครงสร้างลักษณะเฉพาะเชิงปริมาณระดับนาโนและผลึกของฟิล์มบางพอลิเมอร์กลุ่มรูปดาว
และฟิล์มบางไฮโม่พอลิเมอร์เหล่านี้ ถูกบ่งบอกโดยใช้ผลลัพธ์จากเทคนิค GIXS และผลกระทบของ

การอบด้วยสารละลาย เช่น โทลูอินและคลอโรฟอร์ม อีกทั้งจำนวนแขนพอลิเมอร์ต่อพฤติกรรมการจัดวางตัวของโมเลกุลอย่างเป็นระเบียบได้ด้วยตนเองของกลุ่มฟิล์มบางพอลิเมอร์ถูกตรวจสอบ



สาขาวิชาฟิสิกส์
ปีการศึกษา 2557

ลายมือชื่อนักศึกษา _____

ลายมือชื่ออาจารย์ที่ปรึกษา _____

ลายมือชื่ออาจารย์ที่ปรึกษาร่วม _____

ลายมือชื่ออาจารย์ที่ปรึกษาร่วม _____

RARM PHINJAROENPHAN : SYNCHROTRON X-RAY SCATTERING
STUDIES OF GLUCOSE OXIDASE IN SOLUTIONS AND PHIC-PCL₁₋₃
AND PHIC-PLLA₁₋₃ IN THIN FILMS. THESIS ADVISOR : PROF. SANTI
MAENSIRI, Ph.D. 216 PP.

SMALL ANGLE X-RAY SCATTERING/ GRAZING INCIDENCE X-RAY
SCATTERING/GLUCOSE OXIDASE/ROD-COIL MIKTOARMS STAR
POLYMER/POLY(N-HEXYL ISOCYANATE)/POLY(ϵ -CAPROLACTONE)/
POLY(L-LACTID ACID)/CRYSTALLINITY

Molecular conformation of glucose oxidase (GOD) enzyme was studied using synchrotron Small Angle X-ray Scattering (SAXS). The effects of acids and alkalis on GOD structures were investigated by performing SAXS measurements on GOD solution with pH conditions ranging from 1 to 10. The results showed that the GOD molecules have compact, globular structure within a wide range of pH conditions, i.e. with the pH values above 4. The molecules were slightly aggregated under more acidic condition and denatured at highly acidic condition where the pH values were 2 and 1. The molecular conformation derived from the solution SAXS was compared with that derived from the 3-dimensional (3D) atomic models obtained from crystallography and it was found that the GOD molecules in solution have larger molecular volume, which may be attributed to the lost of carbohydrate in the crystalline form.

Two series with different number average molecular weight of rod-coil type miktoarms star polymers in thin films form; PHIC (5,000 g/mol)-PCL₁₋₃ (17,000

g/mol) and PHIC (10,000 g/mol)-PCL₁₋₃ (10,000 g/mol), (poly(n-hexyl isocyanate)-*block*-poly(ϵ -caprolactone)), consisting of poly(n-hexyl isocyanate) (PHIC) arm and one to three poly(ϵ -caprolactone) arms (PCL_n: $n = 1-3$), as well as the other set of the miktoarms star polymers thin films; PHIC (10,000 g/mol)-PLLA₁₋₃ (10,000 g/mol) (poly(n-hexyl isocyanate)-*block*-poly(L-lactid acid)), with the last block being one to three poly(L-lactid acid) (PLLA_n: $n = 1-3$) arms, together with the homopolymer films, PHIC (5,400 g/mol, 10,400 g/mol), PCL (15,000 g/mol, 10,500 g/mol), and PLLA (10,200 g/mol), were studied by synchrotron Grazing Incidence X-ray Scattering (GIXS). The nanostructures and crystal conformation of these star polymer films and the homopolymer films were quantitatively characterized using the GIXS results. The effects of solvent annealing such as toluene and CHCl₃ and the number of arms on the self-assembled behavior of the polymers were also investigated.

School of Physics

Academic Year 2014

Student's Signature_____

Advisor's Signature_____

Co-advisor's Signature_____

Co-advisor's Signature_____

ACKNOWLEDGEMENTS

I would like to thank many people for their assistance, support and guidance in various ways during the development of this thesis work. There is no doubt that this work would not be completed without their contribution.

First of all, I would like to express my sincere gratitude to Prof. Dr. Santi Maensiri and Asst. Prof. Dr. Supagorn Rugmai, my thesis advisor and co-advisor, for their invaluable guidance and kind support on all problems throughout this work.

I am also very grateful to my co-advisor Prof. Dr. Moonhor Ree for his great advice, kind patience, inspiration, guidance, help, encouragement, and support in this work.

I would like to thank Assoc. Prof. Dr. Prayoon Songsiriritthigul, Asst. Prof. Dr. Worawat Meevasana, and Dr. Siriwat Soontaranon for being on my thesis committee.

I would also like to thank Dr. Kyeong Sik Jin, Beamline Researcher at BL.4C SAXS, Pohang Accelerator Laboratory (PAL), Pohang, South Korea, for his help and guidance.

I would like to acknowledge all fellow students who work under Prof. Moonhor Ree for their assistance and friendship. Especially, all assistance from Mr. Young Yong Kim and Miss Kim Mihee is very much appreciated.

I am grateful to all staff members at SAXS beamline, Synchrotron Light Research Institute, and all graduate students and staff members at School of Physics, Suranaree University of Technology, for their friendship and sincereness.

Moreover, I am deeply grateful to Suranaree University of Technology for the financial support.

I would also like to thank PHRAKRU SOOTHAPANYATORN, Pholkrang Ecclesiastical Commune-Chiefs, Abbot of Srimumbhuraparam Temple for encouragement and good advices throughout my studies.

Finally, I would like to express appreciation to my parents, sisters and brother for great support, encouragement, and good advices to me over the years of my life.

Rarm Phinjaroenphan



CONTENTS

	Page
ABSTRACT IN THAI.....	I
ABSTRACT IN ENGLISH	III
ACKNOWLEDGEMENTS.....	V
CONTENTS.....	VII
LIST OF TABLES.....	XI
LIST OF FIGURES	XIII
LIST OF ABBREVIATIONS.....	XXXVI
CHAPTER	
I INTRODUCTION.....	1
1.1 Motivation.....	1
1.2 X-ray Scattering Method.....	3
1.2.1 Small Angle X-ray Scattering	4
1.2.2 Grazing Incident X-ray Scattering	5
1.3 Outline of Thesis	7
II THEORETICAL BACKGROUND FOR SMALL ANGLE X-RAY	
SCATTERING DATA ANALYSIS OF ENZYME SOLUTION.....	8
2.1 SAXS Geometry	8
2.2 Scattering Intensity of Enzyme Solution	13
2.3 Pair Distribution Function.....	15
2.4 Guinier Approximation.....	17

CONTENTS (Continued)

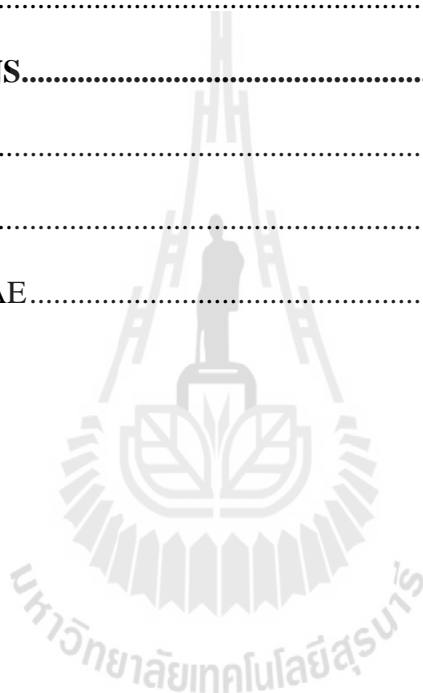
	Page
2.5 Porod Volume	20
2.6 Kratky Plot	21
2.7 3D Reconstruction Model	22
2.7.1 DAMMIN and DAMAVER	23
2.7.2 Protein Data Bank	26
2.7.3 SUPCOMB	26
2.7.4 CRY SOL	27
III EFFECT OF ACIDS AND ALKALIS ON CONFORMATION OF GLUCOSE OXIDASE BY SMALL ANGLE X-RAY SCATTERING.....	30
3.1 Introduction	30
3.2 Experimental Section	32
3.2.1 Sample Preparation	32
3.2.2 Measurements	32
3.4 Results and Discussions	33
3.4 Conclusion	44
IV THEORETICAL BACKGROUND FOR GRAZING INCIDENCE X-RAY SCATTERING DATA ANALYSIS OF POLYMER THIN FILMS.....	45
4.1 GIXS Geometry	46
4.2 GIXS Theory	48

CONTENTS (Continued)

	Page
4.2.1 Form factor: lamellar model, multibilayer model, and orthorhombic model.	54
4.2.2 Structure Factor: Paracrystal	59
4.3 Crystal Orientation and Distribution	62
4.4 Second-Order Orientation Factor	62
V CHARACTERIZATION OF POLY(N-HEXYL ISOCYANATE)-BLOCK-POLY(ϵ-CAPROLACTONE) MIKTOARM STAR POLYMERS THIN FILMS BY GRAZING X-RAY SCATTERING	64
5.1 Introduction	65
5.2 Experimental Section	67
5.2.1 Materials and Thin Films Preparation	67
5.2.2 Measurements	68
5.3 Results and Discussions	69
5.4 Conclusion	107
VI STRUCTURAL ANALYSIS OF POLY(N-HEXYL ISOCYANATE)-BLOCK-POLY(L-LACTIC ACID) MIKTOARM STAR POLYMERS THIN FILMS BY GRAZING X-RAY SCATTERING	114
6.1 Introduction	114
6.2 Experimental Section	115
6.2.1 Materials and Thin Films Preparation	115

CONTENTS (Continued)

	Page
6.2.2 Measurements	116
6.3 Results and Discussions	117
6.4 Conclusion	142
VII CONCLUSIONS	147
REFERENCES	151
APPENDIX.....	165
CURRICULUM VITAE.....	216



LIST OF TABLES

Table	Page
3.1 The structure parameters from enzyme at pH 1 to 10 and crystal (1CF3) of GOD derived from Guinier plots and the pair distance distribution function.....	37
3.2 The excluded GOD volumes from pH 3 to 10 and of crystal structure (1CF3) calculated by the Porod law.....	44
5.1 Fundamental properties of the PHIC and PCL homopolymers and PHIC-PCL ₁₋₃ miktoarm star polymers used in the study..	70
5.2 Nanostructural parameters of the toluene-annealed thin films of the PHIC(5.4k) and PCL(15k) homopolymers and PHIC(5k)-PCL ₁₋₃ (17k) miktoarm star polymers, determined by GISAXS analysis.....	81
5.3 Nanostructural parameters under the toluene and CHCl ₃ annealing in thin films of the PHIC(10.4k) and PCL(10.5k) homopolymers and PHIC(10k)-PCL ₁₋₃ (10k) miktoarm star polymers, determined by GISAXS analysis.....	92
5.4 Structural parameters of the toluene-annealed thin films of the PHIC(5.4k) and PCL(14.5k) and PHIC(5k)-PCL ₁₋₃ (17k) miktoarm star polymers, determined by GIWAXS analysis.....	103
5.5 Structural parameters of the toluene-annealed thin films of the PHIC (10.4k) and PCL (10.5k) homopolymers and PHIC(10k)-PCL ₃ (10k)	

LIST OF TABLES (Continued)

Table	Page
miktoarm star polymers, determined by GIWAXS analysis... ..	104
5.6 Structural parameters of CHCl ₃ -annealed thin films of PHIC(10.4k) and PCL(10.5k) homopolymers and PHIC(10k)-PCL ₁₋₃ (10k) miktoarm star polymers films, determined by GIWAXS analysis.....	105
6.1 Fundamental properties of the PHIC and PLLA homopolymers and PHIC-PLLA ₁₋₃ miktoarm star polymers used in the study... ..	116
6.2 Nanostructural parameters of the CHCl ₃ - and thermal-annealed thin films of the PHIC and PLLA homopolymers and PHIC-PLLA ₁₋₃ miktoarm star polymers, determined by GISAXS analysis.....	131
6.3 Structural parameters of the CHCl ₃ -annealed thin films of the PHIC and PLLA homopolymers and PHIC-PLLA ₁₋₃ miktoarm star polymers, determined by GIWAXS analysis.....	140
6.4 Structural parameters of the thermal-annealed thin films of the PHIC and PLLA homopolymers and PHIC-PLLA ₁₋₃ miktoarm star polymers, determined by GIWAXS analysis.....	141

LIST OF FIGURES

Figure	Page
2.1	Schematic representation of SAXS geometry. The incident X-rays beam is directed to a sample (protein solution) with wave vector \vec{k}_i and exits as the scattering X-ray beam at exit angle 2θ with wave vectors (\vec{k}_f). The scattering data is detected by a two dimensions charge-couple detector (2D CCD) depending on the scattering vector \vec{q} . The distance between the sample and the detector is SDD..... 9
2.2	The scattering geometry from the two point scatterers system..... 10
2.3	The pair distribution function $P(r)$ for geometrical protein (unfolded multidomain and globular) with their maximum dimension length D_{max} (Putnam <i>et al.</i> , 2007)..... 17
2.4	Calculated R_g from the slope of the Guinier plot with the limit in q range. Besides, the linearity of slope can identify the aggregation properties of protein [adapted from (Putnam <i>et al.</i> , 2007)]. 18
2.5	The Kratky plot of folded, unfolded, and partially unfolded of the protein sample. For folded state, the plot presents a bell-shaped curve, while the unfolded state lacks the curve and increases noticeably in the large q region. The partially unfolded state shows a broad peak and not goes down to zero in the high q region (Putnam <i>et al.</i> , 2007). 22

LIST OF FIGURES (Continued)

Figure	Page
2.6	The illustration of protein particle in dilute solution... .. 30
3.1	The SAXS intensity of GOD enzymes at pH 1 to 10.. .. 35
3.2	The Kratky plot of the scattering profiles of GOD enzymes at pH 1 to 10..... 35
3.3	The Guinier plot of GOD enzyme at pH 1 to 10 and GOD crystal (1CF3).... 36
3.4	The calculated pair distance distribution function ($P(r)$) of GOD enzyme at pH 3 to 10 and GOD crystal (1CF3)..... 36
3.5	Schematic representation of the filtered atomic models of GOD enzyme at pH 5 to 10 superimposed onto the dimer of GOD crystal structure, which was created from monomeric GOD crystal structure (1CF3.pdb, represented by solid ribbon) by PyMol software. Filtered reconstruction model of GOD crystal (1CF3) superimposed on its crystal structure (1CF3.pdb, shown in solid ribbon) (Continued)..... 39-40
3.6	Scattering intensity between monomer (1CF3) and dimer (Di_1CF3) of GOD crystal structures, as well as GOD enzyme at pH 1 to 10 42
3.7	The Porod plot of GOD enzyme and of GOD crystal structure (1CF3) 43
4.1	(a) Schematic picture of GIXS geometry; the sample is placed on the x-y plane. The 2D CCD detector is positioned in the perpendicular to the surface plane (y-z plane) with the distance between sample and detector (SDD). The incident X-ray beam (x-axis) with wave vector \vec{k}_i impinges

LIST OF FIGURES (Continued)

Figure	Page
<p>on the surface under grazing angle α_i and scatter at the exit angle α_f and $2\theta_f$ with wave vector \vec{k}_f. The q_x, q_y, and q_z are the components of the scattering vector \vec{q}. (b) The illustration of the polymer thin film, having thickness d, contains particles, fabricated in Si-substrate. (c) The picture of the scattering events in the polymer film; event 1, the scattering from the particles; event 2, the reflection at the interface followed by scattering from the particles; event 3, the scattering from the particles followed by reflection at the interface; event 4, the reflection at the interface followed by scattering from the particles, then reflection again.....</p>	50
<p>4.2 Schematic picture of the three layers (dense, less dense, and interfacial layers) lamellar structural model. (a) A 3D representation structure of the lamellar model where φ_1 is an orientation angle of the model, which is between the vector \mathbf{n}_1 and the out-of-plane of the film. (b) A 2D representation structure of the lamellar model. The inner and outer layers in (a) correspond to the dense and interfacial layers in (b) respectively; the orange colored layer in (b) corresponds to the less dense layer. The dimension of the lamellar structure is defined by L (long period), L_x, L_y, $\ell_1 (= H_{inner})$, $\ell_2 (= (H_{outer} - H_{inner})/2)$, and $\ell_3 (= L - H_{outer})$..</p>	57
<p>4.3 Illustration picture of the multibilayer (dense and less dense layer) model (a) A 3D representation structure of the two layers lamellar model</p>	

LIST OF FIGURES (Continued)

Figure	Page
<p>where φ_2 is an orientation angle of the model, which is between the vector \mathbf{n}_2 and the out-of-plane of the film. (b) top and side views of the laterally packed <i>n</i>-hexyl bristles where d_1 is the mean distance between the <i>n</i>-hexyl bristles of the neighboring polymer chains whose repeat units are matched in position along their backbones, d_2 is the mean distance between the nearest <i>n</i>-hexyl bristles along the polymer backbone, d_3 is the mean distance between the <i>n</i>-hexyl bristles and the nearest neighboring <i>n</i>-hexyl bristles, and β is the angle between the d_3 and d_2 directions. The dimension of the lamellar structure is determined by d_L (long period), l_x, l_y, $\ell_1 (= H_{inner})$, h (dense layer thickness) and $(d_L - h)$ (less dense layer thickness).....</p>	58
<p>4.4 The picture of the molecular cylinders orthorhombic lattice model. (a) A 3D representation structure of the orthorhombic model where φ_3 is an orientation angle of the model, which is between the vector \mathbf{n}_3 and the out-of-plane of the film. (b) Top views of the orthorhombic system with dimension length (<i>d</i>-spacing values) are defined by d_{100}, d_{200}, d_{010}, d_{020}, d_{001}, d_{002}, and d_{110}.....</p>	59
<p>5.1 2D GISAXS patterns of toluene-annealed PHIC(5.4k) and PCL(15k) homopolymer films (120 nm thick) measured with an incidence angle α_i of 0.140° at RT using an X-ray wavelength λ of 0.1180 nm; (a) PHIC</p>	

LIST OF FIGURES (Continued)

Figure	Page
<p>film; (b) out-of-plane profile extracted from the data in (a) along the α direction at $2\theta_f = 0.100^\circ$; (c) in-plane profile extracted from the data in (a) along the $2\theta_f$ direction at $\alpha_f = 0.170^\circ$; (d) PCL film; (e) out-of-plane profile extracted from the data in (d) along the α_f direction at $2\theta_f = 0.100^\circ$; (f) in-plane profile extracted from the data in (d) along the $2\theta_f$ direction at $\alpha_f = 0.170^\circ$; (g) 2D image of PCL film reconstructed from the structural parameters in Table 5.2 using the GIXS formula derived for lamellar structure model; (h) lamellar structure model where \mathbf{n}_1 is the orientation vector of the structure model and φ_1 is the polar angle between the \mathbf{n}_1 vector and the out-of-plane of the film. In (e) and (f), the black circular symbols are the measured data, and the red solid lines represented as a fitting result from the GIXS formula.....</p>	72
<p>5.2 2D GISAXS patterns of toluene-annealed PHIC(10.4k) and PCL(10.5k) homopolymer films (80 nm thick) measured with an incidence angle α_i of 0.130° at RT using an X-ray wavelength λ of 0.1170 nm; (a) PHIC film; (b) out-of-plane profile extracted from the data in (a) along the α_f direction at $2\theta_f = 0.090^\circ$; (c) in-plane profile extracted from the data in (a) along the $2\theta_f$ direction at $\alpha_f = 0.140^\circ$; (d) PCL film; (e) out-of-plane profile extracted from the data in (d) along the α_f direction at $2\theta_f = 0.090^\circ$; (f) in-plane profile extracted from the data in (d) along the $2\theta_f$ direction at $\alpha_f = 0.140^\circ$; (g) 2D image of PCL film reconstructed from</p>	

LIST OF FIGURES (Continued)

Figure	Page
<p>the structural parameters in Table 5.3 using the GIXS formula derived for three layer lamellar structural model; (h) lamellar structure model where \mathbf{n}_1 is the orientation vector of the structure model and φ_4 is the polar angle between the \mathbf{n}_1 vector and the out-of-plane of the film. In (e) and (f), the black circular symbols are the measured data, and the red solid lines represented as a fitting result from the GIXS formula</p>	73
<p>5.3 2D GISAXS patterns of CHCl_3-annealed PHIC(10.4k) and PCL(10.5k) films (80 nm thick) measured with an incidence angle α_i of 0.130° at RT using an X-ray wavelength λ of 0.1170 nm; (a) PHIC film; (b) out-of-plane profile extracted from the data in (a) along the α_f direction at $2\theta_f = 0.090^\circ$; (c) in-plane profile extracted from the data in (a) along the $2\theta_f$ direction at $\alpha_f = 0.140^\circ$; (d) PCL film; (e) out-of-plane profile extracted from the data in (d) along the α_f direction at $2\theta_f = 0.090^\circ$; (f) in-plane profile extracted from the data in (d) along the $2\theta_f$ direction at $\alpha_f = 0.140^\circ$; (g) 2D image of PCL film reconstructed from the structural parameters in Table 5.3 using the GIXS formula derived for lamellar structure model; (h) lamellar structure model where \mathbf{n}_1 is the orientation vector of the structure model and φ_4 is the polar angle between the \mathbf{n}_1 structure model; (h) lamellar structure model where \mathbf{n}_1 is the orientation vector of the structure model and φ_4 is the polar angle between the \mathbf{n}_1</p>	

LIST OF FIGURES (Continued)

Figure	Page
<p>vector and the out-of-plane of the film. In (e) and (f), the black circular symbols are measured data, and the red solid lines represented as a fitting result from the formula.....</p>	74
<p>5.4 2D GISAXS pattern of toluene-annealed PHIC(5.1k)-PCL(17.5k) film (120 nm thick) measured at room temperature using an X-ray wavelength $\lambda = 0.1180$ nm; (a) measured with $\alpha_i = 0.110^\circ$ at a sample-to-detector distance (SDD) of 902 mm; (b) measured with $\alpha_i = 0.140^\circ$ at SDD = 2922 mm; (c) out-of-plane scattering profile extracted from the data in (a) and (b) along the α_f direction at $2\theta_f = 0.140^\circ$ where the black circular symbols are the measured data, and the red solid lines were obtained by fitting the data using the GIXS formula; (d) in-plane scattering profile extracted from the data in (a) and (b) along the $2\theta_f$ direction at $\alpha_f = 0.190^\circ$; (e) 2D scattering image reconstructed from the structural parameters in Table 5.2 using the GIXS formula derived for lamellar structure model.</p>	77
<p>5.5 2D GISAXS pattern of toluene-annealed PHIC(5.2k)-PCL₂(18k) film (120 nm thick) deposited on silicon substrates, measured at room temperature using an X-ray wavelength $\lambda = 0.1180$ nm; (a) measured with $\alpha_i = 0.110^\circ$ at SDD = 902 mm; (b) measured with $\alpha_i = 0.140^\circ$ at SDD = 2922 mm; (c) out-of-plane scattering profile extracted from the</p>	

LIST OF FIGURES (Continued)

Figure	Page
<p>data in (a) and (b) along the α_f direction at $2\theta_f = 0.160^\circ$ where the black circular symbols are the measured data, and the red solid lines were obtained by fitting the data using the GIXS formula; (d) in-plane scattering profile extracted from the data in (a) and (b) along the $2\theta_f$ direction at $\alpha_f = 0.190^\circ$; (e) 2D scattering image reconstructed from the structural parameters in Table 5.2 using the GIXS formula derived for lamellar structure model.....</p>	79
<p>5.6 2D GISAXS pattern of toluene-annealed PHIC(5.2k)-PCL₃(17.4k) film (120 nm thick) deposited on silicon substrates, measured at room temperature using an X-ray wavelength $\lambda = 0.1180$ nm; (a) measured with $\alpha_i = 0.110^\circ$ at SDD = 902 mm; (b) 2D scattering pattern measured with $\alpha_i = 0.140^\circ$ at SDD = 2922 mm; (c) out-of-plane scattering profile extracted from the data in (a) and (b) along the α_f direction at $2\theta_f = 0.160^\circ$ where the black circular symbols are the measured data, and the red solid lines were obtained by fitting the data using the GIXS formula; (d) in-plane scattering profile extracted from the data in (a) and (b) along the $2\theta_f$ direction at $\alpha_f = 0.190^\circ$; (e) 2D scattering image reconstructed from the structural parameters in Table 5.2 using the GIXS formula derived for lamellar structure model.....</p>	80

LIST OF FIGURES (Continued)

Figure	Page
5.7 2D GISAXS pattern of toluene-annealed PHIC(10.3k)-PCL(10.6k) film (80 nm thick) deposited on silicon substrates measured at RT using an X-ray beam ($\lambda = 0.1170$ nm); (a) measured with $\alpha_i = 0.110^\circ$ at a sample-to-detector distance (SDD) of 902 mm; (b) measured with $\alpha_i = 0.130^\circ$ at SDD = 2,935 mm; (c) out-of-plane scattering profile extracted from the data in (a) and (b) along the α_f direction at $2\theta_f = 0.100^\circ$ where the black circular symbols are the measured data, and the red solid lines were obtained by fitting the data using the GIXS formula; (d) in-plane scattering profile extracted from the data in (a) and (b) along the $2\theta_f$ direction at $\alpha_f = 0.160^\circ$; (e) 2D scattering image reconstructed from the structural parameters in Table 5.3 using the GIXS formula derived for lamellar structure model.....	83
5.8 2D GISAXS pattern of toluene-annealed PHIC(10.9k)-PCL ₂ (11.1k) film (80 nm thick) deposited on silicon substrates measured at RT using an X-ray beam ($\lambda = 0.1210$ nm); (a) measured with $\alpha_i = 0.110^\circ$ at SDD = 902 mm; (b) measured with $\alpha_i = 0.130^\circ$ at SDD = 2,935 mm; (c) out-of-plane scattering profile extracted from the data in (a) and (b) along the α_f direction at $2\theta_f = 0.100^\circ$ where the black circular symbols are the measured data, and the red solid lines were obtained by fitting the data	

LIST OF FIGURES (Continued)

Figure	Page
<p>using the GIXS formula; (d) in-plane scattering profile extracted from the data in (a) and (b) along the $2\theta_f$ direction at $\alpha_f = 0.160^\circ$; (e) 2D scattering image reconstructed from the structural parameters in Table 5.3 using the GIXS formula derived for lamellar structure model.</p>	85
<p>5.9 2D GISAXS pattern of toluene-annealed PHIC(9.6k)-PCL₃(11.0k) film (80 nm thick) deposited on silicon substrates measured at RT using an X-ray beam ($\lambda = 0.1170$ nm); (a) measured with $\alpha_i = 0.110^\circ$ at SDD = 902 mm; (b) 2D scattering pattern measured with $\alpha_i = 0.130^\circ$ at SDD = 2,935 mm; (c) out-of-plane scattering profile extracted from the data in (a) and (b) along the α_f direction at $2\theta_f = 0.100^\circ$ where the black circular symbols are the measured data, and the red solid lines were obtained by fitting the data using the GIXS formula; (d) in-plane scattering profile extracted from the data in (a) and (b) along the $2\theta_f$ direction at $\alpha_f = 0.160^\circ$; (e) 2D scattering image reconstructed from the structural parameters in Table 5.3 using the GIXS formula derived for lamellar structure model.....</p>	86
<p>5.10 2D GISAXS pattern of CHCl₃-annealed PHIC(10.3k)-PCL(10.6k) film (80 nm thick) measured at RT using an X-ray beam ($\lambda = 0.1210$ nm); (a) measured with $\alpha_i = 0.110^\circ$ at a sample-to-detector distance (SDD) of</p>	

LIST OF FIGURES (Continued)

Figure	Page
<p>902 mm; (b) measured with $\alpha_i = 0.120^\circ$ at SDD = 2,935 mm; (c) out-of-plane scattering profile extracted from the data in (a) and (b) along the α_f direction at $2\theta_f = 0.080^\circ$ where the black circular symbols are the measured data, and the red solid lines were obtained by fitting the data using the GIXS formula; (d) in-plane scattering profile extracted from the data in (a) and (b) along the $2\theta_f$ direction at $\alpha_f = 0.140^\circ$; (e) 2D scattering image reconstructed from the structural parameters in Table 5.3 using the GIXS formula derived for lamellar structure model.</p>	89
<p>5.11 2D GISAXS pattern of CHCl_3-annealed PHIC(10.9k)-PCL₂(11.1k) film (80 nm thick) measured at RT using an X-ray beam ($\lambda = 0.1170$ nm); (a) measured with $\alpha_i = 0.110^\circ$ at SDD = 902 mm; (b) measured with $\alpha_i = 0.140^\circ$ at SDD = 2,935 mm; (c) out-of-plane profile extracted from the data in (a) and (b) along the α_f direction at $2\theta_f = 0.060^\circ$ where the black circular symbols are the measured data, and the red solid lines were obtained by fitting the data using the GIXS formula; (d) in-plane profile extracted from the data in (a) and (b) along the $2\theta_f$ direction at $\alpha_f = 0.140^\circ$; (e) 2D scattering image reconstructed from the structural parameters in Table 5.3 using the GIXS formula derived for lamellar structure model.....</p>	90

LIST OF FIGURES (Continued)

Figure	Page
5.12 2D GISAXS pattern of CHCl_3 -annealed PHIC(9.6k)-PCL ₃ (11k) film (80 nm thick) measured at RT using an X-ray beam ($\lambda = 0.1170$ nm); (a) measured with $\alpha_i = 0.110^\circ$ at SDD = 902 mm; (b) 2D scattering pattern measured with $\alpha_i = 0.140^\circ$ at SDD = 2,935 mm; (c) out-of-plane profile extracted from the data in (a) and (b) along the α_f direction at $2\theta_f = 0.060^\circ$ where the black circular symbols are the measured data, and the red solid lines were obtained by fitting the data using the GIXS formula; (d) in-plane profile extracted from the data in (a) and (b) along the $2\theta_f$ direction at $\alpha_f = 0.140^\circ$; (e) 2D scattering image reconstructed from the structural parameters in Table 5.3 using the GIXS formula derived for lamellar structure model.....	91
5.13 2D GIWAXS pattern of toluene-annealed PHIC(5.4k) and PCL(14.5k) homopolymer and PHIC(5k)-PCL ₁₋₃ (17k) films (120 nm thick) deposited on silicon substrates, measured with $\alpha_i = 0.130^\circ$ at room temperature using an X-ray beam ($\lambda = 0.1120$ nm); (a) PHIC; (b) PCL; (c) PHIC-PCL; (d) PHIC-PCL ₂ ; (e) PHIC-PCL ₃ ; (f) out-of-plane scattering profiles extracted from the data in (a–e) along the α_f direction at $2\theta_f = 0.0^\circ$; (g) in-plane scattering profiles extracted from the data in (a–e) along the $2\theta_f$ direction at $\alpha_f = 0.390^\circ$. In (f) and (g), the black	

LIST OF FIGURES (Continued)

Figure	Page
<p>circular symbols are the measured data, and the red solid lines were obtained by fitting the data using the GIXS formulae.</p>	100
<p>5.14 2D GIWAXS pattern of toluene-annealed PHIC(10.4k) and PCL(10.5k) homopolymer and the PHIC(10k)-PCL₁₋₃(10k) films (80 nm thick) measured at RT using an X-ray beam ($\lambda = 0.1120$ nm) $\alpha_i = 0.130^\circ$ at SDD = 229 mm; (a) PHIC; (b) PCL; (c) PHIC-PCL; (d) PHIC-PCL₂; (e) PHIC-PCL₃; (f) out-of-plane scattering profiles extracted from the data in (a–e) along the α_f direction at $2\theta_f = 0.0^\circ$; (g) in-plane scattering profiles extracted from the data in (a–e) along the $2\theta_f$ direction at $\alpha_f = 0.300^\circ$. In (f) and (g), the black circular symbols are the measured data, and the red solid lines were obtained by fitting the data using the GIXS formulae.</p>	101
<p>5.15 2D GIWAXS pattern of CHCl₃-annealed PHIC(10.4k) and PCL(10.5k) homopolymer and the PHIC(10k)-PCL₁₋₃(10k) films (80 nm thick) measured at RT using an X-ray beam with $\alpha_i = 0.140^\circ$ at SDD = 229 mm; the X-ray wavelength $\lambda = 0.1180$ nm was used in (a) PHIC; $\lambda = 0.1110$ nm was used in (b) PCL; in (c) PHIC-PCL; in (d) PHIC-PCL₂; in (e) PHIC-PCL₃; (f) out-of-plane scattering profiles extracted from the data in (a–e) along the α_f direction at $2\theta_f = 0.0^\circ$; (g) in-plane scattering profiles extracted from the data in (a–e) along the $2\theta_f$ direction at $\alpha_f =$</p>	

LIST OF FIGURES (Continued)

Figure	Page
<p>0.260°. In (f) and (g), the black circular symbols are the measured data, and the red solid lines were obtained by fitting the data using the GIXS formulae.....</p>	102
<p>5.16 Schematic representations of molecular chain conformation in CHCl₃-annealed PHIC (10.4k) thin films (a); (b) horizontal multibilayer structure where \mathbf{n}_2 is the orientation vector of the structure model and φ_2 is the polar angle between the \mathbf{n}_2 vector and the out-of-plane of the film; (c) top and side views of molecular chain conformation and packing order with no interdigitation in the structure (b); (d) relative electron density profile along the out-of-plane of the multibilayer structure where ρ_L and ρ_H are the relative electron densities of less and highly dense sublayer respectively; (e) the picture of molecular chain conformation in toluene-annealed PHIC (5.4k, 10.4k) thin films; (f) horizontal and vertical multibilayer structure; (g) side view of molecular chain conformation and packing order with no interdigitation in the horizontal structure (f).....</p>	108
<p>5.17 Schematic representation of molecular chain conformation and packing order in toluene-annealed PCL(15k) and toluene- and CHCl₃-annealed PCL(10.5k) films; (a–c) horizontal lamellar structure in PCL film where \mathbf{n}_1 is the orientation vector has the axis normal to the structure and φ_l is</p>	

LIST OF FIGURES (Continued)

Figure	Page
<p>the polar angle between the \mathbf{n}_1 vector and the out-of-plane direction of the film; (d) the relative electron density profile which ρ_c, ρ_i, and ρ_a are the relative electron densities of crystal, interface, and amorphous layers respectively; (e) molecular chain conformations in the amorphous layers and molecular chain order in the crystalline layers; (f) horizontally oriented orthorhombic crystal lattice where \mathbf{n}_3 is the orientation vector of the structure model and φ_3 is the polar angle between the \mathbf{n}_3 vector and the out-of-plane of the film; (g) vertically oriented orthorhombic crystal lattice.....</p>	109
<p>5.18 Schematic representations of molecular chain conformations and packing orders in toluene-annealed PHIC(5k)-PCL₁₋₃(17k) and toluene- and CHCl₃-annealed PHIC(10k)-PCL₁₋₃(10k) films: (a-c) horizontal lamellar structure and the orientation vector \mathbf{n}_1 of the structure model; (d) the relative electron densities profile where ρ_{PHIC}, ρ_i, and ρ_{PCL} are the relative electron densities of PHIC, interface, and PCL layers respectively. (e) horizontal multibilayer structure formed in the PHIC lamella where \mathbf{n}_2 is the orientation vector of the structure model. (f) vertical multibilayer structure formed in the PHIC lamella; (g) top and side views of molecular chain and packing order; (h) relative electron density profile along the out-of-plane of the multibilayer structure; (i)</p>	

LIST OF FIGURES (Continued)

Figure	Page
molecular chain conformations and order in the PCL layers; (j) horizontally oriented orthorhombic crystal lattice where \mathbf{n}_3 is the orientation vector of the structure model; (k) vertically oriented orthorhombic crystal lattice	110
6.1 2D GISAXS patterns of CHCl_3 -annealed PHIC and PLLA homopolymer films in approximate 80 nm thick measured with an incidence angle α_i of 0.130° at room temperature using an X-ray beam with a wavelength λ of 0.1170 nm; (a) PHIC film; (b) out-of-plane 1D scattering profile extracted from the data in (a) along the α_f direction at $2\theta_f = 0.100^\circ$; (c) in-plane 1D scattering profile extracted from the data in (a) along the $2\theta_f$ direction at $\alpha_f = 0.170^\circ$; (d) PLLA film; (e) out-of-plane scattering profile extracted from the data in (d) along the α_f direction at $2\theta_f = 0.100^\circ$; (f) in-plane scattering profile extracted from the data in (d) along the $2\theta_f$ direction at $\alpha_f = 0.170^\circ$; where α_f and $2\theta_f$ are the exit angles of the X-ray beam with respect to the film surface and to the plane of incidence respectively.....	119
6.2 2D GISAXS patterns of thermal annealing on PLLA homopolymer films in approximate 80 nm thick measured with an incidence angle α_i of 0.130° at room temperature using an X-ray beam with a wavelength λ of 0.1210 nm; (a) PLLA film; (b) out-of-plane 1D scattering profile	

LIST OF FIGURES (Continued)

Figure	Page
<p>extracted from the data in (a) along the α_f direction at $2\theta_f = 0.080^\circ$; (c) in-plane 1D scattering profile extracted from the data in (a) along the $2\theta_f$ direction at $\alpha_f = 0.150^\circ$; (d) 2D image of PCL film reconstructed from the structural parameters in Table 6.2 using the GIXS formula derived for three layer lamellar structural model; (e) lamellar structure model where \mathbf{n}_1 is the orientation vector of the structure model and φ_4 is the polar angle between the \mathbf{n}_1 vector and the out-of-plane of the film. In (b) and (c), the black circular symbols are the measured data, and the red solid lines represented as a fitting result from the GIXS formula.</p>	120
<p>6.3 2D GISAXS pattern of CHCl_3-annealed PHIC-PLLA film (approximate 75 nm thick) measured at room temperature using an X-ray beam ($\lambda = 0.1140$ nm); (a) measured with $\alpha_i = 0.110^\circ$ at a sample-to-detector distance (SDD) of 2,917 mm; (b) out-of-plane scattering profile extracted from the data in (a) along the α_f direction at $2\theta_f = 0.070^\circ$; (c) in-plane scattering profile extracted from the data in (a) along the $2\theta_f$ direction at $\alpha_f = 0.140^\circ$ where the black circular symbols are the measured data, and the red solid lines were obtained by fitting the data using the GIXS formula; (d) 2D scattering image reconstructed from the structural parameters in Table 6.2 using the GIXS formula derived for lamellar structure model.</p>	122

LIST OF FIGURES (Continued)

Figure	Page
6.4 2D GISAXS pattern of toluene-annealed PHIC-PLLA ₂ film (approximate 75 nm thick) measured at room temperature using an X-ray beam ($\lambda = 0.1140$ nm); (a) measured with $\alpha_i = 0.110^\circ$ at SDD = 2,917 mm; (b) out-of-plane scattering profile extracted from the data in (a) along the α_f direction at $2\theta_f = 0.070^\circ$ where the black circular symbols are the measured data, and the red solid lines were obtained by fitting the data using the GIXS formula; (c) in-plane scattering profile extracted from the data in (a) along the α_f direction at $\alpha_f = 0.140^\circ$ where the black circular symbols are the measured data, and the red solid lines were obtained by fitting the data using the GIXS formula; (d) 2D scattering image reconstructed from the structural parameters in Table 6.2 using the GIXS formula derived for lamellar structure model.	125
6.5 2D GISAXS pattern of toluene-annealed PHIC-PLLA ₃ film (approximate 75 nm thick) measured at room temperature using an X-ray beam ($\lambda = 0.1140$ nm); (a) measured with $\alpha_i = 0.110^\circ$ at SDD = 2,917 mm; (b) out-of-plane scattering profile extracted from the data in (a) and (b) along the α_f direction at $2\theta_f = 0.070^\circ$; (c) in-plane scattering profile extracted from the data in (a) and (b) along the $2\theta_f$ direction at $\alpha_f = 0.140^\circ$ where the black circular symbols are the measured data, and the red solid lines were obtained by fitting the data using the GIXS formula; (d) 2D scattering image reconstructed from the structural	

LIST OF FIGURES (Continued)

Figure	Page
parameters in Table 6.2 using the GIXS formula derived for lamellar structure model.....	126
6.6 2D GISAXS pattern of thermal annealing on PHIC-PLLA film (approximate 75 nm thick) measured at room temperature using an X-ray beam ($\lambda = 0.1210$ nm); (a) measured with $\alpha_i = 0.140^\circ$ at a sample-to-detector distance (SDD) 2,917 mm; (b) out-of-plane scattering profile extracted from the data in (a) along the α_f direction at $2\theta_f = 0.070^\circ$; (c) in-plane scattering profile extracted from the data in (a) along the $2\theta_f$ direction at $\alpha_f = 0.150^\circ$ where the black circular symbols are the measured data, and the red solid lines were obtained by fitting the data using the GIXS formula; (d) 2D scattering image reconstructed from the structural parameters in Table 6.4 using the GIXS formula derived for lamellar structure model.	128
6.7 2D GISAXS pattern of thermal annealing on PHIC-PLLA ₂ film (approximate 75 nm thick) measured at room temperature using an X-ray beam ($\lambda = 0.1210$ nm); (a) measured with $\alpha_i = 0.140^\circ$ at SDD =2,917 mm; (b) out-of-plane scattering profile extracted from the data in (a) along the α_f direction at $2\theta_f = 0.070^\circ$; (c) in-plane scattering profile extracted from the data in (a) along the $2\theta_f$ direction at $\alpha_f = 0.150^\circ$ where the black circular symbols are the measured data, and the red solid lines were obtained by fitting the data using the GIXS formula; (d) 2D	

LIST OF FIGURES (Continued)

Figure	Page
<p>scattering image reconstructed from the structural parameters in Table 6.4 using the GIXS formula derived for lamellar structure model.....</p>	129
<p>6.8 2D GISAXS pattern of thermal annealing on PHIC-PLLA₃ film (approximate 80 nm thick) measured at room temperature using an X-ray beam ($\lambda = 0.1210$ nm); (a) measured with $\alpha_i = 0.140^\circ$ at SDD = 2,917 mm; (b) out-of-plane scattering profile extracted from the data in (a) along the α_f direction at $2\theta_f = 0.070^\circ$; (c) in-plane scattering profile extracted from the data in (a) along the $2\theta_f$ direction at $\alpha_f = 0.150^\circ$ where the black circular symbols are the measured data, and the red solid lines were obtained by fitting the data using the GIXS formula. (d) 2D scattering image reconstructed from the structural parameters in Table 6.4 using the GIXS formula derived for lamellar structure model.</p>	130
<p>6.9 2D GIWAXS pattern of CHCl₃-annealed PHIC and PLLA homopolymer (approximate 80 nm thick) and the star polymers films (approximate 75 nm thick) deposited on silicon substrates, measured at room temperature using an X-ray beam ($\lambda = 0.1120$ nm and 0.1180 nm) $\alpha_i = 0.160^\circ$ at SDD = 240 mm; (a) PHIC; (b) PLLA; (c) PHIC-PLLA; (d) PHIC-PLLA₂; (e) PHIC-PLLA₃; (f) out-of-plane scattering profiles extracted from the data in (a–e) along the α_f direction at $2\theta_f = 0.0^\circ$; (g) in-plane</p>	

LIST OF FIGURES (Continued)

Figure	Page
<p>scattering profiles extracted from the data in (a–e) along the $2\theta_f$ direction at $\alpha_f = 0.280^\circ$. In (f) and (g), the black circular symbols are the measured data, and the red solid lines were obtained by fitting the data using the GIXS formulae.....</p>	138
<p>6.10 2D GIWAXS pattern of thermal annealing on PLLA homopolymer (approximate 80 nm thick) and the PHIC-PLLA₁₋₃ films (approximate 75 nm thick) measured at room temperature using an X-ray beam ($\lambda = 0.1120$ nm) $\alpha_i = 0.160^\circ$ at SDD = 240 mm; (a) PLLA; (b) PHIC-PLLA; (c) PHIC-PLLA₂; (d) PHIC-PLLA₃; (e) out-of-plane scattering profiles extracted from the data in (a–d) along the α_f direction at $2\theta_f = 0.0^\circ$; (f) in-plane scattering profiles extracted from the data in (a–d) along the $2\theta_f$ direction at $\alpha_f = 0.290^\circ$. In (e) and (f), the black circular symbols are the measured data, and the red solid lines were obtained by fitting the data using the GIXS formulae</p>	139
<p>6.11 Schematic representations of molecular chain conformation in CHCl₃-annealed PHIC thin films (a); (b) horizontal multibilayer structure where \mathbf{n}_2 is the orientation vector of the structure model and φ_2 is the polar angle between the \mathbf{n}_2 vector and the out-of-plane of the film; (c) top and side views of molecular chain conformation and packing order with no interdigitation in the structure (b); (d) relative electron density profile</p>	

LIST OF FIGURES (Continued)

Figure	Page
<p>along the out-of-plane of the multibilayer structure where ρ_L and ρ_H are the relative electron densities of less and highly dense sublayer respectively; (e) vertical multibilayer structure; (f) side view of molecular chain conformation and packing order with no interdigitation in the structure (e).....</p>	143
<p>6.12 schematic representations of molecular chain conformation and packing order in thermal- and CHCl_3-annealed PLLA film in (a) and (i) respectively; (b–d) horizontal lamellar structure in PLLA film where \mathbf{n}_1 is the orientation vector has the axis normal to the structure and φ_l is the polar angle between the \mathbf{n}_1 vector and the out-of-plane direction of the film; (e) the relative electron density profile which ρ_c, ρ_i, and ρ_a are the relative electron densities of crystal, interface, and amorphous layers respectively; (f) molecular chain conformations in the amorphous layers and molecular chain order in the crystalline layers; (g) horizontally oriented orthorhombic crystal lattice where \mathbf{n}_3 is the orientation vector of the structure model and φ_3 is the polar angle between the \mathbf{n}_3 vector and the out-of-plane of the film; (h) vertically oriented orthorhombic crystal lattice.....</p>	144
<p>6.13 schematic representations of molecular chain conformations and packing orders in CHCl_3- and thermal-annealed PHIC-PLLA₁₋₃ films: (a-c)</p>	

LIST OF FIGURES (Continued)

Figure	Page
<p>vertical lamellar structure and the orientation vector \mathbf{n}_1 of the structure model; (d) the relative electron densities profile where ρ_{PHIC}, ρ_i, and ρ_{PLLA} are the relative electron densities of PHIC, interface, and PLLA layers respectively; (e) horizontal multibilayer structure formed in the PHIC lamella where \mathbf{n}_2 is the orientation vector of the structure model; (f) vertical multibilayer structure formed in the PHIC lamella; (g) top and side views of molecular chain and packing order with no interdigitation in the structure; (h) relative electron density profile along the out-of-plane of the multibilayer structure; (i) horizontally oriented orthorhombic crystal lattice in the PLLA layers where \mathbf{n}_3 is the orientation vector of the structure model; (j) vertically oriented orthorhombic crystal lattice in the PLLA layers. The structure in (e-j) could not obtain in the thermal-annealed PHIC-PLLA₃ film.....</p>	145

LIST OF ABBREVIATIONS

SAXS	=	Small Angle X-rays Scattering
GIXS	=	Grazing Incident X-ray Scattering
GOD	=	Glucose oxidase
PHIC-PCL	=	Poly(n-hexyl isocyanate)- <i>block</i> -Poly(ϵ -caprolactone)
PHIC	=	Poly(n-hexyl isocyanate)
PCL	=	Poly(ϵ -caprolactone)
PHIC-PLLA	=	Poly(n-hexyl isocyanate)- <i>block</i> -Poly(L-lactid acid)
PLLA	=	Poly(L-lactid acid)
NMR	=	Nuclear Magnetic Resonance
TEM	=	Transmission Electron Microscopy
SEM	=	Scanning Electron Microscopy
STM	=	Scanning Tunneling Microscopy
AFM	=	Atomic Force Microscopy
2D CCD	=	Two Dimensions Charge Couple Detector
SDD	=	Sample to Detector Distance
BA	=	Born Approximation
PDB	=	Protein Data Bank
NSD	=	Normalized Spatial Discrepancy
FAD	=	Flavin Adenine Dinucleotide
SDS	=	Sodium Dodecyl Sulfate

LIST OF ABBREVIATIONS (Continued)

GISAXS	=	Grazing Incident Small Angle X-rays Scattering
GIWAXS	=	Grazing Incident Wide Angle X-ray Scattering
DWBA	=	Distorted Wave Born approximation
FWHM	=	Full Width at Half Maximum
PAL	=	Pohang Accelerator Laboratory



CHAPTER I

INTRODUCTION

1.1 Motivation

Nanomaterials have important applications in many fields of research and industry. Industrial developments are moving toward applications of nanostructures in everyday life (Teichert, 2002). For instance, the continuing trend of reducing the size in electronics is reaching the scale of nanometer. In fact, it is impossible to avoid nanoobjects in real life, as they are frequently mixed into a complex matrix of the finished products. These can be found in consumer products, including cosmetics and health care, and also in food and feeds products.

Nanomaterials are usually defined as materials having structural size in the nanometer range, i.e. one to a few hundred nanometers in at least one dimension. At this scale, their physical and chemical properties change significantly by comparison to their macroscopic properties. One reason is that quantum effects will become dominant at this small scale. In addition, behaviors of nano objects, due to the optical, electrical and magnetic properties, are very different from their macroscale counterparts. For example, the catalytic reactions made of supported metallic nanoparticles depend on the particle size, shape and internal structures (Henry, 1998; Meyer *et al.*, 2004). Also, the magnetic storage properties of FePt nanoparticles and ferromagnetic FePt nanocrystals superlattice assemblies are related to particle size, composition, crystal structure and interparticle spacing (Sun *et al.*, 2000). The other

reason is that nanomaterials have a larger surface area per volume compared to macroscopic materials. Thus, the nanomaterials have higher chemical reactive strength. One example is gold, which is chemically inert in their macroscale form, but at nanoscale, with the larger surface area per volume, gold nanoparticles can behave as a chemical catalyst (Meyer *et al.*, 2004). The combination of nanoparticles and polymer also provides strong interfacial interactions influencing properties of the material due to large surface interface of the polymer nanocomposites (Ash *et al.*, 2002).

Since properties of nanomaterials depend much on their nanostructures, understanding the material properties therefore involves characterization of the nanostructures. This requires characterization tools that allow objects to be examined with sufficient precision in nanoscale. The X-ray scattering techniques such as Small Angle X-ray Scattering (SAXS) and Grazing Incident X-ray Scattering (GIXS) are powerful analytical techniques that enable us to examine morphological information, such as shape, size, and structure, of an object in the range of nanoscale.

The fundamental of SAXS and GIXS is based on an X-ray scattering method that uses the scattering phenomena of an X-ray to analyze structures of interested material, particularly in the nanometer range. SAXS method has capability of monitoring morphology and structures of samples in bulk solid and solution forms (Glatter, and Kratky, 1982; Guinier, and Fournet, 1995; Brumberger, 1993), while GIXS allows us to investigate samples in thin film form (Renaud, Lazzari, and Leroy, 2009; Müller-Buschbaum, 2009). It should be kept in mind that the morphology and structures of material in the bulk and/or solution forms are different from those of the thin film form, even though they are the same kind of material (Hamley, 2009). Since

the film thickness is very thin, typically in order of nanometers, it has an effect on the self-assembly behavior of the material in the film, thus their morphology and structure could be different from those in the solid and/or solution state. In addition, these characterization techniques usually require the use of high intensity monochromatic X-ray beam with very low divergence, they therefore require an x-ray beam from a synchrotron light source.

In this thesis, we used high brilliance synchrotron SAXS and GIXS techniques to characterize nanostructure information of material. In particular, we used SAXS to investigate the molecular structure of Glucose oxidase (GOD) enzyme. By using this method, the effects of acids and alkalis on GOD conformations (folded, unfolded, and partially unfolded state) were revealed. For GIXS study, the rod-coil type miktoarm star polymers thin films have been characterized. The GIXS studied samples were PHIC-PCL₁₋₃ (poly(n-hexyl isocyanate)-*block*-poly(ϵ -caprolactone)) with a number-average molecular weight (M_n) of approximate 5,000 for PHIC arm and one to three poly(ϵ -caprolactone) arms (PCL_{*n*}: $n = 1-3$) with a total M_n of approximate 17,000. Another series of PHIC-PCL₁₋₃, having a total approximate M_n of PHIC domain was 10,000 and of the one to three poly(ϵ -caprolactone) domain was 10,000. Another samples was PHIC-PLLA₁₋₃ (poly(n-hexyl isocyanate)-*block*-poly(L-lactid acid)) with the M_n of approximate 10,000 for both PHIC arm and one to three poly(L-lactid acid) (PLLA_{*n*}: $n = 1-3$) arms. The effects of solvent and thermal annealing on the self-assembled behavior of these polymer films were determined.

1.2 X-ray scattering method

The principle of the X-ray scattering method involves interaction between an X-

ray and an electron cloud of an object. When the X-ray hit the object, the incident X-ray waves oscillate the electrons, then the oscillated electrons generate and emerge the scattering waves come out in all directions. Where the collision is elastic or the X-ray wavelength is conserved, this process is known as coherent scattering. However, if the X-ray wavelength is changed during the process, it is called the incoherent scattering. SAXS and GIXS are the examples of the coherent scattering process.

1.2.1 Small angle X-rays scattering

By letting the X-ray directs toward the object, then the X-ray beam encounters with electrons, then scatter. After that, a CCD detector was placed far away from the object in order to collect the scatter beam at small scattering angle. This measurement is known as small angle X-ray scattering (SAXS) technique. SAXS is the standard tool to characterize the morphology and structure of a nanomaterial. The technique is also able to reveal other valuable pieces of information such as molecular weight (Brumberger, 1993), volume fraction (Brumberger, 1993; Cabane, Duplessix, and Zemb, 1985), total surface area per volume (Brumberger, 1993; Hayter, and Penfold, 1983; Cabane, Duplessix, and Zemb, 1985; Wignall, and Bates, 1987), specific surface area (Brumberger, 1993; Hayter, and Penfold, 1983; Cabane, Duplessix, and Zemb, 1985; Wignall, and Bates, 1987), and the characteristic distances between ordered or partially ordered structures. Several types of samples can be used, including liquid, solid, powder, polymer, fiber and gel. The advantages of SAXS approach can be explained as follow (Glatter, and Kratky, 1982; Guinier, and Fournet, 1995; Brumberger, 1993; Agbabiaka, Wiltfong, and Park, 2013). The method is fast experiment and easy to measure. Moreover, the technique is non-destructive, easy and needs small amount of sample in sample preparation. It is allowed to examine during

the chemical interaction and phase transition. It also can be performed under various environments (from gas atmospheres to high vacuum) and in situ experiment. Furthermore, it gives the average structure over all illuminated sample. Due to these wide applications and advantages, SAXS has been utilized in various branches of science, including metallurgy, polymer science, nanomaterials science and biology (Glatter, and Kratky, 1982; Guinier, and Fournet, 1995; Brumberger, 1993).

For the study of protein structure, SAXS and other techniques such as Crystallography and Nuclear magnetic resonance (NMR) spectroscopy have been conducted as a complementary method due to their limitations (Svergun, 2007). Crystallography technique needs to make a crystalline protein, and NMR spectroscopy has the upper limit on molecular weight of the protein. SAXS can provide only the low resolution data, while Crystallography and NMR spectroscopy give the high resolution results. The SAXS studies on protein structure usually need to compare with the protein structure from Crystallography and/or NMR spectroscopy in order to check and confirm the accuracy of the structure (Putnam *et al.*, 2007; Svergun, and Koch, 2003).

1.2.2 Grazing incident X-rays scattering

It is similar to the SAXS technique that the X-ray is used to collide on the object, but the incident angle of the X-ray is in the grazing angle which is very small and in between a critical angle of the object and a substrate. From this result, the X-ray cannot transmit through the substrate. It will pass through the surface or nearly surface interface of the object. Thus, grazing incident X-ray scattering (GIXS) provides the possibilities to investigate the surface and interface of the sample. GIXS is also one of the most powerful tools to study morphological (size and shape) and

structure information of the surface and interface of a nanomaterial. Moreover, the method has been used widely characterized surfaces, interface surfaces, buried interfaces, thin layer, and multilayer (Renaud, Lazzari, and Leroy, 2009; Müller-Buschbaum, 2009).

There are some other methods which capable to provide information of the surface structure of nanomaterials as well, i.e. transmission electron microscopy (TEM), scanning electron microscopy (SEM), scanning tunneling microscopy (STM) and atomic force microscopy (AFM). Although these methods can give that information, they still have some limitations (Müller-Buschbaum, 2009). For example, TEM needs the thin sample and has limit of averaged statistical sample which is difficult to do in situ experiments. STM requires conduction sample and takes time in the experiment. Moreover, all these techniques can not probe the particles burry or below a surface and inner structures of a surface layers.

GIXS has several advantages that overcome those methods and can be summarized as follows (Renaud, Lazzari, and Leroy, 2009; Müller-Buschbaum, 2009). Firstly, the technique is not invasive and destructive a sample. Secondly, it gives the averaged information over the entire illuminated surface sample. Thirdly, the method has ability to examine from surface to buried interface by using the different incident angles. Fourthly, GIXS can probe the structure in any kind of environment from ultra-high vacuum to gas atmospheres, chemical reactions, phase transitions, and in situ. Lastly, it can measure without any special treatment and preparation on sample. Due to their advantages that describe above, GIXS technique has been well known and used widely to analyze the polymer films for many years

(Renaud, Lazzari, and Leroy, 2009; Müller-Buschbaum, 2009; Müller-Buschbaum, 2003; Xu *et al.*, 2004; Lee *et al.*, 2005; Yoon *et al.*, 2008).

1.3 Outline of Thesis

This thesis contains the details of the analytical powerful tools, i.e. SAXS and GIXS as well as their utilization on determine morphological information and structure of Glucose oxidase (GOD) enzyme and PHIC-PCL₁₋₃ and PHIC-PLLA₁₋₃ rod-coil type miktoarms star polymers thin films. SAXS has been used to determine the Glucose oxidase structure, while GIXS has been used to characterize the PHIC-PCL₁₋₃ and PHIC-PLLA₁₋₃ thin films structure. The organization of this thesis is as follows. In Chapter II, the review of SAXS geometry and theory on the study of the GOD enzyme structure is given. In Chapter III, the effects of acids and alkalis on the folded, unfolded, and partially unfolded states of the GOD enzyme are revealed and discussed. The brief details of GIXS geometry and theoretical study of the structure of polymer in the film form is given in Chapter IV. The quantitative GIXS analyses on the self-assembled behaviors of the PHIC-PCL₁₋₃ films under the toluene and CHCl₃ annealing have been investigated in Chapter V. The self-assembled behaviors due to the effects of CHCl₃ and thermal annealing on the PHIC-PLLA₁₋₃ films have been also studied and discussed in Chapter VI. Finally, the conclusions of the thesis are given in Chapter VII.

CHAPTER II

THEORETICAL BACKGROUND FOR SMALL ANGLE X-RAY SCATTERING ANALYSIS OF ENZYME

SOLUTION

Small angle X-ray scattering (SAXS) is a technique used to investigate the morphology and structural information of a material in a range of nanometer. The basic of the technique involves with the X-rays collide on an object. When the X-ray hits the object, the photons of the X-rays interact with the electrons of the object, after that, the X-rays scatter. Lastly, a detector is placed quite a distance from the object to detect the scattering data at small angle. The scattering data correspond to the nanostructure of the object.

In this work, we focus on the analysis of biological macromolecules in solution, i.e. glucose oxidase (GOD) enzyme, using SAXS method. The theoretical methodology utilized for characterizing the enzyme structure is reviewed in this chapter.

2.1 SAXS Geometry

In a typical SAXS experiment, a monochromatic X-rays beam from a high brilliance synchrotron radiation source hit on a sample with a wave vector \vec{k}_i . Later,

the X-rays beam scatter into a detector at the scattering angle 2θ , with the wave vector \vec{k}_f as shown in Figure 2.1.

The X-ray scattering method can be considered as the incoming X-ray waves interact with electrons. After that, the X-ray waves scatter in all directions. When the scattering waves emerge in a detector direction, the waves interfere with each other causes the waves are constructive and destructive due to they are in phase and out of phase, respectively. Therefore, the X-ray scattering data at the detector are the result of the wave interference. The interference relates to the scatterers positions, thus it refers to structure information of the sample.

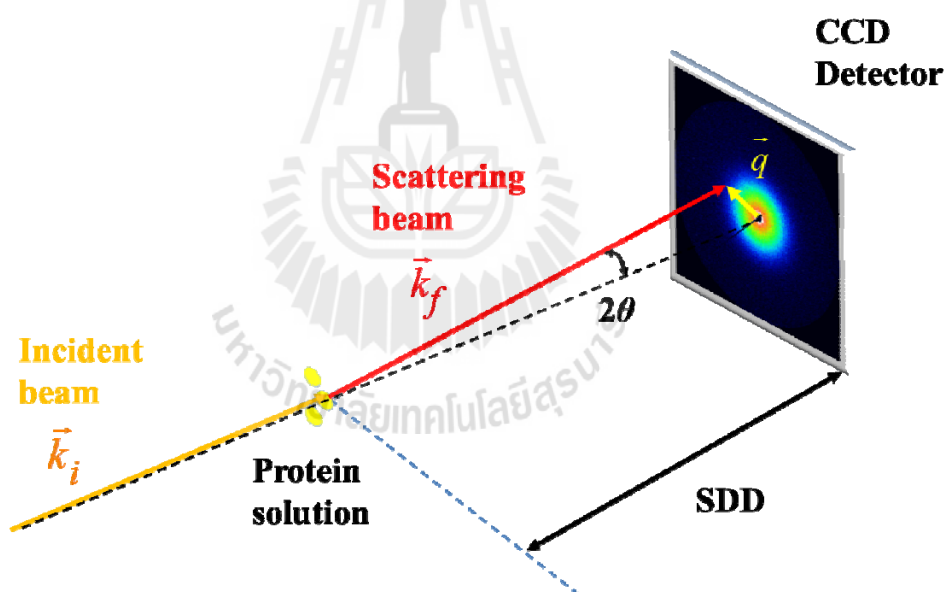


Figure 2.1 Schematic representation of SAXS geometry. The incident X-rays beam is directed to a sample (protein solution) with wave vector \vec{k}_i and exits as the scattering X-ray beam at exit angle 2θ with wave vectors (\vec{k}_f). The scattering data is detected by a two dimensions charge-couple detector (2D CCD) depending on the scattering vector \vec{q} . The distance between the sample and the detector is SDD.

To understand more about the X-ray scattering, it is very convenient to consider the X-ray scattering from only the two point scatterers system as shown in Figure 2.2. The incoming plane waves travel along a vector \vec{S}_0 and hit on the scatterers at point j and k with their relative position is \vec{r} . Then, scatter as a spherical waves in a direction along a vector \vec{S} , lastly, interference and collected by the detector. When the waves scatter from the point j and k at the detector are in phase. The scattering data are the combination of the two scattering waves that have the same amplitude but difference in phase position. The phase difference ($\Delta\phi$) is defined from the difference of path length between the two point scatterers (δ) as

$$\Delta\phi = \frac{2\pi\delta}{\lambda} \quad (2.2)$$

$$\Delta\phi = \frac{-2\pi}{\lambda} (\vec{S}\cdot\vec{r} - \vec{S}_0\cdot\vec{r}) = \frac{-2\pi}{\lambda} \vec{s}\cdot\vec{r} \quad (2.3)$$

Where \vec{s} is

$$\vec{s} = \vec{S} - \vec{S}_0 \quad (2.4)$$

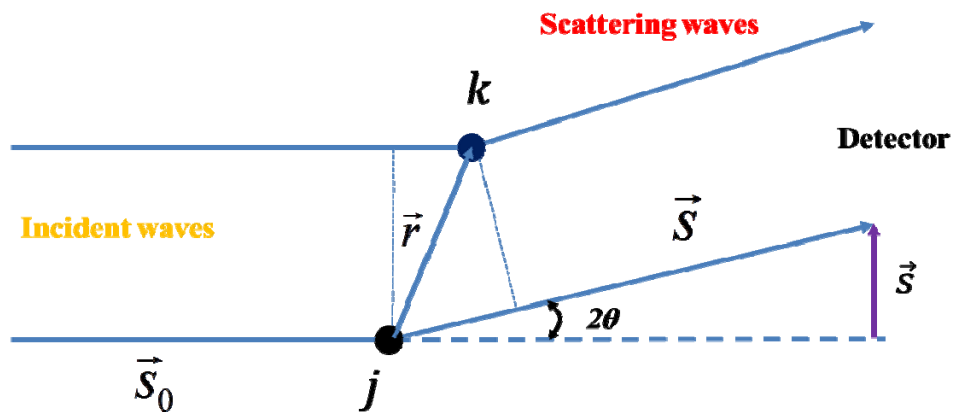


Figure 2.2 The scattering geometry from the two point scatterers system.

And, the magnitude of \vec{s} is

$$s = 2 \sin \theta \quad (2.5)$$

Here, λ is the X-ray wavelength and θ is half a scattering angle. Moreover, the term of scattering vector \vec{q} can be given from the \vec{s} as

$$\vec{q} = \frac{2\pi\vec{s}}{\lambda} \quad (2.6)$$

Also, the magnitude of \vec{q} is written as

$$q = \frac{2\pi s}{\lambda} = \frac{4\pi}{\lambda} \sin \theta \quad (2.7)$$

In addition, the scattering vector \vec{q} can be defined from the difference of scattering (\vec{k}_f) and incident (\vec{k}_i) wave vectors as

$$\vec{q} = \vec{k}_f - \vec{k}_i = \frac{2\pi}{\lambda} (\vec{S} - \vec{S}_0) \quad (2.8)$$

Since the scattering waves $A(x, t)$ can be considered as a wave with a magnitude A_0 oscillates with a frequency ν and wavelength λ traveling in the x direction to the detector at time t that is

$$A(x, t) = A_0 b e^{i2\pi(\nu t - x/\lambda)} \quad (2.9)$$

Here, b is known as a scattering length that refers to the ability of scattering from a scatterer.

Therefore, the scattering amplitude from the two scatteres at point j ($A_j(x, t)$) and k ($A_k(x, t)$) which arrives at the detector will be

$$A_{jk}(x, t) = A_j(x, t) + A_k(x, t) \quad (2.10)$$

$$= A_0 b e^{i2\pi(\nu t - x/\lambda)} (1 + e^{-i\vec{q} \cdot \vec{r}}) \quad (2.11)$$

The magnitude of the scattered waves is

$$F_{jk} = |A_{jk}(x, t)|^2 = A_{jk}(x, t)A_{jk}^*(x, t) \quad (2.12)$$

$$= A_0^2 b^2 (1 + e^{-i\vec{q} \cdot \vec{r}})(1 + e^{i\vec{q} \cdot \vec{r}}) \quad (2.13)$$

The magnitude F_{jk} does not depend on the $e^{i2\pi(vt-x/\lambda)}$ term as the term of $e^{i2\pi(vt-x/\lambda)}$ and $e^{-i2\pi(vt-x/\lambda)}$ are cancel each other. Thus, we can consider the scattering amplitude as

$$A_{jk}(\vec{q}) = A_0 b (1 + e^{-i\vec{q} \cdot \vec{r}}) \quad (2.14)$$

Since the X-ray scattering phenomena happen from the X-ray waves interact with an object. Besides, there are many electrons inside of the object, hence the scattering amplitude $A(\vec{q})$ can be obtained by summing all scattering waves due to scattered electrons over the whole irradiated volume (V). The scattering amplitude can be defined as

$$A(\vec{q}) = A_0 b \sum_{i=1}^N e^{-i\vec{q} \cdot \vec{r}_i} \quad (2.15)$$

where N is number of scatterers and \vec{r}_i denotes as the position from center to the scatterer i^{th} .

Furthermore, considering a small volume dV at \vec{r} position, it will contain electrons as $n(\vec{r}) dV$. Where $n(\vec{r})$ is the number of electrons per volume (V). When the dV is close to zero or the value of $n(\vec{r})$ is vary continuously, the summation notation can be replaced by an integral form. The scattering amplitude can be determined as

$$A(\vec{q}) = A_0 b \int n(\vec{r}) e^{-i\vec{q} \cdot \vec{r}} dV \quad (2.16)$$

The term of $bn(\vec{r})$ is equal to

$$bn(\vec{r}) = \rho(\vec{r}) \quad (2.17)$$

When $\rho(\vec{r})$ is the scattering length density distribution. Thus, the scattering waves can be given in the term of $\rho(\vec{r})$ as

$$A(\vec{q}) = A_0 \int \rho(\vec{r}) e^{-i\vec{q}\cdot\vec{r}} dV \quad (2.18)$$

Here, the differential cross section is given by ratio of the absolute square of the scattering amplitude and the absolute square of the incident amplitude as

$$\frac{d\sigma}{d\Omega} = \frac{|A(\vec{q})|^2}{|A_0|^2} \quad (2.19)$$

In addition, the intensity can be defined from the differential cross section as

$$I(\vec{q}) = \frac{d\sigma}{d\Omega} \quad (2.20)$$

2.2 Scattering Intensity of Enzyme Solution

In this work, we are interested in an enzyme that is suspended in the solvent or considering in a monodisperse enzyme solution (assuming that the enzyme particles have the same size and shape with no interaction between the enzyme particles). Only molecular morphology of the enzyme is investigated not its orientation and relative position. Thus, the scattering intensity of the enzyme solution is isotropic and corresponds to the scattering intensity from the single enzyme particle with average all directions (Guinier, and Fournet, 1955; Glatter, and Kratky, 1982).

As from the equations (2.18)-(2.20), the observed scattering intensity from all the scattered electrons can be written as

$$I(\vec{q}) = A^*(\vec{q})A(\vec{q}) = \iint \rho(\vec{r}_1)\rho(\vec{r}_2)e^{i\vec{q}\cdot(\vec{r}_1-\vec{r}_2)}dV_1dV_2 \quad (2.21)$$

Let $\vec{r} = \vec{r}_1 - \vec{r}_2$ or $\vec{r}_2 = \vec{r}_1 - \vec{r}$, where \vec{r} is the relative distance for every pair of the electrons. Then, we consider the auto-correlation ($\tilde{\rho}^2(\vec{r})$) function, which is the average value of scattering length density of the electron pair at the separate \vec{r} distance over the whole sample, is defined as

$$\tilde{\rho}^2(\vec{r}) = \int \rho(\vec{r}_1)\rho(\vec{r}_1 - \vec{r})dV_1 \quad (2.22)$$

Therefore, the $I(\vec{q})$ is rewritten as

$$I(\vec{q}) = \int \tilde{\rho}^2(\vec{r})e^{i\vec{q}\cdot\vec{r}}dV \quad (2.23)$$

Due to the scattering from the monodisperse solution, this scattering system is isotropic. The parameter $\tilde{\rho}^2(\vec{r})$ depends on modulus of r but not the direction of \vec{r} and the value of $e^{i\vec{q}\cdot\vec{r}}$ can be determined as the averaged in all the \vec{r} directions. By integrating the solid angle in spherical coordinate on the equation (2.23), the intensity will be

$$I(q) = \int 4\pi r^2 \tilde{\rho}^2(r) \frac{\sin qr}{qr} dr \quad (2.24)$$

According to the $\tilde{\rho}^2(\vec{r})$ function (equation 2.22), when r is very small or close to zero, the $\tilde{\rho}^2(\vec{r})$ will be

$$\tilde{\rho}^2(r \rightarrow 0) = \langle \rho^2 \rangle V \quad (2.25)$$

Where $\langle \dots \rangle$ is defined as an average notation.

If r is very large, the term of $\tilde{\rho}^2(\vec{r})$ will be

$$\tilde{\rho}^2(r \rightarrow \infty) = \langle \rho \rangle^2 V \quad (2.26)$$

The parameter $\langle \rho \rangle^2 V$ is constant and does not depend on the r value as there is no correlation at large r . The parameter $\langle \rho \rangle^2 V$ behaves as a blank object and has no effects on the scattering pattern. Therefore, SAXS data generates from the excess of scattering length density ($\Delta\rho(r)$). Since we consider the scattering from the enzyme dissolved in solvent, the excess scattering length density ($\Delta\rho(r) = \rho(r) - \rho$) is the contrast between the enzyme solution ($\rho(r)$) and the solvent (ρ). Additionally, the auto-correlation function of the density contrast should be used instead of the auto-correlation ($\tilde{\rho}^2(\vec{r})$) function and expressed as

$$\Delta\tilde{\rho}^2(r) = \overline{(\rho(r) - \rho)^2} \quad (2.27)$$

Therefore, the scattering intensity of the enzyme solution is given by

$$I(q) = \int 4\pi r^2 \Delta\tilde{\rho}^2(r) \frac{\sin qr}{qr} dr \quad (2.28)$$

2.3 Pair Distribution Function

When the auto-correlation function of the density contrast is divided by volume V , it is called the correlation function $\gamma(r)$.

$$\gamma(r) = \frac{\Delta\tilde{\rho}^2(r)}{V} \quad (2.29)$$

The intensity relates to the correlation function as

$$I(q) = 4\pi V \int \gamma(r) \frac{\sin qr}{qr} r^2 dr \quad (2.30)$$

The $\gamma(r)$ can also be derived by the inverse Fourier transform of the $I(q)$ as

$$V\gamma(r) = \frac{1}{2\pi^2} \int I(q) \frac{\sin qr}{qr} q^2 dq \quad (2.31)$$

Moreover, the pair distribution function $P(r)$ can be given from the correlation function $\gamma(r)$ (Guinier, and Fournet, 1955; Glatter, and Kratky, 1982) as

$$P(r) = r^2 \gamma(r) = \frac{r^2}{2\pi^2 V} \int I(q) \frac{\sin qr}{qr} q^2 dq \quad (2.32)$$

Since the term of $\gamma(r)$ depends on $\Delta\tilde{\rho}^2(r)$, it must be confined in a finite region. The value of $\gamma(r)$ is equal to zero when $r \geq D_{max}$ (where D_{max} is the maximum distance of the particle diameter) due to there is no the excess density.

Therefore, the term $P(r)$ is rewritten as

$$P(r) = \frac{r^2}{2\pi^2 V} \int_0^{D_{max}} I(q) \frac{\sin qr}{qr} q^2 dq \quad (2.33)$$

The pair function describes the distance between the volume elements within a particle. Hence, the characteristic of the $P(r)$ value for a particle with the finite size will start at zero, then increasing, lastly, goes down to zero again at the maximum dimension length of the particle (D_{max}), as shown in Figure 2.3. The shape of the $P(r)$ function is consequence of the particle geometry. In particular, the $P(r)$ function for a spherical shape (perfect globular shape) will display a Gaussian curve (Guinier, and Fournet, 1955; Glatter, and Kratky, 1982; Feigin, and Svergun, 1987; Putnam *et al.*, 2007).

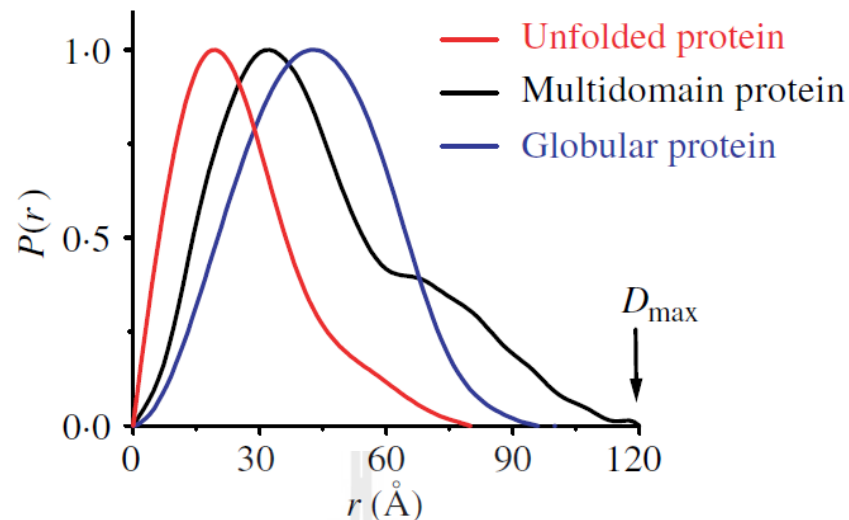


Figure 2.3 The pair distribution function $P(r)$ for geometrical protein (unfolded multidomain and globular) with their maximum dimension length D_{max} (Putnam *et al.*, 2007).

2.4 Guinier Approximation

The scattering intensity at small scattering vector q can be approximated as

$$I(q \rightarrow 0) = I(0)(1 - q^2 R_g^2 / 3) = I(0)e^{-q^2 R_g^2 / 3} \quad (2.34)$$

It is well known as Guinier approximation, firstly derived by Guinier (Guinier, and Fournet, 1955; Glatter, and Kratky, 1982; Feigin, and Svergun, 1987). The parameter R_g is called radius of gyration, defined as the mean distance of excess electrons from center of gravity of a particle. It is very useful to estimate the size of a particle, for example, the R_g of a spherical particle is related to the spherical particle radius R as $R_g = R\sqrt{3/5}$ (Glatter, and Kratky, 1982; Feigin, and Svergun, 1987; Putnam *et al.*, 2007; Svergun, and Koch, 2003).

In practice, we can find the R_g by applying the logarithm on the equation (2.34)

as

$$\ln I(q) = \ln I(0) + \frac{-R_g^2 q^2}{3} \quad (2.35)$$

Then, plot graph between $\ln I(q)$ and q^2 , the slope (m) of the graph is denoted as $m = -R_g^2 / 3$ and intercept is $\ln I(0)$, thus the term R_g is given by

$$R_g = \sqrt{-3m} \quad (2.36)$$

However, the q range of the Guinier approximation must be satisfied with condition $q < 1/R_g$. In the monodisperse solution, the linearity of the Guinier plots can identify an aggregation effect on the enzyme particle. If the plot shows the non-linear line, it suggests that the particle is aggregate, whereas the straight line indicates the non-aggregate particle (Figure 2.4) (Putnam *et al.*, 2007; Svergun, and Koch, 2003).

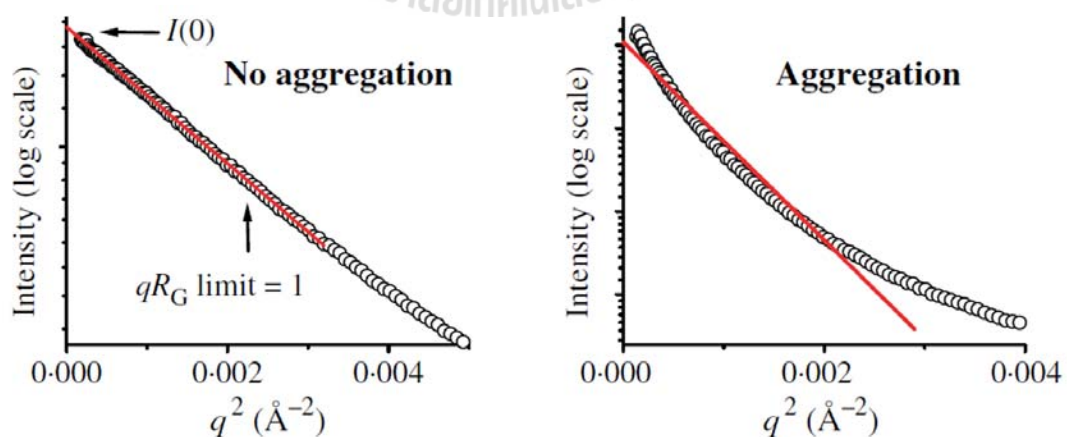


Figure 2.4 Calculated R_g from the slope of the Guinier plot with the limit in q range. Besides, the linearity of slope can identify the aggregation properties of protein [adapted from (Putnam *et al.*, 2007)].

When q is very low or near zero, the term of $\frac{\sin qr}{qr}$ can be approximate in a

McLaurin series expansion as

$$\frac{\sin qr}{qr} \cong 1 - \frac{q^2 r^2}{6} + \dots \quad (2.37)$$

When q is very low or near zero, the term of $\frac{\sin qr}{qr}$ can be approximate in a

McLaurin series expansion as

$$\frac{\sin qr}{qr} \cong 1 - \frac{q^2 r^2}{6} + \dots \quad (2.37)$$

Therefore, the intensity, from equation (2.30), at low q can be approximate without high order term of q^4 as

$$I(q) = 4\pi V \int \gamma(r) r^2 dr \left[1 - \frac{q^2 \int \gamma(r) r^4 dr}{6 \int \gamma(r) r^2 dr} \right] \quad (2.38)$$

or

$$I(q) = I(0) \left[1 - \frac{q^2 \int \gamma(r) r^4 dr}{6 \int \gamma(r) r^2 dr} \right] \quad (2.39)$$

where

$$I(0) = 4\pi V \int \gamma(r) r^2 dr \quad (2.40)$$

As from comparing equation (2.38) with equation (2.34), the R_g can be read out as

$$R_g^2 = \frac{\int \gamma(r)r^4 dr}{2 \int \gamma(r)r^2 dr} \quad (2.41)$$

We are also able to write in the term of the pair function $P(r)$ as

$$R_g^2 = \frac{\int_0^{D_{\max}} P(r)r^2 dr}{2 \int_0^{D_{\max}} P(r)dr} \quad (2.42)$$

According to the equation (2.42), we can also extract the R_g information from the pair function. Furthermore, the R_g from this method is more reliable than that from the Guinier approximation because we use the whole range of q value from the measurement while the Guinier law is valid in low q region.

2.5 Porod Volume

As from equation (2.31), the correlation function at $r = 0$ is defined as

$$V\gamma(r=0) = \langle \Delta\rho^2 \rangle = \frac{1}{2\pi^2} \int_0^\infty I(q)q^2 dq = \frac{Q}{2\pi^2} \quad (2.43)$$

Where Q is known as the invariance that is denoted as

$$Q = \int_0^\infty I(q)q^2 dq \quad (2.44)$$

From equation (2.40), the value of $I(0)$ is rewritten as

$$I(0) = 4\pi V \int \gamma(r)r^2 dr = V \langle \Delta\rho^2 \rangle \quad (2.45)$$

All scattering waves are in phase at $q = 0$, thus the intensity is equivalent to the summation of scattering amplitude from only the excess density over the irradiated volume V . In practice, we are not able to measure the value of the intensity at low q because the intensity is very high due to the scattering waves are in phase. We usually put the beam stop to block that intensity. Therefore, we normally derive the intensity at zero q by extrapolating the scattering intensity data.

From equation (2.43) and (2.45), the Porod volume or the enzyme volume (V) can be defined as (Glatter, and Kratky, 1982; Feigin, and Svergun, 1987; Putnam *et al.*, 2007; Svergun, and Koch, 2003)

$$V = \frac{2\pi^2 I(0)}{Q} = \frac{2\pi^2 I(0)}{\int_0^{\infty} I(q)q^2 dq} \quad (2.46)$$

2.6 Kratky Plot

The folded, unfolded, and partially unfolded of the enzyme sample can be determined by considering the Kratky plot or the plot of scattering data between $q^2 I(q)$ versus q without any modeling (Figure 2.5) (Putnam *et al.*, 2007; Svergun, and Koch, 2003).

For a folded globular enzyme (roughly spherical form), the Kratky plot will present a bell-shape curve at low q and converges to zero at high q . While the completely unfolded enzyme, the enzyme is form as the Gaussian chain or known as Random coil model (the model is described by the N beads are freely to join in a random direction). The plot for the unfolded state will behave differently from the previous case as there is no peak at low q and show a plateau at high q region. For the incompletely unfolded protein, the Kratky plot shows a broad peak (broader than

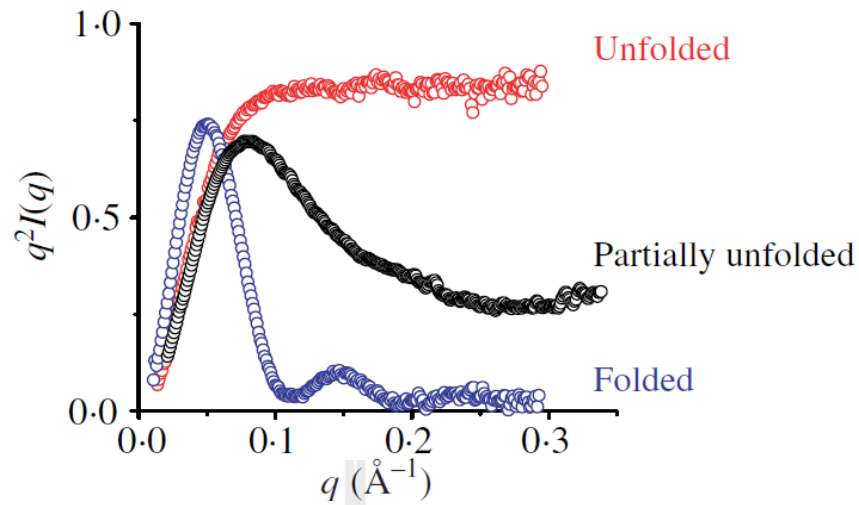


Figure 2.5 The Kratky plot of folded, unfolded, and partially unfolded of the protein sample. For folded state, the plot presents a bell-shaped curve, while the unfolded state lacks the curve and increases noticeably in the large q region. The partially unfolded state shows a broad peak and not goes down to zero in the high q region (Putnam *et al.*, 2007).

folded state) at low q and not converges to zero but remains at high value in the high q region.

2.7 3D Reconstruction Model

The SAXS intensity profile of the monodisperse solution is proportional to the scattering intensity in isotropic system of the enzyme particle with average all directions. The scattering profile will contain information of the particle morphology.

We can generate the three-dimension (3D) structure of the particle from the one-dimension (1D) scattering profile even though the profile is average and has limitation in q measurement. To obtain the 3D structure from the 1D profile, the dummy atomic model, given by Svergun and co-workers (Putnam *et al.*, 2007;

Svergun, and Koch, 2003, Svergun, 1999), has been proposed. The model is described by considering N spherical beads (representing as dummy atom) were pack tightly. The position of each dummy atom (bead) is assigned to be either the enzyme or the solvent. The model can only show roughly molecular enzyme structure due to it gives smooth shapes but not the details of the sharp edges or corners. Hence, this model is also known as the low resolution model. Additionally, the programs that are used to create the dummy atomic model, then average and filtered the atomic model to get the most correct one are DAMMIN (Svergun, 1999) and DAMAVER (Volkov, and Svergun, 2003), respectively.

Furthermore, we check the accuracy of the 3D atomic model by comparing with the enzyme structure, which was obtained from X-ray crystallography techniques, using superimpose method through SUPCOMB software. Also, compare their 1D profiles via CRY SOL program.

2.7.1 DAMMIN and DAMAVER

The DAMMIN program is used to reconstruct 3D enzyme structure from the 1D scattering profiles using the dummy atomic model. The correct dummy model with minimizing error is performed with simulated annealing. Since the DAMMIN models do not give a unique result, the averaged and filtered atomic model using DAMAVER program needs to be performed in order to derive the most optimized reconstruction enzyme structure.

For a globular particle in solution, the DAMMIN software creates the enclosure particle volume is defined with a radius R and filled with N dummy atoms (beads with radius r_0) and densely packed of $r_0 \ll R$ with having multiphase. For the enzyme solution (consisted of enzyme and solvent phases) with fixed atomic positions, all

dummy atoms position can be described by a vector \vec{X} with N components where $N \approx (R/r_0)^3$ and corresponds to the phase that it belongs as X_j (where $X_j = 0$ for solvent and $X_j = k$ for enzyme with $0 \leq k \leq K$). Thus, the scattering intensity of the dummy model can be written as

$$I(q) = \left\langle \left[\sum_{k=1}^K \Delta\rho_k A_k(q) \right]^2 \right\rangle_{\Omega} \quad (2.47)$$

where $\Delta\rho_k$ and $A_k(q)$ are the electron density contrast and the scattering amplitude of the k^{th} phase, respectively. Beside, $\langle \rangle_{\Omega}$ is denoted as the average over all particle orientations in the solid angle. The amplitude $A_k(q)$ is defined through spherical harmonics $Y_{lm}(\Omega)$ as

$$A_k(q) = \sum_{l=0}^{\infty} \sum_{m=-l}^l A_{lm}^{(k)}(q) Y_{lm}(\Omega) \quad (2.48)$$

The dummy model intensity is obtains as

$$I(q) = 2\pi^2 \sum_{l=0}^{\infty} \sum_{m=-l}^l \left\{ \sum_{k=1}^K \left[\Delta\rho_k A_{lm}^{(k)}(q) \right]^2 + 2 \sum_{n>k} \Delta\rho_k A_{lm}^{(k)}(q) \Delta\rho_n [A_{lm}^{(n)}(q)]^* \right\} \quad (2.49)$$

where $A_{lm}^{(k)}(q)$ is the partial scattering amplitudes of the k^{th} phase that is denoted as

$$A_{lm}^{(k)}(q) = i^l \sqrt{\frac{2}{\pi}} f(q) \sum_{j=1}^{N_k} j_1(qr_j) Y_{lm}^*(\omega_j) \quad (2.50)$$

The r_j and ω_j are the polar coordinates of the k^{th} phase of the dummy atoms, respectively, $j_l(x)$ is the spherical Bessel function, and $f(q)$ is the scattering from factor of a single atom. Then, the goal function has been considered and compared to find the lowest difference from the SAXS experimental and the given model. The goal function $f(X)$ is written as follow

$$f(X) = \chi^2 + \alpha P(X) \quad (2.51)$$

Where $P(X)$ is the looseness penalty (is in order of 10^{-2} for compact structure) and α is the penalty weight (≈ 10). Furthermore, the χ^2 represents the different function between the measurement and the model that is

$$\chi^2 = \frac{1}{M} \sum_{i=1}^M \sum_{j=1}^{N(i)} \left[\frac{(I_{\text{exp}}^{(i)}(q_j) - I^{(i)}(q_j))}{\sigma(q_j)} \right]^2 \quad (2.52)$$

Where M is a set of contrast variation, $N(i)$ is the number of point in the i^{th} curves, and $\sigma(q_j)$ is defined as a standard deviation of the experiment.

The simulated annealing method (Kirkpatrick, Gelatt, and Vecchi, 1983)] has been applied in order to get the minimized goal function. The method begins by heating on the dummy atomic model (dummy atoms can move randomly). After that, let the temperature goes down slowly until the dummy atoms arrange themselves in the lowest energy state. During the annealing process, the goal functions are created and compared with each another until it reaches minimum. The brief algorithm details of the approach are explained as follows.

1. The process starts at high temperature with a random configuration X_0 such as $T_0 = f(X_0)$.
2. A new configuration X' is obtained from a changing position and phase of the random dummy atom. The configuration difference is defined as $\Delta = f(X') - f(X)$.
3. If $\Delta < 0$, the new configuration X' is accepted. However, if $\Delta > 0$, the new configuration is accepted with a probability $\exp(-\Delta/T)$.

4. Step 2 and 3 are repeated until the system reaches either $100N$ reconfigurations or $10N$ successfully reconfigurations at constant T .
5. Then, the system is cooled down to $T' = 0.9T$, repeat the step 2 to 4. It continues cooling temperature until the $f(X)$ reaches the minimum.

Since only one dummy atom is moved per one process, this method takes time and depends on the efficiency of a computer.

In this work, we generated ten atomic models by DAMMIN program, then all models have been done average and filtered (cut off the volume that has low dummy atomic density) by using DAMAVER program to get the most reliable reconstruction model.

2.7.2 Protein Data Bank

Protein data bank (PDB) is a worldwide data resource that provides information about the 3D structures of biological macromolecules, i.e. enzyme, normally derived by X-ray crystallography and/or NMR spectroscopy (Berman *et al.*, 2000; Berman, 2008). It also gives details of atomic coordinates, the primary and secondary structure information, sequence database references, and ligand and biological assembly information. The PDB data files (PDB format files) can be accessed freely via the Internet at <http://www.rcsb.org/pdb/>.

2.7.3 SUPCOMB

To confirm the accuracy of the 3D reconstruction SAXS model with the 3D enzyme structure (obtained from other techniques), SUPCOMB software has been used (Kozin, and Svergun, 2001). As explained previously, SAXS is a low resolution technique, thus it can show only the shape of the enzyme structure but not the internal structure.

The SUBCOMB program is automatic software that allows us to superimpose the low resolution models from solution X-ray scattering and the high resolution structure, such as from crystallographic atomic. The ideal of this method is to consider crystal structure as an object (S_1) that be superimposed onto the SAXS atomic model as a template (S_2). These two models are in the best matching when minimizes of normalized spatial discrepancy (NSD), where NSD has been introduced as a quantitative of similarity between the models.

In the program, each input model is considered as an ensemble of points (bead or atom). If the two models are represented as a set of points, for every points ($s_{1,i}$) in the first model is $S_1 = \{s_{1,i}, i = 1, \dots, N_1\}$ while all points ($s_{2,i}$) in the second model is $S_2 = \{s_{2,i}, i = 1, \dots, N_2\}$. The lowest distance value between the point ($s_{1,i}$) and the all points in the S_2 is assumed as $\rho(s_{1,i}, S_2)$, similarly the lowest distance value between point ($s_{2,i}$) and all points in the S_1 is denoted as $\rho(s_{2,i}, S_1)$. The NSD can be given as the combine of these distances and normalized average distances between the neighboring points for the two sets

$$NSD = \rho(S_1, S_2) = \left\{ \frac{1}{2} \left[\frac{1}{N_1 d_2^2} \sum_{i=1}^{N_1} \rho^2(s_{1,i}, S_2) + \frac{1}{N_2 d_1^2} \sum_{i=1}^{N_2} \rho^2(s_{2,i}, S_1) \right] \right\}^{1/2} \quad (2.53)$$

where N_1 and N_2 are the number of points corresponding to S_1 and S_2 , respectively.

The fineness d_1 and d_2 are the average distance between the neighboring points in S_1 and S_2 , respectively.

When the two structures are in perfect match, the NSD value will be zero, however, if the structures are different from each other, the NSD will be more than one.

2.7.4 CRY SOL

It is not only the 3D model that can be used to examine the similarity of the SAXS structure and the enzyme structure, but the 1D profiles are also able to check the identical of those structures using CRY SOL software (Svergun, Barberato, and Koch 1995). The program has been used to extract the profiles from the enzyme structure and fit the SAXS profiles. The perfect matches of these profiles confirm the identical of the two structures.

The SAXS intensity of the particle in dilute solution (Figure 2.6) is proportional to the averaged intensity over all orientations, which can be given by

$$I(q) = \left\langle \left| A_a(q) - \rho_0 A_c(q) + \Delta\rho A_b(q) \right|^2 \right\rangle_{\Omega} \quad (2.54)$$

Here, $\Delta\rho = \rho_b - \rho_0$ is the electron density contrast between the electron densities of the hydration shell ρ_b (border layer that surround the particle with effective thickness (δ)) and the average electron density of solvent ρ_0 . $\langle \rangle_{\Omega}$ represents the average over all particle orientations in the solid angle. Moreover, $A_a(q)$ are the scattering amplitude of the particles in vacuum, which are defined as

$$A_a(q) = \sum_{l=0}^{\infty} \sum_{m=-l}^l A_{lm}(q) Y_{lm}(\Omega) \quad (2.55)$$

Where $A_{lm}(q)$ are the partial amplitudes that are assumed as

$$A_{lm}(q) = 4\pi i^l \sum_{j=1}^N f_j(q) j_l(qr_j) Y_{lm}^*(\omega_j) \quad (2.56)$$

where $f_j(q)$ are the atomic form factors of the particle, $j_l(qr_j)$ are the spherical Bessel functions, $Y_{lm}(\Omega)$ are the spherical harmonics, and r_j is the atomic coordinates ($r_j = (r_j, \omega_j) = (r_j, \theta_j, \phi_j)$).

Where $A_c(q)$ are the scattering amplitudes of the excluded volume represented by dummy atom that is written in the term of partial amplitudes $C_{lm}(q)$ as

$$A_c(q) = C_{lm}(q) = 4\pi i^l \sum_{j=1}^N g_j(q) j_l(qr_j) Y_{lm}^*(\omega_j) \quad (2.57)$$

where $g_j(q)$ are the atomic form factors of the dummy atoms.

Lastly, $A_b(q)$ are the scattering amplitudes of the border layer that can also be written in the term of partial amplitudes $B_{lm}(q)$ as

$$B_{lm}(q) = i^l \sqrt{\frac{2}{\pi}} \int_0^\infty \rho_{lm}(r) j_l(qr) r^2 dr \quad (2.58)$$

where

$$\rho_{lm}(r) = \int \rho_b(r) Y_{lm}^*(\omega) d\omega \quad (2.59)$$

All cross terms can be canceled out due to the orthogonal properties of the spherical harmonics. Therefore, the SAXS intensity is given by

$$I(q) = \sum_{l=0}^L \sum_{m=-l}^l \left| A_{lm}(q) - \rho_0 C_{lm}(q) + \Delta\rho B_{lm}(q) \right|^2 \quad (2.60)$$

where L defines the resolution of the particle.

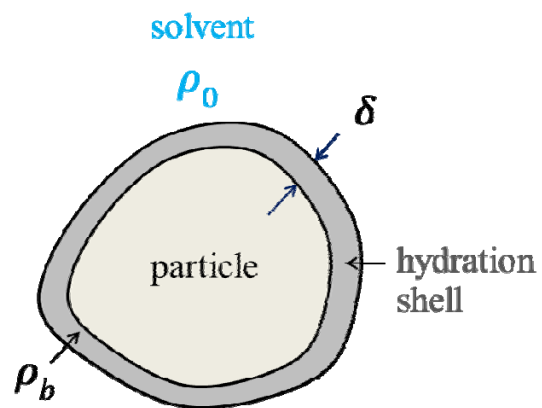
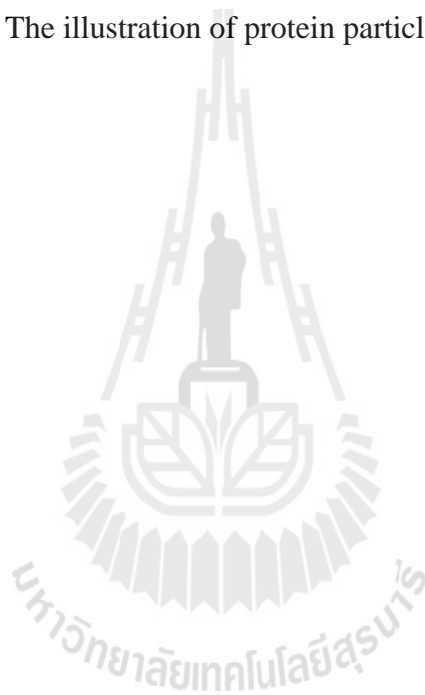


Figure 2.6 The illustration of protein particle in dilute solution.



CHAPTER III

EFFECT OF ACIDS AND ALKALIS ON CONFORMATION OF GLUCOSE OXIDASE BY SMALL ANGLE X-RAY SCATTERING

3.1 Introduction

Glucose oxidase (GOD) is a glycosylated enzyme purified from *Aspergillus niger*. GOD is capable to catalyze the oxidation of β -D-glucose and oxygen to D-gluconolactone and hydrogen peroxide (H_2O_2). The enzyme has been used widely in various industries. For instance, GOD is used in food industry to produce gluconic acid (Fiedurek, 2001; Ramachandran, 2006) and to remove glucose and oxygen in food preservation (Parpinello *et al.*, 2002). More importantly, GOD is considered a diagnostic and analytical tool since it works as a biosensor that is able to determine the quantitative of β -D-glucose in samples such as blood, body fluids, food, agricultural fermentation, and beverages (Wilson, and Turner, 1992; Ho *et al.*, 2007; Jaffar, and Turner, 1995; Yang, and Liang, 2005).

Glucose oxidase is a homodimer with molecular weight of 160 kDa (Tsuge, Natsuaki, and Ohashi, 1975), comprising two identical monomers with equivalent molecular weight of 80 kDa. Each monomer consists of one mole of flavin adenine dinucleotide (FAD) as co-enzyme (Pazur, Kleppe, and Cepure, 1965; O'Malley, and Weaver, 1972; Nakamura, and Fujiki, 1968) and one mole of iron. GOD is a highly

glycosylated enzyme containing carbohydrate moieties of approximately 18% of its molecular weight (16% neutral sugar and 2% amino sugar) (Tsuge, Natsuaki, and Ohashi, 1975). The enzyme was reported to be very stable for storage (Pazur, Kleppe, and Cepure, 1965) and resistant to denaturing agents such as sodium dodecyl sulfate (SDS) and urea (Akhtar, Ahmad, and Bhakuni, 2002). The enzyme has also been found to have the optimum pH at 5.5, with a wide active pH range between 4 to 7 (Pazur, and Kleppe, 1964).

To gain more knowledge of an enzyme, studies of folding and denaturing process are essential. One such study is conformation of the enzyme under conditions of acids and/or alkalis. Structural studies of GOD affected by acids and alkalis have been done using various methods, such as quenching and subunit status studies (Khatun Haq, Faiz Ahmad, and Hasan Khan, 2003), fluorescence spectroscopy, circular dichroism measurements (Khatun Haq, Faiz Ahmad, and Hasan Khan, 2003; Sohail Akhtar, and Bhakuni, 2003) limited proteolysis, size exclusion chromatography, and cross-linking measurements (Sohail Akhtar, and Bhakuni, 2003). Studies have been carried out to investigate the structure of GOD using Small Angle X-ray Scattering (SAXS) technique, in which GOD conformation in solutions were reported at pH 4.5, 7 and 9 (Niebuhr, 2004).

In this work, we used SAXS technique to examine effects of acids and alkalis on GOD conformation. The GOD solutions were investigated for a wide range of pH between 1 to 10 (1.05, 2.02, 3.02, 4.08, 5.02, 6.08, 6.96, 7.93, 8.94 and 10.08). The sizes, shapes, volumes and 3-dimensional atomic models of these enzymes were studied. Comparison of the models and the volumes of these GOD enzyme structure were made between the obtained results and those from a reported GOD crystal

structure.

3.2 Experimental Section

3.2.1 Sample preparation

Glucose oxidase was purchased from Sigma Chemical Co., Ltd. in high purity powder form. Commercial GOD was dissolved in 50 mM sodium phosphate buffer with the concentration of 10 mg/mL. HCl and NaOH were used to adjust the pH of the sample solution for the desired final pH range from 1 to 10 (1.05, 2.02, 3.02, 4.08, 5.02, 6.08, 6.96, 7.93, 8.94, and 10.08). The pH values of these solutions were determined using a glass electrode of a digital pH meter, pH 210 from HANNA instruments Co.

3.2.2 Measurements

Small Angle X-ray Scattering measurements were carried out at the SAXS beamline (BL 4C) of Pohang Accelerator Laboratory (PAL), Pohang, South Korea and at the BL1.3W-SAXS beamline of the Synchrotron Light Research Institute, Nakhon Ratchasima, Thailand. The scattering intensities were measured as a function of the scattering vector q , defined as $q = \frac{4\pi}{\lambda} \sin \theta$ when 2θ is the scattering angle and λ is the X-ray wavelength, which is 1.49 \AA . The scattering data were collected using a CCD detector with an active area of 165 mm (Mar SX165). The SAXS measurements were performed at two samples to detector distances of 1 and 4 meters. The sample and the buffer solutions were exposed for 10 seconds, which was short enough to avoid radiation damage of the samples. All measurements were performed at the room temperature.

3.3 Results and Discussions

The measured SAXS intensity of GOD enzyme under pH conditions are shown in Figure 3.1. It can be seen that the scattering profiles of the GOD at pH 1 and 2 differed markedly from the other pH values. This clearly indicates that the acids significantly affect GOD structures. To see more clearly the Kratky plot (Glatter, and Kratky, 1982) of the measured scattering profiles is shown in Figure 3.2. The plot showed bell-shape curves for the profiles at pH 3 to 10, indicating that the enzymes were in compact, globular structures. At pH 1 and 2, the plot lacked bell-shape curves, and the values of $q^2I(q)$ continued to increase noticeably in the large q region, indicating that the enzymes were unfolded or denatured. In addition, the peak positions of the Kratky plot at pH 1 and 2 were at smaller q values than those of pH 3 to 10, implying that the enzymes at pH 1 and 2 were larger, possibly aggregated due to the denaturing process.

Furthermore, we analyzed the sizes and the aggregation of GOD by considering the radius of gyration (R_g). The Guinier plot for a globular particle, a plot of $\ln I(q)$ against q^2 at small q values (Glatter, and Kratky, 1982; Guinier, and Fournet, 1955) for each sample was obtained from the measured intensity. The radius of gyration R_g was obtained from the slope of the Guinier plot. Figure 3.3 shows the Guinier plots and the linear fit of measured data. The Guinier plots for pH 3 to 10 were observed to be straight lines, but at pH 1 and 2 the data appeared to be nonlinear. These suggest that GOD enzyme was denatured and aggregated at pH 1 and 2. From the slopes of the linear fits, we calculated the R_g values by considering AUTORG software (Petoukhov *et al.*, 2007), shown in Table 3.1.

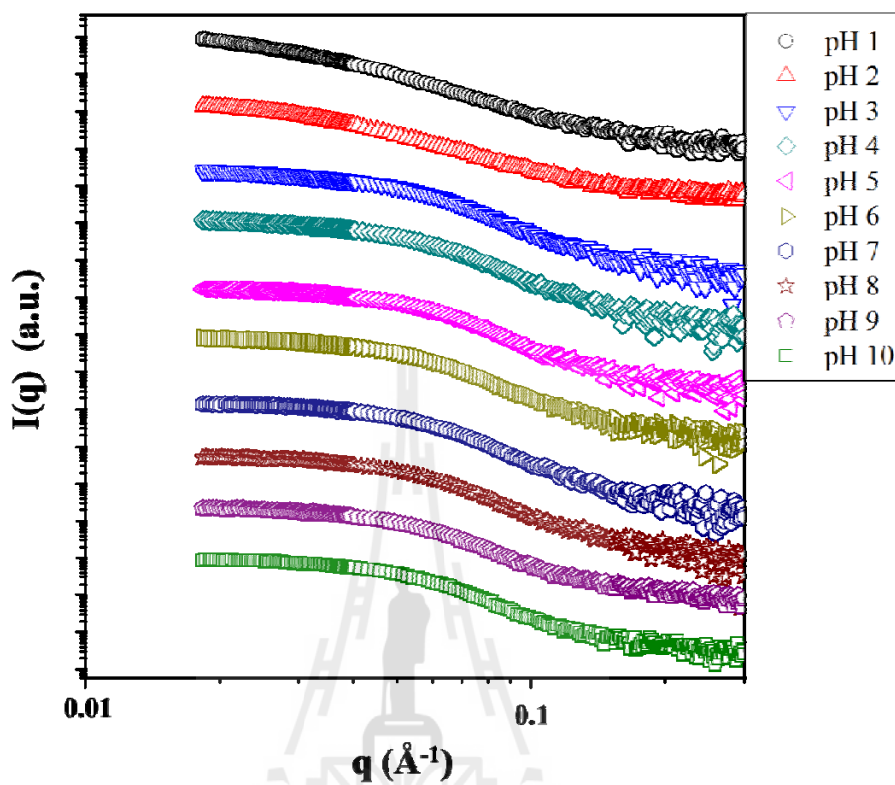


Figure 3.1 The SAXS intensity of GOD enzymes at pH 1 to 10.

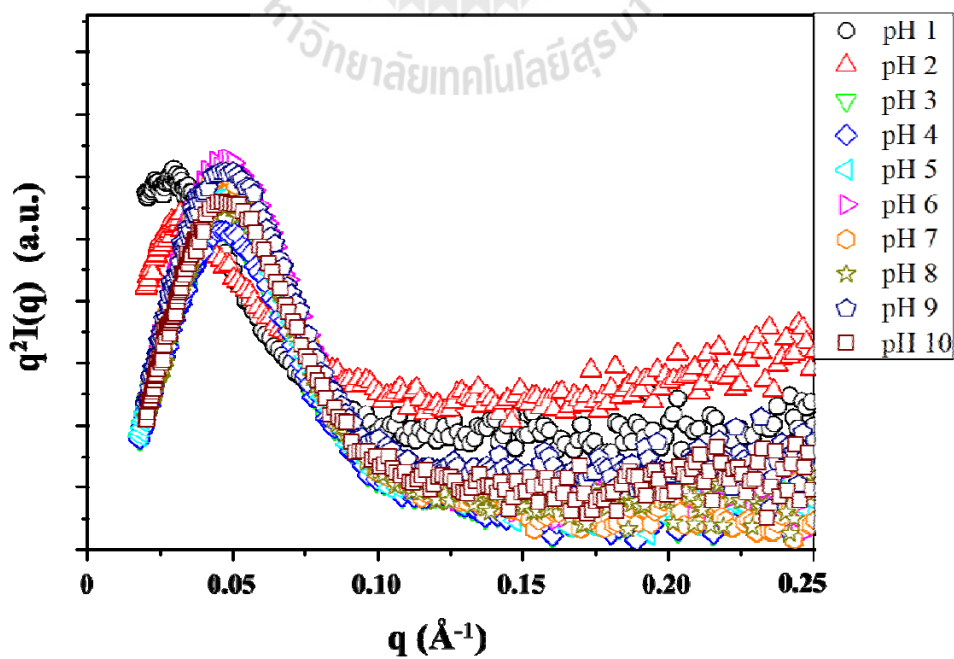


Figure 3.2 The Kratky plot of the scattering profiles of GOD enzymes at pH 1 to 10.

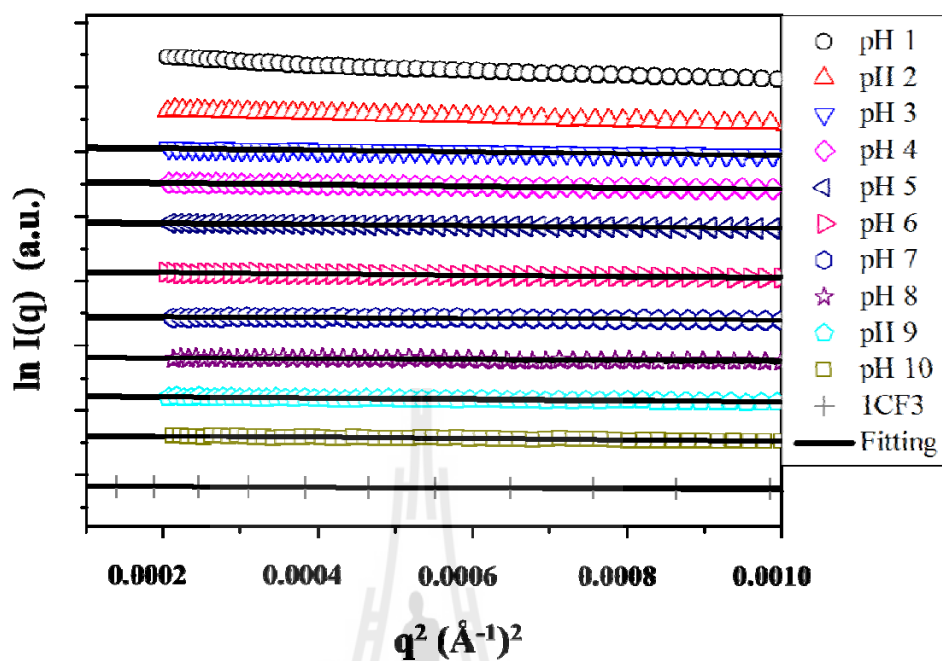


Figure 3.3 The Guinier plot of GOD enzyme at pH 1 to 10 and GOD crystal (1CF3).

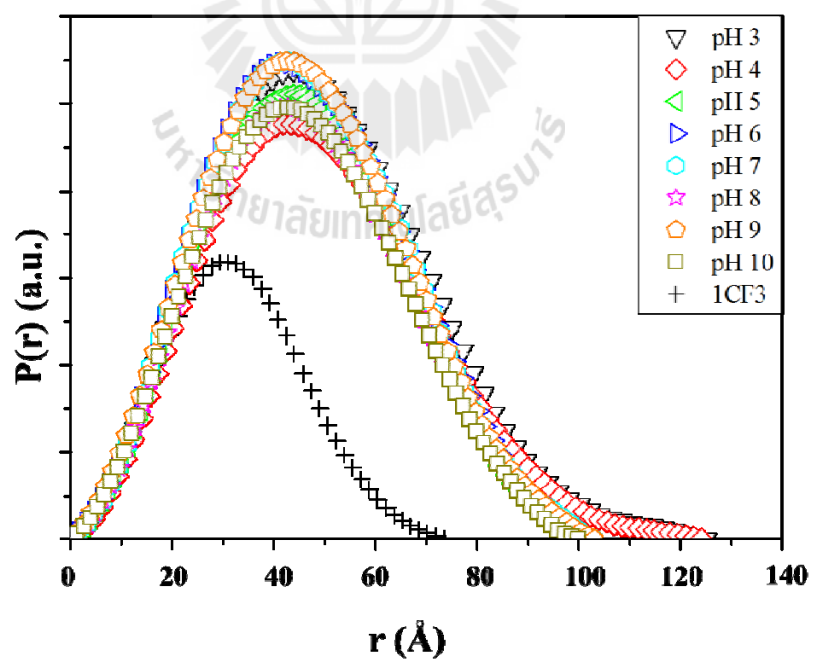


Figure 3.4 The calculated pair distance distribution function ($P(r)$) of GOD enzyme at pH 3 to 10 and GOD crystal (1CF3).

The radii of gyration were alternatively obtained from the pair distance distribution function $P(r)$, calculated from the measured data. The calculations were carried out using GNOM program package (Svergun, 1999). With this method, we were able to derive not only R_g , but also the maximum linear distance of scattering particle, D_{max} .

Figure 3.4 illustrates the pair distance distribution functions of the GOD samples in the range of pH 3 to 10, and the obtained values of R_g and D_{max} from this pH range were summarized in Table 1. The values of R_g from both methods were in

Table 3.1 The structure parameters from enzyme at pH 1 to 10 and crystal (1CF3) of GOD derived from Guinier plots and the pair distance distribution function.

Sample	R_g (Å) [Guinier] ^a	R_g (Å) [P(r)] ^b	D_{max} (Å)
pH 1	Aggregation	-	-
pH 2	Aggregation	-	-
pH 3	40.18±1.34	37.72±0.090	125
pH 4	38.35±0.24	37.48±0.092	124
pH 5	35.84±0.25	35.32±0.036	101
pH 6	33.72±0.13	35.20±0.029	100
pH 7	33.48±0.19	35.46±0.045	103
pH 8	33.01±1.58	35.36±0.044	103
pH 9	34.25±0.41	35.34±0.045	103
pH 10	34.23±0.67	34.93±0.043	100
1CF3	24.99±0.00	24.87±0.003	73.5

^a Radius of gyration was calculated from Guinier approximation

^b Radius of gyration was calculated from Pair distance distribution function

good agreement with each other. It is noted here that, the values of R_g and D_{max} at pH 7 and 9 from our results were in agreement with the values reported in (Niebuhr, 2004).

From Figure 3.4, the pair distances distribution functions of pH 3 to 10 appeared to have Gaussian shapes, indicating that the GOD had a globular shape across pH 3 to 10. At pH 3 and 4, the curves showed long tails, and their values of R_g and D_{max} were a little higher than those at pH 5 to 10. These suggest that the enzyme molecules at pH 3 and 4 were either a little larger than those at pH 5 to 10 or slightly aggregated. The values of R_g and D_{max} were similar for pH 5 to 10, suggesting that GOD structures were stable in this pH range.

Furthermore, we examined 3-dimensional atomic models of GOD using DAMMIN program (Svergun, 1999) and investigated the averaged and filtered atomic models using DAMAVER program (Volkov, and Svergun, 2003) to get the most optimized reconstruction of the enzyme structures. The low resolution envelope structures of GOD enzyme from pH 5 to 10 are shown in Figure 3.5.

From Figure 3.5, the structural models of GOD enzyme at pH 5 to 10 appeared to be globular shapes. These atomic models supported our experimental results in that the enzyme was stable at pH 5 to 10.

It has been known that acids have the effects of increasing charge repulsive force which is the main force generating the partially unfolded and unfolded state of the enzyme molecules (Niebuhr, 2004; Fink *et al.*, 1994; Ahmad, Akhtar, and Bhakuni, 2001). The intra-molecular charge repulsive force disrupts interaction of the hydrophobic regions within the molecule, allowing the hydrophobic residues to interact with those from the other enzyme molecules. This process results in enzyme

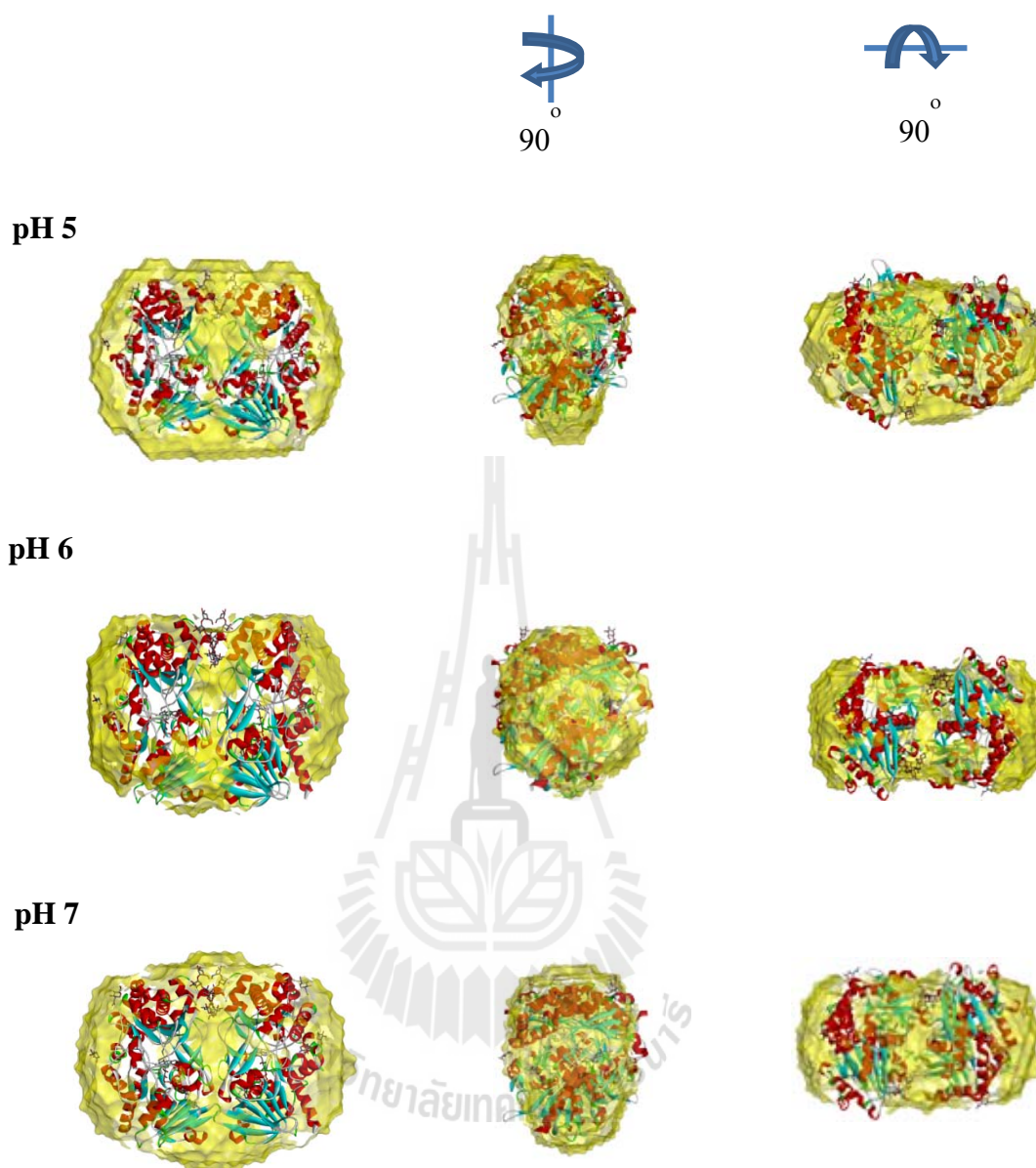


Figure 3.5 Schematic representation of the filtered atomic models of GOD enzyme at pH 5 to 10 superimposed onto the dimer of GOD crystal structure, which was created from monomeric GOD crystal structure (1CF3.pdb, represented by solid ribbon) by PyMol software. Filtered reconstruction model of GOD crystal (1CF3) superimposed on its crystal structure (1CF3.pdb, shown in solid ribbon).

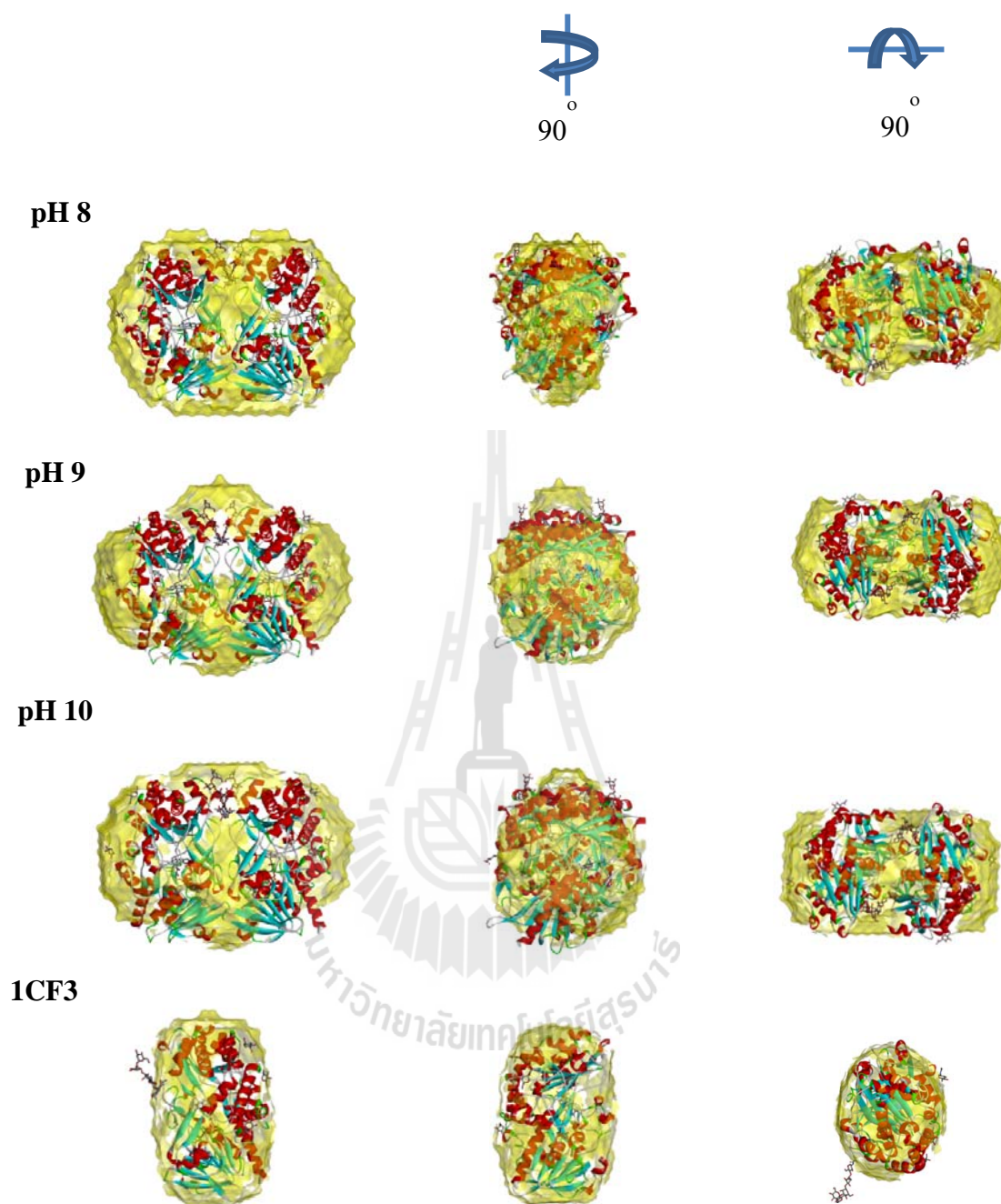


Figure 3.5 Schematic representation of the filtered atomic models of GOD enzyme at pH 5 to 10 superimposed onto the dimer of GOD crystal structure, which was created from monomeric GOD crystal structure (1CF3.pdb, represented by solid ribbon) by PyMol software. Filtered reconstruction model of GOD crystal (1CF3) superimposed on its crystal structure (1CF3.pdb, shown in solid ribbon) (Continued).

aggregation. Therefore, GOD enzyme lost their folded structure and presented slightly aggregate at pH 3 and 4, also became denature at pH 1 and 2.

We also considered the GOD crystal structure from *Aspergillus niger* in order to compare with the structure of GOD enzyme. The GOD crystal conformation was a monomer and almost extracted carbohydrate moiety, as well as available in Protein Data Bank (PDB) reference file as 1CF3.pdb (Wohlfahrt *et al.*, 1999). In Figure 3.5, we presented the atomic model of GOD crystal structure (1CF3) superimposed onto the crystal structure of GOD (1CF3.pdb) itself. Using CRY SOL program (Svergun, Barberato, and Koch, 1995), we derived the SAXS scattering intensity profile from this crystal structure, then the amount of R_g and D_{max} of the crystal from Guinier approximation and pair distance distribution function were determined, as reported in Table 3.1. The atomic model of GOD crystal was observed as a globular shape, which according to the analysis of the pair function of GOD crystal due to its pair function profile was represented as a Gaussian curve. The values of R_g and D_{max} of GOD crystal were less than those values of GOD enzyme, hence the size of the crystal was less than the enzyme, which supported the results that the enzyme was a dimer. However, the amount of R_g and D_{max} of the enzyme were less than twice time of those values from the crystal, as it might be due to the enzyme was in compact conformation.

Moreover, dimeric GOD crystal structure in symmetric unit was produced through the asymmetric unit of monomeric GOD crystal structure with space group $P3_121$ (1CF3.pdb) by using PyMol software (DeLano, 2002). The dimeric crystal structure was superimposed on the envelope model of GOD enzyme, presented in Figure 3.5. The crystal structure can be docked well inside the envelope model

indicated that the enzyme structure is in dimer form. These results were also consistent with the other researches (Khatun Haq, Faiz Ahmad, and Hasan Khan, 2003; Sohail Akhtar, and Bhakuni, 2003).

Figure 3.6 shows the compared intensity profiles. It can be seen that the dimer of GOD crystal structure differed from the structure of GOD enzyme in solution. This can be attributed to the difference of the carbohydrate quantity in these two structures.

Approximately 95% of carbohydrate in the crystal structure is cleaved and removed (Kaliz *et al.*, 1991), while the enzyme is containing carbohydrate with

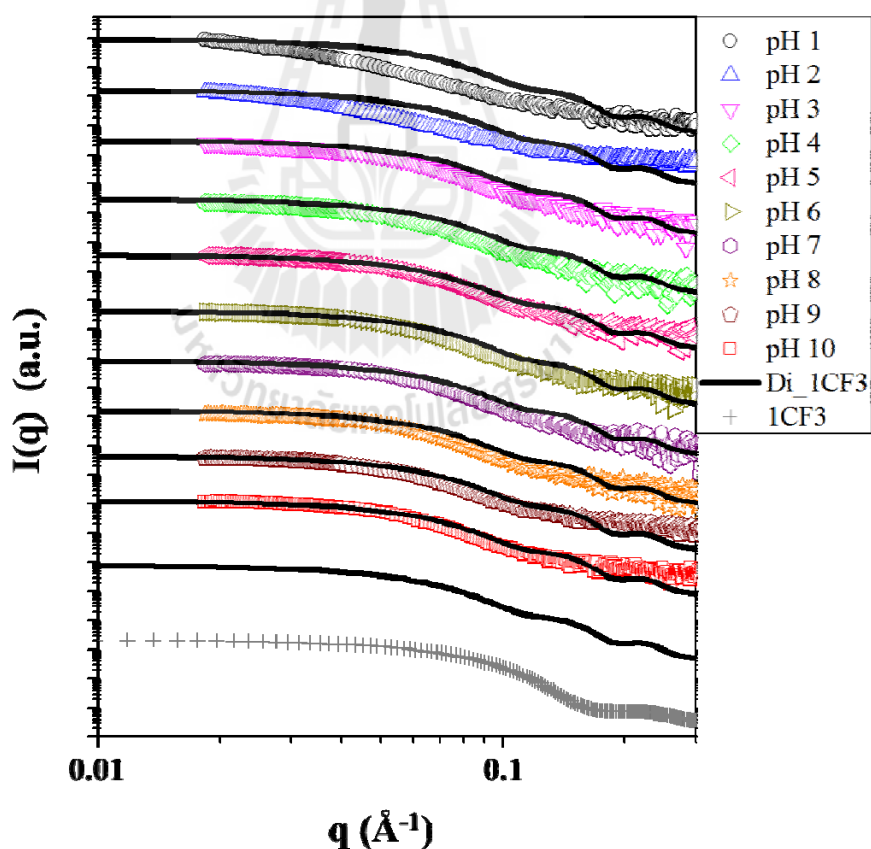


Figure 3.6 Scattering intensity between monomer (1CF3) and dimer (Di_1CF3) of GOD crystal structures, as well as GOD enzyme at pH 1 to 10.

approximately 18% of its molecular weight (Tsuge, Natsuaki, and Ohashi, 1975). The disagreement of intensity profiles from crystal and enzyme structures was also reported in (Niebuhr, 2004).

Notably, it is seen from Figure 3.6 that the level of discrepancy between the two structures depends on the pH condition. The discrepancy was small in the cases of pH 5 to 10, and increased with lower pH values, in which the discrepancy was largest at pH 1. These results were in line with our prior observation that the enzyme structure was stable at pH 5 to 10, began to aggregate at pH 4 and highly aggregated at pH 1 and 2.

Additionally, we studied the GOD excluded volumes of both enzyme and crystal structures using the Porod law (Glatter, and Kratky, 1982; Feigin, and Svergun, 1987; Putnam *et al.*, 2007; Svergun, and Koch, 2003). The Porod plot is

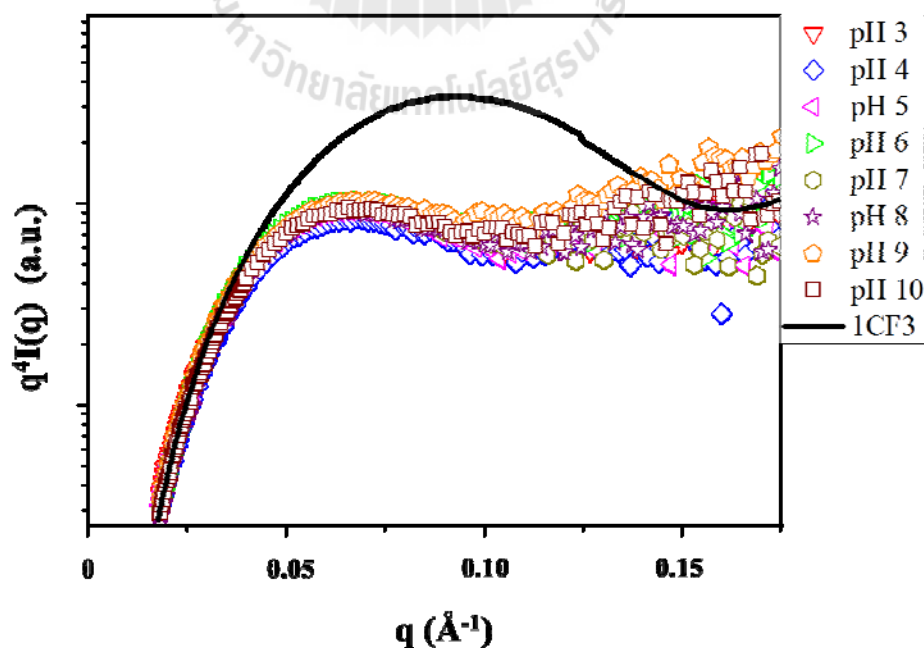


Figure 3.7 The Porod plot of GOD enzyme and of GOD crystal structure (1CF3).

shown in Figure 3.7. The enzyme volumes at pH 3 to 10 and the crystal volume were calculated using PRIMUS program (Konarev *et al.*, 2003), and reported in Table 3.2.

According to these results, the enzyme volumes at pH 5 to 10 were similar, while at pH 3 and 4 the enzyme appeared enlarged. This trend of enzyme volumes corresponded to the obtained structures of the GOD, which depended on the pH condition. The volume of the GOD crystal structure was more than twice as small as those of the enzyme at stable pH conditions. This result confirmed that the GOD crystal structure is a monomer, in which almost all of its carbohydrate is extracted.

Table 3.2 The excluded GOD volumes from pH 3 to 10 and of crystal structure (1CF3) calculated by the Porod law.

Sample	V(\AA^3)
pH 3	262,020
pH 4	229,880
pH 5	205,930
pH 6	199,580
pH 7	204,370
pH 8	182,910
pH 9	187,160
pH 10	184,880
1CF3	70,692

3.4 Conclusion

In this study, we used Small Angle X-ray Scattering (SAXS) technique to investigate effects of acids and alkalis on conformation of glucose oxidase (GOD). Experimental results for GOD solutions with pH ranging from 1 to 10 showed that the enzyme was stable and in folding, globular structures at pH 5 to 10. When pH was decreased to 3 and 4, the enzyme still presented globular shapes but slightly aggregated. When pH was reduced further to 1 and 2, the enzyme was aggregated and subsequently denaturing.

Moreover, we compared the 3-dimensional atomic models, the scattering intensity profile, and the excluded volumes of these GOD enzyme structures to those of the GOD crystal structure. The results showed discrepancy between these enzyme and crystal structures. The discrepancy can be attributed to the fact that the enzyme is a dimer containing significant amount of carbohydrate, while the crystal structure is a monomer with most carbohydrate removed.

CHAPTER IV

THEORETICAL BACKGROUND FOR GRAZING INCIDENCE X-RAY SCATTERING DATA ANALYSIS OF POLYMER THIN FILMS

X-ray scattering under the grazing incident angle (GIXS) is one of the most powerful tools to study morphology and structural order information of the surface and interface of nanomaterials. Since the GIXS technique is usually performing by letting an X-ray beam incident under grazing angle, which is very close and in between critical angle of a polymer sample and a substrate, the X-ray beam will pass through the surface or nearly surface interface of the sample but unable to transmit the substrate. Thus, GIXS provides the possibilities to investigate the surface structure, interface surfaces, buried interfaces, thin layer, and multilayer. The technique can also utilize for characterization in many kinds of material such as metals, semiconductors, polymers, biopolymers, and soft matters.

Due to their advantages, the polymer in thin film form has been used to analyze the morphology and structural order by GIXS technique for decades (Mueller-Buschbaum, 2003; Xu *et al.*, 2004; Lee *et al.*, 2005; Lee *et al.*, 2005). Moreover, the GIXS methods can be divided into grazing incidence angle at small angle (GISAXS) and at wide angle (GIWAXS). The GISAXS technique has been used to examine the nanoscale morphology of the polymer in thin films form, while the GIWAXS

technique gives information about crystal arrangement of the polymer films. In this works, we will study the characterization of star polymers thin films by GIXS (GISXS and GIWAXS) methods. The studied samples are poly(n-hexyl isocyanate)-*block*-poly(ϵ -caprolactone), or PHIC-PCL₁₋₃ with a number-average molecular weight (M_n) of approximate 5,000 for PHIC arm and one to three poly(ϵ -caprolactone) arms (PCL_{*n*}: *n* = 1–3) with a total M_n of approximate 17,000. Another set of PHIC-PCL₁₋₃ films with the M_n of approximate 10,000 in both of PHIC and PCL₁₋₃ arms. The last block copolymers films is PHIC-PLLA₁₋₃ (poly(n-hexyl isocyanate)-*block*-poly(L-lactid acid)) with the M_n of approximate 10,000 for both PHIC arm and one to three poly(L-lactid acid) (PLLA_{*n*}: *n* = 1–3) arms. Furthermore, the outline of GIXS theory for characterization of the star polymers films is presented in this chapter.

4.1 GIXS Geometry

A typical geometry of GIXS experimental set up can be illustrated in Figure 4.1. A monochromatic X-ray beam from high brilliance synchrotron radiation source, defined in x-axis, of wave vector \vec{k}_i with wave number k ($k = \frac{2\pi}{\lambda}$), incident onto a sample surface, positioned parallel to x axis, perpendicular to y-axis, and normal to z-axis, under a grazing incident angle (α_i). Normally, the incident angle is small, constant, and in between critical angle (α_c) of the polymer and substrate. Thus, the incident X-ray beam will be scattered by electron of the surface and interface sample and emerge scattering waves at the exit angle (α_f) with wave vector \vec{k}_f . The wave vector \vec{k}_f is usually composed of two components, one is defined in the perpendicular

to the surface plane or out-of-plane (y-z plane) with the angle (α_f), the other one is parallel to the surface plane or in-plane (x-y plane), corresponds to scattering angle $2\theta_f$. Finally, the charge coupled detector (CCD) is used to collect the two-dimensional (2D) scattering data (the detector is placed in y-z plane). Since, the energy is conserved, the wave number of $\vec{k}_i = \vec{k}_f = k = \frac{2\pi}{\lambda}$. Furthermore, the scattering wave vector \vec{q} can be defined as $\vec{q} = \vec{k}_i - \vec{k}_f$, also be written into Cartesian coordinate as

$$\vec{q} = (q_x, q_y, q_z) \quad (4.1)$$

When

$$q_x = \frac{2\pi}{\lambda} [\cos(\alpha_f) \cos(2\theta_f) - \cos(\alpha_i)] \quad (4.2)$$

$$q_y = \frac{2\pi}{\lambda} [\cos(\alpha_f) \sin(2\theta_f)] \quad (4.3)$$

$$q_z = \frac{2\pi}{\lambda} [\sin(\alpha_f) + \sin(\alpha_i)] \quad (4.4)$$

When the value of $2\theta_f = 0$, $\alpha_f \neq 0$ ($q_x = 0, q_y = 0, q_z \neq 0$), the out-of-plane structures were probed or it is known as a specular scattering, applied to study the depth sensitivity information of sample such as layer, layer thickness, height of cluster and roughness. For off-specular scattering or diffuse scattering or when $2\theta_f \neq 0$ ($q_x \neq 0, q_y \neq 0$), the in-plane structures were observed. The details of shape and size distribution as well as surface structure will be derived.

4.2 GIXS Theory

The basic ideas of GIXS measurement on the polymer film sample have been considered as the X-ray beam under grazing angle impinges on the polymer particles inside the film layer as shown in Figure 4.2(a). It is unlikely from the SAXS technique that the X-ray scatters only from the particles, the reflections due to the interface between the film and the substrate also occur. The scattering events in GIXS experiment can be describe as follows (Figure 4.2(c)); firstly, the scattering from the particles; secondly, the reflection at the interface followed by scattering from the particles; thirdly, the scattering from the particles followed by reflection at the interface; lastly, the reflection at the interface followed by scattering from the particles, then reflection again. These scattering processes are known as Distorted Wave Born approximation (DWBA) (Sinha *et al.*, 1988; Rauscher, Paniago, and Metzger, 1999), which can be considered as a perturbation terms from Born Approximation.

Therefore, the scattered waves ($\psi_{sc}(r)$) due to the scattering from the particles inside the film layer are sum of the four events (Lee *et al.*, 2005; Park *et al.*, 2005), which can be written as

$$\psi_{sc}(r) = -\frac{e^{ik_0r}}{4\pi r} \left[T_i T_f F(q_{\parallel}, q_{1,z}) + T_i R_f F(q_{\parallel}, q_{2,z}) + T_f R_i F(q_{\parallel}, q_{3,z}) + R_i R_f F(q_{\parallel}, q_{4,z}) \right] \quad (4.5)$$

where T_i and T_f are transmission coefficients of incoming and outgoing X-ray wave of the film, while R_i and R_f are reflection coefficients of incoming and outgoing X-ray wave of the interface between the film and the substrate. Here, $F(q_{\parallel}, q_{i,z})$ is the amplitude of scattered wave from the particles in the film. The scattering vector \vec{q} that parallel to the surface plane is $q_{\parallel} = \sqrt{q_x^2 + q_y^2}$ and perpendicular is $q_{i,z}$.

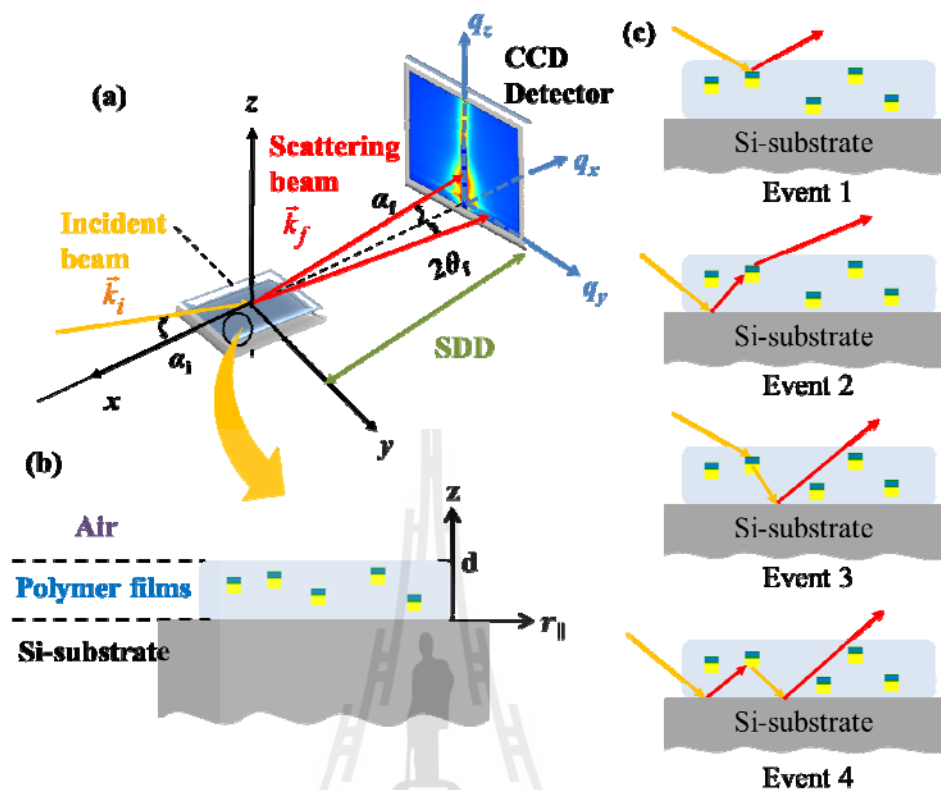


Figure 4.1 (a) Schematic picture of GIXS geometry; the sample is placed on the x - y plane. The 2D CCD detector is positioned in the perpendicular to the surface plane (y - z plane) with the distance between sample and detector (SDD). The incident X-ray beam (x -axis) with wave vector \vec{k}_i impinges on the surface under grazing angle α_i and scatter at the exit angle α_f and $2\theta_f$ with wave vector \vec{k}_f . The q_x , q_y , and q_z are the components of the scattering vector \vec{q} . (b) The illustration of the polymer thin film, having thickness d , contains particles, fabricated in Si-substrate. (c) The picture of the scattering events in the polymer film; event 1, the scattering from the particles; event 2, the reflection at the interface followed by scattering from the particles; event 3, the scattering from the particles followed by reflection at the interface; event 4, the reflection at the interface followed by scattering from the particles, then reflection again.

Where $q_{1,z} = k_{z,f} - k_{z,i}$, $q_{2,z} = -k_{z,f} - k_{z,i}$, $q_{3,z} = k_{z,f} + k_{z,i}$, and $q_{4,z} = -k_{z,f} + k_{z,i}$, which $k_{z,i} = k_0 \sqrt{n^2 + \cos^2 \alpha_i}$ and $k_{z,f} = k_0 \sqrt{n^2 + \cos^2 \alpha_f}$ with $k_0 = \frac{2\pi}{\lambda}$ are the z-axis component of the wave vector of the incoming and outgoing X-ray waves of the film, respectively. Also, λ is the X-ray wavelength, n is the reflective index of the film with $n = 1 - \delta + i\beta$ where δ is the dispersion, and β is the absorption, α_i and α_f denote the incident and scattering angles of the X-ray beam, respectively.

Since the scattering beam is emerged from the film in all directions as a spherical wave, which scattered into a unit solid angle $d\Omega$, the term of scattered intensity (I_{GLXS}) and differential cross section ($\frac{d\sigma}{d\Omega}$) from the film can be defined as

$$I_{GLXS} = \frac{d\sigma}{d\Omega} = r^2 (\psi_{sc}(r) \psi_{sc}^*(r)) \quad (4.6)$$

The I_{GLXS} can also be written in term of independent ($I_{independent}$) and cross (I_{cross}) scattering as

$$I_{GLXS} = \frac{1}{16\pi^2} \{ I_{independent} + I_{cross} \} \quad (4.7)$$

Where

$$I_{independent} = (|T_i T_f F(q_{\parallel}, q_{1,z})|^2 + |T_i R_f F(q_{\parallel}, q_{2,z})|^2 + |T_f R_i F(q_{\parallel}, q_{3,z})|^2 + |R_i R_f F(q_{\parallel}, q_{4,z})|^2) \quad (4.8)$$

And

$$I_{cross} = 2 \left\{ \begin{array}{l} \text{Re}[T_i T_f T_i^* R_f^* \cdot F(q_{\parallel}, q_{1,z}) F^*(q_{\parallel}, q_{2,z})] + \\ \text{Re}[T_i T_f T_f^* R_i^* \cdot F(q_{\parallel}, q_{1,z}) F^*(q_{\parallel}, q_{3,z})] + \\ \text{Re}[T_i T_f R_i^* R_f^* \cdot F(q_{\parallel}, q_{1,z}) F^*(q_{\parallel}, q_{4,z})] + \\ \text{Re}[T_i R_f T_f^* R_i^* \cdot F(q_{\parallel}, q_{2,z}) F^*(q_{\parallel}, q_{3,z})] + \\ \text{Re}[T_i R_f R_i^* R_f^* \cdot F(q_{\parallel}, q_{2,z}) F^*(q_{\parallel}, q_{4,z})] + \\ \text{Re}[T_f R_i R_i^* R_f^* \cdot F(q_{\parallel}, q_{3,z}) F^*(q_{\parallel}, q_{4,z})] \end{array} \right\} \quad (4.9)$$

where $\text{Re}(x)$ is the real part of x .

Since the term $I_{independent}$ (equation 4.8) shows the positive values, while the I_{cross} (equation 4.9) can be positive and negative values. Therefore, the averaged ensemble of the $I_{independent}$ does not need to be concern (Lee *et al.*, 2005; Omote, Ito, and Kawamura, 2003; Lazzari, 2002) but the averaged ensemble of I_{cross} has to be considered carefully. The positive and negative value of the I_{cross} depends on some parameters (Park *et al.*, 2005; Lee *et al.*, 2005; Levine *et al.*, 1989), for instance R_i depend on the grazing incident angle, the refractive index, the thickness of the film, the particles size distribution, and the divergence of the incident X-ray beam. Moreover, the values of F and their complex terms may be changed depend on the film thickness, the particles size distribution, and any incoherent in the incident X-ray beam. According from these reasons, the averaged ensemble of I_{cross} might be disappearing or very small, which are able to be neglected.

By considering the averaged ensemble of I_{cross} , the form of the I_{GLXS} will be reduced to

$$I_{GLXS} \cong \frac{1}{16\pi^2} I_{independent} \quad (4.10)$$

$$I_{GLXS} = \frac{1}{16\pi^2} (|T_i T_f F(q_{\parallel}, q_{1,z})|^2 + |T_i R_f F(q_{\parallel}, q_{2,z})|^2 + |T_f R_i F(q_{\parallel}, q_{3,z})|^2 + |R_i R_f F(q_{\parallel}, q_{4,z})|^2) \quad (4.11)$$

Although the scattering amplitude $F(q_{\parallel}, q_{1,z})$ is in the complex form of the scattering vector $q_{i,z}$, the parameter $|F(q_{\parallel}, q_{1,z})|^2$ can be derived by using a correlation function (Rauscher, Salditt, and Spohn, 1995). For simplicity, we firstly consider only the parameter $|F(q_{\parallel}, q_{1,z})|^2$ as

$$|F(q_{\parallel}, q_{1,z})|^2 = \iint d^2 r_{\parallel} e^{-iq_{\parallel} r_{\parallel}} \int_0^d dz_2 \int_0^d dz_1 e^{-iq_{1,z} z_1} e^{iq_{1,z}^* z_2} C_w(|r_{\parallel}|, z_1, z_2) \quad (4.12)$$

$$|F(q_{\parallel}, q_{1,z})|^2 = \iint d^2 r_{\parallel} e^{-iq_{\parallel} r_{\parallel}} \int_0^d dz_2 \int_0^d dz_1 e^{-i\text{Re}(q_{1,z})(z_1 - z_2)} e^{-\text{Im}(q_{1,z})(z_1 + z_2)} C_w(|r_{\parallel}|, z_1, z_2) \quad (4.13)$$

where $C_w(|r_{\parallel}|, z_1, z_2)$ is the particle-particle correlation function and d is the film thickness layer. In addition, $\text{Im}(x)$ represents the imaginary part of x .

Let $z = z_1 - z_2$ or $z_1 = z + z_2$

$$|F(q_{\parallel}, q_{1,z})|^2 = \iint d^2 r_{\parallel} e^{-iq_{\parallel} r_{\parallel}} \int_0^d dz \int_0^d dz_2 e^{-i\text{Re}(q_{1,z})(z)} e^{\text{Im}(q_{1,z})(z)} e^{2\text{Im}(q_{1,z})(z_2)} C_w(|r_{\parallel}|, z) \quad (4.14)$$

The integrated over z_2 can be calculated directly, hence

$$|F(q_{\parallel}, q_{1,z})|^2 = \frac{1 - e^{2\text{Im}(q_{1,z})d}}{2\text{Im}(q_{1,z})} \iiint d^3 r e^{-iq_{\parallel} r_{\parallel}} e^{-i\text{Re}(q_{1,z})(z)} C_w(r) \quad (4.15)$$

The Fourier transform of the correlation function $C_w(r)$ is related to the scattering intensity (I_1) from the particles inside the films. Thus, the term of $|F(q_{\parallel}, q_{1,z})|^2$ can be rewritten as

$$|F(q_{\parallel}, q_{1,z})|^2 = \frac{1 - e^{2\text{Im}(q_{1,z})d}}{2\text{Im}(q_{1,z})} I_1(q_{\parallel}, \text{Re}(q_{1,z})) \quad (4.16)$$

Where,

$$I_1(q_{\parallel}, \text{Re}(q_{1,z})) = \iiint d^3 r e^{-iq_{\parallel} r_{\parallel}} e^{-i\text{Re}(q_{1,z})(z)} C_w(r) \quad (4.17)$$

The other scattering amplitudes, i.e. $F(q_{\parallel}, q_{2,z})$, $F(q_{\parallel}, q_{3,z})$, and $F(q_{\parallel}, q_{4,z})$ will be considered as the same method. They are also directly relate to the intensity I_1 but different the scattering vector $q_{i,z}$.

Beside, when the X-ray beam reflects from the film, the α_i must be lower than the critical angle of the film (α_c), the approximation of the imaginary part of $q_{i,z}$ can be denoted as

$$\text{Im}(q_{i,z}) = \text{Im}(q_z) = |\text{Im}(k_{z,f})| + |\text{Im}(k_{z,i})| \quad (4.18)$$

From the equations (4.16) and (4.18), the intensity I_{GIXS} that depends on the scattering angle α_f and $2\theta_f$ can be determined as (Lee *et al.*, 2005; Jin *et al.*, 2007; Yoon *et al.*, 2008; Heo *et al.*, 2006.)

$$I_{GIXS}(\alpha_f, 2\theta_f) = \frac{1}{16\pi^2} \frac{1 - e^{2\text{Im}(q_z)d}}{2\text{Im}(q_z)} \left[\begin{array}{l} |T_i T_f|^2 I_1(q_{\parallel}, \text{Re}(q_{1,z})) + \\ |T_i R_f|^2 I_1(q_{\parallel}, \text{Re}(q_{2,z})) + \\ |T_f R_i|^2 I_1(q_{\parallel}, \text{Re}(q_{3,z})) + \\ |R_i R_f|^2 I_1(q_{\parallel}, \text{Re}(q_{4,z})) \end{array} \right] \quad (4.19)$$

The term I_1 is the most valuable parameter as it gives the structural details of the particles in the film that can be defined as

$$I_1(\vec{q}) = P(\vec{q}) \cdot S(\vec{q}) \quad (4.20)$$

where $P(\vec{q})$ is the form factor that relate to the shape, size, and orientations of the particles in thin film. $S(\vec{q})$ is the structure factor that give the details of the positions of the particles and the relative positions between the particles, for example crystal lattice parameters, orientation, dimension, symmetry and the mean distance in an ordered structure.

4.2.1 Form factor: lamellar model, multilayer model, and orthorhombic model

The 2D patterns from GISAXS experiments of the studied polymer thin films such as the miktoarm star polymers PHIC-PCL₁₋₃ and PHIC-PLLA₁₋₃ and the homopolymer, PHIC, PCL, and PLLA were indicated that lamellar structures were formed. Thus, the lamellar model is used to perform a quantitative analysis on those samples. In addition, the model is consisted of three layers, composed of a dense sub-layer, a less dense sub-layer, and an interfacial sub-layer as shown in Figure 4.2.

The form factor for the lamellar three layer model ($P_{lm}(\vec{q})$) can be assumed as

$$P_{lm}(\vec{q}) = \left[\begin{array}{l} 4L_x L_y H_{inner} (\rho_{inner} - \rho_{outer}) \cdot \frac{\sin(q_x L_x)}{q_x L_x} \cdot \frac{\sin(q_y L_y)}{q_y L_y} \cdot \frac{\sin(q_z H_{inner})}{q_z H_{inner}} + \\ 4L_x L_y H_{outer} (\rho_{outer} - \rho_{matrix}) \cdot \frac{\sin(q_x L_x)}{q_x L_x} \cdot \frac{\sin(q_y L_y)}{q_y L_y} \cdot \frac{\sin(q_z H_{outer})}{q_z H_{outer}} \end{array} \right]^2 \quad (4.21)$$

where L_x and L_y are length and width of the lamellar structure respectively, H_{inner} and H_{outer} are the inner and outer layer heights with the relative electron densities of the inner (ρ_{inner}) and outer layers (ρ_{outer}) respectively. Also, ρ_{matrix} is the relative electron density of the matrix layer.

For the lamellar structure formed in the PCL homopolymer film, H_{inner} corresponds to the crystal layer thickness ($= \ell_1 = \ell_c$) and ρ_{inner} ($= \rho_c$) relates to the relatively electron density of the crystal layer. The interfacial layer thickness ($= \ell_i$) is estimated from H_{inner} and H_{outer} : $\ell_i = (H_{outer} - H_{inner})/2$ with a relatively electron density ρ_{outer} ($= \rho_i$). The amorphous layer thickness ℓ_3 ($= \ell_a$) having the relatively electron density ρ_{matrix} ($= \rho_a$) is obtained by $\ell_a = (L - \ell_c - 2\ell_i)$, where the long period L is derived from the structure factor $S(\vec{q})$.

For the lamellar structures formed in the PHIC-PCL₁₋₃ and PHIC-PLLA₁₋₃ films, H_{inner} corresponds to the dense layer thickness ($= \ell_1 = \ell_{\text{PCL/PLLA}}$) with the relatively electron density ρ_{inner} ($= \rho_{\text{PCL/PLLA}}$). The interfacial layer thickness ($= \ell_i$) is determined from H_{inner} and H_{outer} : $\ell_i = (H_{outer} - H_{inner})/2$ having the relatively electron density ρ_{outer} ($= \rho_i$). The less dense layer thickness $\ell_3 (= \ell_{\text{PHIC}})$ having a relatively electron density ρ_{matrix} ($= \rho_{\text{PHIC}}$) is obtained from the long period L as $\ell_{\text{PHIC}} = (L - \ell_{\text{PCL}} - 2\ell_i)$ that is extracted from the structure factor $S(\vec{q})$.

As from the GIWAXS measurements on the polymer films, the multibilayer structure was formed in the PHIC homopolymer film and the PHIC phase in the PHIC-PCL₁₋₃ and PHIC-PLLA₁₋₃ films. Since The PHIC is composed of the polymer backbone and *n*-hexyl bristles (polymer side group), which take part in the lateral structure with interfacial layer (between the backbone and side group) be sharp and narrow, the lamellar bilayer with two layer model is able to analyze.

The form factor $P_{mm}(\vec{q})$ of the multibilayer model (Figure 4.3a) can be defined as (Yoon *et al.*, 2007; Rho *et al.*, 2012)

$$P_{mm}(\vec{q}) = \exp \left[\frac{1}{4\pi} (l_x^2 q_x^2 + l_y^2 q_y^2 + h^2 q_z^2) \right] \quad (4.22)$$

Where l_x and l_y are the length and width of the multibilayer structure, which can divide into a dense layer ($= \ell_1$) with thickness h and a less dense layer with thickness ℓ_2 . The thickness ℓ_2 is also obtained from the long period d_L that is derived from the structure factor $S(\vec{q})$: $\ell_2 = (d_L - \ell_1)$. The *n*-hexyl bristles were totally extended and packed laterally in the PHIC and the PHIC phase of the PHIC-PCL₁₋₃

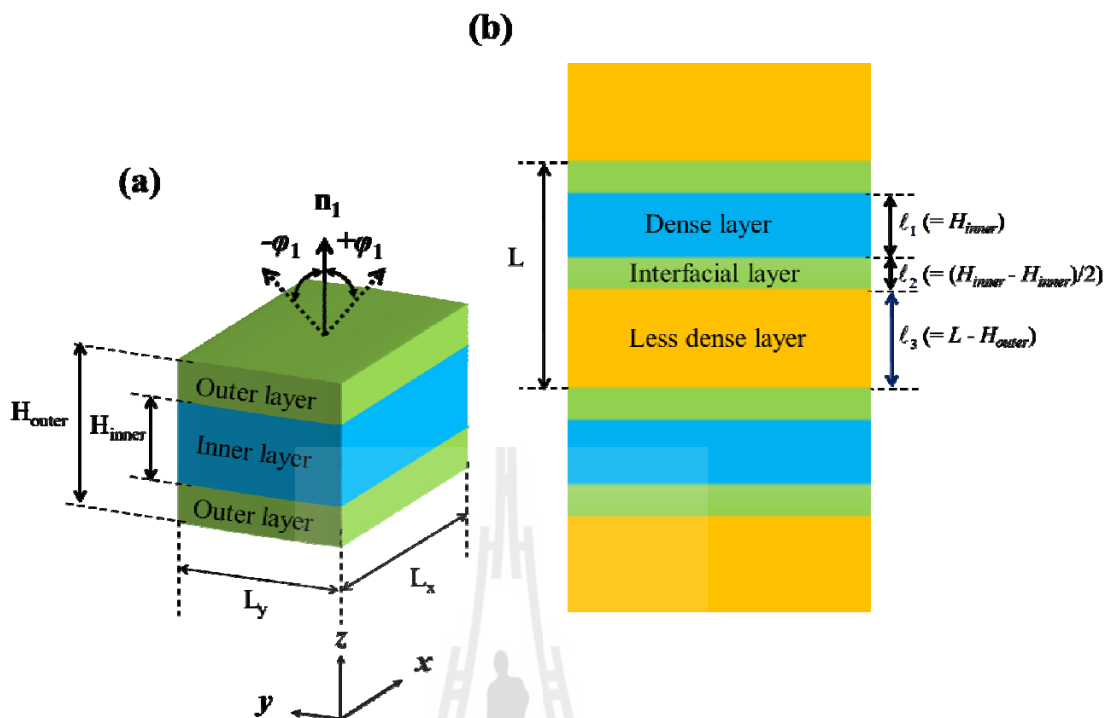


Figure 4.2 Schematic picture of the three layers (dense, less dense, and interfacial layers) lamellar structural model. (a) A 3D representation structure of the lamellar model where φ_1 is an orientation angle of the model, which is between the vector \mathbf{n}_1 and the out-of-plane of the film. (b) A 2D representation structure of the lamellar model. The inner and outer layers in (a) correspond to the dense and interfacial layers in (b) respectively; the orange colored layer in (b) corresponds to the less dense layer. The dimension of the lamellar structure is defined by L (long period), L_x , L_y , $\ell_1 (= H_{inner})$, $\ell_2 (= (H_{outer} - H_{inner})/2)$, and $\ell_3 (= L - H_{outer})$.

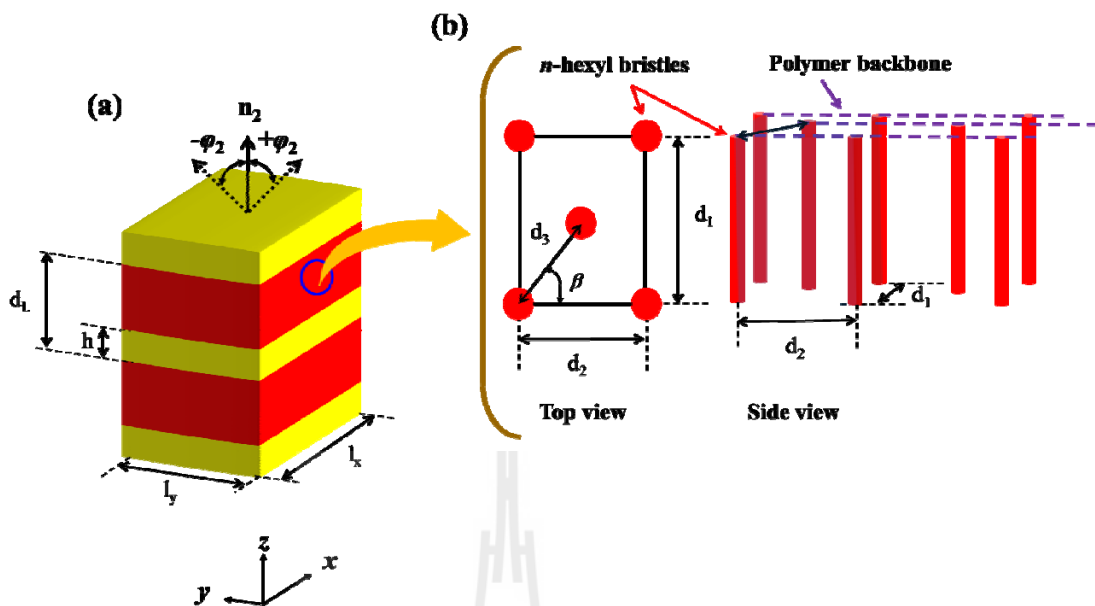


Figure 4.3 Illustration picture of the multilayer (dense and less dense layer) model.

(a) A 3D representation structure of the two layers lamellar model where φ_2 is an orientation angle of the model, which is between the vector \mathbf{n}_2 and the out-of-plane of the film. (b) top and side views of the laterally packed n -hexyl bristles where d_1 is the mean distance between the n -hexyl bristles of the neighboring polymer chains whose repeat units are matched in position along their backbones, d_2 is the mean distance between the nearest n -hexyl bristles along the polymer backbone, d_3 is the mean distance between the n -hexyl bristles and the nearest neighboring n -hexyl bristles, and β is the angle between the d_3 and d_2 directions. The dimension of the lamellar structure is determined by d_L (long period), l_x , l_y , $l_1 (= H_{inner})$, h (dense layer thickness) and $(d_L - h)$ (less dense layer thickness).

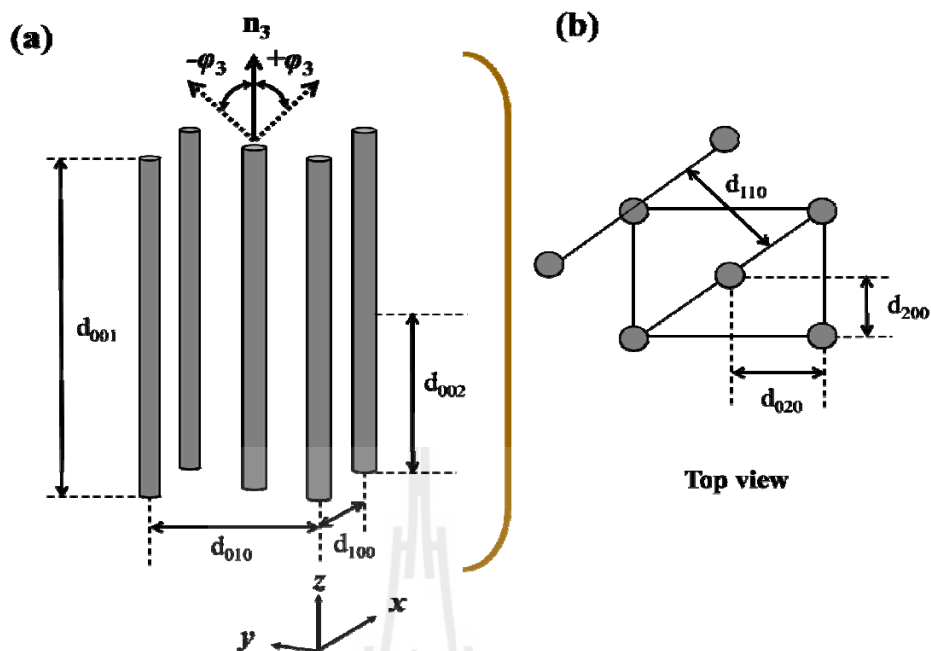


Figure 4.4 The picture of the molecular cylinders orthorhombic lattice model. (a) A 3D representation structure of the orthorhombic model where φ_3 is an orientation angle of the model, which is between the vector \mathbf{n}_3 and the out-of-plane of the film. (b) Top views of the orthorhombic system with dimension length (d -spacing values) are defined by d_{100} , d_{200} , d_{010} , d_{020} , d_{001} , d_{002} , and d_{110} .

and PHIC-PLLA₁₋₃ films. Besides, they were presented as cylindrical particles (Figure 4.3b) with the form factor $P_{om}(\vec{q})$ (equation 4.23).

In case of the PCL homopolymer film and the PCL phase of the PHIC-PCL₁₋₃ and PHIC-PLLA₁₋₃ films, the 2D GIWAXS signals suggested that an orthorhombic lattice was formed in the polymer films. Furthermore, the PCL chain can be considered as cylindrical particles (Figure 4.4) with the orthorhombic lattice form factor $P_{om}(\vec{q})$ can be denoted as (Yoon *et al.*, 2007; Rho *et al.*, 2012)

$$P_{om}(\vec{q}) = \left[2\pi R^2 H \cdot \frac{J_1(q_{\parallel} R)}{q_{\parallel} R} \cdot \frac{\sin(q_z H / 2)}{q_z H / 2} \right]^2 \quad (4.23)$$

where R and H are the radius and length of cylindrical particles.

All of structural parameters from the above form factors are also further assumed a Gaussian distribution $G(A)$ as

$$G(A) = \frac{1}{\sqrt{2\pi}\sigma_A} \exp\left[-\frac{(A - \bar{A})^2}{2\sigma_A^2}\right] \quad (4.24)$$

Where A is one of the parameters, \bar{A} is the mean value, and σ_A is the standard deviation of A from \bar{A} .

4.2.2 Structure factor: paracrystal

The appropriate structure factor $S(\vec{q})$ for the lamellar morphology, the multibilayer conformation, and the orthorhombic crystal structure of the polymer films has been found as a paracrystal model. The model can be treated as the Fourier transform of a complete set of lattice points (Lee *et al.*, 2005; Heo *et al.*, 2006; Kim *et al.*, 2014). The paracrystal model with distortion of the second kind, its lattice points are not fixed, hence the position of those lattice points can be explained as a positional distribution function or g-factor. When the autocorrelation function of a crystal lattice is determined from the convolution product of the Gaussian distribution function of the lattice points along three axes, $S(\vec{q})$ can be written as (Yoon *et al.*, 2007; Rho *et al.*, 2012)

$$S(\vec{q}) = \prod_{k=1}^3 Z_k(\vec{q}) \quad (4.25)$$

Where the lattice factor $Z_k(\vec{q})$ in the k component is

$$Z_k(\vec{q}) = 1 + \frac{F_k(\vec{q})}{1 - F_k(\vec{q})} + \frac{F_k^*(\vec{q})}{1 - F_k^*(\vec{q})} \quad (4.26)$$

where

$$F_k(\vec{q}) = |F_k(\vec{q})| e^{-i\vec{q} \cdot \vec{a}_k} \quad (4.27)$$

$$|F_k(\vec{q})| = \exp \left[-\frac{1}{2} (q_1^2 g_1^2 + q_2^2 g_2^2 + q_3^2 g_3^2) \right] \quad (4.28)$$

Here g_1 , g_2 , and g_3 are the components of the g -factor defined as

$$g_1 = \Delta \vec{a}_1 / \vec{a}_1 \quad (4.29)$$

$$g_2 = \Delta \vec{a}_2 / \vec{a}_2 \quad (4.30)$$

$$g_3 = \Delta \vec{a}_3 / \vec{a}_3 \quad (4.31)$$

where \vec{a}_k is the component of the fundamental vector \vec{a} of the domain structure and $\Delta \vec{a}_k$ is the displacement of the vector \vec{a}_k .

The scattering vector \vec{q} for the lamellar morphology with three layers is defined as

$$q_1 = \vec{a}_1 \cdot \vec{q}_x = |d_x \times q_x| \quad (4.32)$$

$$q_2 = \vec{a}_2 \cdot \vec{q}_y = |d_y \times q_y| \quad (4.33)$$

$$q_3 = \vec{a}_3 \cdot \vec{q}_z = |L \times q_z| \quad (4.34)$$

where d_x and d_y are the lattice dimension parameters (d -spacing values) along x and y directions as well as q_x and q_y are the scattering vector in the x and y directions. L is the long period along z direction and q_z is the scattering vector in z directions (Figure 4.2).

For the multibilayer structure, the components of the vector \vec{q} are assumed as

$$q_1 = \vec{a}_1 \cdot \vec{q}_x = |d_x \times q_x| \quad (4.35)$$

$$q_2 = \vec{a}_2 \cdot \vec{q}_y = |d_y \times q_y| \quad (4.36)$$

$$q_3 = \vec{a}_3 \cdot \vec{q}_z = |d_L \times q_z| \quad (4.37)$$

where d_x and d_y are also the lattice dimension parameters (d -spacing values), while d_L is the long period along the q_x and q_y and q_z directions (Figure 4.3a).

In addition, the scattering vector \vec{q} for the laterally structure of n -hexyl bristles in the multibilayer structure can be written as

$$q_1 = \vec{a}_1 \cdot \vec{q}_x + \vec{a}_1 \cdot \vec{q}_y = |d_3 \sin \beta \times q_x + d_3 \cos \beta \times q_y| \quad (4.38)$$

$$q_2 = \vec{a}_2 \cdot \vec{q}_x + \vec{a}_2 \cdot \vec{q}_y = |0 \times q_x + d_2 \times q_y| \quad (4.39)$$

$$q_3 = \vec{a}_3 \cdot \vec{q}_x + \vec{a}_3 \cdot \vec{q}_y = |d_1 \times q_x + 0 \times q_y| \quad (4.40)$$

where d_1 is the mean distance between the n -hexyl bristles of the neighboring polymer chains whose repeat units are matched in position along their backbones, d_2 is the mean distance between the nearest n -hexyl bristles along the polymer backbone, d_3 is the mean distance between the n -hexyl bristles and the nearest neighboring n -hexyl bristles, and β is the angle between the d_3 and d_2 directions (Figure 4.3b).

In case of the orthorhombic conformation, the vector components of \vec{q} can be defined as

$$q_1 = \vec{a}_1 \cdot \vec{q}_x + \vec{a}_1 \cdot \vec{q}_y = |d_{020} \times q_x + d_{200} \times q_y| \quad (4.41)$$

$$q_2 = \vec{a}_2 \cdot \vec{q}_x + \vec{a}_2 \cdot \vec{q}_y = |0 \times q_x + (2 \cdot d_{200}) \times q_y| \quad (4.42)$$

$$q_3 = \vec{a}_3 \cdot \vec{q}_z = |d_{002} \times q_z| \quad (4.43)$$

where d_{020} and d_{200} are the lattice dimension parameters (d -spacing values) of the orthorhombic system as shown in Figure 4.4.

4.3 Crystal Orientation and Distribution

The crystal orientation information of the above structures can be obtained from vector \mathbf{n}_i with aligned in the normal direction to the film surface. The polar angle φ is measured between the \mathbf{n}_i vector with aligned in the normal direction to the film surface and the out-of-plane of the film (also see in Figures 4.2a, 4.3a, and 4.4a), for example, when φ is zero, the \mathbf{n}_i vector (crystal orientation) will be parallel in the normal direction to the film plane.

In addition, the distribution of the orientation vector \mathbf{n}_i is given by a function $D(\varphi)$, which can be considered as a Gaussian distribution and written as

$$D(\varphi) = \frac{1}{\sqrt{2\pi}\sigma_\varphi} \exp\left[-\frac{(\varphi - \bar{\varphi})^2}{2\sigma_\varphi^2}\right] \quad (4.44)$$

where $\bar{\varphi}$ and σ_φ are the mean angle and standard deviation of φ from $\bar{\varphi}$, respectively.

4.4 Second-order Orientation Factor

The observed scattering intensity $I_{GIXS,\varphi}(\vec{q})$ can be obtained by integrating $I_{GIXS}(\vec{q})$ over the possible orientations of the crystal lattice

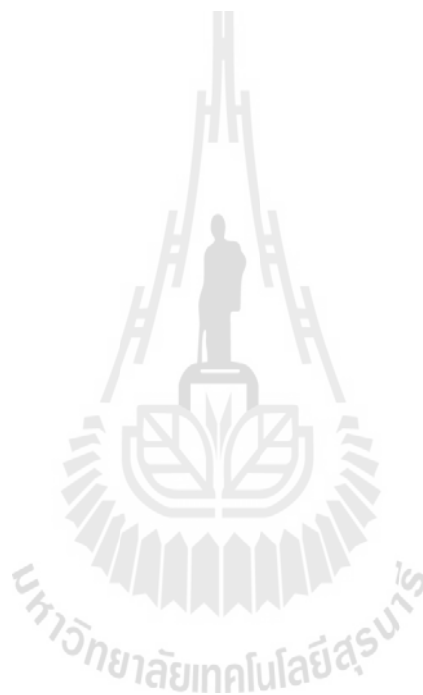
$$I_{GIXS,\varphi}(\vec{q}) = \int_{-\pi}^{\pi} I_{GIXS}(\vec{q}) D(\varphi) d\varphi \quad (4.45)$$

Furthermore, the second-order orientation factor O_s (Kim *et al.*, 2014; Yoon *et al.*, 2007) can be defined as

$$O_s = \int D(\varphi) \frac{(3\cos^2 \varphi - 1)}{2} d\varphi \quad (4.46)$$

When the value of O_s is equal to 1, it corresponds to perfect crystalline orientation in the 0^0 ($=\varphi$) and O_s is equal to -0.5, it agrees with the perfectly crystal

orientation in the $90^0 (= \varphi)$. On the other hand, if the orientation is entirely random, the O_s will be 0. Thus, the O_s is a quantitative measure of the structural orientation deviates from the direction of interest.



CHAPTER V

CHARACTERIZATION OF POLY(N-HEXYL ISOCYANATE)-BLOCK-POLY(ϵ -CAPROLACTONE) MIKTOARM STAR POLYMERS THIN FILMS BY GRAZING X-RAY SCATTERING

5.1 Introduction

Miktoarm star polymers with a rod-coil type are composed of chemically different block polymers joined at a single junction point to form a star shape. The miktoarm star polymers are interesting and get more attention from many researchers because of their important applications in nanoscience (Iatrou, and Hadjichristidis, 1992; Pitsikalis *et al.*, 1998; Hadjichristidis *et al.*, 2001; Khanna, Varshney, and Kakkar, 2010). In particular, the thin film form of the miktoarm star polymers are a novel class of advanced nanomaterials with applications in microelectronic, optical, and optoelectronic devices.

The self-organized behavior of the miktoarm star polymers in bulk and solution forms have been examined with many techniques (Babin *et al.*, 2005; Gitsas *et al.*, 2010; Junnila *et al.*, 2010; Touris *et al.*, 2008; Rahman *et al.*, 2008) but not widely in thin film form. Since film thickness has effect on the self-assemble behavior of the polymers in thin film form, their structures could be different from those in the solid

or solution state. The molecular configuration can be affected by interactions between the polymers and substrate and between the polymers and air or a vacuum at the interfaces (Hamley, 2009; Huang, Chen, and Tung, 2012). The rod-coil miktoarm star polymers have been introduced as a new class of miktoarm star polymers and present unique properties due to the effects from the rigid-rod of arm component. Moreover, the rod-coil miktoarm star polymers showed self-assembled behavior dissimilar from the conventional coil-coil miktoarm copolymers even their volume fraction can be comparable (Rahman *et al.*, 2008).

The rod-coil type miktoarm star polymers, PHIC-PCL₁₋₃, composed of a rigid rod-like poly(*n*-hexyl isocyanate) (PHIC) arm with a number-average molecular weight M_n of 5100–5200 g/mol and one to three semi-crystalline coil-like poly(ϵ -caprolactone) arms (PCL_{*n*}: *n* = 1–3) with a total molecular weight M_n of 17400–18000 g/mol, i.e. PHIC(5.1k)-PCL(17.5k), PHIC (5.2k)-PCL₂(18.0k), and PHIC(5.2k)-PCL₃(17.4k), also another series of the PHIC-PCL₁₋₃ with M_n of PHIC arm around 9,600-10,900 g/mol and one to three PCL arms (PCL_{*n*}: *n* = 1–3) with the M_n approximate 10,600-11,100 g/mol, i.e. PHIC(10.3k)-PCL(10.6k), PHIC(10.9k)-PCL₂(11.1k), and PHIC(9.6k)-PCL₃(11.0k) have been successfully synthesized and reported in the previous research (Sato *et al.*, 2014) but their nanoscale morphology and structural ordering in thin film form have been not yet investigated. PHIC is a rigid rod polymer with a persistence length around 20-60 nm. It has application on the field of liquid crystals, optical switches, and chiral sensing (Rho *et al.*, 2012). PCL is known as biodegradable polymer. It has been used in medical, biomedical engineering, and drug delivery system (Woodruff and Hutmacher, 2010).

In this research, we used GIXS techniques to characterize the molecular and crystal structures of the PHIC-PCL₁₋₃ thin films with various numbers of PCL arms and length, annealed by toluene and CHCl₃. The effects due to the number and length of PCL arms on the self-organized behavior of the PHIC-PCL₁₋₃ films were examined. Also, the structures of homopolymer films, PHIC with M_n around 5,400 and 10,400 g/mol and PCL with the M_n approximate 15,000 and 10,500 g/mol, respectively, under toluene and CHCl₃ annealing, were also characterized in order to compare with those of the PHIC-PCL₁₋₃ films.

5.2 Experimental Section

5.2.1 Materials and Thin Films Preparation

PHIC-PCL₁₋₃ miktoarm star polymers as well as PHIC and PCL homopolymer were synthesized by living coordination polymerization method. The fundamental properties i.e. approximate number of averaged molecular weight M_n , polydispersity index, and volume fraction of these homopolymer and star polymers were reported in Table 5.1. The preparation of each polymer product in the thin film form was as the following. PHIC and PCL homopolymer and PHIC-PCL₁₋₃ in powder form were dissolved in chloroform (CHCl₃) and filtered using a disposable syringe equipped with polytetrafluoroethylene filter with the pore size of 0.2 μm , resulting in a 1.0 wt% solution. The filtered solutions were coated onto pre-cleaned silicon substrates by spin coater using the speed 1,500-2,000 round per second for 50-60 second and dried in vacuum at room temperature for one day. The polymer thin films with thickness of around 80-120 nm, determined by a spectroscopic ellipsometer (model M2000, J. A. Woollam, Lincoln, NE, USA), were obtained. After that, the polymer films were

annealed with toluene and CHCl_3 . For PHIC(5k)-PCL₁₋₃(17k), PHIC(5.4k), and PCL(14.5k) films, they were annealed by toluene for 2.5 hours. For PHIC(10k)-PCL₁₋₃(10k), as well as PHIC(10.4k) and PCL(10.5k) films, they were annealed in both toluene and CHCl_3 with different time conditions. In more details, the PHIC-PCL, the PHIC, and the PCL films were annealed under toluene for 2 hours, while the PHIC-PCL₂ and the PHIC-PCL₃ films were under toluene annealing for 4 hours and 3.5 hours, respectively. In case of annealing under CHCl_3 for 30 minutes in both the PHIC and PCL films, and 3 hours, 1.5 hours, and 45 minutes for the PHIC-PCL film, the PHIC-PCL₂ film, and the PHIC-PCL₃ film, respectively.

5.2.2 Measurements

The various of M_n of PHIC and PCL homopolymer films and of PHIC-PCL₁₋₃ miktoarm star polymer thin films, under toluene and/or CHCl_3 annealing, were measured with grazing incidence X-ray scattering (GIXS) technique at Pohang Accelerator Laboratory (PAL), Pohang, South Korea. Grazing incidence small angle X-ray scattering (GISAXS) experiments were performed with sample to detector distance (SDD) of 2,922 mm and 992 mm at the beamline 3C (Yoon *et al.*, 2008; Lee *et al.*, 2005; Lee *et al.*, 2005; Rho *et al.*, 2014), and grazing incidence wide angle X-ray scattering (GIWAXS) measurements were performed with the SDD of 229 mm at the beamline 9A (Yoon *et al.*, 2008; Lee *et al.*, 2005; Lee *et al.*, 2005; Rho *et al.*, 2014). The scattering intensities were measured as a function of the scattering angles α_f and $2\theta_f$, with the X-ray wavelength(λ) of 1.21 Å, 1.18 Å, 1.17 Å, and 1.12 Å. The GIXS measurements were performed at room temperature with the exposure time of 30 – 60 s. The incidence angle α_i of the X-ray beam was set in the range of 0.110-0.140°, which is between the critical angles of the star polymers or the homopolymers

films and the silicon substrate. The scattering data were collected using a 2D charge-coupled detector (CCD) (Rayonix MAR CCD). The polystyrene-*b*-polyethylene-*b*-poly-butadiene-*b*-polystyrene block copolymer and silver behenate powder (TCI, Tokyo, Japan) were used as a calibration standard for the SDD. Aluminum foil strip were attached as a semitransparent beam stop in order to protect the detector due to the high intensity of specular reflection beam from the substrate.

5.3 Results and Discussions

The series of M_n of PHIC-PCL₁₋₃ miktoarm star polymers, PHIC and PCL homopolymer in thin films formed were annealed by toluene and CHCl₃ in order to induce well-organized structure govern in the films and then characterized with GIXS (GISAXS and GIWAXS) technique.

Figures 5.1a-5.1c and 5.2a-5.2c presented 2D GISAXS patterns and scattering profiles along the out-of-plane (α_f) and in-plane ($2\theta_f$) directions of toluene-annealed PHIC(5.4k) and PHIC(10.4k) films, respectively, while 2D GISAXS patterns and scattering profiles in the both out-of-plane and in-plane directions of CHCl₃-annealed PHIC(10.4k) were shown in Figure 5.3a. All the PHIC films were featureless and could not be characterized by GISAXS.

However, in case of PCL homopolymer films, the PCL(15k, 10.5k) under toluene annealing and the PCL(10.5k) in CHCl₃ annealing showed a similar feature in the 2D GISAXS data as shown in Figures 5.1d, 5.2d, and 5.3d, respectively. In addition, their out-of-plane profiles displayed a broad scattering weak peak at 0.40–0.80° (Figures 5.1e, 5.2e, and 5.3e), which occurring due to the heavy overlap

Table 5.1 Fundamental properties of the PHIC and PCL homopolymers and PHIC-PCL₁₋₃ miktoarm star polymers used in the study.

Polymer	$M_{n,NMR}^a$	M_w/M_n^b	f_{PHIC}^c (%)
PHIC	5400	1.05	100
	10,400	1.11	100
PCL	15,000	1.10	0
	10,500	1.04	0
PHIC-PCL	22,600	1.09	23
	20,900	1.07	53
PHIC-PCL ₂	23,200	1.07	23
	22,000	1.17	53
PHIC-PCL ₃	22,600	1.09	23
	20,600	1.09	50

^a Number-average molecular weight determined in CDCl₃ by ¹H NMR spectroscopy analysis.

^b Polydispersity determined by size exclusion chromatography (SEC) in THF using polystyrene standards.

^c Volume fraction of PHIC arm: $f_{PHIC} = (M_{n,NMR,PHIC}/d_{PHIC}) / (M_{n,NMR,PHIC}/d_{PHIC} + M_{n,NMR,PCL}/d_{PCL})$; $d_{PHIC} = 1.00 \text{ g/cm}^3$ and $d_{PCL} = 1.15 \text{ g/cm}^3$.

from the reflected and transmitted X-ray beams gathered at the chosen grazing incidence angle α_i (0.013°-0.140°). In case of the PCL(10.5k), the second broad and weak peak was presented as well. The scattering peak along the $2\theta_f$ direction could not be observed (Figures 5.2f, and 5.3f) except for the PCL(15k) (Figure 5.1f). The intensity profiles showed peak at $\alpha_f = 0.525^\circ$, which corresponds to the d-spacing (d_s) of 12.9 nm and very broad and weak peak at $2\theta_f = 0.30^\circ$ - 0.80° , for the PCL(15k), at $\alpha_f = 0.513^\circ$ and 1.442° , corresponding to the d-spacing (d_s) of 13.1 nm for the toluene-annealed PCL(10.5k), and at $\alpha_f = 0.503^\circ$ and 1.432° , corresponding to $d_s = 13.3 \text{ nm}$. These scattering characteristics suggested that the main structure of all the PCL(15k, 10.5k) films formed a horizontally oriented structure. However, only the PCL(15k) showed a very small number of the vertical lamellar conformation was formed.

The out-of-plane and in-plane profiles could be satisfactorily fitted using the GIXS formula for a three layer lamellar model (Yoon *et al.*, 2007; Yoon *et al.*, 2008; Ahn *et al.*, 2010; Ahn *et al.*, 2013). The lamellar model is explained in the Chapter IV. The fitting results, derived for a three layer lamellar structural model (Figures 5.1h, 5.2h, and 5.3h), are shown in Figure 5.1e-5.1f, 5.2e-5.2f, and 5.3e-5.3f. The structural parameters obtained from the GIXS formula for the PCL(15k) and PCL(10.5k) are also reported in Tables 5.2 and 5.3, respectively.

The GIXS analysis reveals that the horizontally oriented lamellar structure of the PCL(15k) had a long period L of 12.6 nm. Each lamella was composed of three sublayers: a highly dense sublayer (l_1) or crystalline layer (l_c), which $l_1 = l_c = 3.3$ nm thick, a less dense sublayer (l_3) or amorphous layer (l_a), $l_3 = l_a = 6.1$ nm thick, and an interfacial layer $l_2 = l_i = 1.6$ nm thick. The lamellar structure displayed a second-order orientation factor $O_{s,1}$ of 0.916. The mean polar angle $\bar{\varphi}_1$ between the orientation vector \mathbf{n}_1 of the horizontal lamellar structure and the out-of-plane direction of the film was 0° , but its standard deviation σ_{φ_1} was 6.3° . The positional distortion factor g of this lamellar structure was 0.35. The g and σ_{φ_1} values were high, indicating the presence of a certain degree of disorder in the horizontal lamellar structure in the PCL thin film. Additionally, the 2D pattern of the PCL(15k) was reconstructed by using the same structure parameters from the GIXS fitting, as presented in Figure 5.1g. It can be seen that the simulated pattern agreed well with the GISAXS measurement data.

Furthermore, the structural parameters from the similarly horizontal lamellar structure obtained from the GIXS fitting of the PCL(10.5k) in toluene and CHCl_3 are reported in Table 5.3. The horizontally oriented lamellar structure of the toluene-

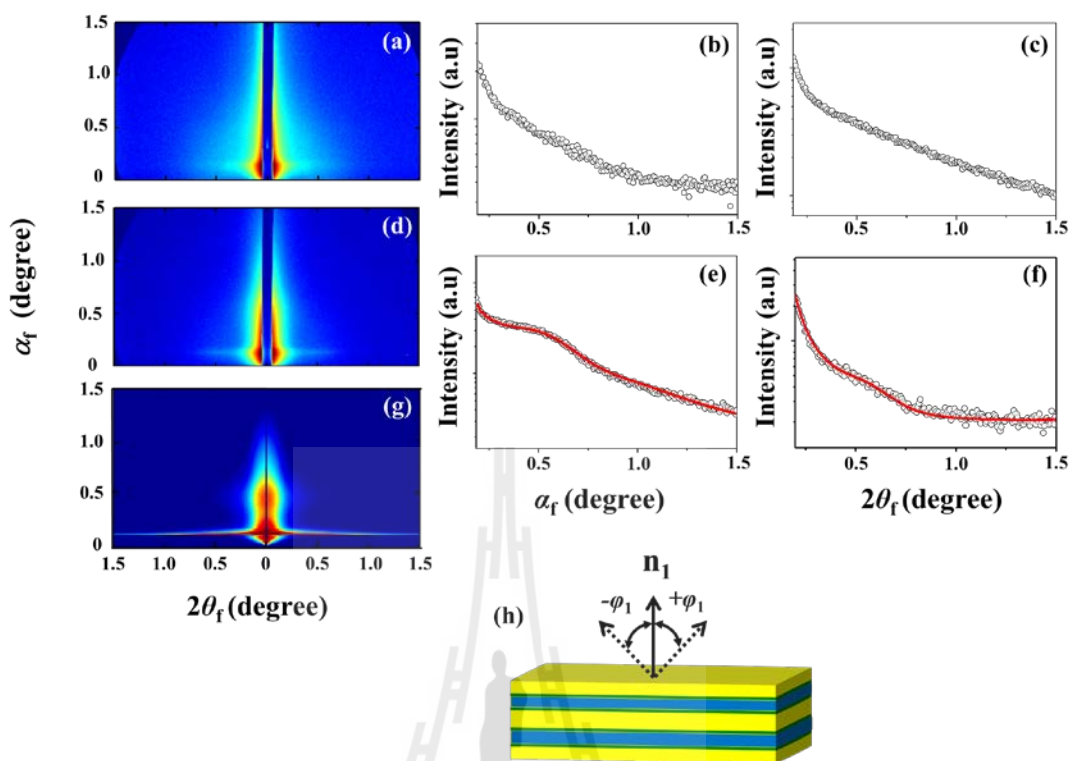


Figure 5.1 2D GISAXS patterns of toluene-annealed PHIC(5.4k) and PCL(15k) homopolymer films (120 nm thick) measured with an incidence angle α_i of 0.140° at RT using an X-ray wavelength λ of 0.1180 nm; (a) PHIC film; (b) out-of-plane profile extracted from the data in (a) along the α_f direction at $2\theta_f = 0.100^\circ$; (c) in-plane profile extracted from the data in (a) along the $2\theta_f$ direction at $\alpha_f = 0.170^\circ$; (d) PCL film; (e) out-of-plane profile extracted from the data in (d) along the α_f direction at $2\theta_f = 0.100^\circ$; (f) in-plane profile extracted from the data in (d) along the $2\theta_f$ direction at $\alpha_f = 0.170^\circ$; (g) 2D image of PCL film reconstructed from the structural parameters in Table 5.2 using the GIXS formula derived for lamellar structure model; (h) lamellar structure model where \mathbf{n}_1 is the orientation vector of the structure model and φ_1 is the polar angle between the \mathbf{n}_1 vector and the out-of-plane of the film. In (e) and (f), the black circular symbols are the measured data, and the red solid lines represented as a fitting result from the GIXS formula.

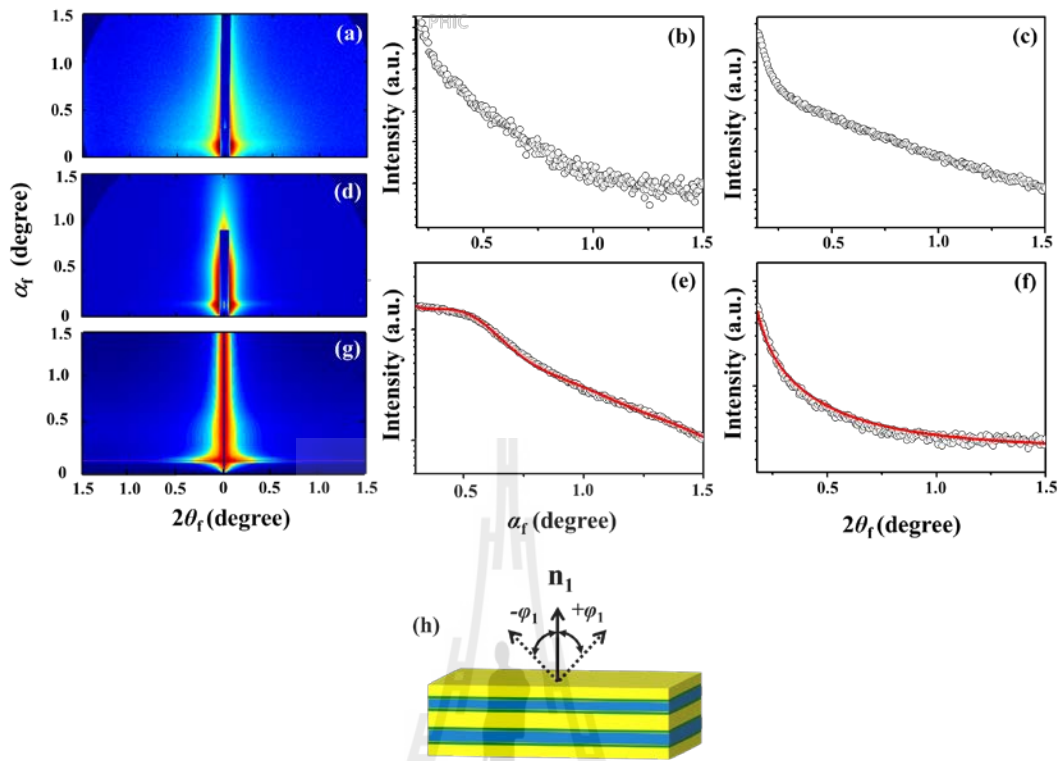


Figure 5.2 2D GISAXS patterns of toluene-annealed PHIC(10.4k) and PCL(10.5k) homopolymer films (80 nm thick) measured with an incidence angle α_i of 0.130° at RT using an X-ray wavelength λ of 0.1170 nm; (a) PHIC film; (b) out-of-plane profile extracted from the data in (a) along the α_f direction at $2\theta_f = 0.090^\circ$; (c) in-plane profile extracted from the data in (a) along the $2\theta_f$ direction at $\alpha_f = 0.140^\circ$; (d) PCL film; (e) out-of-plane profile extracted from the data in (d) along the α_f direction at $2\theta_f = 0.090^\circ$; (f) in-plane profile extracted from the data in (d) along the $2\theta_f$ direction at $\alpha_f = 0.140^\circ$; (g) 2D image of PCL film reconstructed from the structural parameters in Table 5.3 using the GIXS formula derived for three layer lamellar structural model; (h) lamellar structure model where \mathbf{n}_1 is the orientation vector of the structure model and φ_4 is the polar angle between the \mathbf{n}_1 vector and the out-of-plane of the film. In (e) and (f), the black circular symbols are the measured data, and the red solid lines represented as a fitting result from the GIXS formula.

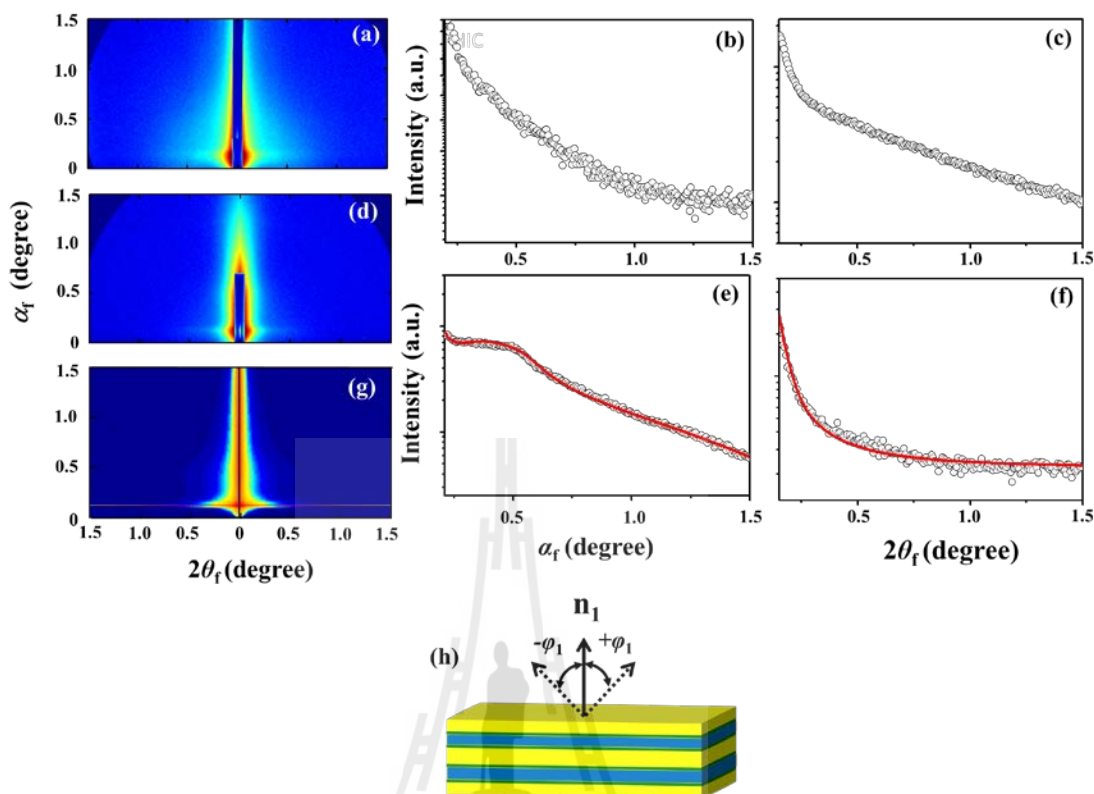


Figure 5.3 2D GISAXS patterns of CHCl_3 -annealed PHIC(10.4k) and PCL(10.5k) films (80 nm thick) measured with an incidence angle α_i of 0.130° at RT using an X-ray wavelength λ of 0.1170 nm; (a) PHIC film; (b) out-of-plane profile extracted from the data in (a) along the α_f direction at $2\theta_f = 0.090^\circ$; (c) in-plane profile extracted from the data in (a) along the $2\theta_f$ direction at $\alpha_f = 0.140^\circ$; (d) PCL film; (e) out-of-plane profile extracted from the data in (d) along the α_f direction at $2\theta_f = 0.090^\circ$; (f) in-plane profile extracted from the data in (d) along the $2\theta_f$ direction at $\alpha_f = 0.140^\circ$; (g) 2D image of PCL film reconstructed from the structural parameters in Table 5.3 using the GIXS formula derived for lamellar structure model; (h) lamellar structure model where \mathbf{n}_1 is the orientation vector of the structure model and φ_1 is the polar angle between the \mathbf{n}_1 vector and the out-of-plane of the film. In (e) and (f), the black circular symbols are measured data, and the red solid lines represented as a fitting result from the formula.

annealed PCL(10.5k) has been found a long period L of 12.4 nm with high dense sublayer $\ell_1 = \ell_c = 3.6$ nm, less dense layer $\ell_3 = \ell_a = 5.8$ nm thick, and an interfacial layer (ℓ_i) with $\ell_2 = \ell_i = 1.5$ nm thick. The orientation of the lamellar structure was also characterized as $\overline{\varphi}_1$ (mean polar angle) between the orientation vector \mathbf{n}_1 of the horizontal lamellar structure and the out-of-plane direction of the film was 0° . Its standard deviation σ_{φ_1} and second-order orientation factor $O_{s,1}$ were found as 6.3° and 0.982, respectively. For the CHCl_3 -annealed PCL(10.5k), the PCL structure had a long period $L = 12.5$ nm composing of high dense sublayer $\ell_1 = \ell_c = 3.6$ nm thick, interfacial layer $\ell_2 = \ell_i = 1.4$ nm thick, and amorphous layer $\ell_3 = \ell_a = 6.1$ nm thick. The positional distortion factor $g = 0.36$. The orientation was also characterized as $\overline{\varphi}_1 = 0^\circ$ with $\sigma_{\varphi_1} = 5.8$ and $O_{s,1} = 0.985$. The positional distortion factor g and σ_{φ_1} values were also high. Figures 5.2g and 5.3g represented the simulated pattern of the toluene and CHCl_3 -annealed PCL(10.5k), respectively, using the same GIXS structural parameters. Here, the simulated patterns agreed well with the measurement data.

Overall, the PCL(15k) and PCL(10.5k) films showed a phase separation between crystalline and amorphous domains formed a horizontally oriented lamellar structure, regardless of toluene and CHCl_3 annealing.

The 2D GISAXS patterns of toluene-annealed PHIC(5k)-PCL₁₋₃(17k) thin films appeared to have more features than that of the PCL film suggested that there were well-order nanostructures developed in these thin films. Figures 5.4a and 5.4b showed 2D GISAXS patterns from different distance between sample and detector and

Figures 5.4c and 5.4d showed the out-of-plane and in-plane scattering profiles of a toluene-annealed PHIC(5.1k)-PCL(17.5k) film. A peak position of the PHIC-PCL was observed at 0.387° along the α_f direction. Another peak was weakly discernible around 1.187° along the α_f direction. These two peaks correspond to the d-spacing of 17.4 nm. These scattering characteristics indicated that a horizontally oriented lamellar structure was present in the PHIC-PCL film. The out-of-plane scattering profile could be satisfactorily fitted using the GIXS formula for the three layer lamellar model (Figure 5.4c).

The obtained structural parameters are summarized in Table 5.2. The PHIC-PCL lamellar structure was characterized by $L = 16.4$ nm, $l_1 = 8.3$ nm (highly dense layer thickness: PCL phase thickness), $l_3 = 4.1$ nm (less dense layer thickness: PHIC phase thickness), $l_i = 2.0$ nm (interfacial layer thickness), $O_{s,1} = 0.916$ ($\bar{\varphi}_1 = 0^\circ$ and $\sigma_{\varphi_1} = 14.0^\circ$), and $g = 0.29$. These structural parameters were also used to simulate the 2D GISAXS image, as shown in Figure 5.4e. Again, this reconstructed image agreed well with the experimental data. Here, the assignment of l_3 and l_1 to the PHIC and PCL phases were made by considering the volume fractions of PHIC and PCL arm components. The interfacial layer (l_2) in the horizontally oriented lamellar structure of the PHIC-PCL film was larger than that formed in the horizontally oriented lamellar structure in the PCL film. Moreover, the scattering profile along the $2\theta_f$ direction presented a very small peak at $2\theta_f = 0.20^\circ$ - 0.30° implied that a small number and poorly ordered vertical structure occurred in the PHIC-PCL film. The in-plan profile was fitted well with the lamellar model as shown in Figure 5.4d and the obtained structural parameters were reported in Table 5.2.

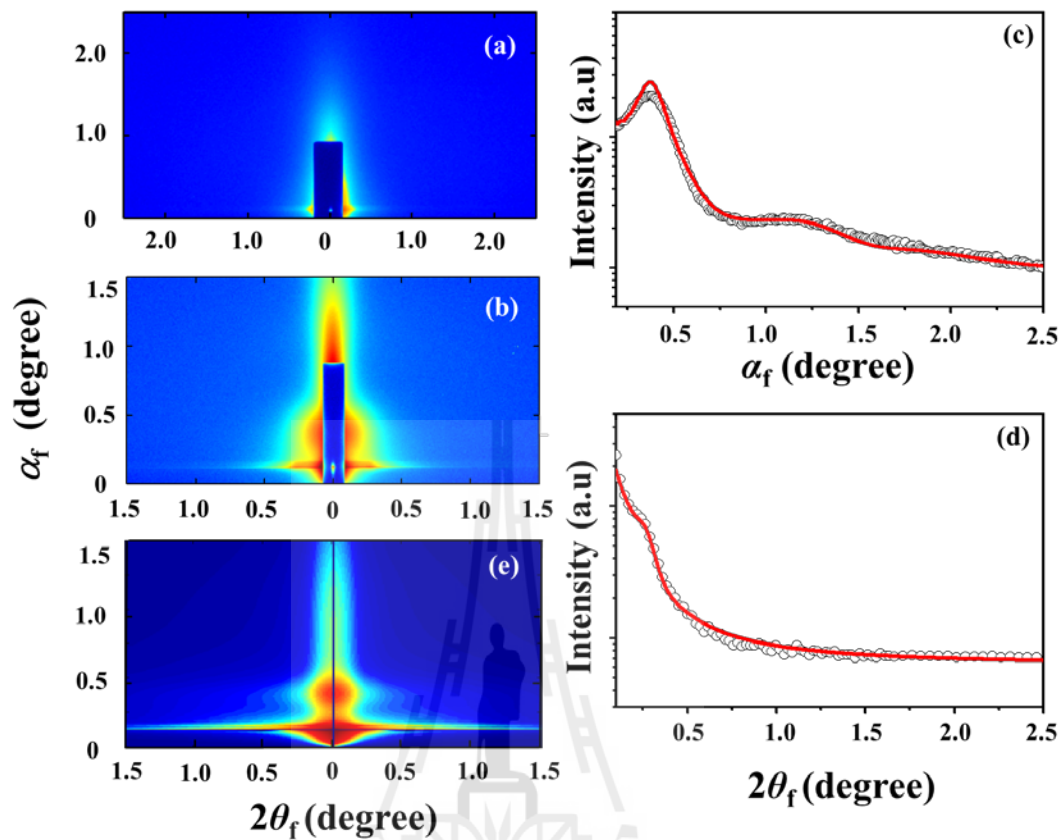


Figure 5.4 2D GISAXS pattern of toluene-annealed PHIC(5.1k)-PCL(17.5k) film (120 nm thick) measured at room temperature using an X-ray wavelength $\lambda = 0.1180$ nm; (a) measured with $\alpha_i = 0.110^\circ$ at a sample-to-detector distance (SDD) of 902 mm; (b) measured with $\alpha_i = 0.140^\circ$ at SDD = 2922 mm; (c) out-of-plane scattering profile extracted from the data in (a) and (b) along the α_f direction at $2\theta_f = 0.140^\circ$ where the black circular symbols are the measured data, and the red solid lines were obtained by fitting the data using the GIXS formula; (d) in-plane scattering profile extracted from the data in (a) and (b) along the $2\theta_f$ direction at $\alpha_f = 0.190^\circ$; (e) 2D scattering image reconstructed from the structural parameters in Table 5.2 using the GIXS formula derived for lamellar structure model.

The above GIXS analysis results suggest that the PHIC-PCL molecules in thin films underwent phase separation (PHIC and PCL domains) during the film formation process and subsequent toluene annealing, thereby forming a major structure as horizontally oriented lamellar.

The 2D GISAXS patterns from PHIC(5.2k)-PCL₂(18k) (Figures 5.5a and 5.5b) and PHIC(5.2k)-PCL₃(17.4k) (Figures 5.6a and 5.6b) films, annealing under toluene, presented similarly pattern to the PHIC-PCL, implying that the horizontally oriented lamellar structure formed. The peak position of the PHIC-PCL₂ was observed at $\alpha_f = 0.402^\circ$. Another weak and broad peak was observed at 1.327° which correspond to d_s value of 16.8 nm. For the PHIC-PCL₃, the scattering peaks occurred at $\alpha_f = 0.410^\circ$ and very weak and broad peak at 1.366° which correspond to d_s value of 16.4 nm. While the scattering peaks along their in-plane directions could not be discernible. Their out-of-plane and in-plane profiles could be successfully fitted using the GIXS formula for the lamellar structural model as shown in Figures 5.5c-5.5d and Figures 5.6c-5.6d. The obtained structural parameters are listed in Table 5.2.

By using the same parameters from the GIXS formula, the 2D reconstructed images of the PHIC-PCL_{2,3} were shown in Figures 5.5e and 5.6e, respectively. The simulations agree well with their 2D GISAXS experimental data. These analyses also indicated that during the film formation process and subsequent toluene annealing, a well ordered horizontal lamellar structure formed in the PHIC-PCL₂₋₃ films by undergoing phase separation of PHIC and PCL arms.

Overall, these GISAXS analyses indicated that horizontally oriented lamellar structure are dominantly formed in the PHIC(5k)-PCL₁₋₃(17k) films during the film formation process and subsequent toluene annealing via phase separations of the

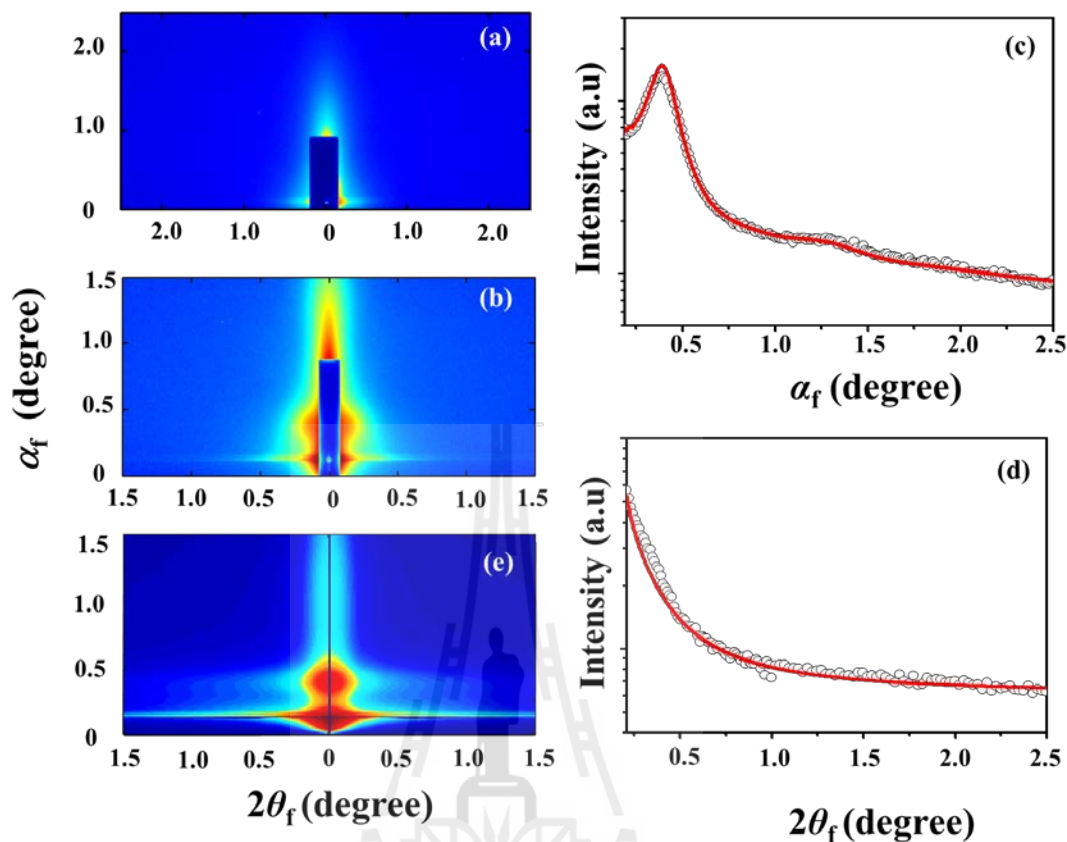


Figure 5.5 2D GISAXS pattern of toluene-annealed PHIC(5.2k)-PCL₂(18k) film (120 nm thick) deposited on silicon substrates, measured at room temperature using an X-ray wavelength $\lambda = 0.1180$ nm; (a) measured with $\alpha_i = 0.110^\circ$ at SDD = 902 mm; (b) measured with $\alpha_i = 0.140^\circ$ at SDD = 2922 mm; (c) out-of-plane scattering profile extracted from the data in (a) and (b) along the α_f direction at $2\theta_f = 0.160^\circ$ where the black circular symbols are the measured data, and the red solid lines were obtained by fitting the data using the GIXS formula; (d) in-plane scattering profile extracted from the data in (a) and (b) along the $2\theta_f$ direction at $\alpha_f = 0.190^\circ$; (e) 2D scattering image reconstructed from the structural parameters in Table 5.2 using the GIXS formula derived for lamellar structure model.

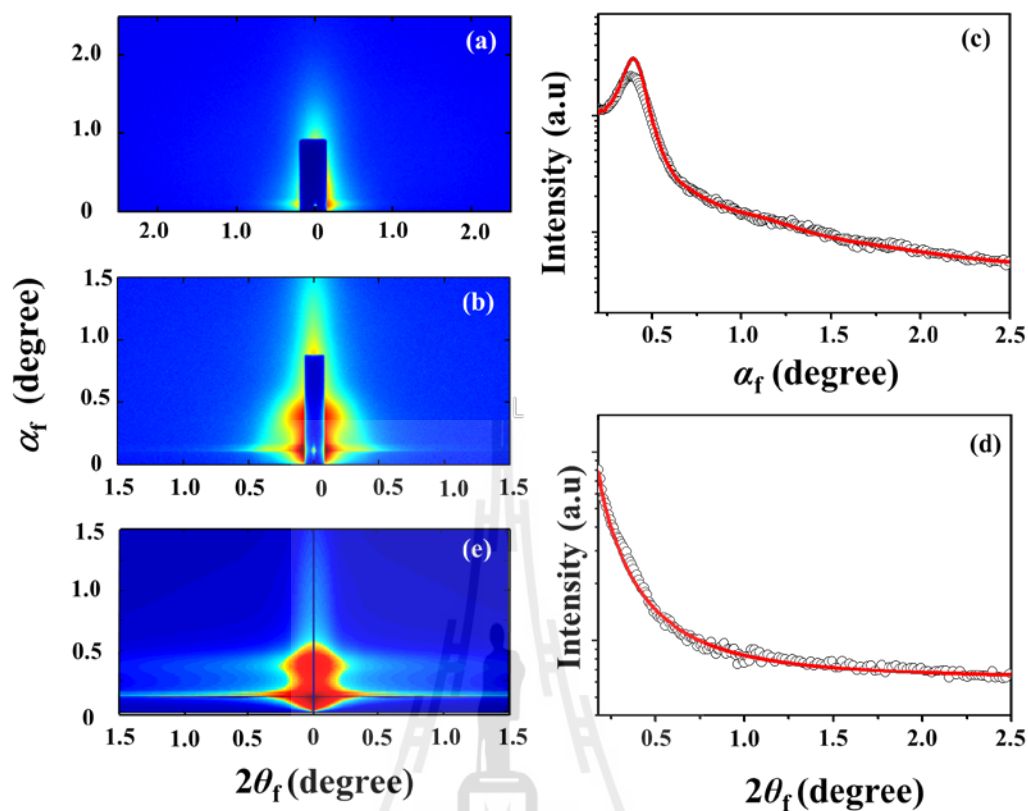


Figure 5.6 2D GISAXS pattern of toluene-annealed PHIC(5.2k)-PCL₃(17.4k) film (120 nm thick) deposited on silicon substrates, measured at room temperature using an X-ray wavelength $\lambda = 0.1180$ nm; (a) measured with $\alpha_i = 0.110^\circ$ at SDD = 902 mm; (b) 2D scattering pattern measured with $\alpha_i = 0.140^\circ$ at SDD = 2922 mm; (c) out-of-plane scattering profile extracted from the data in (a) and (b) along the α_f direction at $2\theta_f = 0.160^\circ$ where the black circular symbols are the measured data, and the red solid lines were obtained by fitting the data using the GIXS formula; (d) in-plane scattering profile extracted from the data in (a) and (b) along the $2\theta_f$ direction at $\alpha_f = 0.190^\circ$; (e) 2D scattering image reconstructed from the structural parameters in Table 5.2 using the GIXS formula derived for lamellar structure model.

Table 5.2 Nanostructural parameters of the toluene-annealed thin films of the PHIC(5.4k) and PCL(15k) homopolymers and PHIC(5k)-PCL₁₋₃(17k) miktoarm star polymers, determined by GISAXS analysis.

Polymer thin film	Nanostructure (observed)	L^a (nm)	ℓ_1^b (nm)	ℓ_2^c (nm)	ℓ_3^d (nm)	σ_1^e (nm)	σ_2^f (nm)	g^g	$\bar{\varphi}_1^h$ (deg.)	$\sigma_{\varphi_1}^i$ (deg.)	O_s^j
PHIC	not identified										
PCL	horizontal lamellae	12.6	3.3	1.6	6.1	0.6	0.4	0.35	0	6.3	0.982
	vertical ^l lamellae	10.6	2.5	1.3	5.5	0.8	0.5	0.40	90		
PHIC-PCL	horizontal lamellae	16.4	8.3	2.0	4.1	1.3	0.7	0.31	0	14.0	0.916
	vertical ^l lamellae	21.8	8.9	3.2	6.5	2.1	1.8	0.38	90		
PHIC-PCL ₂	horizontal lamellae	16.2	8.0	2.1	4.0	1.6	0.7	0.265	0	13.1	0.926
PHIC-PCL ₃	horizontal lamellae	16.0	7.7	2.2	3.9	1.8	0.9	0.27	0	13.4	0.923

^a Long period of lamellar structure.

^b Thickness of more dense (i.e., crystalline) layer ($=\ell_c$) in the lamellar structure formed in PCL homopolymer films; thickness of more dense layer (i.e., PCL arm phase: ℓ_{PCL}) in the lamellar structured PHIC-PCL_m films.

^c Thickness of interfacial layer (ℓ_i) between the highly dense and less dense layers in lamellar structure.

^d Thickness of less dense (i.e., amorphous) layer ($=\ell_a$) in the lamellar structure formed in PCL homopolymer films; thickness of less dense layer (i.e., PHIC arm phase: ℓ_{PHIC}) in the lamellar structured PHIC-PCL_m films.

^e Standard deviation for the more dense layer in lamellar structure.

^f Standard deviation for the interfacial layer in lamellar structure.

^g Paracrystal distortion factor along the direction parallel to the long period of lamellar structure.

^h Mean value of the polar angle φ_1 (i.e., orientation angle) between the orientation vector \mathbf{n}_1 (which is set along the direction parallel to the long period of lamellar structure) and the out-of-plane of the film.

ⁱ Standard deviation for the orientation angle φ_1 of lamellar structure.

^j Second order orientation factor.

^l Vertical lamellar structure was formed in a very minor fraction.

PHIC and PCL arms regardless of the PCL arms number present. Interestingly, the rod-coil PHIC(5k)-PCL₁₋₃(17k) miktoarm star polymers with $f_{\text{PHIC}} \sim 23\%$ presented difference structure from the conventional coil-coil diblock copolymers, which is usually formed hexagonal cylinder packing, in the same volume fraction (Bates, and Fredrickson, 1990).

The other set of studied polymer films, the PHIC(10k)-PCL₁₋₃(10k) miktoarm star polymers films, as well as, PHIC(10.4k) and PCL(10.5k) homopolymer films, annealed by toluene and CHCl₃, were also characterized using GIXS technique. Another interesting result was found that the structure of the PHIC(10k)-PCL₁₋₃(10k) formed lamellar conformation with difference in orientation depends on the toluene and/or CHCl₃ annealing as well as the PCL arms number.

The GISAXS measurement of toluene-annealed PHIC(10k)-PCL₁₋₃(10k) miktoarm star polymers thin films presented feature in the out-of-plane direction, suggesting that there were nanoscale structures well-developed in the normal direction to the films surface in these polymer films. The 2D patterns and scattering profiles along in-plane and out-of-plane directions of the toluene annealed PHIC(10.3k)-PCL(10.6k) film were presented in Figures 5.7a-5.7d. The scattering peaks along the out-of-plane profile of the PHIC-PCL were observed at $\alpha_f = 0.316^\circ$ and 1.232° , corresponding to the d-spacing of 21.2 nm. These peaks implied that a horizontally oriented lamellar structure was formed in the PHIC-PCL. Therefore, the GIXS formula for the lamellar structural model was applied on the out-of-plane profile (Figure 5.7c). The structural parameters from the GIXS formula are summarized in Table 5.3. The PHIC-PCL horizontal lamellar structure was characterized by $L = 19.2$ nm, $l_1 = l_{\text{PCL}} = 6.2$ nm (highly dense layer thickness: PCL phase thickness), $l_3 = l_{\text{PHIC}} =$

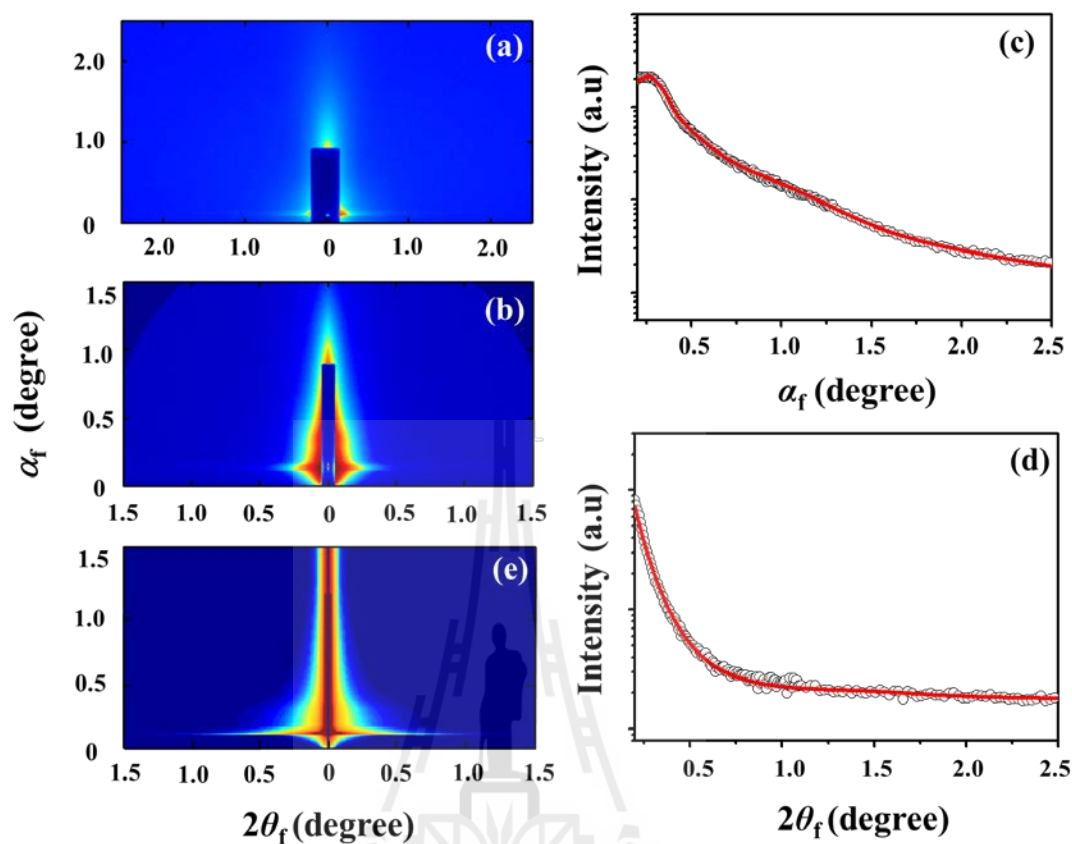


Figure 5.7 2D GISAXS pattern of toluene-annealed PHIC(10.3k)-PCL(10.6k) film (80 nm thick) deposited on silicon substrates measured at RT using an X-ray beam ($\lambda = 0.1170$ nm); (a) measured with $\alpha_i = 0.110^\circ$ at a sample-to-detector distance (SDD) of 902 mm; (b) measured with $\alpha_i = 0.130^\circ$ at SDD = 2,935 mm; (c) out-of-plane scattering profile extracted from the data in (a) and (b) along the α_f direction at $2\theta_f = 0.100^\circ$ where the black circular symbols are the measured data, and the red solid lines were obtained by fitting the data using the GIXS formula; (d) in-plane scattering profile extracted from the data in (a) and (b) along the $2\theta_f$ direction at $\alpha_f = 0.160^\circ$; (e) 2D scattering image reconstructed from the structural parameters in Table 5.3 using the GIXS formula derived for lamellar structure model.

8.6 nm (less dense layer thickness: PHIC phase thickness), $l_2 = l_i = 2.2$ nm (interfacial layer thickness), $O_{s,1} = 0.953$ ($\bar{\phi}_4 = 0^\circ$ and $\sigma_{\phi_4} = 10.3^\circ$), and $g = 0.32$. The 2D reconstructed pattern was also created by using the structure parameters from the GIXS formula and agreed well with the experimental data as shown in Figure 5.7e. The in-plane profile of the PHIC-PCL was fitted with the GIXS formula as shown in Figure 5.7d.

The 2D GISAXS patterns from the toluene-annealed PHIC-PCL₂₋₃ films were also presented features that indicating to the horizontally oriented lamellar structure was formed in the films, as shown in Figures 5.8a and 5.8b for the PHIC(10.9k)-PCL₂(11.1k) and Figures 5.9a and 5.9b for the PHIC(9.6k)-PCL₃(11k). The scattering peaks along the out-of-plane profiles were observed at $\alpha_f = 0.291^\circ$ and 0.566° ($d_s = 23.8$ nm) for the PHIC-PCL₂ and $\alpha_f = 0.347^\circ$ and 1.264° ($d_s = 19.3$ nm) for the PHIC-PCL₃, respectively. The out-of-plane profiles of the PHIC-PCL₂ and the PHIC-PCL₃ could be satisfactory fitted with GIXS formula for the lamellar model and their structural parameters were reported in Table 5.3. Moreover, the out-of-plane profile of the PHIC-PCL₂ revealed clear peaks at $\alpha_f = 1.360^\circ$ ($d_s = 5.1$ nm), $\alpha_f = 1.638^\circ$ ($d_s = 4.2$ nm), and $\alpha_f = 1.857^\circ$ ($d_s = 3.7$ nm) (Figure 5.8c). These scattering peaks were related to the mean distance of PCL crystal layer of 3.7-5.1 nm due to crystallizable of PCL phase. The in-plane profiles of the PHIC-PCL_{2,3} were also fitted with GIXS formula for the lamellar model, as presented in Figures 5.8d and 5.9d, respectively. Also, the unmatched GIXS fitting around $2\theta_f = 0.370^\circ$ - 1.270° for the PHIC-PCL₃ happened due to the very small amount and poorly ordered vertical structure generated in the film (Figure 5.9d).

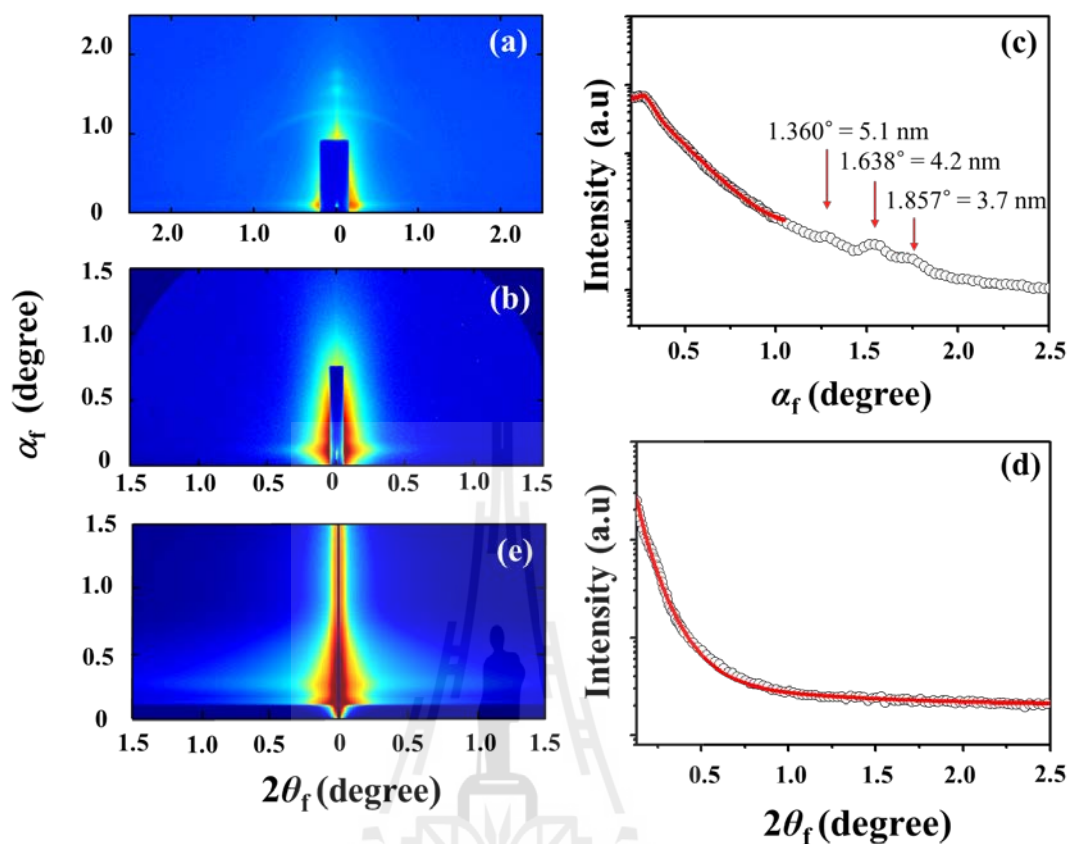


Figure 5.8 2D GISAXS pattern of toluene-annealed PHIC(10.9k)-PCL₂(11.1k) film (80 nm thick) deposited on silicon substrates measured at RT using an X-ray beam ($\lambda = 0.1210 \text{ nm}$); (a) measured with $\alpha_i = 0.110^\circ$ at SDD = 902 mm; (b) measured with $\alpha_i = 0.130^\circ$ at SDD = 2,935 mm; (c) out-of-plane scattering profile extracted from the data in (a) and (b) along the α_f direction at $2\theta_f = 0.100^\circ$ where the black circular symbols are the measured data, and the red solid lines were obtained by fitting the data using the GIXS formula; (d) in-plane scattering profile extracted from the data in (a) and (b) along the $2\theta_f$ direction at $\alpha_f = 0.160^\circ$; (e) 2D scattering image reconstructed from the structural parameters in Table 5.3 using the GIXS formula derived for lamellar structure model.

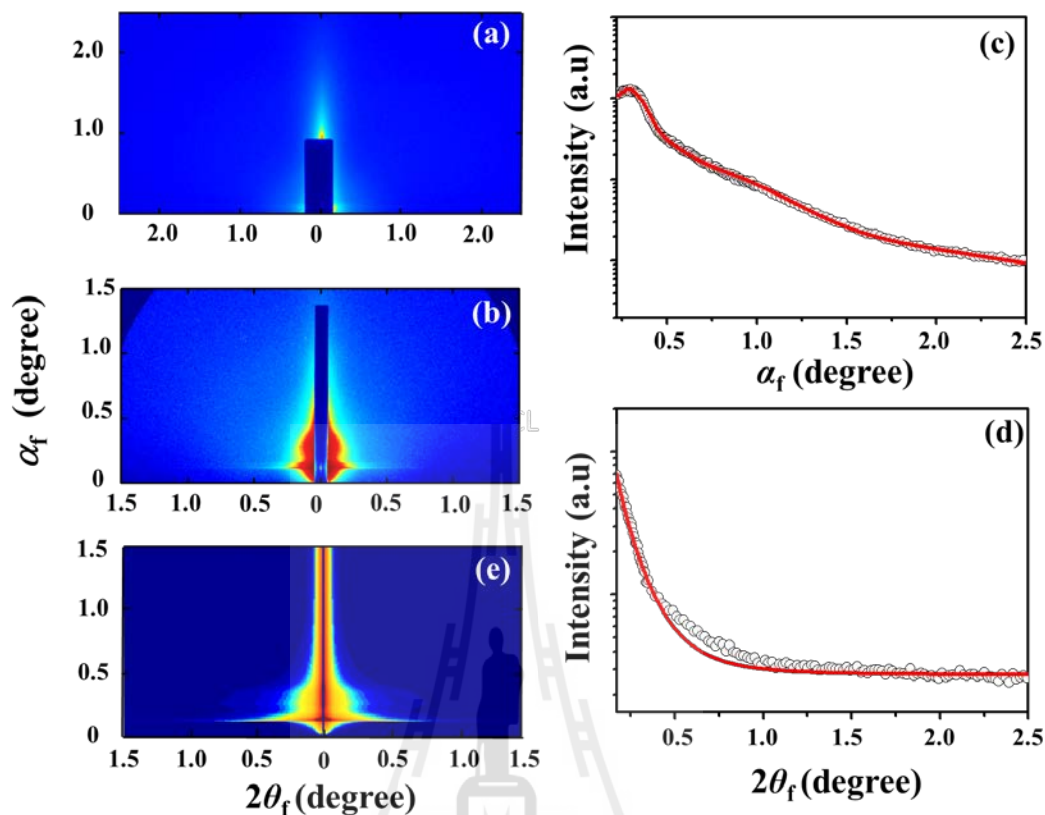


Figure 5.9 2D GISAXS pattern of toluene-annealed PHIC(9.6k)-PCL₃(11.0k) film (80 nm thick) deposited on silicon substrates measured at RT using an X-ray beam ($\lambda = 0.1170$ nm); (a) measured with $\alpha_i = 0.110^\circ$ at SDD = 902 mm; (b) 2D scattering pattern measured with $\alpha_i = 0.130^\circ$ at SDD = 2,935 mm; (c) out-of-plane scattering profile extracted from the data in (a) and (b) along the α_f direction at $2\theta_f = 0.100^\circ$ where the black circular symbols are the measured data, and the red solid lines were obtained by fitting the data using the GIXS formula; (d) in-plane scattering profile extracted from the data in (a) and (b) along the $2\theta_f$ direction at $\alpha_f = 0.160^\circ$; (e) 2D scattering image reconstructed from the structural parameters in Table 5.3 using the GIXS formula derived for lamellar structure model.

From the preceding GISAXS results, the PHIC(10k)-PCL₁₋₃(10k) molecules in the thin films underwent separate phase (PHIC and PCL domains) during the toluene annealing, thereby forming horizontally oriented lamellar structures regardless of the number of PCL arms present.

2D GISAXS patterns of the PHIC(10k)-PCL₁₋₃(10k) films in CHCl₃ annealing also showed features. In addition, the CHCl₃-annealed PHIC(10.3k)-PCL(10.6k) film showed different pattern from the CHCl₃-annealed PHIC(10.3k)-PCL₂(10.3k) and CHCl₃-annealed PHIC(10.3k)-PCL₃(10.3k) films, thus the morphology and structural ordering of this PHIC-PCL film would be different from the PHIC-PCL_{2,3} films.

The 2D patterns (Figures 5.10a and 5.10b) and scattering profiles (Figures 5.10c and 5.10d) of the PHIC-PCL were observed some feature that indicating to the horizontally oriented lamellar structure was form. The out-of-plane scattering peaks were obtained at $\alpha_f = 0.266^\circ$ and 0.525° , agreeing with $d_s = 26.1$ nm. The scattering profiles were satisfactory fitted with GIXS model for the three layer lamellar model (Figures 5.10c and 5.10d) and the structural parameters were extracted and reported in Table 5.3. The horizontal lamellar structure of the PHIC-PCL presented long period $L = 22.6$ nm with PCL phase thickness (highly dense layer) $l_1 = l_{\text{PCL}} = 6.8$ nm, interfacial layer thickness $l_2 = l_i = 2.2$ nm, and PHIC phase thickness (less dense layer) $l_3 = l_{\text{PHIC}} = 11.4$ nm, also positional distortion factor $g = 0.32$. The orientation angle was $\overline{\varphi}_1 = 0^\circ$ with $\sigma_{\varphi_1} = 9.0^\circ$ and $O_{s,1} = 0.964$. Moreover, the 2D simulated pattern of the PHIC-PCL was created and matched well with the experimental data (Figure 5.10e.)

It is very unlikely that the 2D GISAXS patterns of the PHIC-PCL_{2,3} presented clearly feature along $2\theta_f$ direction as presented in Figures 5.11a-5.11b and 5.12a-

5.12b, respectively. Moreover, the in-plane profiles showed scattering peaks at $2\theta_f = 0.222^\circ$ and 0.553° ($d_s = 30.3$ nm) for the PHIC-PCL₂ and $2\theta_f = 0.274^\circ$ and 0.660° ($d_s = 24.7$ nm) for the PHIC-PCL₃ suggested that a vertically oriented lamellar structure governed in these films. The in-plane profiles were fitted with GIXS formula for the lamellar model as shown in Figures 5.11d and 5.12d, respectively. The structural parameters were obtained and summarized in Table 5.3. The GIXS results explained that the long period (L) of the PHIC-PCL₂ was 29.1 nm, PCL thickness (highly dense layer) $l_1 = l_{\text{PCL}} = 11.4$ nm, interfacial layer thickness $l_2 = l_i = 2.3$ nm, and PHIC phase thickness (less dense layer) $l_3 = l_{\text{PHIC}} = 13.1$ nm with positional distortion factor $g = 0.19$. The PHIC-PCL₃ lamellar structure were presented long period $L = 24.0$ nm with PCL phase thickness (highly dense layer) $l_1 = l_{\text{PCL}} = 8.6$ nm, interfacial layer thickness $l_2 = l_i = 2.4$ nm, PHIC phase thickness (less dense layer) $l_3 = l_{\text{PHIC}} = 10.6$ nm, and positional distortion factor $g = 0.20$. The orientation parameters were found as $\bar{\varphi}_1 = 90^\circ$, $\sigma_{\varphi_1} = 12.7$, and $O_{s,1} = -0.430$ for the PHIC-PCL₂, and $\bar{\varphi}_1 = 90^\circ$, $\sigma_{\varphi_1} = 10.8$, and $O_{s,1} = -0.448$ for the PHIC-PCL₃, respectively.

The out-of-plane profiles showed small broad peaks at about $\alpha_f = 1.016^\circ$ ($d_s = 6.6$ nm) for the PHIC-PCL₂ (Figure 5.11c) and $\alpha_f = 1.223^\circ$ ($d_s = 5.5$ nm) and $\alpha_f = 2.062^\circ$ ($d_s = 3.3$ nm) for the PHIC-PCL₃ (Figure 5.12c). These peaks related to the mean PCL intercrystal due to crystallizable of PCL arms, about 6.6 nm for the PHIC-PCL₂ and 5.5 nm for the PHIC-PCL₃. The simulation of the PHIC-PCL_{2,3} were constructed using their own GIXS structural parameters as shown in Figures 5.11e and 5.12e. The simulated patterns also agreed well with the experimental data.

From the preceding GISAXS analysis of the PHIC-PCL₁₋₃ films underwent separate phase (PHIC and PCL phases) during the CHCl₃ annealing, revealing that

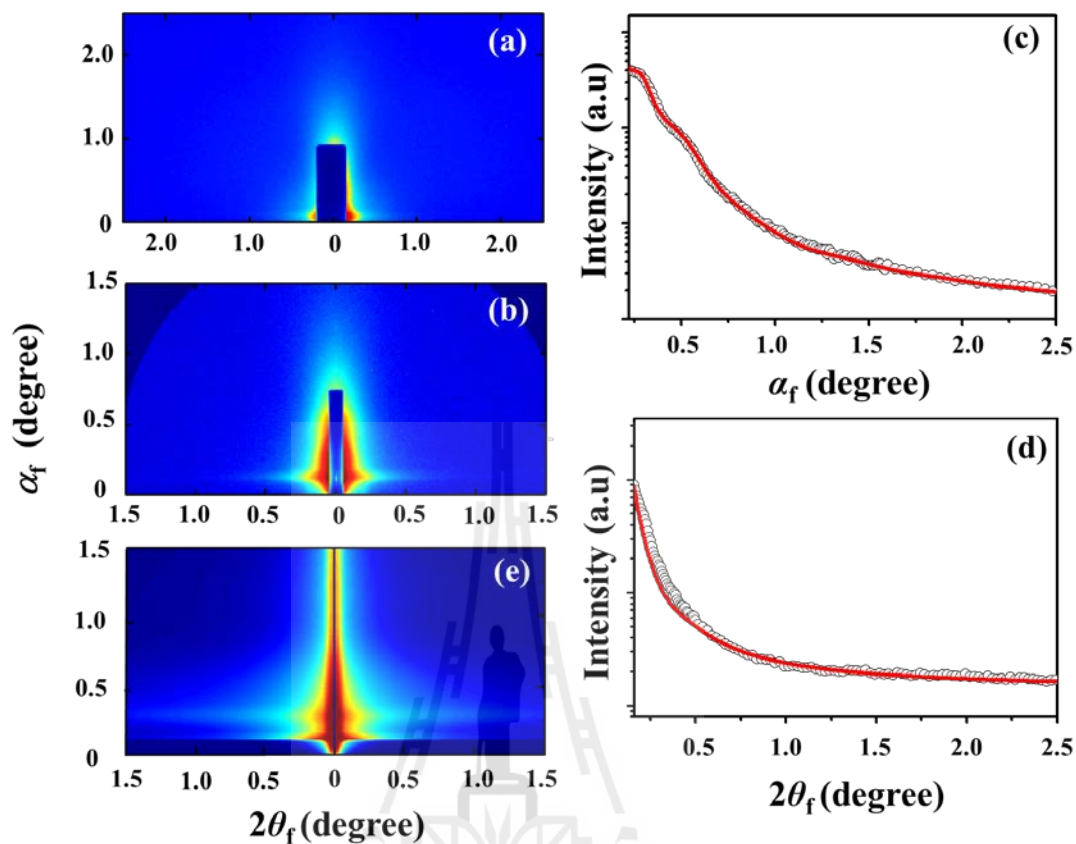


Figure 5.10 2D GISAXS pattern of CHCl_3 -annealed PHIC(10.3k)-PCL(10.6k) film (80 nm thick) measured at RT using an X-ray beam ($\lambda = 0.1210$ nm); (a) measured with $\alpha_i = 0.110^\circ$ at a sample-to-detector distance (SDD) of 902 mm; (b) measured with $\alpha_i = 0.120^\circ$ at SDD = 2,935 mm; (c) out-of-plane scattering profile extracted from the data in (a) and (b) along the α_f direction at $2\theta_f = 0.080^\circ$ where the black circular symbols are the measured data, and the red solid lines were obtained by fitting the data using the GIXS formula; (d) in-plane scattering profile extracted from the data in (a) and (b) along the $2\theta_f$ direction at $\alpha_f = 0.140^\circ$; (e) 2D scattering image reconstructed from the structural parameters in Table 5.3 using the GIXS formula derived for lamellar structure model.

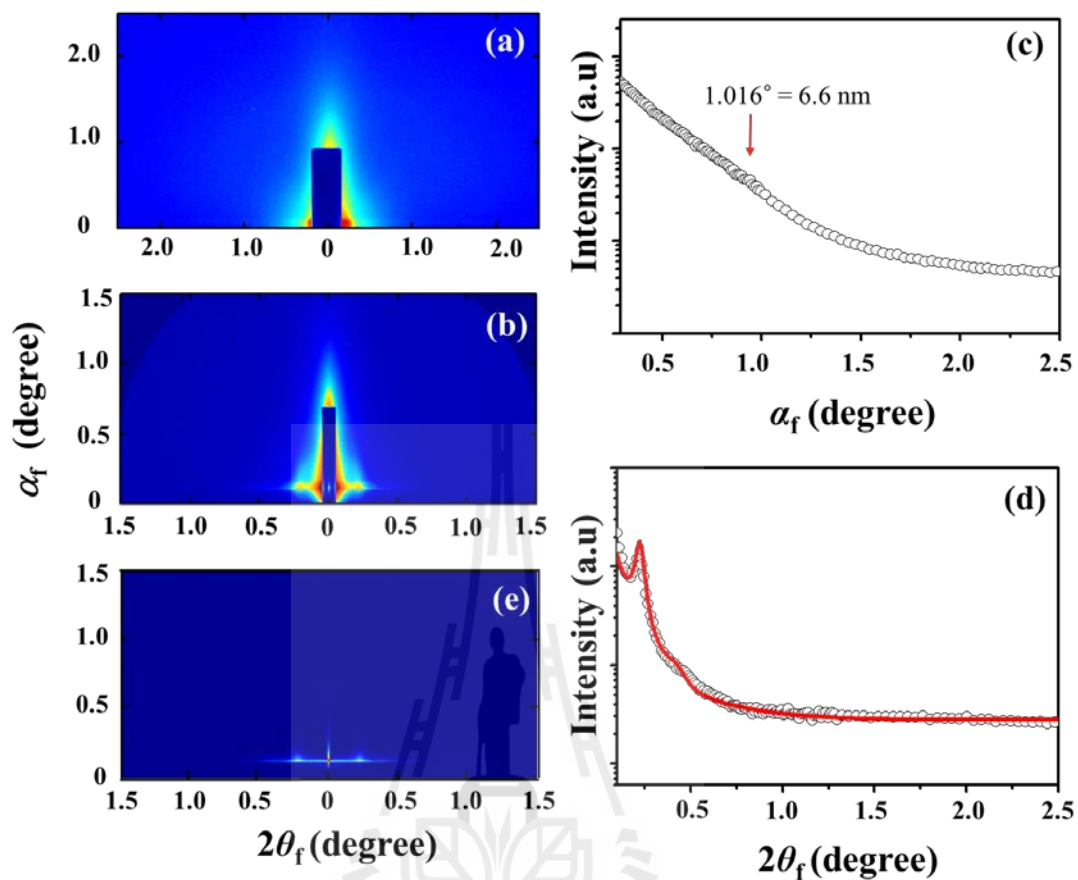


Figure 5.11 2D GISAXS pattern of CHCl_3 -annealed PHIC(10.9k)-PCL₂(11.1k) film (80 nm thick) measured at RT using an X-ray beam ($\lambda = 0.1170$ nm); (a) measured with $\alpha_i = 0.110^\circ$ at SDD = 902 mm; (b) measured with $\alpha_i = 0.140^\circ$ at SDD = 2,935 mm; (c) out-of-plane profile extracted from the data in (a) and (b) along the α_f direction at $2\theta_f = 0.060^\circ$ where the black circular symbols are the measured data, and the red solid lines were obtained by fitting the data using the GIXS formula; (d) in-plane profile extracted from the data in (a) and (b) along the $2\theta_f$ direction at $\alpha_f = 0.140^\circ$; (e) 2D scattering image reconstructed from the structural parameters in Table 5.3 using the GIXS formula derived for lamellar structure model.

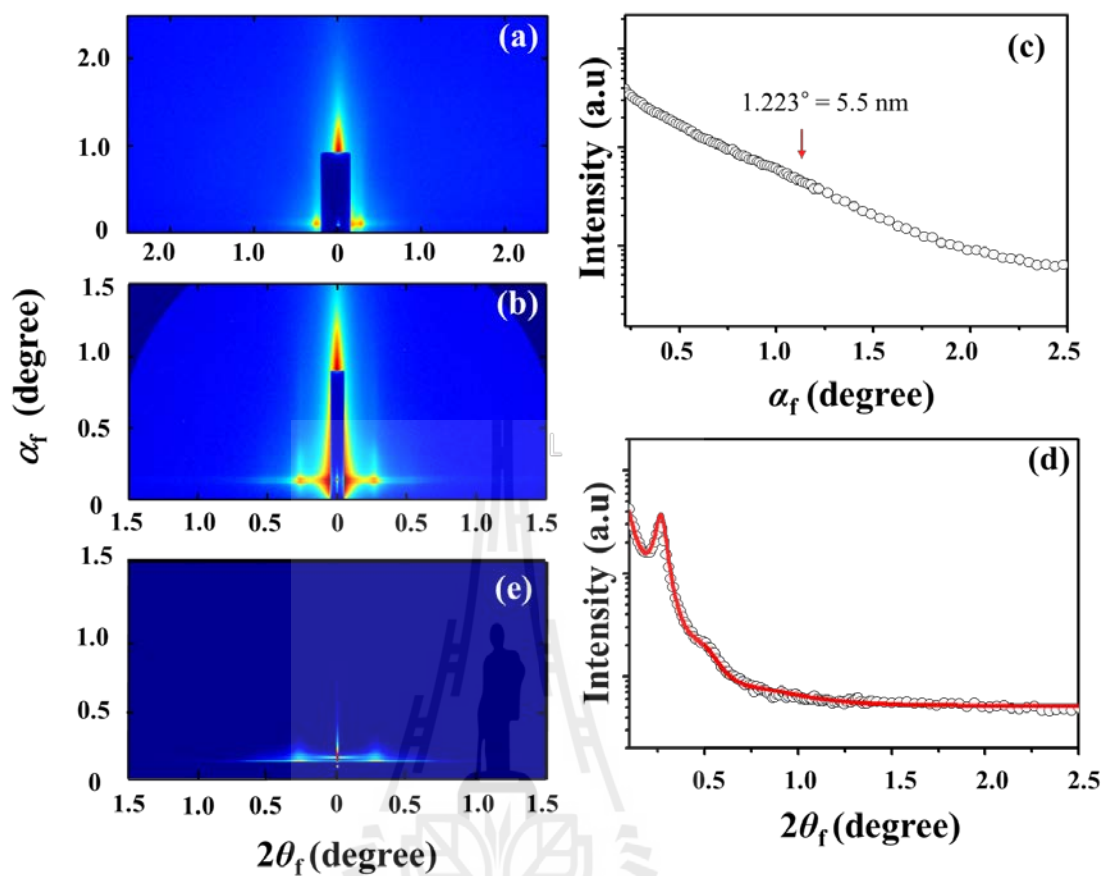


Figure 5.12 2D GISAXS pattern of CHCl₃-annealed PHIC(9.6k)-PCL₃(11k) film (80 nm thick) measured at RT using an X-ray beam ($\lambda = 0.1170$ nm); (a) measured with $\alpha_i = 0.110^\circ$ at SDD = 902 mm; (b) 2D scattering pattern measured with $\alpha_i = 0.140^\circ$ at SDD = 2,935 mm; (c) out-of-plane profile extracted from the data in (a) and (b) along the α_f direction at $2\theta_f = 0.060^\circ$ where the black circular symbols are the measured data, and the red solid lines were obtained by fitting the data using the GIXS formula; (d) in-plane profile extracted from the data in (a) and (b) along the $2\theta_f$ direction at $\alpha_f = 0.140^\circ$; (e) 2D scattering image reconstructed from the structural parameters in Table 5.3 using the GIXS formula derived for lamellar structure model.

Table 5.3 Nanostructural parameters under the toluene and CHCl₃ annealing in thin films of the PHIC(10.4k) and PCL(10.5k) homopolymers and PHIC(10k)-PCL₁₋₃(10k) miktoarm star polymers, determined by GISAXS analysis.

Polymer thin film	Nanostructure (observed)	L^a (nm)	ℓ_1^b (nm)	ℓ_2^c (nm)	ℓ_3^d (nm)	σ_1^e (nm)	σ_2^f (nm)	g^g	$\bar{\varphi}_1^h$ (deg.)	$\sigma_{\varphi_1}^i$ (deg.)	O_s^j	ℓ^k (nm)
Toluene-annealed films												
PHIC	not identified											
PCL	horizontal lamellae	12.4	3.6	1.5	5.8	0.5	0.5	0.36	0	6.3	0.982	
PHIC-PCL	horizontal lamellae	19.2	6.2	2.2	8.6	1.7	0.7	0.32	0	10.3	0.953	
PHIC-PCL ₂	horizontal lamellae	22.9	7.1	2.3	11.2	2.3	0.7	0.34	0	8.2	0.970	3.7-5.1
PHIC-PCL ₃	horizontal lamellae	18.5	5.6	2.4	8.1	1.5	0.8	0.31	0	13.7	0.919	
CHCl₃-annealed films												
PHIC	not identified											
PCL	horizontal lamellae	12.5	3.6	1.4	6.1	0.5	0.6	0.36	0	5.8	0.985	
PHIC-PCL	horizontal lamellae	22.6	6.8	2.2	11.4	2.7	0.8	0.32	0	9.0	0.964	
PHIC-PCL ₂	horizontal lamellae	29.1	11.4	2.3	13.1	3.5	1.1	0.19	90	12.7	-0.430	6.6
PHIC-PCL ₃	horizontal lamellae	24.0	8.6	2.4	10.6	2.4	0.6	0.20	90	10.8	-0.448	5.5

^a Long period of lamellar structure.

^b Thickness of more dense (i.e., crystalline) layer ($=\ell_c$) in the lamellar structure formed in PCL homopolymer films; thickness of more dense layer (i.e., PCL arm phase: ℓ_{PCL}) in the lamellar structured PHIC-PCL_m films.

^c Thickness of interfacial layer (ℓ_1) between the highly dense and less dense layers in lamellar structure.

^d Thickness of less dense (i.e., amorphous) layer ($=\ell_a$) in the lamellar structure formed in PCL homopolymer films; thickness of less dense layer (i.e., PHIC arm phase: ℓ_{PHIC}) in the lamellar structured PHIC-PCL_m films.

^e Standard deviation for the more dense layer in lamellar structure.

^f Standard deviation for the interfacial layer in lamellar structure.

^g Paracrystal distortion factor along the direction parallel to the long period of lamellar structure.

- ^h Mean value of the polar angle φ_1 (i.e., orientation angle) between the orientation vector \mathbf{n}_1 (which is set along the direction parallel to the long period of lamellar structure) and the out-of-plane of the film .
- ⁱ Standard deviation for the orientation angle φ_1 of lamellar structure.
- ^j Second order orientation factor.
- ^k Mean interdistance of the crystals formed in the PCL arm phase layers along the out-of-plane of the film.

the PHIC-PCL formed horizontally oriented lamellar structure but the PHIC-PCL_{2,3} formed vertical lamellar structures.

Overall, the PHIC(10k)-PCL₁₋₃(10k) molecules in the thin films can formed either horizontally oriented lamellar structure or vertically oriented lamellar structure depending on toluene and CHCl₃ annealing, as well as the number of PCL arms present.

Furthermore, the crystal morphology and orientation of the series of miktoarm star polymers films, PHIC(5k, 10k)-PCL₁₋₃(17k, 10k), and the homopolymer films, PHIC(5.4k, 10.4k) and the PCL(15k, 10.5k), under toluene and CHCl₃ annealing, were investigated with GIWAXS technique. The structural information obtained from the PHIC and PCL films has been considered as a reference to compare with those from the PHIC-PCL₁₋₃ films.

2D GIWAXS pattern of the toluene-annealed PHIC(5.4k) and toluene-annealed PHIC(10.4k) showed peak features (Figures 5.13a and 5.14a), indicating that the PHIC can form crystal structure. The scattering profiles in the both directions of the PHIC(5.4k) and PHIC(10.4k) presented similarly. The profiles revealed periodic arc peaks at $\alpha_f = 2\theta_f = 3.85^\circ$, 7.69° , and 11.52° along α_f and $2\theta_f$ direction, corresponding to $d_s = 1.67$ nm for the PHIC(5.4k), as shown in Figures 5.13f and 5.13g and at $\alpha_f = 2\theta_f = 3.87^\circ$, 7.70° , and 11.56° along α_f and $2\theta_f$ direction with d_s value was 1.66 nm for

the PHIC(10.4k) (Figures 5.14f and 5.14g). The other arc peaks also appeared at $\alpha_f = 2\theta_f = 9.56^\circ$, corresponding to $d_s = 0.67$ nm, $\alpha_f = 2\theta_f = 12.93^\circ$, corresponding to $d_s = 0.50$ nm, and $\alpha_f = 2\theta_f = 14.40^\circ$, corresponding to $d_s = 0.45$ nm for the PHIC(5.4k) and at $\alpha_f = 2\theta_f = 9.53^\circ$ ($d_s = 0.67$ nm), $\alpha_f = 2\theta_f = 12.99^\circ$ ($d_s = 0.50$ nm), and $\alpha_f = 2\theta_f = 14.43^\circ$ ($d_s = 0.45$ nm) for the PHIC(10.4k).

These scattering peaks from the PHIC(5.4k) and PHIC(10.4k) suggested that the crystal conformation of the PHIC was a well ordered multibilayer structure. The PHIC crystal structure was characterized with the GIXS formula base on multibilayer structure model (the model are described in the Chapter IV) (Yoon *et al.*, 2007; Yoon *et al.*, 2008; Ahn *et al.*, 2010; Ahn *et al.*, 2013). The profiles of all the PHIC could be successfully fitted as shown in Figures 5.13f-5.13g and 5.14f-5.14g. The obtained structural parameters from the PHIC(5.4k) and the PHIC(10.4k) are quite similar and listed in Tables 5.4 and 5.5, respectively.

The details of PHIC multibilayer structure can be given as follows. The lamellar bilayer had long period d_L . The lamellar bilayer also composed of dense sublayer, which was polymer backbones and inner parts of n-hexyl side groups with thickness ℓ_1 , and less dense layer, which was the remaining part of n-hexyl side groups with thickness ℓ_2 . The n-hexyl bristles were fully extended and packed laterally with no interdigitation, since the length of the fully extended n-hexyl bristle was 0.83 nm. The mean inter-distance of n-hexyl bristles, whose polymer chains and neighboring polymer chains were matched in position along their backbones, was found to be d_1 . The value of the mean inter-distance of n-hexyl side groups along the backbone was d_2 and the mean inter-distance of nearest neighboring n-hexyl side groups was d_3 .

Here, the positional distortion factor along the out-of-plane direction is g_{dL} and along the lateral direction is g_{d1} , g_{d2} , and g_{d3} .

The orientation of the PHIC(5.4k) and the PHIC(10.4k) multibilayer conformation was observed to be horizontal and vertical directions. The orientation parameters of the horizontal structure were obtained at $\bar{\varphi}_2 = 0^\circ$ ($\bar{\varphi}_2$ is the mean polar angle between the orientation vector \mathbf{n}_2 of the horizontal multibilayer structure and the out-of-plane direction of the film) and a standard deviation σ_{φ_2} with a second order orientation factor $O_{s,2,0}$. While the vertical multibilayer structure presented $\bar{\varphi}_2 = 90^\circ$, with σ_{φ_2} and $O_{s,2,90}$, respectively. The relative volume fraction of the PHIC horizontal and vertical structures are given by $\phi_{h,2}/\phi_{v,2}$. According to the volume fraction of the PHIC(5.4k) ($\phi_{h,2}/\phi_{v,2} = 80/20$) and the PHIC(10.4k) ($\phi_{h,2}/\phi_{v,2} = 77/22$), their crystal conformation majority were horizontal multibilayer structure. Additionally, the GIWAXS analysis results of the PHIC(5.4k) and the PHIC(10.4k), under toluene annealing, agreed well with those of toluene-annealed PHIC(10k) from the previous research (Kim *et al.*, 2014).

On the other hand, the profiles of CHCl_3 -annealed PHIC(10.4k) showed the periodic arc peaks appeared only in the out-of-plane direction, hence the PHIC formed only a horizontal structure. Figures 5.15f and 5.15g presented the scattering profiles of the CHCl_3 -annealed PHIC(10.4k), which were observed clearly at $\alpha_f = 4.10^\circ$, 8.18° , and 12.16° with d_s value equal to 1.65 nm. The other scattering peaks along $2\theta_f$ direction were also observed at $2\theta_f = 4.10^\circ$ ($d_s = 1.65$ nm), $\alpha_f = 2\theta_f = 10.04^\circ$ ($d_s = 0.67$ nm), $2\theta_f = 13.52^\circ$ ($d_s = 0.50$ nm), and $2\theta_f = 15.14^\circ$ ($d_s = 0.45$ nm). The GIXS formula for the multibilayer structure model was applied on the scattering

profiles as shown in Figures 5.15f and 5.15g. The structural parameters are reported in Table 5.6. The GIXS analysis reviewed that the long period of the lamellar bilayer PHIC(10.4k) was 1.65 nm, which dense ($=\ell_1$) and less dense ($=\ell_2$) layer (backbones and inner parts of n -hexyl bristles and remaining part of n -hexyl bristles) thickness were 0.76 nm and 0.89 nm, respectively. The polymer backbones were packed laterally. The n -hexyl bristles were fully extended, packed laterally, and no interdigitation. The mean inter-distance of n -hexyl bristles was about 0.67 nm ($=d_1$); when the bristles and neighboring bristles positions were matched along their backbones. Additionally, the mean inter-distance of n -hexyl bristles along the backbone ($=d_2$) and nearest neighboring n -hexyl bristles ($=d_3$) were 0.50 nm and 0.45 nm, respectively. The positional distribution of the lamellar bilayer was very small ($g_{dL} = 0.048$) but high for the n -hexyl bristles position ($g_{d1} = 0.100$, $g_{d2} = 0.100$, and $g_{d3} = 0.110$). The orientation parameters of PHIC lamellar bilayer were explained as $\bar{\varphi}_2 = 0^\circ$ with $\sigma_{\varphi_2} = 3.70^\circ$ and $O_{s,2,0} = 0.994$. The relative volume fraction of horizontal and vertical structure ($\phi_{h,2}/\phi_{v,2}$) were found at 100/0, confirming the PHIC structure formed only horizontal multibilayer conformation.

From the GIWAXS characterization of the PCL(15k) and the (10.5k) films, the results demonstrated that all the PCL films formed an orthorhombic system with the space group $P2_12_12_1$ (Brittger, Marchessault, and Niegsch, 1970). The 2D GIWAXS patterns and the scattering profiles of all the PCL films presented the same features and showed the similar characteristic profiles. For the toluene-annealed PCL(15k), the pattern and profiles were shown in Figures 5.13b and 5.13f-5.13g, respectively. The scattering peaks of the PCL were observed at $\alpha_f = 7.32^\circ$ with $d_s = 0.88$ nm, corresponding to the reflection plane $\{002\}$. The other peaks also appeared at $\alpha_f =$

14.67°, with $d_s = 0.44$ nm, corresponding to reflection plane {004} and {110} reflections, and $\alpha_f = 16.17^\circ$ with $d_s = 0.40$ nm, which could be assigned to the {200} reflections. In the in-plane profile, the PCL peaks appeared at $2\theta_f = 14.67^\circ$ with $d_s = 0.44$ nm, corresponding to reflection plane {110}. Another peak occurred at $2\theta_f = 16.17^\circ$ with $d_s = 0.40$ nm, and could be assigned to the {200} reflections. Moreover, the other two peaks could be indexed as the {101} and {102} reflections. These scattering peaks are contributed to the orthorhombic structure was formed in the PCL. By using GIXS formula for an orthorhombic lattice model (the model details were described in the Chapter IV), the scattering profiles of the PCL could be successfully fitted, as shown in Figures 5.13f and 5.13g. The structural parameters are listed in Table 5.4. The GIXS results review that the cell edge length of the orthorhombic as $a = 0.80$ nm, $b = 0.53$ nm, and $c = 1.76$ nm, with a small position distribution value of $g = 0.060$.

Moreover, the PCL crystal orientations were found to be in the parallel ($\bar{\varphi}_3 = 0^\circ$) and perpendicular ($\bar{\varphi}_3 = 90^\circ$) directions to the surface plane. Here, $\bar{\varphi}_3$ denotes the mean polar angle between the orientation vector \mathbf{n}_3 of the orthorhombic lattice and the out-of-plane direction of the film. At $\bar{\varphi}_3 = 0^\circ$ showed distribution value as σ_{φ_3} and second order orientation factor $O_{s,3,0}$ values were 10.6° and 0.950, respectively. At $\bar{\varphi}_3 = 90^\circ$ of the values were $\sigma_{\varphi_3} = 14.3$ and $O_{s,3,90} = -0.412$. The volume ratio of the vertically and horizontally oriented orthorhombic structure ($\phi_{v,3}/\phi_{h,3}$) was 71/29, suggesting that the majority of the PCL crystal structure was a vertically oriented orthorhombic system.

In case of the PCL(10.5k) in both toluene and CHCl_3 annealing, their 2D patterns and profiles also showed the reflection plane such as {002}, {102}, {004}, {110}, {200}, and {200} (Figures 5.14b and 5.14f-5.14g, 5.15b and 5.14f-5.14). We applied GIXS formula for the orthorhombic lattice model on their profiles, which could be satisfactory fitted as shown in Figures 5.14f-5.14g and 5.15f-5.15g. The structural parameters are reported in Tables 5.5 and 5.6.

The GIXS results presented that the toluene-annealed PCL(10.5k) had the dimension edge lengths of the orthorhombic unit cell as $a = 0.80$ nm, $b = 0.53$ nm, and $c = 1.74$ nm. The crystal orientation also presented as parallel ($\bar{\varphi}_3 = 0^\circ$) and perpendicular ($\bar{\varphi}_3 = 90^\circ$) directions to the film surface. The horizontal orthorhombic lattice conformation showed distribution value as $\sigma_{\varphi_3} = 8.8$ and $O_{s,3,0} = 0.966$, while the vertical orthorhombic structure presented higher distribution value as $\sigma_{\varphi_3} = 17.30$ and $O_{s,3,90} = -0.375$. Additionally, the volume ratio of the vertical and horizontal orthorhombic structure ($\phi_{v,3}/\phi_{h,3}$) was about 93/7, indicating that the majority of the crystal structure was vertically oriented orthorhombic system. While the dimension length of orthorhombic crystal of the CHCl_3 -annealed PCL(10.5k) were identical with those of the toluene-annealed PCL(10.5k). The orientation angle was $0^\circ (= \bar{\varphi}_3)$ with distribution 8.1 ($= \sigma_{\varphi_3}$) and 0.971 ($= O_{s,3,0}$) and $90^\circ (= \bar{\varphi}_3)$ with distribution 7.2 ($= \sigma_{\varphi_3}$) and -0.477 ($= O_{s,3,90}$). The relative volume fraction also high in vertical direction as 79/21 ($= \phi_{v,9}/\phi_{h,9}$).

The 2D GIWAXS patterns and scattering profiles of the PHIC(5k, 10k)-PCL₁₋₃(17k, 10k) revealed complex crystalline peaks, which were match with those peaks from the PHIC(5.4k, 10.4k) and the PCL(15k, 10.5k), as shown in Figures 5.13c-

5.13e, 5.14c-5.14e, and 5.15c-5.15, respectively. They suggested that the crystal morphology of all the PHIC-PCL₁₋₃ originated from the PHIC and PCL crystal structures. In addition, the intensity profiles of all the PHIC-PCL₁₋₃ displayed peaks at the same scattering angles as the PHIC and PCL, independent of the PCL arm numbers, confirming that these star polymers have a similar crystal structure regardless of the number of PCL arms. The scattering intensity profiles were satisfactorily fitted using combination of the multilayer structural model and the orthorhombic crystal lattice model, as shown in Figures 5.13f-5.13g, 5.14f-5.14g, and 5.15f-5.15g, respectively. The structural and orientation parameters were also summarized and reported in Tables 5.4-5.6.

The GIXS analyses of the PHIC(5k, 10k)-PCL₁₋₃(17k, 10k) showed that the crystal orientations of the PHIC phase were observed to be in the parallel ($\overline{\varphi_2} = 0^\circ$) and perpendicular ($\overline{\varphi_2} = 90^\circ$) directions to the surface plane. The volume ratio ($\phi_{h,2}/\phi_{v,2}$), together with the standard deviation and the second order orientation factor ($\sigma_{\varphi_2,0}, O_{s,2,0}$ and $\sigma_{\varphi_2,90}, O_{s,2,90}$). In case of the toluene-annealed PHIC(5k, 10k)-PCL₁₋₃(17k, 10k), the majority structure in the PHIC domain was vertically oriented multilayer conformation in all the PCL arm series. However, the CHCl₃-annealed PHIC(10k)-PCL₁₋₃(10k) were observed difference as the majority structure due to PHIC phase was horizontal lamellar bilayer for the PHIC-PCL. The majority structure of PHIC phase changed to the vertical conformation when the number of PCL arms increased.

For the PCL domain orthorhombic structure of the PHIC(5k, 10k)-PCL₁₋₃(17k, 10k), their orientation angles and volume fraction have been found differently and influenced by PCL arm numbers. The PCL domain of the PHIC(5k)-PCL(17k) was

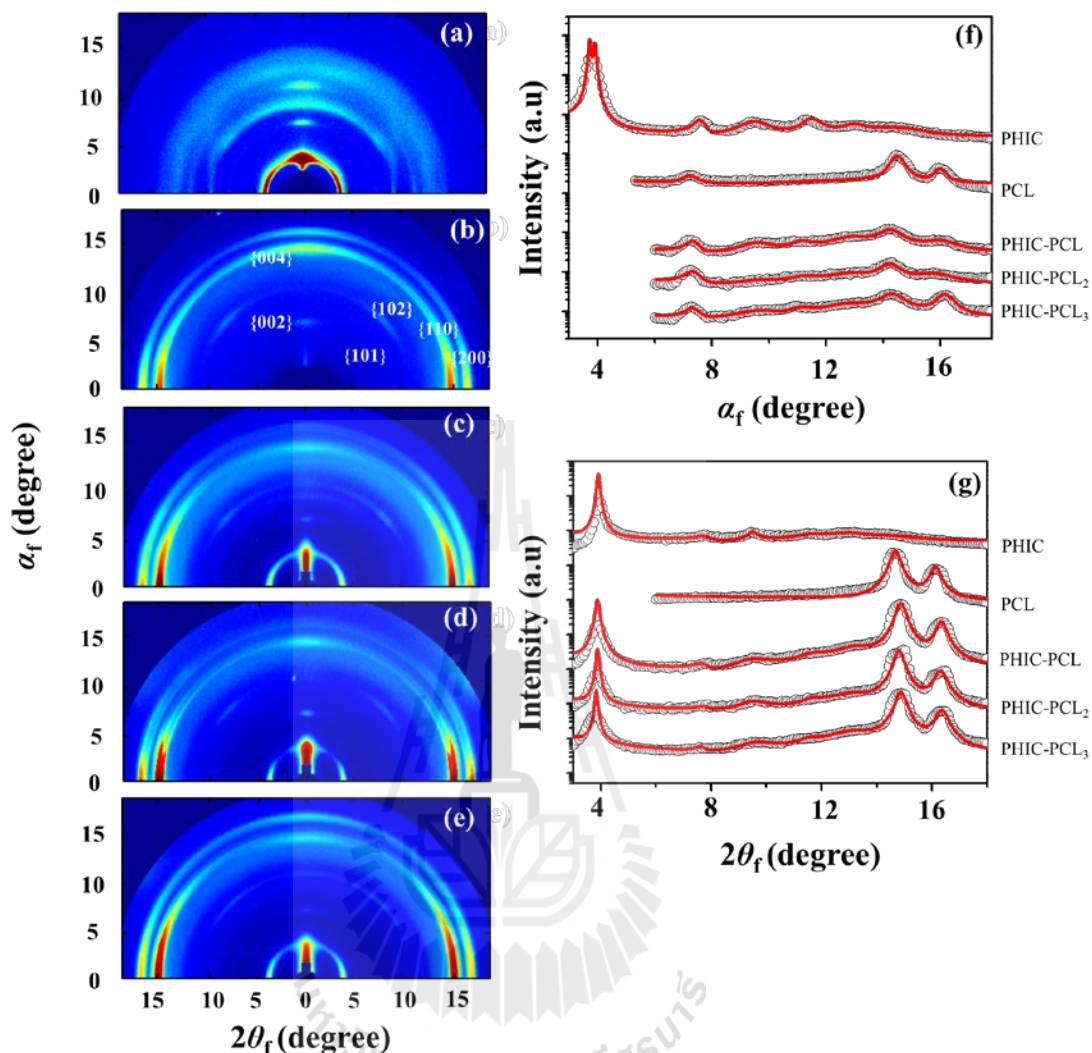


Figure 5.13 2D GIWAXS pattern of toluene-annealed PHIC(5.4k) and PCL(14.5k) homopolymer and PHIC(5k)-PCL₁₋₃(17k) films (120 nm thick) deposited on silicon substrates, measured with $\alpha_i = 0.130^\circ$ at room temperature using an X-ray beam ($\lambda = 0.1120$ nm); (a) PHIC; (b) PCL; (c) PHIC-PCL; (d) PHIC-PCL₂; (e) PHIC-PCL₃; (f) out-of-plane scattering profiles extracted from the data in (a–e) along the α_f direction at $2\theta_f = 0.0^\circ$; (g) in-plane scattering profiles extracted from the data in (a–e) along the $2\theta_f$ direction at $\alpha_f = 0.390^\circ$. In (f) and (g), the black circular symbols are the measured data, and the red solid lines were obtained by fitting the data using the GIXS formulae.

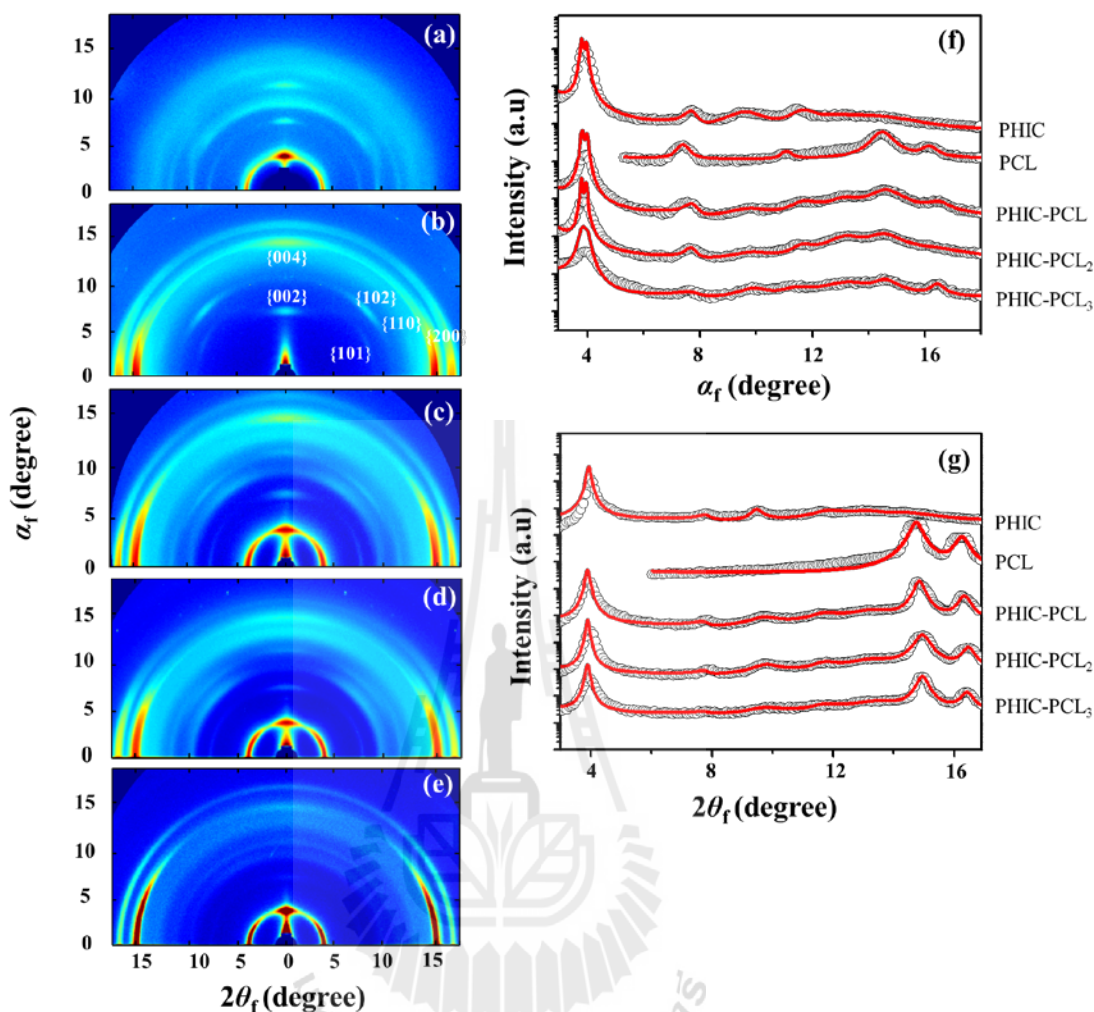


Figure 5.14 2D GIWAXS pattern of toluene-annealed PHIC(10.4k) and PCL(10.5k) homopolymer and the PHIC(10k)-PCL₁₋₃(10k) films (80 nm thick) measured at RT using an X-ray beam ($\lambda = 0.1120$ nm) $\alpha_i = 0.130^\circ$ at SDD = 229 mm; (a) PHIC; (b) PCL; (c) PHIC-PCL; (d) PHIC-PCL₂; (e) PHIC-PCL₃; (f) out-of-plane scattering profiles extracted from the data in (a–e) along the α_f direction at $2\theta_f = 0.0^\circ$; (g) in-plane scattering profiles extracted from the data in (a–e) along the $2\theta_f$ direction at $\alpha_f = 0.300^\circ$. In (f) and (g), the black circular symbols are the measured data, and the red solid lines were obtained by fitting the data using the GIXS formulae.

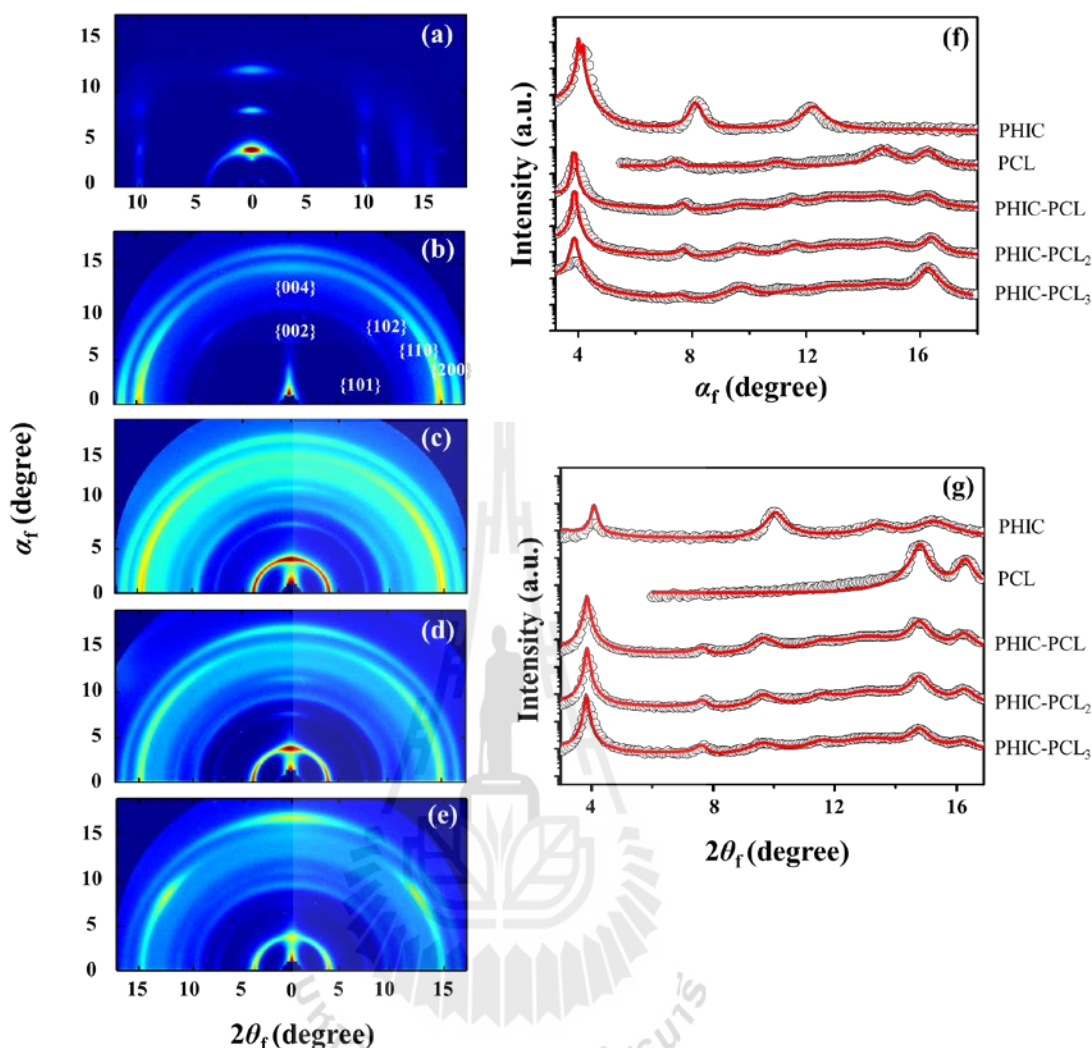


Figure 5.15 2D GIWAXS pattern of CHCl_3 -annealed PHIC(10.4k) and PCL(10.5k) homopolymer and the PHIC(10k)-PCL₁₋₃(10k) films (80 nm thick) measured at RT using an X-ray beam with $\alpha_i = 0.140^\circ$ at SDD = 229 mm; the X-ray wavelength $\lambda = 0.1180$ nm was used in (a) PHIC; $\lambda = 0.1110$ nm was used in (b) PCL; in (c) PHIC-PCL; in (d) PHIC-PCL₂; in (e) PHIC-PCL₃; (f) out-of-plane scattering profiles extracted from the data in (a–e) along the α_f direction at $2\theta_f = 0.0^\circ$; (g) in-plane scattering profiles extracted from the data in (a–e) along the $2\theta_f$ direction at $\alpha_f = 0.260^\circ$. In (f) and (g), the black circular symbols are the measured data, and the red solid lines were obtained by fitting the data using the GIXS formulae.

Table 5.4 Structural parameters of the toluene-annealed thin films of the PHIC(5.4k) and PCL(14.5k) and PHIC(5k)-PCL₁₋₃(17k) miktoarm star polymers, determined by GIWAXS analysis.

Structural Parameter	PHIC	PCL	PHIC-PCL	PHIC-PCL ₂	PHIC-PCL ₃
d_L^a (nm)	1.67		1.67	1.67	1.67
l_1^b (nm)	0.77		0.77	0.77	0.77
l_2^c (nm)	0.90		0.90	0.90	0.90
d_1^d (nm)	0.67		0.67	0.67	0.67
d_2^e (nm)	0.50		0.50	0.50	0.50
d_3^f (nm)	0.45		0.45	0.45	0.45
g_{dL}^g (nm)	0.056		0.078	0.065	0.065
g_{d1}^h (nm)	0.140		0.170	0.140	0.160
g_{d2}^i (nm)	0.120		0.140	0.150	0.160
g_{d3}^j (nm)	0.160		0.110	0.110	0.110
φ_2^k (deg.)	0		0	0	0
$\sigma_{\varphi_2,0}^l$ (deg)	4.70		4.20	5.10	6.30
$O_{s,2,0}^m$	0.990		0.992	0.988	0.982
φ_2 (deg.)	90		90	90	90
$\sigma_{\varphi_2,90}$ (deg)	20.10		18.60	17.90	21.8
$O_{s,2,90}$	-0.336		-0.357	-0.367	-0.311
$\phi_{h,2}/\phi_{v,2}^n$ (v/v)	80/20		41/59	46/54	38/62
a^o (nm)		0.80	0.80	0.80	0.80
b^p (nm)		0.53	0.53	0.53	0.53
c^q (nm)		1.76	1.76	1.76	1.76
g^r		0.060	0.064	0.064	0.064
φ_3^s (deg.)		0			0
$\sigma_{\varphi_3,0}^t$ (deg)		10.6			10.10
$O_{s,3,0}^u$		0.950			0.955
φ_3 (deg.)		90	90	90	90
$\sigma_{\varphi_3,90}$ (deg)		14.30	18.70	17.80	18.50
$O_{s,3,90}$		-0.412	-0.356	-0.368	-0.359
$\phi_{v,3}/\phi_{h,3}^v$ (v/v)		71/29	100/0	100/0	85/15

Table 5.5 Structural parameters of the toluene-annealed thin films of the PHIC(10.4k) and PCL(10.5k) homopolymers and PHIC(10k)-PCL₁₋₃(10k) miktoarm star polymers, determined by GIWAXS analysis.

Structural parameter	PHIC	PCL	PHIC-PCL	PHIC-PCL ₂	PHIC-PCL ₃
d_L^a (nm)	1.66		1.66	1.66	1.66
ℓ_1^b (nm)	0.76		0.76	0.76	0.76
ℓ_2^c (nm)	0.90		0.90	0.90	0.90
d_1^d (nm)	0.67		0.67	0.67	0.67
d_2^e (nm)	0.50		0.50	0.50	0.50
d_3^f (nm)	0.45		0.45	0.45	0.45
g_{dL}^g (nm)	0.067		0.069	0.069	0.089
g_{d1}^h (nm)	0.140		0.160	0.160	0.155
g_{d2}^i (nm)	0.110		0.110	0.110	0.140
g_{d3}^j (nm)	0.130		0.130	0.130	0.150
φ_2^k (deg.)	0		0	0	0
$\sigma_{\varphi_2,0}^l$ (deg)	5.10		7.90	8.50	7.70
$O_{s,2,0}^m$	0.988		0.972	0.968	0.974
φ_2 (deg.)	90		90	90	90
$\sigma_{\varphi_2,90}$ (deg)	14.40		17.80	22.30	20.10
$O_{s,2,90}$	-0.411		-0.368	-0.304	-0.336
$\phi_{h,2}/\phi_{v,2}^n$ (v/v)	77/22		32/68	23/77	28/72
a^o (nm)		0.80	0.80	0.80	0.80
b^p (nm)		0.53	0.53	0.53	0.53
c^q (nm)		1.74	1.74	1.74	1.74
g^r		0.060	0.065	0.070	0.070
φ_3^s (deg.)		0	0		
$\sigma_{\varphi_3,0}^t$ (deg)		8.8	7.8		
$O_{s,3,0}^u$		0.966	0.973		
φ_3 (deg.)		90	90	90	90
$\sigma_{\varphi_3,90}$ (deg)		17.30	18.80	20.40	23.00
$O_{s,3,90}$		-0.375	-0.355	-0.332	-0.293
$\phi_{v,3}/\phi_{h,3}^v$ (v/v)		93/7	95/5	100/0	100/0

Table 5.6 Structural parameters of CHCl_3 -annealed thin films of PHIC(10.4k) and PCL(10.5k) homopolymers and PHIC(10k)-PCL₁₋₃(10k) miktoarm star polymers films, determined by GIWAXS analysis.

Structural parameter	PHIC	PCL	PHIC-PCL	PHIC-PCL ₂	PHIC-PCL ₃
d_L^a (nm)	1.65		1.65	1.65	1.65
ℓ_1^b (nm)	0.76		0.76	0.76	0.76
ℓ_2^c (nm)	0.89		0.89	0.89	0.89
d_1^d (nm)	0.67		0.67	0.67	0.67
d_2^e (nm)	0.50		0.50	0.50	0.50
d_3^f (nm)	0.45		0.45	0.45	0.45
g_{dL}^g (nm)	0.048		0.056	0.069	0.089
g_{d1}^h (nm)	0.100		0.140	0.130	0.130
g_{d2}^i (nm)	0.100		0.150	0.150	0.150
g_{d3}^j (nm)	0.110		0.150	0.150	0.145
φ_2^k (deg.)	0		0	0	0
$\sigma_{\varphi_2,0}^l$ (deg)	3.70		8.70	8.90	5.40
$O_{s,2,0}^m$	0.994		0.966	0.975	0.987
φ_2 (deg.)			90	90	90
$\sigma_{\varphi_2,90}$ (deg)			18.30	18.60	13.40
$O_{s,2,90}$			-0.362	-0.357	-0.422
$\phi_{h,2}/\phi_{v,2}^n$ (v/v)	100/0		60/40	48/52	37/63
a^o (nm)		0.80	0.80	0.80	0.80
b^p (nm)		0.53	0.53	0.53	0.53
c^q (nm)		1.74	1.74	1.74	1.74
g^r		0.065	0.072	0.075	0.075
φ_3^s (deg.)		0	0	0	0
$\sigma_{\varphi_3,0}^t$ (deg)		8.1	12.2	14.9	8.2
$O_{s,3,0}^u$		0.971	0.935	0.905	0.970
φ_3 (deg.)		90	90	90	90
$\sigma_{\varphi_3,90}$ (deg)		7.2	9.30	9.90	
$O_{s,3,90}$		-0.477	-0.462	-0.457	
$\phi_{v,3}/\phi_{h,3}^v$ (v/v)		79/21	22/78	29/71	0/100

^a Long period of the molecular multibilayer PHIC structure.

^b Thickness of more dense layer in the molecular multibilayer PHIC structure.

^c Thickness of less dense layer in the molecular multibilayer PHIC structure.

^d Mean interdistance between the *n*-hexyl bristles of the neighboring polymer chains whose repeat units are matched in position along their backbones.

^e Mean interdistance between the nearest *n*-hexyl bristles along the polymer backbone.

^f Mean interdistance between the *n*-hexyl bristles of the nearest neighboring polymer chains.

^g Paracrystal distortion factor along the direction parallel to the long period of molecular multibilayer structure.

^h Paracrystal distortion factor along *n*-hexyl bristles of the neighboring polymer chains whose repeat units are matched in position along their backbones.

- ⁱ Paracrystal distortion factor along the nearest *n*-hexyl bristles along the polymer backbone.
- ^j Paracrystal distortion factor along the *n*-hexyl bristles of the nearest neighboring polymer chains.
- ^k Mean value of the polar angle φ_2 (i.e., orientation angle) between the orientation vector \mathbf{n}_2 (which is set along the direction parallel to the long period of molecular multilayer PHIC structure) and the out-of-plane of the film.
- ^l Standard deviation for the orientation angle φ_2 of molecular multilayer PHIC structure.
- ^m Second order orientation factor of the molecular multilayer PHIC structure.
- ⁿ Volume fraction ratio of the horizontal and vertical multilayer PHIC structures.
- ^o A unit cell dimension along the *a*-axis of orthorhombic PCL crystals.
- ^p A unit cell dimension along the *b*-axis of orthorhombic PCL crystals.
- ^q A unit cell dimension along the *c*-axis of orthorhombic PCL crystals.
- ^r Paracrystal distortion factor of the PCL crystal.
- ^s Mean value of the polar angle φ_3 (i.e., orientation angle) between the orientation vector \mathbf{n}_3 (which is set along the direction parallel to the long period of lamellar structure) and the out-of-plane of the film.
- ^t Standard deviation for the orientation angle φ_3 of lamellar structure.
- ^u Second order orientation factor of lamellar PCL crystal structure.
- ^v Volume fraction ratio of the horizontal and vertical lamellar PCL crystal structures.

observed only at $\overline{\varphi_3} = 90^\circ$ with $\sigma_{\varphi_3,90} = 18.7$, $O_{s,3,90} = -0.356$, and $\phi_{v,3}/\phi_{h,3} = 100/0$.

The PHIC(5k)-PCL₂(17k) orientation angle was also observed only at $\overline{\varphi_3} = 90^\circ$ with $\sigma_{\varphi_3,90} = 17.8$, $O_{s,3,90} = -0.368$ and $\phi_{v,3}/\phi_{h,3} = 100/0$. While the PHIC(5k)-PCL₃(17k) presented in both angle at $\overline{\varphi_3} = 0^\circ$ ($\sigma_{\varphi_3,90} = 10.1$, $O_{s,3,90} = 0.955$) and $\overline{\varphi_3} = 90^\circ$ ($\sigma_{\varphi_3,90} = 18.5$, $O_{s,3,90} = -0.359$) with $\phi_{v,3}/\phi_{h,3} = 85/15$. It should be noted that the first peak of the PHIC(5k)-PCL₁₋₃(17k) profiles along the out-of-plane direction were smear by the X-ray reflection due to the Si substrate.

The PCL phase of the toluene-annealed PHIC(10k)-PCL₁₋₃(10k) were obtained and reported (Table 5.5) as the orientation angle of the PHIC-PCL was $\overline{\varphi_3} = 0^\circ$ ($\sigma_{\varphi_3,0} = 7.8$, $O_{s,3,0} = 0.973$) and $\overline{\varphi_3} = 90^\circ$ ($\sigma_{\varphi_3,90} = 18.8$, $O_{s,3,90} = -0.355$) and relative volume fraction $\phi_{v,3}/\phi_{h,3} = 95/5$. However, the angle of the PHIC-PCL_{2,3} were observed only $\overline{\varphi_3} = 90^\circ$ ($\sigma_{\varphi_3,90} = 20.4$, $O_{s,3,90} = -0.332$ for the PHIC-PCL₂ and $\sigma_{\varphi_3,90} = 23.0$, $O_{s,3,90} = 0.293$ for the PHIC-PCL₃). The PCL orthorhombic phase of the CHCl₃-

annealed PHIC(10k)-PCL_{1,2}(10k) was revealed the orientation angles at 0° ($=\overline{\varphi_3}$) with the distribution $\sigma_{\varphi_3,0} = 12.2$, $O_{s,3,0} = 0.935$ for the PHIC-PCL and $\sigma_{\varphi_3,0} = 14.9$, $O_{s,3,0} = 0.905$ for the PHIC-PCL₂, also at 90° ($=\overline{\varphi_3}$) with the distribution $\sigma_{\varphi_3,90} = 9.30$, $O_{s,9,0} = -0.462$ for the PHIC-PCL and $\sigma_{\varphi_3,90} = 9.90$, $O_{s,9,0} = -0.457$ for the PHIC-PCL₂. While the CHCl₃-annealed PHIC(10k)-PCL₃(10k) presented the angle at $\overline{\varphi_3} = 0^\circ$ with the distribution $\sigma_{\varphi_3,0} = 8.2$, $O_{s,9,0} = 0.970$. The volume fraction between vertically and horizontally oriented orthorhombic system ($\phi_{v,3}/\phi_{h,3}$) were obtained 22/78 (PHIC-PCL), 29/71 (PHIC-PCL₂), and 0/100 (PHIC-PCL₃).

From the above quantitative analyses of GISAXS and GIWAXS on the molecular morphology and structural ordering of the toluene-annealed PHIC(5k)-PCL₁₋₃(17k) and the toluene- and CHCl₃-annealed PHIC(10k)-PCL₁₋₃(10k) miktoarm star polymer films as well as toluene-annealed PHIC(5.4k) and PCL(10.5k) and the toluene- and CHCl₃-annealed PHIC(10.4k) and PCL(10.5k) homopolymer films, their morphology and structural ordering could be illustrated in Figures 5.16-5.18.

5.4 Conclusion

The series thin films of PHIC-PCL₁₋₃, the rod-coil type miktoarm star polymers, were quantitatively characterized using GISAXS and GIWAXS techniques. The PHIC-PCL₁₋₃ are consisted of the crystallizable PHIC arm and one to three of the crystallizable PCL arms (PCL_n; $n = 1-3$) with the M_n of the PHIC arm around 5,100-5,200 g/mol and of the PCL arms approximate 17,400-18,000 g/mol (PHIC(5.1k)-PCL(17.4k), PHIC(5.2k)-PCL₂(18k), and PHIC(5.2k)-PCL₃(17.0k)), also with the M_n of the PHIC arm about 9,600-10,900 g/mol and of the PCL arms approximate 10,600-

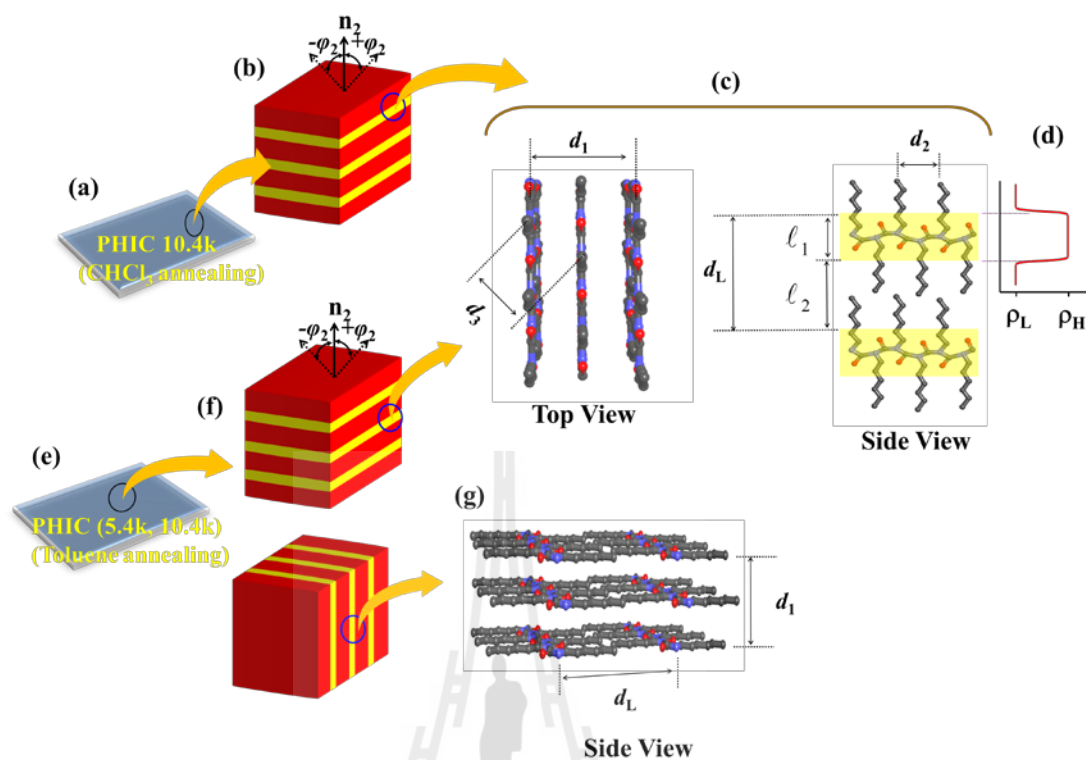


Figure 5.16 Schematic representations of molecular chain conformation in CHCl₃-annealed PHIC (10.4k) thin films (a); (b) horizontal multibilayer structure where \mathbf{n}_2 is the orientation vector of the structure model and φ_2 is the polar angle between the \mathbf{n}_2 vector and the out-of-plane of the film; (c) top and side views of molecular chain conformation and packing order with no interdigitation in the structure (b); (d) relative electron density profile along the out-of-plane of the multibilayer structure where ρ_L and ρ_H are the relative electron densities of less and highly dense sublayer respectively; (e) the picture of molecular chain conformation in toluene-annealed PHIC (5.4k, 10.4k) thin films; (f) horizontal and vertical multibilayer structure; (g) side view of molecular chain conformation and packing order with no interdigitation in the horizontal structure (f).

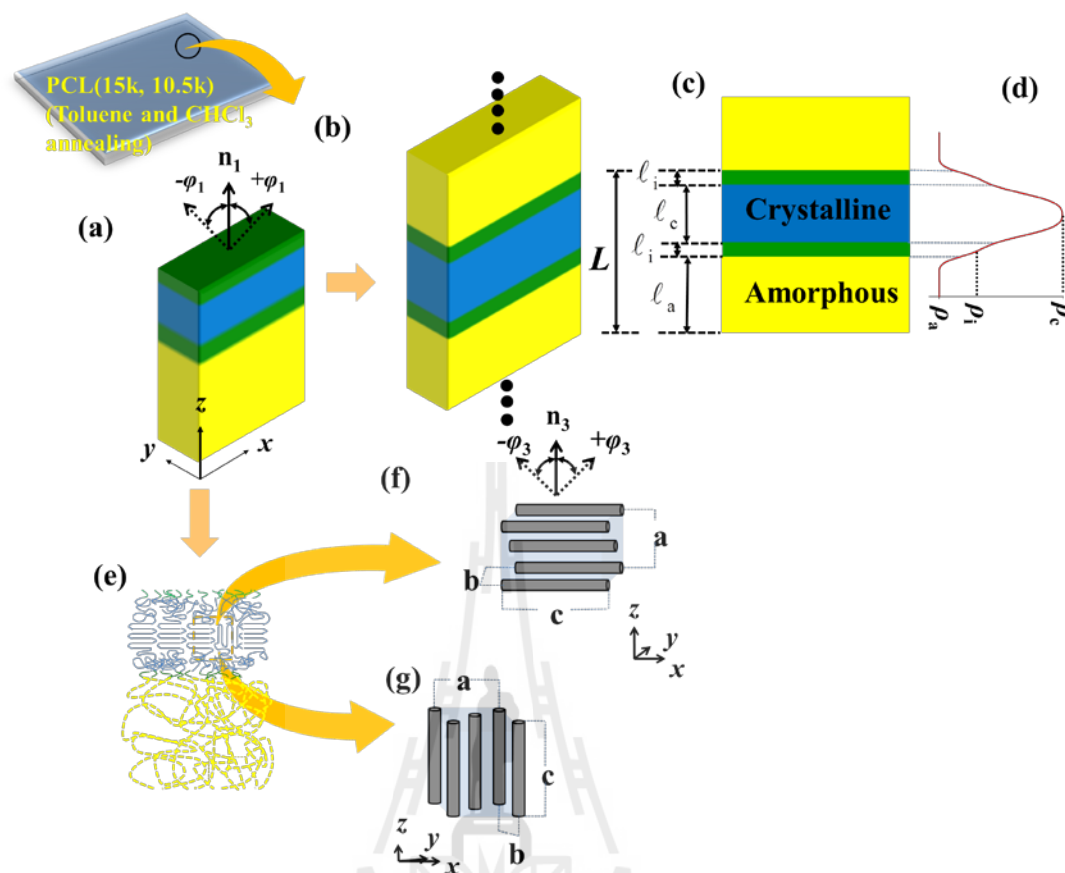


Figure 5.17 Schematic representation of molecular chain conformation and packing order in toluene-annealed PCL(15k) and toluene- and CHCl_3 -annealed PCL(10.5k) films; (a–c) horizontal lamellar structure in PCL film where \mathbf{n}_1 is the orientation vector has the axis normal to the structure and φ_1 is the polar angle between the \mathbf{n}_1 vector and the out-of-plane direction of the film; (d) the relative electron density profile which ρ_c , ρ_i , and ρ_a are the relative electron densities of crystal, interface, and amorphous layers respectively; (e) molecular chain conformations in the amorphous layers and molecular chain order in the crystalline layers; (f) horizontally oriented orthorhombic crystal lattice where \mathbf{n}_3 is the orientation vector of the structure model and φ_3 is the polar angle between the \mathbf{n}_3 vector and the out-of-plane of the film; (g) vertically oriented orthorhombic crystal lattice.

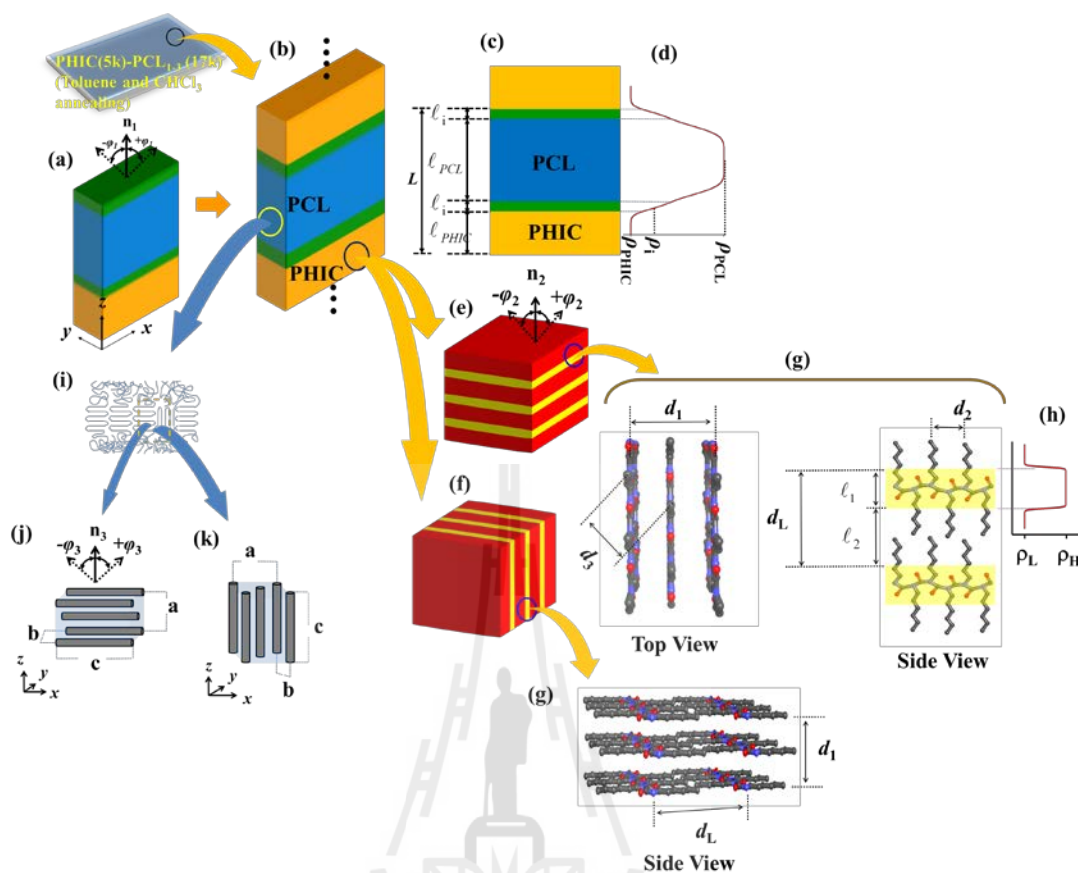


Figure 5.18 Schematic representations of molecular chain conformations and packing orders in toluene-annealed PHIC(5k)-PCL₁₋₃(17k) and toluene- and CHCl₃-annealed PHIC(10k)-PCL₁₋₃(10k) films: (a-c) horizontal lamellar structure and the orientation vector \mathbf{n}_1 of the structure model; (d) the relative electron densities profile where ρ_{PHIC} , ρ_i , and ρ_{PCL} are the relative electron densities of PHIC, interface, and PCL layers respectively. (e) horizontal multibilayer structure formed in the PHIC lamella where \mathbf{n}_2 is the orientation vector of the structure model. (f) vertical multibilayer structure formed in the PHIC lamella; (g) top and side views of molecular chain and packing order; (h) relative electron density profile along the out-of-plane of the multibilayer structure; (i) molecular chain conformations and order in the PCL layers; (j) horizontally oriented orthorhombic crystal lattice where \mathbf{n}_3 is the orientation vector of the structure model; (k) vertically oriented orthorhombic crystal lattice.

11,100 g/mol (PHIC(10.3k)-PCL(10.6k), PHIC(10.9k)-PCL₂(11.1k), and PHIC(9.6k)-PCL₃(11.0k)), respectively. Furthermore, the PHIC (M_n approximate 5,400 and 10,400 g/mol) and PCL (M_n around 15,000 and 10,500 g/mol) homopolymer films were analyzed with the same methods.

The quantitative molecular conformation GISAXS analyses of the PHIC(5k)-PCL₁₋₃(17k) and PCL(15k) films, under toluene annealing, were found to have a predominant horizontally oriented lamellar structure. The star polymers films demonstrated a phase-separation of the PHIC and PCL domains, with a higher thickness layer in the PCL phase. The structural parameters of the lamellar structures were slightly influenced by the number of the PCL arms. The above results of the PHIC(5k)-PCL₁₋₃(17k) films are unusual for the common diblock copolymers, which were observed in the same volume fraction.

In case of the PHIC(10k)-PCL₁₋₃(10k) films, they also presented interesting results as they formed lamellar structures with different orientation depend on the toluene and/or CHCl₃ annealing as well as the number of PCL arms present. The quantitative GISAXS analyses of the toluene-annealed PHIC-PCL₁₋₃ formed horizontally oriented lamellar structure regardless PCL arm numbers. Unlikely, the PHIC-PCL₁₋₃ films under CHCl₃ annealing, formed lamellar structures with different orientation depend on the number of PCL arms present. In particular, the PHIC-PCL film was found to have horizontal lamellar structure, while the PHIC-PCL_{2,3} films were revealed to have vertical lamellar structure. Moreover, the molecular structure of the PHIC-PCL₁₋₃ films in both annealing showed a phase-separated of PHIC and PCL domains that have higher thickness layer in PCL phase.

The PCL(15k) and PCL(10.5k) films also showed a phase-separation of crystal and amorphous states, with higher thickness in the amorphous layer. While all the PHIC(5.4k) and PHIC(10.4k) films did not display a GISAXS structure during the range of the collected scattering data, which happened either the domain structure of the PHIC were larger than the scattering data range or the electron density fluctuation of the PHIC was very small.

The quantitative GIWAXS analyses on the crystal conformations of the PHIC(5.4k) and PHIC(10.4k) under toluene annealing revealed the horizontally and vertically oriented multibilayer (backbone and alkyl chain layers) structure and the horizontally and vertically oriented orthorhombic structure, respectively. The CHCl₃-annealed PHIC successfully formed a well self-organized structure as horizontal multibilayer conformation. All the PCL(15k) and PCL(10.5k) films in both toluene and CHCl₃ annealing revealed the horizontally and vertically oriented orthorhombic structure, respectively.

The crystal morphology of the toluene-annealed PHIC(5k)-PCL₁₋₃(17k) and the toluene- and CHCl₃-annealed PHIC(10k)-PCL₁₋₃(10k) films displayed the multibilayer structure (due to the PHIC phase) and the orthorhombic structure (due to the PCL phase). Moreover, the crystal structures of the PHIC phase were formed as a mixed between horizontally and vertically oriented lamellar multibilayers, which the majority of the structure was horizontally multibilayers except the CHCl₃-annealed PHIC(10k)-PCL(10k). The PCL phase displayed both horizontally and vertically oriented orthorhombic systems in case of the toluene-annealed PHIC(5k)-PCL₃(17k), the toluene-annealed PHIC(10k)-PCL₁₋₃(10k), and the CHCl₃-annealed PHIC(10k)-PCL_{1,2}(10k), presented only vertical orthorhombic lattice in case of the toluene-

annealed PHIC(5k, 10k)-PCL_{2,3}(17k, 10k), showed only horizontal orthorhombic crystal in case of the CHCl₃-annealed PHIC(10k)-PCL₃(10k).



CHAPTER VI

STRUCTURAL ANALYSIS OF POLY(N-HEXYL ISOCYANATE)-*BLOCK*-POLY(L-LACTIC ACID) MIKTOARM STAR POLYMERS THIN FILMS BY GRAZING X-RAY SCATTERING

6.1 Introduction

Other rod-coil type miktoarm star polymers, PHIC-PLLA₁₋₃ have been also successfully synthesized and reported in the previous research (Satoh *et al.*, 2014). The rod-coil PHIC-PLLA₁₋₃ miktoarm star polymers are composed of a rigid rod-like PHIC (poly(n-hexyl isocyanate)) arm polymer and one to three semi-crystalline coil-like PLLA (poly(L-lactic acid)) arms polymer. The totally number-average molecular weight (M_n) of PHIC arm around 9,600-10,900 g/mol and one to three PLLA (PLLA_n; $n = 1-3$) arms approximate 9,600-10,100 g/mol; PHIC(10.3k)-PLLA(9.6k), PHIC(10.9k)-PLLA₂(9.8k), and PHIC(9.6k)-PLLA₃(10.1k), respectively. PLLA has been also known as a biodegradable polymer, which is used in the area of medical, surgery, and drug delivery system (Montes De Oca, and Ward, 2007).

Since the PHIC-PLLA₁₋₃ have not yet been investigated in thin film forms, we prepared and characterized the molecular morphology and structural ordering of the PHIC-PLLA₁₋₃ thin films by using grazing incident X-ray scattering (GIXS)

techniques. The CHCl_3 annealing has been found and used in order to induced a well self-organized govern in the PHIC- PLLA_{1-3} films. Not only was the CHCl_3 annealing but also the thermal annealing was studied. Moreover, the effects due to the number of PLLA arms on the self-organized behavior of the polymers films were reviewed. The morphology and structural details of PHIC(10.4k) and PLLA(10.2k) homopolymer films were also investigated along the star polymers films.

6.2 Experimental Section

6.2.1 Materials and Thin Films Preparation

The fundamental properties of the rod-coil PHIC- PLLA_{1-3} miktoarm star polymers, i.e. the numbers of averaged molecular weight M_n , polydispersity index, and volume fraction were presented in Table 6.1. The studied polymers in powder form were dissolved in chloroform (CHCl_3) producing 0.5 wt% solution and then filtered by using polytetrafluoroethylene filter with the pore size of 0.2 μm . The filtered solution were fabricated onto pre-cleaned silicon substrates by spin coater (1,500 rps with 50s) and dried in vacuum at room temperature for one day. The polymers-coated films were annealed in CHCl_3 with different time conditions (15 minutes for PHIC- $\text{PLLA}_{1,2}$, 16 hours for PHIC- PLLA_3). Another set of the PHIC- PLLA_{1-3} films also annealed by CHCl_3 using the same conditions as the previous cases and then heating at approximately 130 $^\circ\text{C}$ for 24 hrs. The thickness of the polymers thin films, determined by a spectroscopic ellipsometer (model M2000, J. A. Woollam, Lincoln, NE, USA), were obtained approximately 70-85 nm.

Table 6.1 Fundamental properties of the PHIC and PLLA homopolymers and PHIC-PLLA₁₋₃ miktoarm star polymers used in the study.

Polymer	$M_{n,NMR}^a$	M_w/M_n^b	f_{PHIC}^c (%)
PHIC	10,400	1.11	100
PLLA	10,200	1.08	0
PHIC-PLLA	19,900	1.06	57
PHIC-PLLA ₂	20,700	1.12	58
PHIC-PLLA ₃	19,700	1.08	54

^a Number-average molecular weight determined in CDCl₃ by ¹H NMR spectroscopy analysis.

^b Polydispersity determined by size exclusion chromatography (SEC) in THF using polystyrene standards.

^c Volume fraction of PHIC arm: $f_{PHIC} = (M_{n,NMR,PHIC}/d_{PHIC}) / (M_{n,NMR,PHIC}/d_{PHIC} + M_{n,NMR,PLLA}/d_{PLLA})$; $d_{PHIC} = 1.00 \text{ g/cm}^3$ and $d_{PLLA} = 1.25 \text{ g/cm}^3$.

6.2.2 Measurements

The rod-coil miktoarm star polymers thin films, PHIC-PLLA₁₋₃ and the homopolymer thin films, PHIC and PLLA, were measured with grazing incidence X-ray scattering (GIXS) techniques at Pohang Accelerator Laboratory (PAL), Pohang, South Korea. The grazing incidence X-ray scattering at small angle (GISAXS) and wide angle (GIWAXS) with sample to detector distance (SDD) of 3m (2,917 mm) and 0.2 m (240 mm) were conducted at the beam line 3C and 9A (Yoon *et al.*, 2008; Lee *et al.*, 2005; Lee *et al.*, 2005; Rho *et al.*, 2014), respectively. The incidence angle α_i of the X-ray beam was set in the range of 0.110-0.160°, which is between the critical angles of the star polymers or the homopolymer films and the silicon substrate. The GIXS measurements were performed at room temperature with the exposure time of 30 – 60 s. The X-ray wavelength (λ) was set at 1.21 Å, 1.18 Å, and 1.12 Å,

respectively. The scattering intensities were measured as a function of the exit scattering angle α_f (normal direction to the film surface) and $2\theta_f$ (parallel direction to the film surface). Polystyrene-*b*-Polyethylene-*b*-Polybutadiene-*b*-Polystyrene (SEBS) block copolymer or silver behenate powder (TCI, Tokyo, Japan) has been used as a standard sample to calibrate the scattering angles. The scattering data were collected by a 2D charge-coupled detector (CCD) (Rayonix MAR CCD).

6.3 Results and Discussions

We studied the quantitative morphology and structural ordering of the rod-coil PHIC-PLLA₁₋₃ miktoarm star polymers and PHIC and PCL homopolymer thin films using GIXS (GISAXS and GIWAXS) technique. These polymers films were annealed by CHCl₃ in order to induce well-developed self-organized structure. Since thermal have been reported to have effects on the PLLA crystal structure (Yasuniwa *et al.*, 2006; Yasuniwa, Iura, and Dan, 2007; Yang *et al.*, 2014), we also investigated the effects of thermal annealing on self-assembled behavior of the PHIC-PLLA₁₋₃ and the PLLA films. The polymers films heated up at temperature approximately 130 °C for 24 hrs.

Figures 6.1a-6.1c presented 2D GISAXS data of the CHCl₃-annealed PHIC film and its profiles along the out-of-plane (α_f) and in-plane ($2\theta_f$) direction, respectively. It should be emphasized that we considered the same CHCl₃-annealed PHIC homopolymer film as it had already been explained the structural details in Chapter V. The PHIC pattern was featureless and the profiles were observed to be no peaks during the range of scattering data. The PLLA film, annealed by CHCl₃, was also observed to have a GISAXS pattern and profiles were featureless as shown in Figure

6.1d-6.1f. However, the GISAXS data and scattering profiles of thermally annealed PLLA film were presented feature as presented in Figures 6.2a and 6.2b-6.2c respectively. The out-of-plane profile presented very weak broad peak at 0.25° – 0.70° (Figure 6.2b), while the in-plane profile was featureless (Figure 6.2c). These characteristic profiles indicated that the horizontal lamellar structure formed in the thermal-annealed PLLA film. Therefore, the GIXS formula for the three layer lamellar structural model (Yoon *et al.*, 2007; Yoon *et al.*, 2008; Ahn *et al.*, 2010; Ahn *et al.*, 2013), already explained in the Chapter IV, was applied on the profiles as shown in Figures 6.2b and 6.2c. The structural parameters were obtained and listed in Table 6.2. The 2D image was created and agreement with the GISAXS data (Figure 6.2d). Additionally, the horizontal lamellar structural model was presented in Figure 6.2e.

The GIXS analysis revealed that the PLLA horizontal lamellar had a long period L of 17.0 nm, composed of three sublayers; high dense sublayer (l_1) or crystalline layer (l_c) with $l_1 = l_c = 4.0$ nm thick, less dense layer (l_3) or amorphous layer (l_a) with $l_3 = l_a = 9.8$ nm thick, and an interfacial layer (l_i) with $l_2 = l_i = 1.6$ nm thick. The orientation of the lamellar structure was also characterized as $\bar{\varphi}_1$ (mean polar angle) between the orientation vector \mathbf{n}_1 of the horizontal lamellar structure and the out-of-plane direction of the film was 0° . Its standard deviation σ_{φ_1} , second-order orientation factor $O_{s,1}$, and positional distortion factor g were found as 6.3° , 0.982, and 0.38, respectively. In contrast, the 2D GISAXS patterns of the PHIC-PLLA₁₋₃ films under CHCl_3 and thermal annealing showed clear feature, suggesting that the self-organized nanostructure successfully developed into these polymers films.

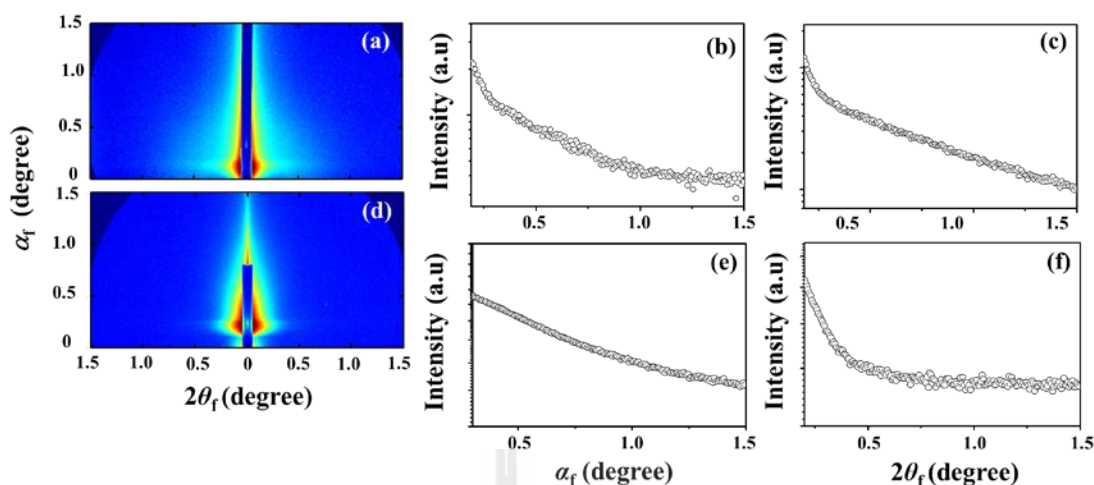


Figure 6.1 2D GISAXS patterns of CHCl_3 -annealed PHIC and PLLA homopolymer films in approximate 80 nm thick measured with an incidence angle α_i of 0.130° at room temperature using an X-ray beam with a wavelength λ of 0.1170 nm; (a) PHIC film; (b) out-of-plane 1D scattering profile extracted from the data in (a) along the α_f direction at $2\theta_f = 0.100^\circ$; (c) in-plane 1D scattering profile extracted from the data in (a) along the $2\theta_f$ direction at $\alpha_f = 0.170^\circ$; (d) PLLA film; (e) out-of-plane scattering profile extracted from the data in (d) along the α_f direction at $2\theta_f = 0.100^\circ$; (f) in-plane scattering profile extracted from the data in (d) along the $2\theta_f$ direction at $\alpha_f = 0.170^\circ$; where α_f and $2\theta_f$ are the exit angles of the X-ray beam with respect to the film surface and to the plane of incidence respectively.

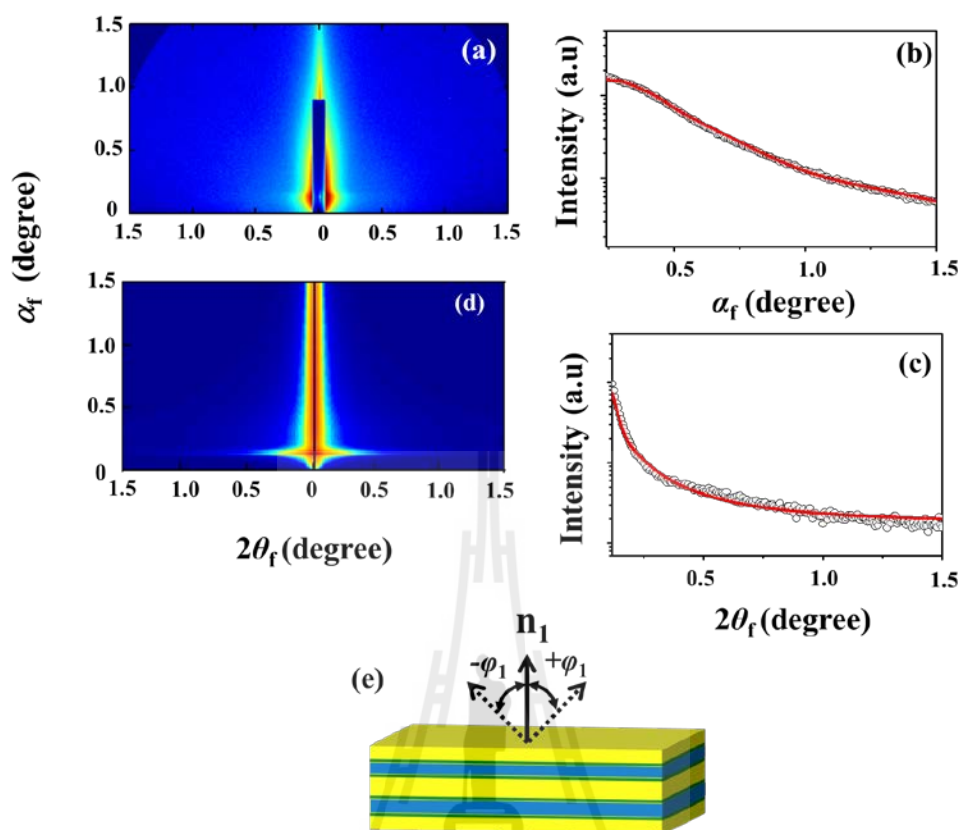


Figure 6.2 2D GISAXS patterns of thermal annealing on PLLA homopolymer films in approximate 80 nm thick measured with an incidence angle α_i of 0.130° at room temperature using an X-ray beam with a wavelength λ of 0.1210 nm; (a) PLLA film; (b) out-of-plane 1D scattering profile extracted from the data in (a) along the α_f direction at $2\theta_f = 0.080^\circ$; (c) in-plane 1D scattering profile extracted from the data in (a) along the $2\theta_f$ direction at $\alpha_f = 0.150^\circ$; (d) 2D image of PCL film reconstructed from the structural parameters in Table 6.2 using the GIXS formula derived for three layer lamellar structural model; (e) lamellar structure model where \mathbf{n}_1 is the orientation vector of the structure model and φ_4 is the polar angle between the \mathbf{n}_1 vector and the out-of-plane of the film. In (b) and (c), the black circular symbols are the measured data, and the red solid lines represented as a fitting result from the GIXS formula.

The 2D pattern of the CHCl_3 -annealed PHIC-PLLA film and the scattering profiles along the α_f and $2\theta_f$ directions were shown in Figures 6.3a-6.3d. The in-plane profile showed periodic scattering peaks at $2\theta_f = 0.195^\circ$ and 0.384° , agreeing with d-spacing (d_s) = 33.4 nm (Figure 6.3d). The 2D feature and scattering profiles results indicated that the PHIC-PLLA film formed a vertically oriented lamellar structure. The in-plane profiles could be satisfactorily fitted using the GIXS formula for the three layer lamellar structural model. The structural parameters from the GIXS fitting were obtained and reported in Table 6.2. The vertical lamellar PHIC-PLLA structure presented long period $L = 32.7$ nm, composed of PLLA phase layer thickness (highly dense layer) $l_1 = l_{\text{PLLA}} = 10.2$ nm, interfacial layer thickness $l_2 = l_i = 2.2$ nm, and PHIC phase layer thickness (less dense layer) $l_3 = l_{\text{PHIC}} = 18.1$ nm. The positional distortion factor of this lamellar structure was small $g = 0.18$. The orientation angle $\bar{\varphi}_1 = 90^\circ$ (the mean polar angle $\bar{\varphi}_1$ between the orientation vector \mathbf{n}_1 of the horizontal lamellar structure and the out-of-plane direction of the film was 0°), standard deviation $\sigma_{\varphi_1} = 12.0^\circ$, and second-order orientation factor $O_{s,1} = -0.437$. By of the horizontal lamellar structure and the out-of-plane direction of the film was 0° , standard deviation $\sigma_{\varphi_1} = 12.0^\circ$, and second-order orientation factor $O_{s,1} = -0.437$. The 2D simulation pattern of the PHIC-PCL was constructed as shown in Figure 6.3e and found agreement with the experimental data.

The out-of-plane profile of the PHIC-PLLA displayed a very weak broad scattering peak at $0.25\text{--}0.70^\circ$ (Figure 6.3e), indicating that a small number of poorly ordered horizontal conformation appeared in the PHIC-PLLA film.

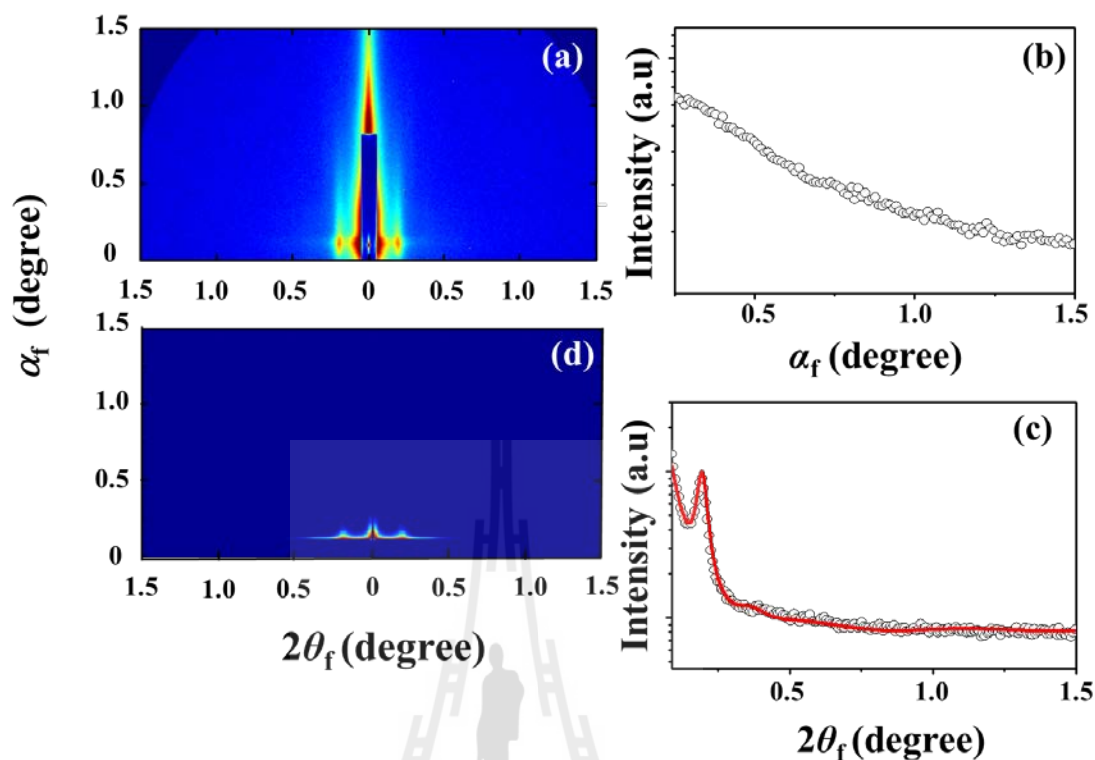


Figure 6.3 2D GISAXS pattern of CHCl_3 -annealed PHIC-PLLA film (approximate 75 nm thick) measured at room temperature using an X-ray beam ($\lambda = 0.1140$ nm); (a) measured with $\alpha_i = 0.110^\circ$ at a sample-to-detector distance (SDD) of 2,917 mm; (b) out-of-plane scattering profile extracted from the data in (a) along the α_f direction at $2\theta_f = 0.070^\circ$; (c) in-plane scattering profile extracted from the data in (a) along the $2\theta_f$ direction at $\alpha_f = 0.140^\circ$ where the black circular symbols are the measured data, and the red solid lines were obtained by fitting the data using the GIXS formula; (d) 2D scattering image reconstructed from the structural parameters in Table 6.2 using the GIXS formula derived for lamellar structure model.

The 2D GISAXS data of the CHCl_3 -annealed PHIC-PLLA_{2,3} displayed similar pattern as the CHCl_3 -annealed PHIC-PLLA, as shown in Figures 6.4a and 6.5a, indicating the vertically oriented lamellar structure. Moreover, the scattering profile of the PHIC-PLLA₂ along the in-plane direction presented scattering peaks at $2\theta_f = 0.201^\circ$ and 0.601° , corresponds to $d_s = 32.4$ nm (Figure 6.4d). The out-of-plane profiles also showed weak board peaks at around $\alpha_f = 0.380^\circ$ and 1.038° , corresponds to $d_s = 17.1$ nm (Figure 6.4b). These scattering results supported that the PHIC-PLLA₂ formed horizontal lamellar as a minor structure and vertical lamellar as a major structure. The GIXS formula for the lamellar model was satisfactory fitted on these profiles as shown in Figures 6.4b and 6.4d and revealed the structural dimension length of the PHIC-PLLA₂ as followed. For the vertical lamellar conformation, the long period was found $L = 32.0$ nm with PLLA phase thickness (highly dense layer) $l_1 = l_{\text{PLLA}} = 9.1$ nm, interfacial layer thickness $l_2 = l_i = 2.3$ nm, and PHIC phase thickness (less dense layer) $l_3 = l_{\text{PHIC}} = 18.3$ nm with small value of positional distortion factor $g = 0.15$. The orientation angle $\bar{\varphi}_1 = 90^\circ$ with distribution $\sigma_{\varphi_1} = 11.6^\circ$ and $O_{s,1} = -0.441$. While the horizontal lamellar structure presented long period $L = 14.5$ nm with PLLA phase thickness (highly dense layer) $l_1 = l_{\text{PLLA}} = 4.2$ nm, interfacial layer thickness $l_2 = l_i = 2.3$ nm, and PHIC phase thickness (less dense layer) $l_3 = l_{\text{PHIC}} = 5.5$ nm with high positional distortion factor $g = 0.38$. These structural parameters were listed in Table 6.2. Figure 6.4e showed the simulated image of the PHIC-PLLA₂ created using the same parameters from the GIXS analysis. The simulation was agreed well with the GISAXS data.

Figures 6.5b and 6.5d displayed scattering profiles along the out-of-plane and in-plane directions of the CHCl_3 -annealed PHIC-PLLA₃ film, respectively. Likely, the

in-plane profile presented the scattering peaks at $2\theta_f = 0.292^\circ$ and 0.606° , corresponds to $d_s = 22.3$ nm, indicating vertically oriented lamellar morphology. While the out-of-plane profile displayed a very broad peak at 0.25° – 0.65° , suggesting that a small number of poorly ordered horizontal structure existed in the PHIC-PLLA₃ film. The in-plane and out-of-plane profiles were also successfully fitted with GIXS formula for the lamellar model and their structural parameters were reported in Table 6.2. The 2D reconstructed pattern of the polymer film was created by the GIXS parameters, also presented in Figure 6.4e. Here, the simulated pattern was corresponding to the 2D GISAXS data.

For the PHIC-PLLA₁₋₃ films in thermal annealing, their 2D GISAXS patterns showed similar feature to those of the PHIC-PLLA₁₋₃ films in CHCl₃ annealing, indicating vertically oriented lamellar structure formed. The 2D data and scattering profiles of the thermal-annealed PHIC-PLLA film were shown in Figures 6.6a and 6.6b-6.6c, respectively. The in-plane profile displayed scattering peaks at $2\theta_f = 0.220^\circ$, corresponds to $d_s = 31.3$ nm and second peak could not be discernible (Figure 6.6c). The in-plane profile was successfully fitted by GIXS formula for the lamellar model (Figure 6.6c). The fitted parameters were reported in Table 6.2. The GIXS analysis revealed that the long period of the PHIC-PLLA vertical lamellar structure was 30.5 nm, composed of PLLA phase thickness (highly dense layer) $l_1 = l_{PCL} = 8.2$ nm, interfacial layer thickness $l_2 = l_i = 2.2$ nm, and PHIC phase thickness (less dense layer) $l_3 = l_{PHIC} = 17.9$ nm. The distortion factor of the PHIC-PLLA structure was observed to be 0.25 (= g). The angle and distribution of the PHIC-PLLA were found at $\bar{\varphi}_1 = 90^\circ$ and quite high $\sigma_{\varphi_1,90} = 15.9^\circ$ with $O_{s,1,90} = -0.393$. The 2D reconstructed pattern was also matched with the experimental data as shown in Figure

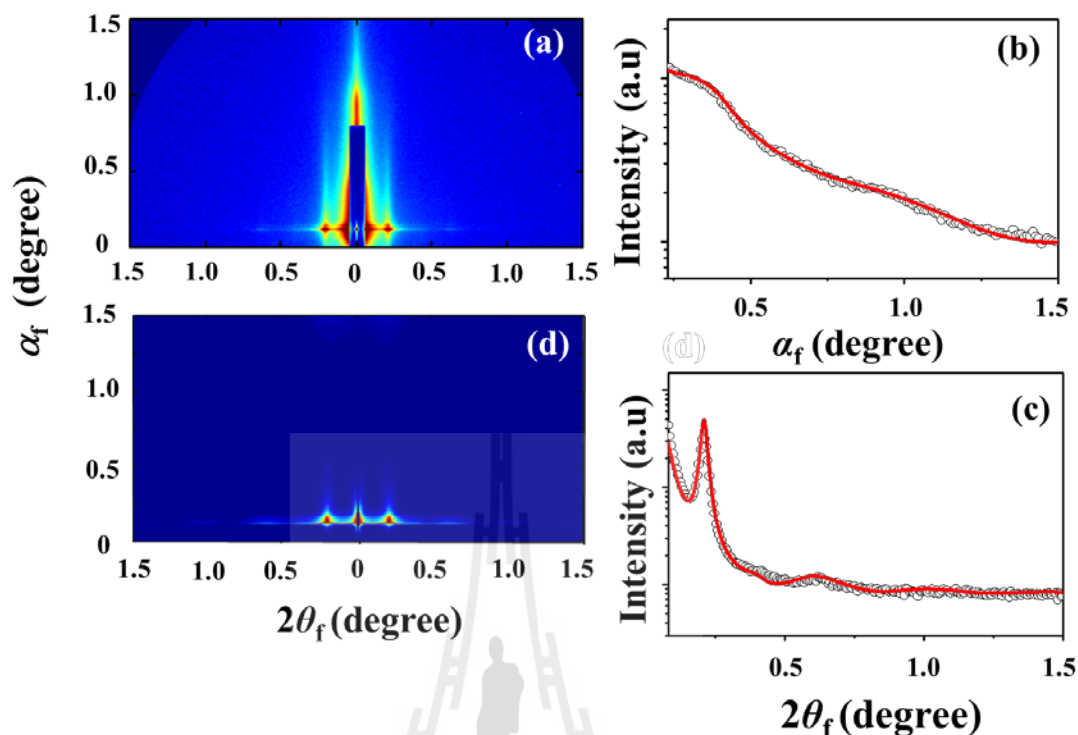


Figure 6.4 2D GISAXS pattern of toluene-annealed PHIC-PLLA₂ film (approximate 75 nm thick) measured at room temperature using an X-ray beam ($\lambda = 0.1140$ nm); (a) measured with $\alpha_i = 0.110^\circ$ at SDD = 2,917 mm; (b) out-of-plane scattering profile extracted from the data in (a) along the α_f direction at $2\theta_f = 0.070^\circ$ where the black circular symbols are the measured data, and the red solid lines were obtained by fitting the data using the GIXS formula; (c) in-plane scattering profile extracted from the data in (a) along the α_f direction at $\alpha_f = 0.140^\circ$ where the black circular symbols are the measured data, and the red solid lines were obtained by fitting the data using the GIXS formula; (d) 2D scattering image reconstructed from the structural parameters in Table 6.2 using the GIXS formula derived for lamellar structure model.

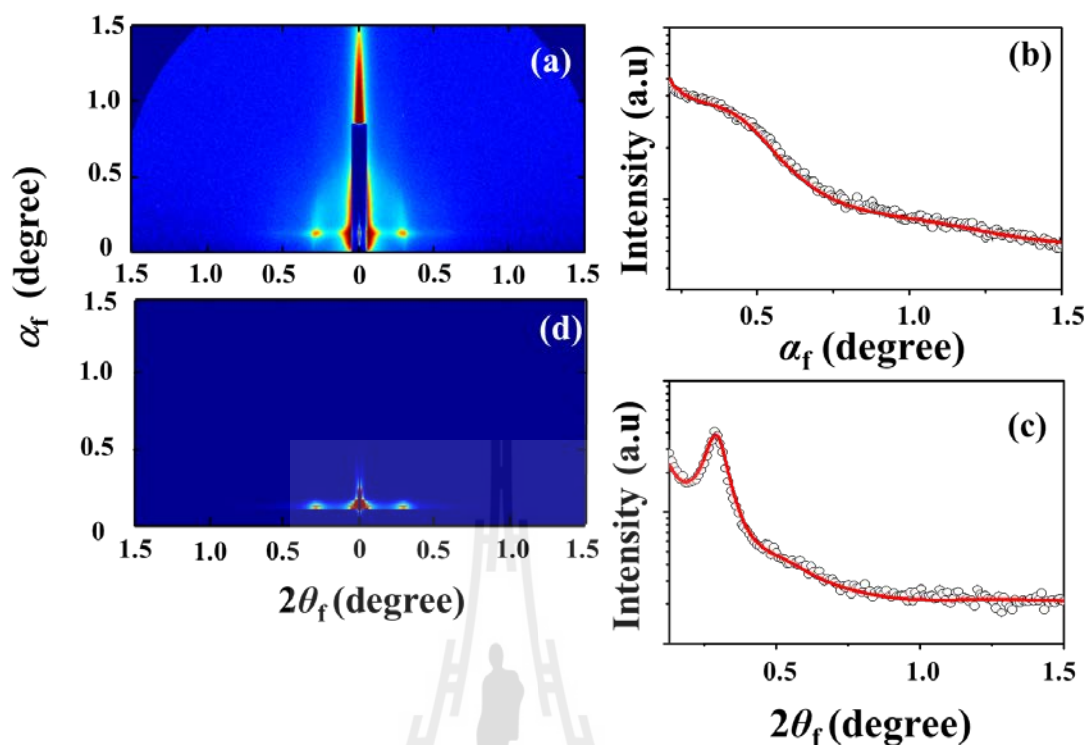


Figure 6.5 2D GISAXS pattern of toluene-annealed PHIC-PLLA₃ film (approximate 75 nm thick) measured at room temperature using an X-ray beam ($\lambda = 0.1140$ nm); (a) measured with $\alpha_i = 0.110^\circ$ at SDD = 2,917 mm; (b) out-of-plane scattering profile extracted from the data in (a) and (b) along the α_f direction at $2\theta_f = 0.070^\circ$; (c) in-plane scattering profile extracted from the data in (a) and (b) along the $2\theta_f$ direction at $\alpha_f = 0.140^\circ$ where the black circular symbols are the measured data, and the red solid lines were obtained by fitting the data using the GIXS formula; (d) 2D scattering image reconstructed from the structural parameters in Table 6.2 using the GIXS formula derived for lamellar structure model.

6.6e. Since the out-of-plane profile displayed weak broad peak at $0.25\text{--}0.65^\circ$ (Figure 6.6b), the very small number of poorly ordered horizontal structure also existed in the PHIC-PLLA film.

The 2D GISAXS patterns of the thermal-annealed PHIC-PLLA_{2,3} films were shown in Figures 6.7a and 6.8a, respectively. The in-plane profiles presented scattering peaks at $2\theta_f = 0.228^\circ$ and 0.673° , agreeing with $d_s = 30.2$ nm for the PHIC-PLLA₂ and $2\theta_f = 0.301^\circ$, corresponding to $d_s = 23.0$ nm for the PHIC-PLLA₃. We applied GIXS formula for the lamellar model on the in-plane profiles as shown in Figures 6.7c and 6.8c. The GIXS structural and orientation parameters were summarized and listed in Table 6.2. Again, the 2D simulated patterns of the PHIC-PLLA_{2,3} created by their structural parameters corresponded well with the experiment data. Moreover, the out-of-plane profiles displayed very weak broad peak at $0.25^\circ\text{--}0.65^\circ$ for the PHIC-PLLA₂ (Figure 6.7b) and at $0.30^\circ\text{--}0.65^\circ$ for the PHIC-PLLA₃ (Figure 6.8b). The poorly ordered minor horizontal structure formed in the PHIC-PLLA_{2,3} film.

According to the preceding GISAXS analysis, the PHIC-PLLA₁₋₃ films under CHCl₃ annealing and heat up at temperature approximately 130°C for 24 hrs. revealed phase separation PHIC and PLLA with higher thickness in the PHIC domain, thereby forming predominant vertically oriented lamellar structures for the CHCl₃-annealed PHIC-PLLA₁₋₃ slightly depended on the PLLA arms numbers present. While the molecules of the thermal-annealed PHIC-PLLA₁₋₃ films also formed mainly vertical lamellar structures regardless of PLLA arms numbers present. Although the thermal process reduced the horizontal structure and tried to make a well-organized structure such as vertically lamellar structure formed in the PHIC-PLLA₁₋₃, it reduced

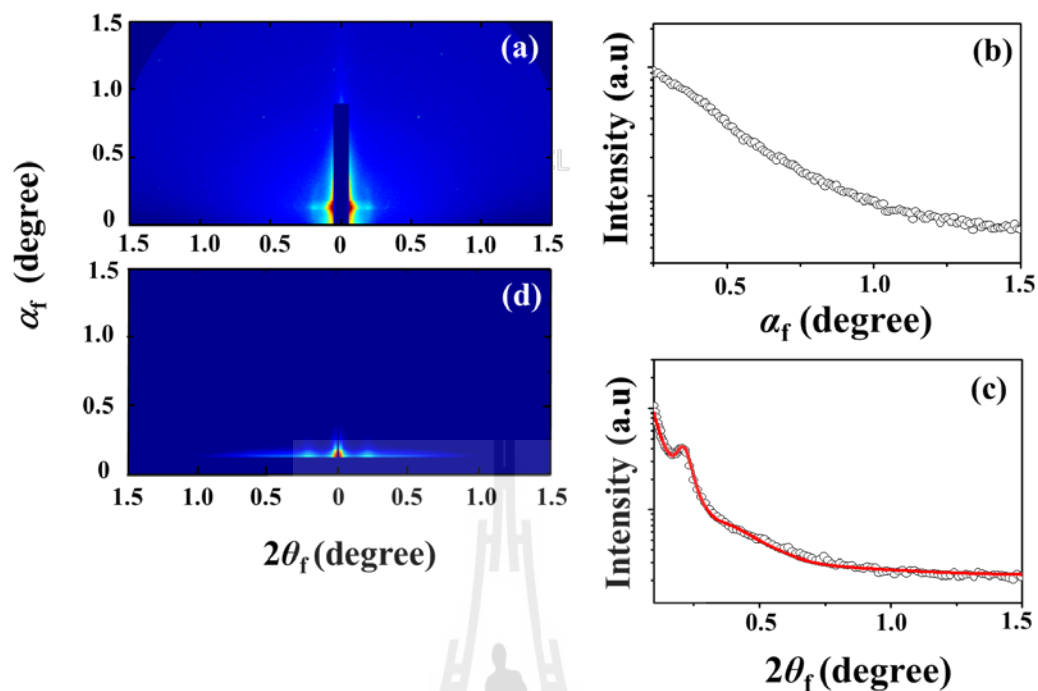


Figure 6.6 2D GISAXS pattern of thermal annealing on PHIC-PLLA film (approximate 75 nm thick) measured at room temperature using an X-ray beam ($\lambda = 0.1210$ nm); (a) measured with $\alpha_i = 0.140^\circ$ at a sample-to-detector distance (SDD) 2,917 mm; (b) out-of-plane scattering profile extracted from the data in (a) along the α_f direction at $2\theta_f = 0.070^\circ$; (c) in-plane scattering profile extracted from the data in (a) along the $2\theta_f$ direction at $\alpha_f = 0.150^\circ$ where the black circular symbols are the measured data, and the red solid lines were obtained by fitting the data using the GIXS formula; (d) 2D scattering image reconstructed from the structural parameters in Table 6.4 using the GIXS formula derived for lamellar structure model.

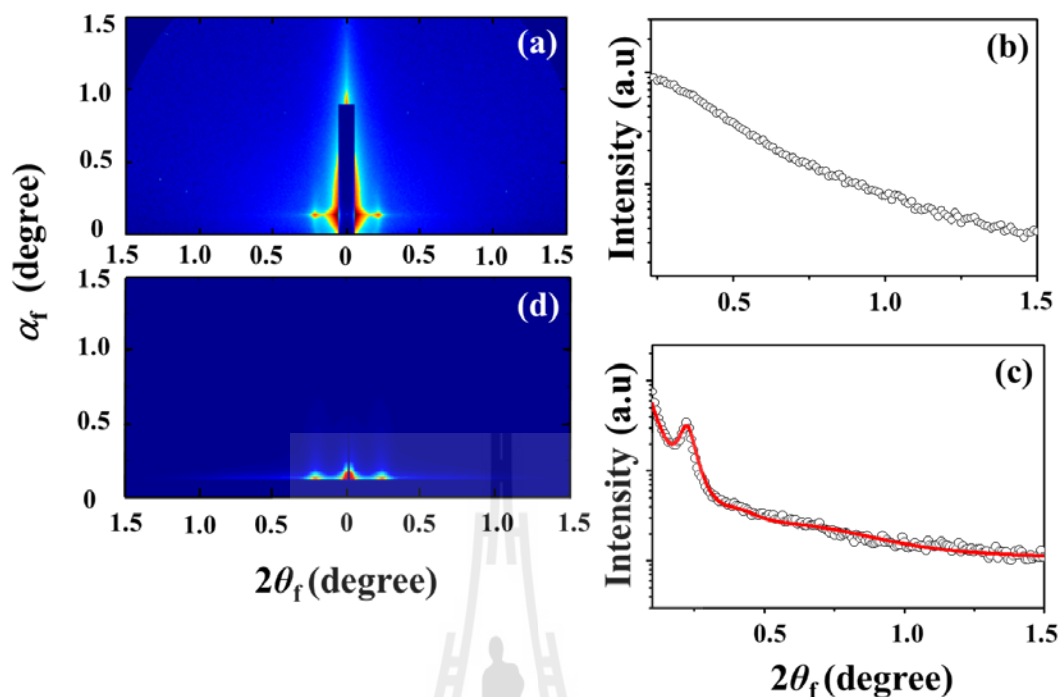


Figure 6.7 2D GISAXS pattern of thermal annealing on PHIC-PLLA₂ film (approximate 75 nm thick) measured at room temperature using an X-ray beam ($\lambda = 0.1210$ nm); (a) measured with $\alpha_i = 0.140^\circ$ at SDD = 2,917 mm; (b) out-of-plane scattering profile extracted from the data in (a) along the α_f direction at $2\theta_f = 0.070^\circ$; (c) in-plane scattering profile extracted from the data in (a) along the $2\theta_f$ direction at $\alpha_f = 0.150^\circ$ where the black circular symbols are the measured data, and the red solid lines were obtained by fitting the data using the GIXS formula; (d) 2D scattering image reconstructed from the structural parameters in Table 6.4 using the GIXS formula derived for lamellar structure model.

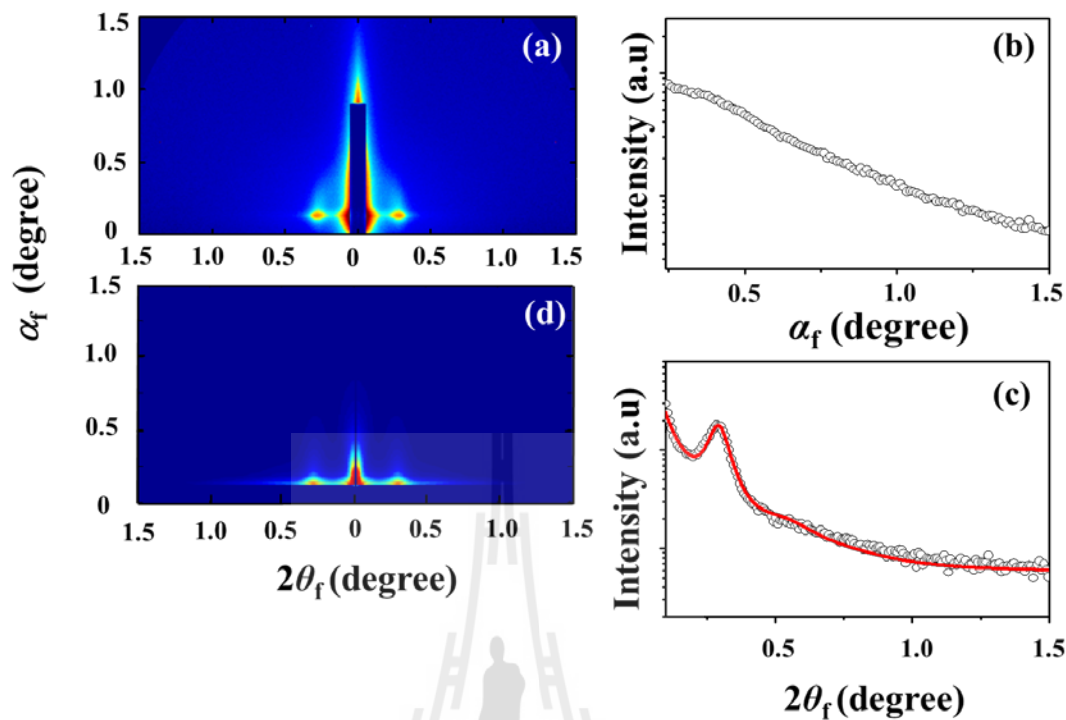


Figure 6.8 2D GISAXS pattern of thermal annealing on PHIC-PLLA₃ film (approximate 80 nm thick) measured at room temperature using an X-ray beam ($\lambda = 0.1210$ nm); (a) measured with $\alpha_i = 0.140^\circ$ at SDD = 2,917 mm; (b) out-of-plane scattering profile extracted from the data in (a) along the α_f direction at $2\theta_f = 0.070^\circ$; (c) in-plane scattering profile extracted from the data in (a) along the $2\theta_f$ direction at $\alpha_f = 0.150^\circ$ where the black circular symbols are the measured data, and the red solid lines were obtained by fitting the data using the GIXS formula. (d) 2D scattering image reconstructed from the structural parameters in Table 6.4 using the GIXS formula derived for lamellar structure model.

Table 6.2 Nanostructural parameters of the CHCl_3 - and thermal-annealed thin films of the PHIC and PLLA homopolymers and PHIC- $\text{PLL}_{A_{1-3}}$ miktoarm star polymers, determined by GISAXS analysis.

Polymer thin film	Nanostructure (observed)	L^a (nm)	ℓ_1^b (nm)	ℓ_2^c (nm)	ℓ_3^d (nm)	σ_1^e (nm)	σ_2^f (nm)	g^g	$\bar{\varphi}_1^h$ (deg.)	$\sigma_{\varphi_1}^i$ (deg.)	O_s^j
CHCl ₃ -annealed films											
PHIC	not identified										
PLLA	not identified										
PHIC- PLL_A	vertical lamellae	32.6	9.6	2.2	18.6	2.0	0.6	0.18	90	12.0	-0.437
PHIC- PLL_{A_2}	horizontal ^k lamellae	14.5	4.2	2.3	5.7	1.7	0.7	0.38	0		
	vertical lamellae	32.0	9.1	2.3	18.3	1.8	0.5	0.15	90	11.6	-0.441
PHIC- PLL_{A_3}	horizontal ^k lamellae	13.0	4.0	2.3	4.4	1.9	0.7	0.39	0		
	vertical lamellae	21.0	6.2	2.4	10.0	1.3	0.9	0.23	90	9.2	-0.462
Thermal-annealed films											
PHIC	not identified										
PLLA	horizontal lamellae	17.0	4.0	1.6	9.8	1.5	0.6	0.38	0	6.2	0.983
PHIC- PLL_A	vertical lamellae	30.5	8.2	2.2	17.9	2.7	0.8	0.25	90	15.9	-0.393
PHIC- PLL_{A_2}	vertical lamellae	29.4	7.5	2.3	17.3	2.0	0.8	0.23	90	9.7	-0.458
PHIC- PLL_{A_3}	vertical lamellae	21.9	6.6	2.4	10.5	1.8	1.0	0.25	90	8.8	-0.465

^a Long period of lamellar structure.

^b Thickness of more dense layer (i.e., PLLA arm phase: ℓ_{PLLA}) in the lamellar structured PHIC- PLL_{A_m} films.

^c Thickness of interfacial layer (ℓ_i) between the highly dense and less dense layers in lamellar structure.

^d Thickness of less dense layer (i.e., PHIC arm phase: ℓ_{PHIC}) in the lamellar structured PHIC- PLL_{A_m} films.

^e Standard deviation for the more dense layer in lamellar structure.

^f Standard deviation for the interfacial layer in lamellar structure.

^g Paracrystal distortion factor along the direction parallel to the long period of lamellar structure.

^h Mean value of the polar angle φ_1 (i.e., orientation angle) between the orientation vector \mathbf{n}_1 (which is set along the direction parallel to the long period of lamellar structure) and the out-of-plane of the film.

ⁱ Standard deviation for the orientation angle φ_1 of lamellar structure.

^j Second order orientation factor.

^k Horizontal lamellar structure was formed in a very minor fraction.

the long-range order of the lamellar structure.

Moreover, the crystal structure and orientation of the PHIC-PLLA₁₋₃ and the PHIC and PLLA films under CHCl₃ and thermal annealing were examined with GIWAXS technique. Due to the crystal structure and orientation of the CHCl₃-annealed PHIC had already been characterized by GIWAXS as present in Chapter V, the structural parameters that obtained from the GIXS analyses were the same and listed in Table 6.3. The 2D GIWAXS data of the CHCl₃-annealed PHIC and its scattering profiles were shown in Figures 6.9a and 6.9f-6.9g, respectively. The PHIC profiles showed the periodic peaks along α_f direction at $\alpha_f = 4.10^\circ$, 8.18° , and 12.16° with d_s value was 1.65 nm (Figure 6.9f) and along $2\theta_f$ direction at $2\theta_f = 4.10^\circ$ ($d_s = 1.65$ nm), $2\theta_f = 10.04^\circ$ ($d_s = 0.67$ nm), $2\theta_f = 13.52^\circ$ ($d_s = 0.50$ nm), and $2\theta_f = 15.14^\circ$ ($d_s = 0.45$ nm) (Figure 6.9g).

In addition, the GIXS formula for the multibilayer structure mode was applied on the PHIC profiles as shown in Figures 6.9f and 6.9g. The PHIC crystal structure presented that the long period of lamellar bilayer (L) was 1.65 nm, consisting of dense layer $\ell_1 = 0.76$ nm and less dense layer $\ell_2 = 0.89$ nm. The dense layer represented polymer backbones and inner parts of n -hexyl bristles while less dense layer presented the outer part of n -hexyl bristles. The n -hexyl bristles were observed to be totally extended and packed laterally with no interdigitation, since the maximum length of extended n -hexyl bristle is 0.83 nm. The polymer backbones also packed laterally. The mean inter-distance of n -hexyl bristles, having the same bristles position along

different backbones, was about 0.67 nm ($= d_1$). Additionally, the mean inter-distance of n -hexyl bristles along the same backbone ($= d_2$) and nearest neighboring n -hexyl bristles ($= d_3$) were 0.50 nm and 0.45 nm, respectively. The position distribution of the lamellar bilayer was small ($g_{dL} = 0.050$) in the out-of-plane direction but showed high distribution of n -hexyl bristles in the in-plane direction ($g_{d1} = 0.100$, $g_{d2} = 0.100$, and $g_{d3} = 0.110$). Furthermore, the PHIC orientation angle was found $\bar{\phi}_2 = 0^\circ$ with distribution $\sigma_{\phi_2,0} = 3.70^\circ$ and $O_{s,2,0} = 0.994$. Here, $\bar{\phi}_2$ is the mean polar angle between the orientation vector \mathbf{n}_2 of the horizontal multibilayer structure and the out-of-plane direction of the film. The relative volume fraction between horizontal and vertical PHIC crystal structure ($\phi_{h,2}/\phi_{v,2}$) was found at 100/0, supporting that the PHIC structure formed only horizontally oriented multibilayer structure.

For CHCl_3 -annealed PLLA homopolymer film, the 2D data and scattering profiles suggested that a crystal structure could form in the PLLA film, as shown in Figures 6.9b and 6.9f-6.9g respectively. The scattering peaks along the out-of-plane direction were obtained at $\alpha_f = 4.39^\circ$ ($d_s = 1.46$ nm) corresponding to reflection plane {002}. The scattering peaks along the in-plane direction was observed at $2\theta_f = 15.43^\circ$ ($d_s = 0.42$ nm) corresponding to reflection plane {204}. The other peaks appeared in both directions at $\alpha_f = 2\theta_f = 8.63^\circ$ ($d_s = 0.74$ nm) and at $\alpha_f = 2\theta_f = 10.47^\circ$ ($d_s = 0.61$ nm) agreeing with reflection plane {004} and {010}, respectively, at $\alpha_f = 2\theta_f = 11.83^\circ$ ($d_s = 0.54$ nm) could be assigned to the {200} and {110}, and at $\alpha_f = 2\theta_f = 11.83^\circ$ ($d_s = 0.54$ nm) corresponding to reflection plane {203}. These peaks supported that the crystal conformation of the PLLA film formed an orthorhombic lattice with space group $P2_12_12_1$ (Pan *et al.*, 2008; Zhang *et al.*, 2005). Therefore, the GIXS formula for an orthorhombic lattice model, explained in the Chapter IV, was considered. The PLLA

profiles were satisfactory fitted by the GIXS model as shown in Figures 6.9f and 6.9g, and the fitted parameters were listed in Table 6.3. The GIXS results presented the orthorhombic cell edge length as $a = 1.08$ nm, $b = 0.61$ nm, and $c = 2.90$ nm with positional distortion factors $g = 0.110$. The PLLA orientation angle, $\bar{\varphi}_3$, revealed at 0° ($=\bar{\varphi}_3$) and 90° ($=\bar{\varphi}_3$). Where $\bar{\varphi}_3$ defined as the mean polar angle between the orientation vector \mathbf{n}_3 of the horizontal orthorhombic lattice and the out-of-plane direction of the film. The horizontal orthorhombic structural distribution was $\sigma_{\varphi_3,0} = 10.1$ and $O_{s,3,0} = 0.955$ while the vertical distribution presented $\sigma_{\varphi_3,90} = 21.0$ and $O_{s,3,90} = -0.323$. The volume fraction of vertical and horizontal structure ($\phi_{v,3}/\phi_{h,3}$) was about 74/26, indicating that the majority of PLLA crystal was vertically oriented orthorhombic system.

For the thermal annealing case of the PLLA film, the 2D GIWAXS pattern and profiles from the thermal-annealed PLLA presented more clearly feature and stronger peaks than those from the CHCl_3 annealed case as presented in Figures 6.10a and 6.10e-6.10f, respectively. The scattering profiles of the PLLA revealed peaks at $\alpha_f = 4.46^\circ$ ($d_s = 1.44$ nm) agreeing with reflection plane $\{002\}$, at $\alpha_f = 2\theta_f = 8.93^\circ$ ($d_s = 0.72$ nm) and at $\alpha_f = 2\theta_f = 10.51^\circ$ ($d_s = 0.61$ nm) agreeing with reflection plane $\{004\}$ and $\{010\}$, respectively. The other peaks, were obtained at $\alpha_f = 2\theta_f = 11.84^\circ$ ($d_s = 0.54$ nm), could be assigned to the $\{200\}$ and $\{110\}$, at $\alpha_f = 2\theta_f = 13.41^\circ$ ($d_s = 0.48$ nm) in corresponding to reflection plane $\{203\}$, at $2\theta_f = 14.68^\circ$ ($d_s = 0.44$ nm) and at $2\theta_f = 15.54^\circ$ ($d_s = 0.41$ nm) in corresponding to reflection plane $\{204\}$ and $\{210\}$, respectively. Moreover, the small peak at $\alpha_f = 16.48^\circ$ ($d_s = 0.38$ nm), could be assigned to $\{213\}$. These peaks characteristic also indicated that the orthorhombic

crystal lattice with space group $P2_12_12_1$ (Sasaki, and Asakura, 2003) was formed in the PLLA film. The scattering profiles were fitted by GIXS formula for the orthorhombic lattice model as shown in Figures 6.10e-6.10f. The structural and orientation parameters were listed in Table 6.4. The PLLA crystal structure formed horizontally and vertically oriented orthorhombic unit cell with a dimension length $a = 1.08$ nm, $b = 0.61$ nm, and $c = 2.88$ nm with positional distortion factors $g = 0.100$. The orientation angle of the orthorhombic structure was obtained at $\bar{\varphi}_3 = 0^\circ$ and 90° . The distribution was $\sigma_{\varphi_3,0} = 8.8$ and $O_{s,3,0} = 0.965$ for the horizontal orthorhombic and $\sigma_{\varphi_3,90} = 19.5$ and $O_{s,3,90} = -0.345$ for the vertical structure. The volume fraction was found higher in vertical orthorhombic structure $\phi_{v,3}/\phi_{h,3} = 78/22$. Although the PLLA crystal morphology formed similarly in both annealing, the PLLA crystal, obtained by heating, presented more stable orthorhombic unit cell, known as α -form crystal (Yang *et al.*, 2014). While the CHCl_3 -annealed PLLA crystal also formed orthorhombic lattice with its polymer side groups were packed looser and more disordered than the α -form crystal, also known as α' -form crystal. The results also indicated that number of PLLA crystal increase during the thermal effect.

Additionally, the 2D GIWAXS patterns and the scattering profiles of the PHIC-PLLA₁₋₃ films under CHCl_3 annealing were presented in Figures 6.9c-6.9e and 6.9f-6.9g, respectively. The PHIC-PLLA_{1,2} revealed crystalline peaks but the PHIC-PLLA₃ did not. Due to the effect of annealing with CHCl_3 for long time (24hrs), the crystal structure of the PHIC-PLLA₃ film disappeared. Moreover, the PHIC-PLLA_{1,2} showed the same crystal conformation as their scattering peak positions were similar. The scattering peaks of the PHIC-PLLA_{1,2} were matched with those peaks from the PHIC and the PLLA because the star polymers structure consisted of the PHIC and PLLA

domains. Hence, we used GIXS formula for the multibilayer model and the orthorhombic lattice model to analyze the PHIC-PLLA_{1,2} data. The PHIC-PLLA_{1,2} profiles were successfully fitted (Figures 6.9f and 6.9g) and their structural and orientation parameters were listed in Table 6.3. The GIXS results suggested that the crystal edge lengths of the PLLA phase revealed equally to those values of the PLLA homopolymer. However, the lengths of the PHIC phase have been obtained slightly longer than the lengths of the PHIC homopolymer. The orientation angle of the PHIC phase was observed to be 0° ($=\overline{\varphi_2}$) and 90° ($=\overline{\varphi_2}$) indicating a mixed between horizontal with standard deviation ($\sigma_{\varphi_2,0}, O_{s,2,0}$) and vertical multibilayer structure with standard deviation ($\sigma_{\varphi_2,90}, O_{s,2,90}$), as well as their volume ratio ($\phi_{h,2}/\phi_{v,2}$). According the volume ratio, the majority of the PHIC domain structure in the PHIC-PLLA_{1,2} was horizontal multibilayer structure. For the PLLA phase, it showed only 0° ($=\overline{\varphi_3}$) or horizontal orthorhombic crystal lattice with standard deviation ($\sigma_{\varphi_3,0}, O_{s,3,0}$) and volume fraction ($\phi_{v,3}/\phi_{h,3}$).

The crystal structure of the PHIC-PLLA₁₋₃ films under thermal annealing was studied by GIWAXS. The 2D GIWAXS patterns and profiles from thermal annealing also presented more clearly feature and stronger peaks than those from the CHCl₃-annealed case as, undeniable in the PHIC-PLLA₃ films as presented in Figures 6.10b-6.10d and 6.10e-6.10f. These results also supported that the PLLA crystal structure increased by heating. Interestingly, the crystal structure of the CHCl₃-annealed PHIC-PLLA₃ can be recovered by the thermal process.

Figures 6.10b-6.10d and 6.10e-6.10f represented GIWAXS data and scattering profiles of thermal annealing PHIC-PLLA₁₋₃ films. The PHIC-PLLA₁₋₃ peaks matched

with those peaks from the PHIC and PLLA due to the crystallisable of PHIC and PLLA phases, respectively. We used the result from the CHCl_3 -annealed PHIC to compare with those of the PHIC phase from the thermal annealing PHIC-PLLA₁₋₃, since the PHIC structure is stable in thermal annealing. The crystal structure of the PHIC-PLLA₁₋₃ were observed both structures, such as multibilayer conformation (PHIC domain) and orthorhombic system (PLLA domain), regardless of PLLA arm numbers. The GIXS formular for the multibilayer plus orthorhombic model was used to fit the profiles as shown in Figures 6.13e-6.13f. Additionally, the PHIC-PLLA₁₋₃ structure and orientation parameters were reported in Table 6.4. The orthorhombic lattice edge lengths of the PLLA phase and the multibilayer dimension lengths of the PHIC phase were obtained similarly to those numbers of the PLLA and the PHIC, respectively. Moreover, the PHIC domain orientation showed horizontal lamellar bilayer conformation ($\overline{\varphi}_2 = 0^\circ$) with distribution ($\sigma_{\varphi_2,0}, O_{s,2,0}$) and vertical lamellar bilayer structures ($\overline{\varphi}_2 = 90^\circ$) with distribution ($\sigma_{\varphi_2,0}, O_{s,2,90}$), as well as the volume fraction of the horizontal and vertical multibilayer structure ($\phi_{h,2}/\phi_{v,2}$). The majority structure due to PHIC phase was horizontal multibilayer for the PHIC-PLLA_{1,2} but vertical multibilayer for the PHIC-PLLA₃. The PLLA phase formed horizontal and vertical orthorhombic structures with the distributions ($\sigma_{\phi_5,0}, O_{s,5,0}$) and ($\sigma_{\phi_5,90}, O_{s,5,90}$), respectively. Also, the volume ratio between vertical and horizontal were reported as $\phi_{v,5}/\phi_{h,5}$ and presented that the major PLLA phase structure of the PHIC-PLLA₁₋₃ was vertical orthorhombic lattice.

From the quantitative GIXS analysis of the PHIC-PLLA₁₋₃ films and the PHIC and PCL films, annealed by CHCl_3 and thermal, the morphology and structural ordering of these polymers films were proposed as in Figures 6.11-6.13.

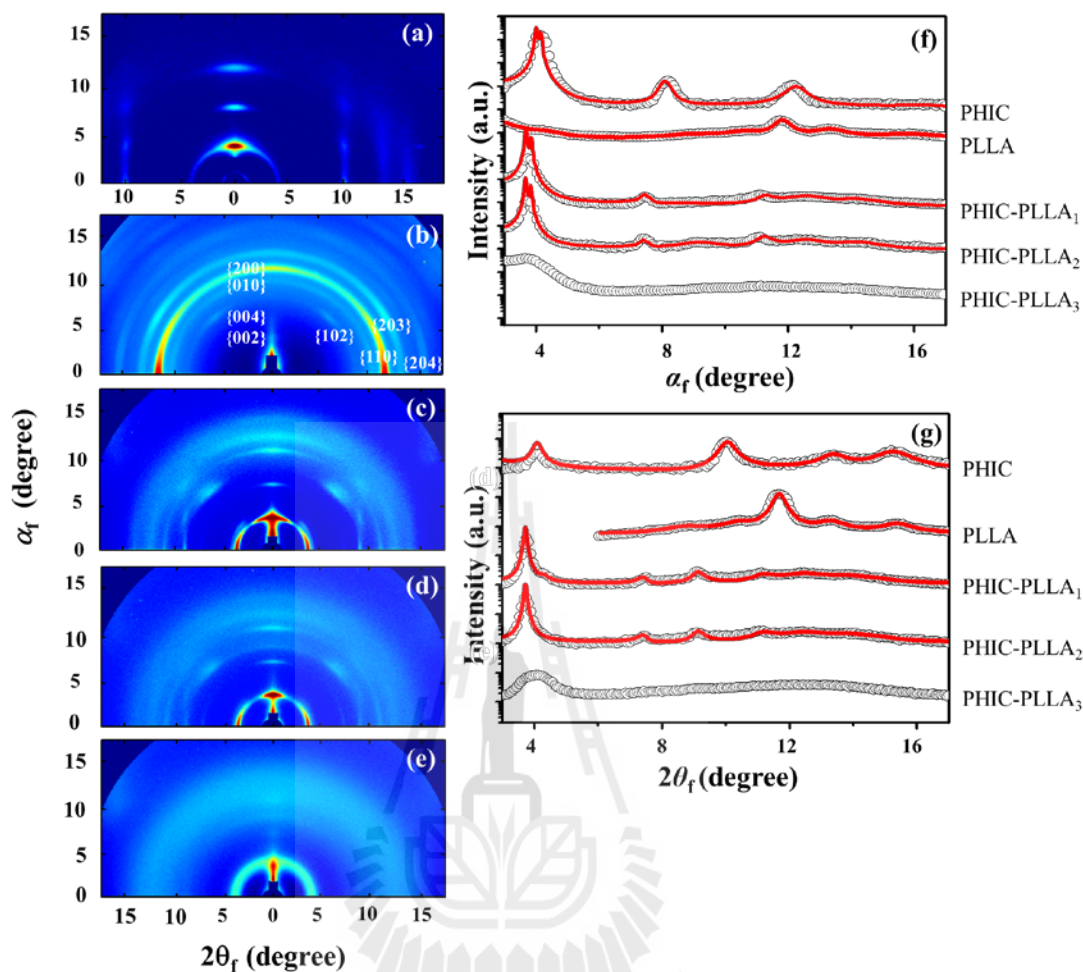


Figure 6.9 2D GIWAXS pattern of CHCl_3 -annealed PHIC and PLLA homopolymer (approximate 80 nm thick) and the star polymers films (approximate 75 nm thick) deposited on silicon substrates, measured at room temperature using an X-ray beam ($\lambda = 0.1120$ nm and 0.1180 nm) $\alpha_i = 0.160^\circ$ at $\text{SDD} = 240$ mm; (a) PHIC; (b) PLLA; (c) PHIC-PLLA; (d) PHIC-PLLA₂; (e) PHIC-PLLA₃; (f) out-of-plane scattering profiles extracted from the data in (a–e) along the α_f direction at $2\theta_f = 0.0^\circ$; (g) in-plane scattering profiles extracted from the data in (a–e) along the $2\theta_f$ direction at $\alpha_f = 0.280^\circ$. In (f) and (g), the black circular symbols are the measured data, and the red solid lines were obtained by fitting the data using the GIXS formulae.

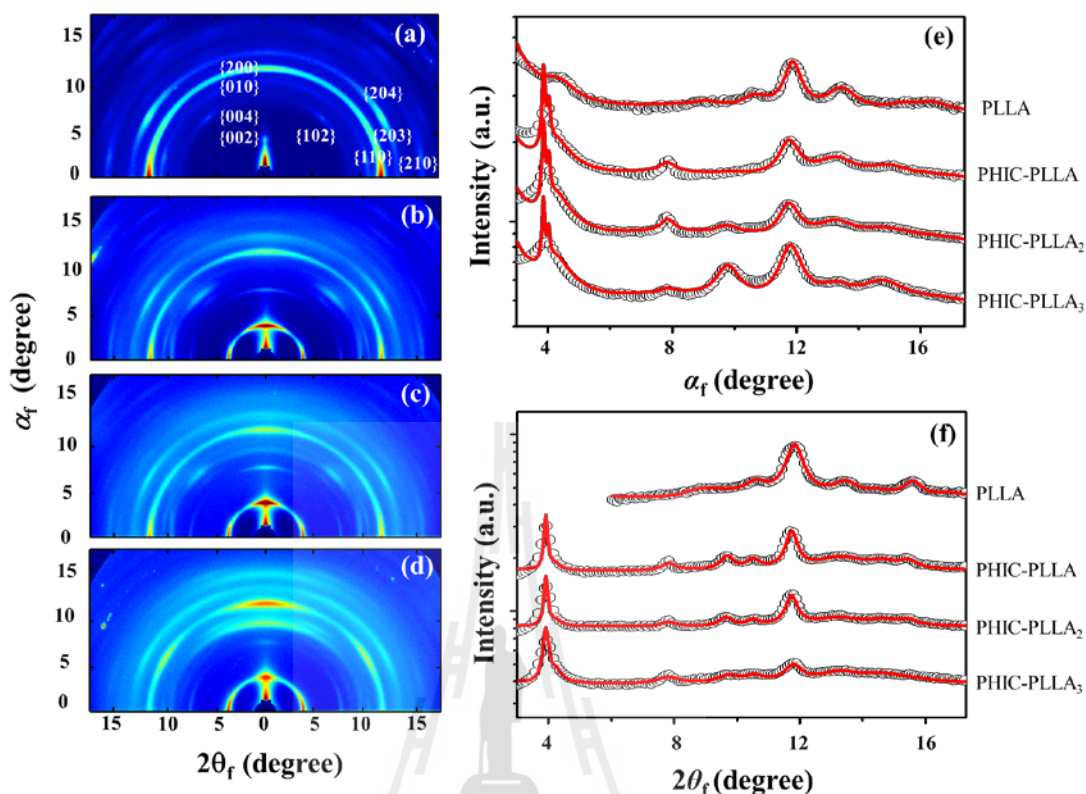


Figure 6.10 2D GIWAXS pattern of thermal annealing on PLLA homopolymer (approximate 80 nm thick) and the PHIC-PLLA₁₋₃ films (approximate 75 nm thick) measured at room temperature using an X-ray beam ($\lambda = 0.1120$ nm) $\alpha_i = 0.160^\circ$ at SDD = 240 mm; (a) PLLA; (b) PHIC-PLLA; (c) PHIC-PLLA₂; (d) PHIC-PLLA₃; (e) out-of-plane scattering profiles extracted from the data in (a–d) along the α_f direction at $2\theta_f = 0.0^\circ$; (f) in-plane scattering profiles extracted from the data in (a–d) along the $2\theta_f$ direction at $\alpha_f = 0.290^\circ$. In (e) and (f), the black circular symbols are the measured data, and the red solid lines were obtained by fitting the data using the GIXS formulae.

Table 6.3 Structural parameters of the CHCl_3 -annealed thin films of the PHIC and PLLA homopolymers and PHIC-PLLA₁₋₃ miktoarm star polymers, determined by GIWAXS analysis.

Structural parameter	PHIC	PLLA	PHIC-PLLA	PHIC-PLLA ₂	PHIC-PLLA ₃
d_L^a (nm)	1.65		1.70	1.70	
ℓ_1^b (nm)	0.76		0.78	0.78	
ℓ_2^c (nm)	0.89		0.92	0.92	
d_1^d (nm)	0.67		0.68	0.68	
d_2^e (nm)	0.50		0.51	0.51	
d_3^f (nm)	0.45		0.45	0.45	
g_{dL}^g (nm)	0.050		0.069	0.069	
g_{d1}^h (nm)	0.100		0.130	0.150	
g_{d2}^i (nm)	0.100		0.140	0.140	
g_{d3}^j (nm)	0.110		0.120	0.130	
φ_2^k (deg.)	0		0	0	
$\sigma_{\varphi_2,0}^l$ (deg)	3.70		5.10	5.40	
$O_{s,2,0}^m$	0.994		0.988	0.987	
φ_2 (deg.)			90	90	
$\sigma_{\varphi_2,90}$ (deg)			12.10	15.40	
$O_{s,2,90}$			-0.436	-0.399	
$\phi_{h,2}/\phi_{v,2}^n$ (v/v)	100/0		62/38	57/43	
a^o (nm)		1.08	1.08	1.08	
b^p (nm)		0.61	0.61	0.61	
c^q (nm)		2.90	2.90	2.90	
g^r		0.110	0.122	0.135	
φ_3^s (deg.)		0	0	0	
$\sigma_{\varphi_3,0}^t$ (deg)		10.1	22.8	21.6	
$O_{s,3,0}^u$		0.955	0.797	0.815	
φ_3 (deg.)		90			
$\sigma_{\varphi_3,90}$ (deg)		21.0			
$O_{s,3,90}$		-0.323			
$\phi_{v,3}/\phi_{h,3}^v$ (v/v)		74/26	0/100	0/100	

Table 6.4 Structural parameters of the thermal-annealed thin films of the PHIC and PLLA homopolymers and PHIC-PLLA₁₋₃ miktoarm star polymers, determined by GIWAXS analysis.

Structural parameter	PLLA	PHIC-PLLA	PHIC-PLLA ₂	PHIC-PLLA ₃
d_L^a (nm)		1.64	1.64	1.64
ℓ_1^b (nm)		0.76	0.76	0.76
ℓ_2^c (nm)		0.88	0.88	0.88
d_1^d (nm)		0.67	0.67	0.67
d_2^e (nm)		0.50	0.50	0.50
d_3^f (nm)		0.45	0.45	0.45
g_{dL}^g (nm)		0.070	0.065	0.085
g_{d1}^h (nm)		0.090	0.100	0.120
g_{d2}^i (nm)		0.120	0.120	0.120
g_{d3}^j (nm)		0.150	0.150	0.150
φ_2^k (deg.)		0	0	0
$\sigma_{\varphi_2,0}^l$ (deg)		7.60	6.20	5.90
$O_{s,2,0}^m$		0.974	0.983	0.984
φ_2 (deg.)		90	90	90
$\sigma_{\varphi_2,90}$ (deg)		11.40	12.00	14.70
$O_{s,2,90}$		-0.443	-0.437	-0.407
$\phi_{h,2}/\phi_{v,2}^n$ (v/v)		70/30	68/32	42/58
a^o (nm)	1.08	1.08	1.08	1.08
b^p (nm)	0.61	0.61	0.61	0.61
c^q (nm)	2.88	2.88	2.88	2.88
g^r	0.100	0.110	0.110	0.115
ϕ_5^s (deg.)	0	0	0	0
$\sigma_{\phi_5,0}^t$ (deg)	8.8	9.2	8.1	7.5
$O_{s,5,0}^u$	0.965	0.962	0.971	0.975
ϕ_5 (deg.)	90	90	90	90
$\sigma_{\phi_5,90}$ (deg)	19.50	17.70	18.40	8.40
$O_{s,5,90}$	-0.345	-0.367	-0.360	-0.468
$\phi_{v,5}/\phi_{h,5}^v$ (v/v)	78/22	76/24	68/33	93/7

^a Long period of the molecular multibilayer PHIC structure.

^b Thickness of more dense layer in the molecular multibilayer PHIC structure.

^c Thickness of less dense layer in the molecular multibilayer PHIC structure.

^d Mean interdistance between the *n*-hexyl bristles of the neighboring polymer chains whose repeat units are matched in position along their backbones.

^e Mean interdistance between the nearest *n*-hexyl bristles along the polymer backbone.

^f Mean interdistance between the *n*-hexyl bristles of the nearest neighboring polymer chains.

^g Paracrystal distortion factor along the direction parallel to the long period of molecular multibilayer structure.

^h Paracrystal distortion factor along *n*-hexyl bristles of the neighboring polymer chains whose repeat units are matched in position along their backbones.

- ⁱ Paracrystal distortion factor along the nearest *n*-hexyl bristles along the polymer backbone.
- ^j Paracrystal distortion factor along the *n*-hexyl bristles of the nearest neighboring polymer chains.
- ^k Mean value of the polar angle φ_2 (i.e., orientation angle) between the orientation vector \mathbf{n}_2 (which is set along the direction parallel to the long period of molecular multilayer PHIC structure) and the out-of-plane of the film.
- ^l Standard deviation for the orientation angle φ_2 of molecular multilayer PHIC structure.
- ^m Second order orientation factor of the molecular multilayer PHIC structure.
- ⁿ Volume fraction ratio of the horizontal and vertical multilayer PHIC structures.
- ^o A unit cell dimension along the *a*-axis of orthorhombic PLLA crystals.
- ^p A unit cell dimension along the *b*-axis of orthorhombic PLLA crystals.
- ^q A unit cell dimension along the *c*-axis of orthorhombic PLLA crystals.
- ^r Paracrystal distortion factor of the PLLA crystal.
- ^s Mean value of the polar angle φ_3 (i.e., orientation angle) between the orientation vector \mathbf{n}_3 (which is set along the direction parallel to the long period of lamellar structure) and the out-of-plane of the film.
- ^t Standard deviation for the orientation angle φ_3 of lamellar structure.
- ^u Second order orientation factor of lamellar PLLA crystal structure.
- ^v Volume fraction ratio of the horizontal and vertical lamellar PLLA crystal structures.

6.4 Conclusion

We have been investigated morphology and structural ordering in thin film form of the rod-coil type PHIC-PLLA₁₋₃ miktoarm star polymers (a rigid rod-like PHIC arm and a flexible coil-like PLLA arm with the number of PLLA arm various from one to three). The total M_n of the PHIC arm approximate 9,600-10,900 g/mol and of the PLLA arms approximate 9,600-10,100 g/mol, such as PHIC(10.3k)-PLLA(9.6k), PHIC(10.9k)-PLLA₂(9.8k), and PHIC(9.6k)-PLLA₃(10.1k), respectively. These polymers were fabricated into pre-clean Si substrate and annealed by CHCl₃ and heating at temperature approximate 130 °C for 24 hrs. Also, the morphology and structural ordering of PHIC and PLLA homopolymer films under CHCl₃ and thermal annealing were studied along the star polymers films.

The studied polymers films have been characterized by GISAXS and GIWAXS techniques. The quantitative GISAXS results suggested that the PHIC-PLLA₁₋₃ films under CHCl₃ and thermal annealing showed a phase-separated of PHIC and PLLA domains that have higher layer thickness in PHIC domain. The CHCl₃-annealed

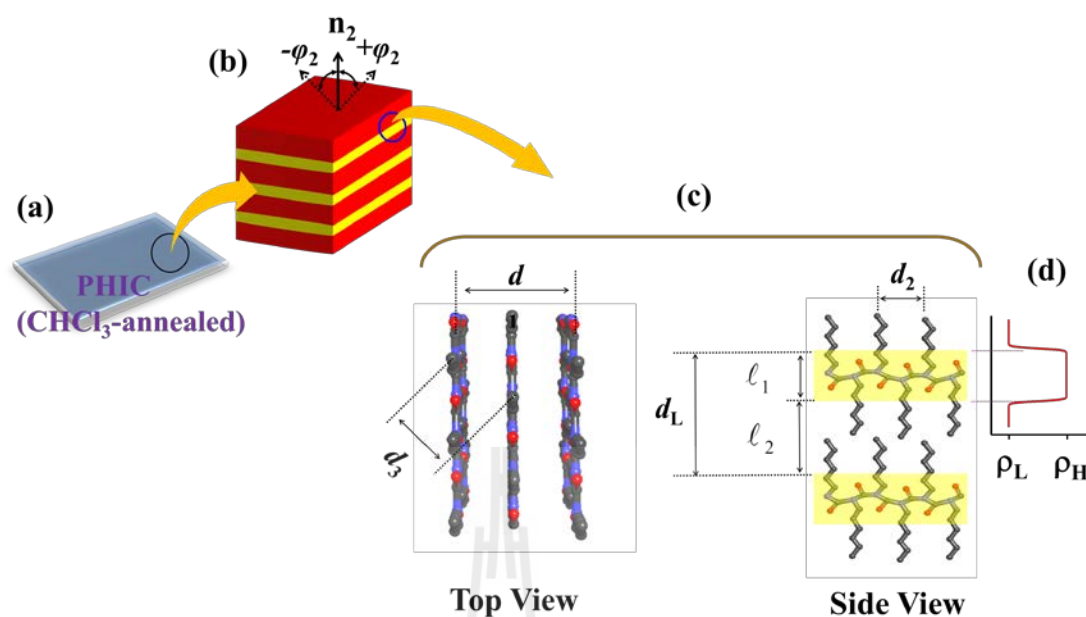


Figure 6.11 Schematic representations of molecular chain conformation in CHCl₃-annealed PHIC thin films (a); (b) horizontal multilayer structure where \mathbf{n}_2 is the orientation vector of the structure model and φ_2 is the polar angle between the \mathbf{n}_2 vector and the out-of-plane of the film; (c) top and side views of molecular chain conformation and packing order with no interdigitation in the structure (b); (d) relative electron density profile along the out-of-plane of the multilayer structure where ρ_L and ρ_H are the relative electron densities of less and highly dense sublayer respectively.

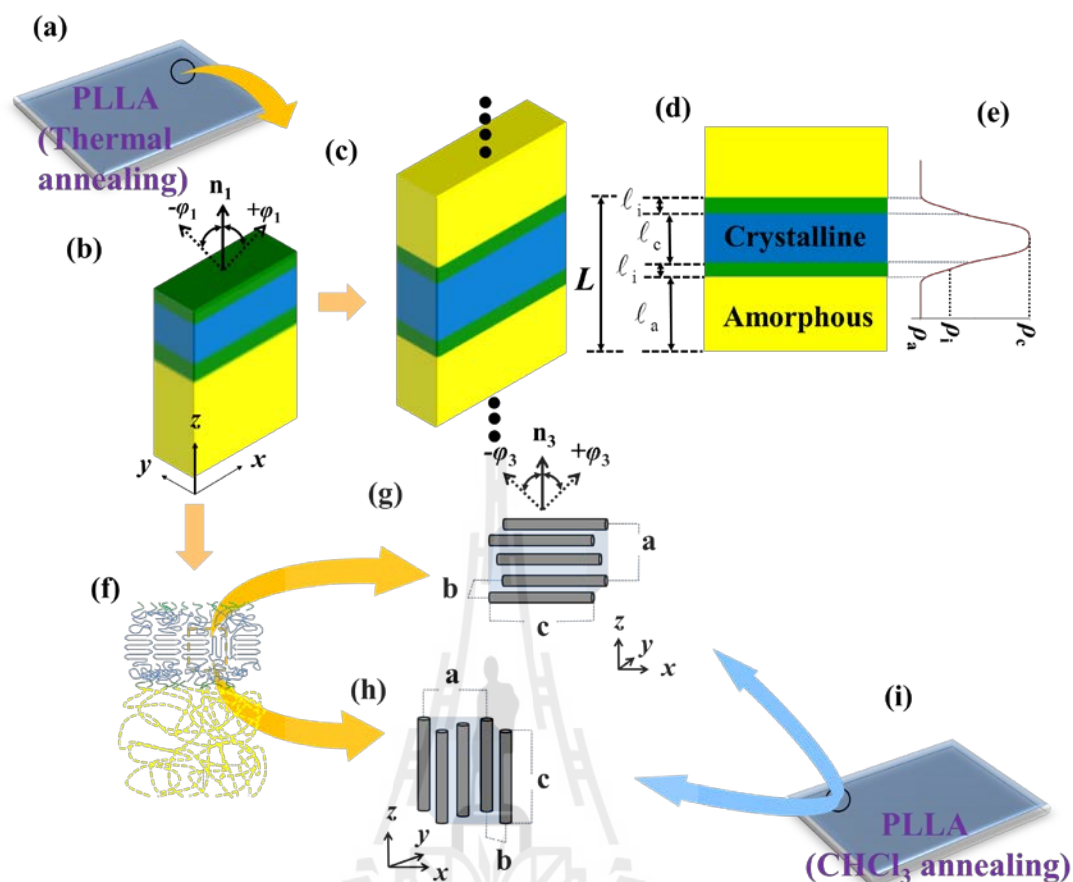


Figure 6.12 schematic representations of molecular chain conformation and packing order in thermal- and CHCl_3 -annealed PLLA film in (a) and (i) respectively; (b–d) horizontal lamellar structure in PLLA film where \mathbf{n}_1 is the orientation vector has the axis normal to the structure and φ_1 is the polar angle between the \mathbf{n}_1 vector and the out-of-plane direction of the film; (e) the relative electron density profile which ρ_c , ρ_i , and ρ_a are the relative electron densities of crystal, interface, and amorphous layers respectively; (f) molecular chain conformations in the amorphous layers and molecular chain order in the crystalline layers; (g) horizontally oriented orthorhombic crystal lattice where \mathbf{n}_3 is the orientation vector of the structure model and φ_3 is the polar angle between the \mathbf{n}_3 vector and the out-of-plane of the film; (h) vertically oriented orthorhombic crystal lattice.

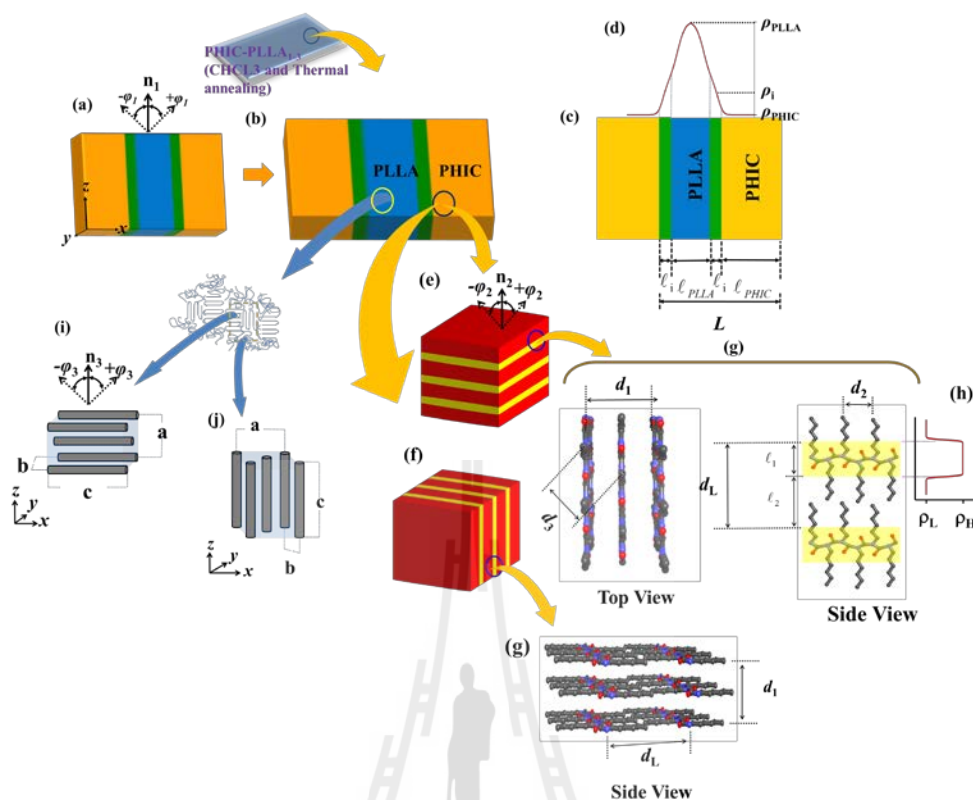


Figure 6.13 schematic representations of molecular chain conformations and packing orders in CHCl_3 - and thermal-annealed PHIC- PLLA_{1-3} films: (a-c) vertical lamellar structure and the orientation vector \mathbf{n}_1 of the structure model; (d) the relative electron densities profile where ρ_{PHIC} , ρ_i , and ρ_{PLLA} are the relative electron densities of PHIC, interface, and PLLA layers respectively; (e) horizontal multibilayer structure formed in the PHIC lamella where \mathbf{n}_2 is the orientation vector of the structure model; (f) vertical multibilayer structure formed in the PHIC lamella; (g) top and side views of molecular chain and packing order with no interdigitation in the structure; (h) relative electron density profile along the out-of-plane of the multibilayer structure; (i) horizontally oriented orthorhombic crystal lattice in the PLLA layers where \mathbf{n}_3 is the orientation vector of the structure model; (j) vertically oriented orthorhombic crystal lattice in the PLLA layers. The structure in (e-j) could not obtain in the thermal-annealed PHIC- PLLA_3 film.

PHIC-PLLA₁₋₃ films formed mainly vertical lamellar structures. The thermal-annealed PHIC-PLLA₁₋₃ films also predominantly formed vertical oriented lamellar structure. The thermal has effect of decreasing the out-of-plane structure and making a well arrangement structure as vertically oriented lamellar structure but the long-range order also was reduced. Moreover, the homopolymer films, the thermal-annealed PLLA presented horizontal lamellar structure but the PHIC and PLLA films annealed by CHCl₃ could not successfully display the GISAXS structure due to their was no electron density contrast of the PHIC and PLLA domain structure and/or the PHIC and PLLA domain structure were too large to be observed in the range of the scattering data.

The GIWAXS results revealed details of crystal morphology and orientation of the PHIC-PLLA₁₋₃, the PHIC and the PLLA films under CHCl₃ and thermal annealing. The PHIC annealed by CHCl₃ presented only horizontal lamellae bilayer while the PLLA crystal was found both horizontal and vertical orthorhombic system in CHCl₃ and thermal annealing. The less ordered PLLA orthorhombic or α' form was observed in the CHCl₃ annealing, while the stable PLLA crystal or α form was obtained in the thermal annealing. The PHIC-PLLA₁₋₃ under annealing both CHCl₃ and thermal showed complicated crystal conformation such as horizontal and vertical multibilayer due to PHIC phase plus horizontal and vertical orthorhombic unit cell due to PLLA phase except the CHCl₃-annealed PHIC-PLLA₃. Not only the PLLA phase but also the PHIC phase derives the effect from the CHCl₃ annealing for 16 hrs. In addition, the scattering peaks from the thermal annealing PHIC-PLLA₁₋₃ and PLLA films were observed clearly and strong as the number of PLLA crystal in the PHIC-PLLA₁₋₃ and PLLA increasing due to the thermal effect.

CHAPTER VII

CONCLUSIONS

In this work, the powerful analytical techniques based on synchrotron X-ray scattering method, i.e. small angle X-ray scattering (SAXS) and grazing incident X-ray scattering (GIXS) techniques were used, to examine molecular shape and size as well as structure of materials. We have been successfully studied the quantitative structural details using high brilliance synchrotron SAXS and GIXS techniques. By applying SAXS approach on the enzyme solution, namely glucose oxidase (GOD), the molecular structure of GOD was observed. The effects of acids and alkalis on the GOD conformation were studied and revealed that the GOD was stable and in folding, globular structures at pH 5 to 10. When pH was decreased to 3 and 4, the enzyme still presented globular shapes but slightly aggregated. When pH was reduced further to 1 and 2, the enzyme was aggregated and subsequently denaturing.

As from the comparisons of 3-dimensional (3D) atomic models, the scattering intensity profile and the excluded volumes of the GOD enzyme structures to those of the GOD crystal structure (obtained by Crystallography method), the results showed discrepancy between the enzyme and crystal structures. The discrepancy can be attributed to the fact that the enzyme is a dimer containing significant amount of carbohydrate, while the crystal structure is a monomer with most carbohydrate removed.

The quantitative analysis on structure the rod-coil type miktoarm star polymers, PHIC-PCL₁₋₃ (poly(n-hexyl isocyanate)-*block*-poly(ϵ -caprolactone)) and PHIC-PLLA₁₋₃ (poly(n-hexyl isocyanate)-*block*-poly(L-lactid acid)), in thin films formed were performed successfully using GIXS method, such as grazing incident small-angle X-ray scattering (GISAXS) and grazing incident wide-angle X-ray scattering (GIWAXS) techniques. The PHIC-PCL₁₋₃ has a number-average molecular weight (M_n) of approximate 5,000 g/mol and 10,000 g/mol for PHIC arm and one to three PCL arms (PCL_n: $n = 1-3$) with a total M_n of approximate 17,000 and 10,000 g/mol, such as PHIC(5k)-PCL₁₋₃(17k) and PHIC(10k)-PCL₁₋₃(10k). While the PHIC-PLLA₁₋₃ has M_n of approximate 10,000 g/mol for PHIC arm and one to three PLLA arms (PLLA_n: $n = 1-3$) with a total M_n of approximate 10,000 g/mol, i.e. PHIC(10k)-PLLA₁₋₃(10k). Furthermore, the structures of homopolymer films of PHIC, PCL and PLLA with M_n of around 5,400 g/mol and 10,400 g/mol for the PHIC, of around 10,500 g/mol and 15,000 g/mol for PCL, and of around 10,200 g/mol for PLLA, i.e. PHIC(5.4k,10.4k), PCL(15k, 10.5k), and PLLA(10.2k), have been studied in order to compare with those of the star polymers films.

The molecular conformation of the PHIC(5k)-PCL₁₋₃(17k) films under toluene annealing was revealed mainly horizontal lamellar structure regardless of the number of PCL arms present. The structure from the PHIC(5k)-PCL₁₋₃(17k) was obtained much difference from the common diblock copolymers even they have similar volume fraction. While the PHIC(10k)-PCL₁₋₃(10k) films presented interesting results as they could form lamellar structures with different orientation depend on the toluene and/or CHCl₃ annealing as well as the number of PCL arms present. The PHIC(10k)-PCL₁₋₃(10k) films under toluene annealing were revealed to be the horizontally

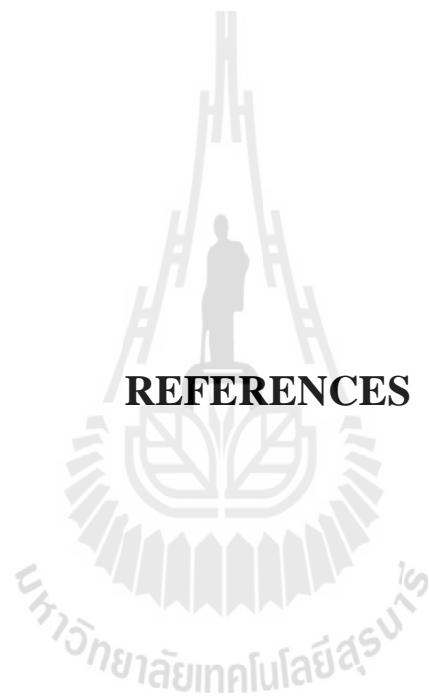
oriented lamellar structure independent of the number of PCL arms present. The CHCl_3 -annealed PHIC-PCL film was also found to have horizontal lamellar structure but the CHCl_3 -annealed PHIC-PCL_{2,3} films were revealed to have vertical lamellar structure. In addition, all the PCL(15k, 10.5k) films were found to have predominantly horizontal lamellar structure. Unlikely, all the PHIC(5.4k, 10.4k) was featureless and could not be characterized by GISAXS during the range of the collected scattering data.

The crystal conformation and orientation of all the PHIC(5k, 10k)-PCL₁₋₃(17k, 10k) presented the complex structure as a mixed horizontally and vertically oriented multibilayer structure (due to the PHIC phase) and a combination of horizontally and vertically orthorhombic structure (due to the PCL phase). For the toluene-annealed PHIC(5.4k, 10.4k), they were found in both horizontal and vertical multibilayer structures but it is exciting that the CHCl_3 -annealed PHIC(10.4k) was found to have a well-orientation structure as only horizontal oriented orthorhombic was formed. While all the PCL(15k, 10.5k) formed horizontally and vertically oriented orthorhombic systems.

GIXS was also utilized to examined the molecular structure of the PHIC(10k)-PLLA₁₋₃(10k) films as well as the PLLA(10.2k) films under CHCl_3 and thermal annealing (heat up to approximate 130 °C for 24 hrs). The CHCl_3 -annealed PHIC-PLLA_{1,3} films predominantly formed vertical lamellar structure. For the thermal annealing cases, the majority structure still was vertically oriented lamellar structure in the PHIC-PLLA₁₋₃ regardless PLLA arm numbers and the horizontal lamellar structure was observed in the PLLA. On the other hand, the CHCl_3 -annealed PLLA film did not display any GISAXS pattern in the collected scattering range data. The

featureless in GISAXS measurement of the PHIC films and the CHCl₃-annealed PLLA film might happen either the domain structure of the PHIC or PLLA were larger than range of the collected scattering data or the electron density contrast of the PHIC or PLLA domain structure could not be notice.

The quantitative crystal morphology and orientation of the PHIC-PLLA_{1,2} films via CHCl₃ were observed to be horizontal and vertical multibilayer due to PHIC phase combined with horizontal orthorhombic unit cell due to PLLA phase. However, the CHCl₃-annealed PHIC-PLLA₃ film could not form any crystal conformation. In addition, the thermal has as influence on the PLLA crystal as it increased the number of PLLA crystallinity. The characteristic scattering peaks from the thermal cases showed more clearly and stronger than those from the CHCl₃ annealing process. In particular, the thermal-annealed PHIC-PLLA₃ film could form crystal unlike the CHCl₃-annealed PHIC-PLLA₃ film. The thermal-annealed PHIC-PLLA₁₋₃ films were also obtained horizontal and vertical multibilayer in PHIC phase but plus with both vertical and horizontal orthorhombic system in PLLA phase. The PLLA films were found both horizontal and vertical orthorhombic system in both CHCl₃ and thermal cases. The less ordered orthorhombic or α' form was observed in the PLLA under the CHCl₃ annealing, while more stable orthorhombic crystal or α form was obtained in the PLLA in the thermal annealing.



REFERENCES

REFERENCES

- Ash, B., Rogers, D., Wiegand, C., Schadler, L., Siegel, R., Benicewicz, B. C., and Apple, T. (2002). Mechanical properties of Al₂O₃/polymethylmethacrylate nanocomposites. **Polym. Compos.** 23: 1014-1025
- Agbabiaka, A., Wiltfong, M., and Park, C. (2013). Small angle X-ray scattering technique for the particle size distribution of nonporous nanoparticles. **J. Nanopart.** 640436: 1-11.
- Akhtar, M. S., Ahmad, A., and Bhakuni, V. (2002). Guanidinium chloride- and urea-induced unfolding of the dimeric enzyme glucose oxidase. **Biochemistry** 41: 3819-3827.
- Ahmad, A., Akhtar, Md. S., and Bhakuni, V. (2001). Monovalent Cation-Induced Conformational Change in Glucose Oxidase Leading to Stabilization of the Enzyme. **Biochemistry.** 40: 1945-1955.
- Ahn, B., Hirai, T., Jin, S., Rho, Y., Kim, K.-W., Kakimoto, M.-A., Gopalan, P., Hayakawa, T., and Ree, M. (2010). Hierarchical structure in nanoscale thin films of a poly(styrene-*b*-methacrylate grafted with POSS) (PS₂₁₄-*b*-PMAPOSS₂₇). **Macromolecules** 43: 10568-10581.
- Ahn, B., Kim, D. M., Hsu, J.-C., Ko, Y.-G., Shin, T. J., Kim, J., Chen, W.-C., and Ree, M. (2013). Tunable film morphologies of brush-linear diblock copolymer bearing difluorene moieties yield a variety of digital memory properties. **ACS. Macro. Letters.** 2: 555-560.

- Brumberger, H. (1993). **Modern aspects of small-angle scattering**. London: Kluwer Academic Publishers.
- Berman, H. M., Westbrook, J., Feng, Z., Gilliland, G., Bhat, T. N., Weissig, H., Shindyalov, L. N., and Bourne, P. E. (2000). The protein data bank. **Nucleic Acids Res.** 28(1): 235-242.
- Berman, H. M. (2008). The Protein Data Bank: a historical perspective. **Acta Crystallogr. A.** 64: 88–95.
- Babin, J., Leroy, C., Lecommandoux, S., Borsali, R., Gnanou, Y., and Taton, D. (2005). Towards an easy access to amphiphilic rod-coil miktoarm star copolymers. **Chem. Commun.** 1993-1995.
- Brittger, H., Marchessault, R. H., and Niegsch, W. D. (1970). Crystal structure of poly- ϵ -caprolactone. **Acta Crystallogr. B.** 26: 1923-1927.
- Bates, F. S., and Fredrickson, G. H. (1990). BLOCK COPOLYMER THERMODYNAMICS: Theory and Experiment. **Annu. Rev. Phys. Chem.** 41: 525-557.
- Cabane, B., Duplessix, R., and Zemb, T. J. (1985). High resolution neutron scattering on ionic surfactant micelles: sds in water. **J. Phys. (Paris)** 46: 2161-2178.
- DeLano, W. L. (2002). **The PyMOL molecular graphics system**. DeLano Scientific, San Carlos, CA, USA.
- Frost, K., Kaminski, D., Kiriwan, G., Lascaris, E., and Shanks, R. (2009). Crystallinity and structure of starch using wide angle X-ray scattering. **Carbohydr Polym.** 78: 543-548.
- Feigin, L. A., and Svergun, D. I. (1987). **Structure analysis by small-angle X-ray and neutron scattering**. New York: Plenum Press.

- Fiedurek, J. (2001). Production of gluconic acid by immobilized in pumice stones mycelium of *Aspergillus niger* using unconventional oxygenation of culture. **Biotechnol. Lett.** 23: 1789-1792.
- Fink, A. L., Calciano, L. J., Goto, Y., Kurotsu, T., and Palleros, D. R. (1994). Classification of Acid Denaturation of Proteins: Intermediates and Unfolded States. **Biochemistry.** 33: 12504-12511.
- Glatter, O., and Kratky, O. (1982). **Small angle X-ray scattering.** London: Academic Press.
- Guinier, A., and Fournet, G. (1995). **Small angle scattering of X-ray.** New York: John Wiley and Sons Inc.
- Gitsas, A., Floudas, G., Mondeshki, M., Lieberwirth, I., Spiess, H. W., Iatrou, H., hadjichristidis, N., and Hirao, A. (2010). Hierarchical Self-Assembly and dynamics of a miktoarm star chimera composed of poly(γ -benzyl-L-glutamate), polystyrene, and polyisoprene. **Macromolecules** 43: 1874-1881.
- Hayter, J. I., and Penfold, J. (1983). Determination of micelle structure and charge by neutron small-angle scattering. **Colloid. Polym. Sci.** 261: 1022-1030.
- Henry, C. (1998). Surface studies of supported model catalysts. **Surf. Sci. Rep.** 31: 231-325.
- Hamley, I. W. (2009). Ordering in thin films of block copolymers: Fundamentals to potential applications. **Prog. Polym. Sci.** 34: 1161-1210.
- Hadjichristidis, N., Pitsikalis, M., Pispas, S., and Iatrou, H. (2001). Polymers with Complex Architecture by Living Anionic Polymerization. **Chem. Rev.** 101: 3747-3792.

- Ho, J. A. A., Wu, L. C., Fan, N. C., Lee, M. S., Kuo, H. Y., and Yang, C. S. (2007). Development of a long-life capillary enzyme bioreactor for the determination of blood glucose. **Talanta**. 71: 391-396.
- Heo, K., Jin, K. S., Yoon, J., Jin, S., Oh, W., and Ree, M. (2006). Synchrotron X-ray scattering study of the mechanism of nanopore generation in nanoporous organosilicate thin films imprinted with a reactive six-armed porogen. **J. Phys. Chem. B**. 110: 15887-15895.
- Huang, W.-H., Chen, P.-Y., and Tung, S.-H. (2012). Effects of Annealing Solvents on the Morphology of Block Copolymer-Based Supramolecular Thin Films. **Macromolecules** 45: 1562-1569.
- Iatrou, H., and Hadjichristidis, N. (1992). Synthesis of a model 3-miktoarmf star terpolymer. **Macromolecules** 25: 4649-4651.
- Jaffar, S. A., and Turner, A. P. F. (1995). Recent advances in amperometric glucose biosensors for *in vivo* monitoring. **Physiol. Meas.** 16: 1-15.
- Jin, S., Yoon, J., Heo, K., Park, H.-W., Shin, T. J., Chang, T., and Ree, M. (2007). Detailed analysis of gyroid structures in diblock copolymer thin films with synchrotron grazing-incidence X-ray scattering. **J. Appl. Crystallogr.** 40: 950-958.
- Junnila, S., Houbenov, N., Hanski, S., Iatrou, H., Hirao, A., Hadjichristidis, N., Ikkala, O. (2010). Hierarchical smectic self-assembly of an ABC miktoarm star terpolymer with a helical polypeptide arm. **Macromolecules** 43: 9071-9076.
- Kim, K., Kim, Y. Y., Park, S., Ko, Y.-G., Rho, Y., Kwon, W., Shin, T. J., Kim, J., and Ree, M. (2014). Nanostructure- and Orientation-Controlled Digital Memory

Behaviors of Linear-Brush Diblock Copolymers in Nanoscale Thin Films.

Macromolecules 47: 4397-4407.

Kim, Y. Y., Jung, S., Kim, C., Ree, B. J., Kawato, D., Nishikawa, N., Suemasa, D.,

Isono, T., Kakuchi, T., Satoh, T., and Ree, M. (2014). Hierarchical Structures

in Thin Films of Miktoarm Star Polymers: Poly(*n*-hexyl isocyanate)(12K)–

Poly(ϵ -caprolactone)_{1–3}(5K). **Macromolecules** 47: 7510-7524.

Kirkpatrick, S., Gelatt, C. D. Jr., and Vecchi, M. P. (1983). Optimization by simulated

annealing. **Science**. 220: 671-680.

Kozin, M. B., and Svergun, D. I. (2001). Automated matching of high- and low-

resolution structural models. **J Appl Cryst.** 34: 33-41.

Konarev, P. V., Volkov, V. V., Sokolova, A. V., Koch, M. H. J., and Svergun, D.I.

(2003). PRIMUS: a Windows PC-based system for small-angle scattering

data analysis. **J. Appl. Cryst.** 36: 1277-1282.

Khatun Haq, S., Faiz Ahmad, Md., and Hasan Khan, R. (2003). The acid-induced

state of glucose oxidase exists as a compact folded intermediate. **Biochem.**

Biophys. Res. Commun. 303: 685-692.

Kalitz, H. M., Hecht, H. J., Schomburg, D., and Schmid, R. D. (1991). Effects of

carbohydrate depletion on the structure, stability and activity of glucose

oxidase from *Aspergillus niger*. **Biochim. Biophys. Acta.** 1080: 138-142.

Khanna, K., Varshney, S., and Kakkar, A. (2010). Miktoarm star polymers: advances

in synthesis, self-assembly, and applications. **Polym. Chem.** 1: 1171-1185.

Lee, B., Yoon, J., Oh, W., Hwang, Y., Heo, K., Jin, K. S., Kim, J., Kim, K.-W., and

Ree, M. (2005). In-situ grazing incidence small-angle X-ray scattering

studies on nanopore evolution in low- k organosilicate dielectric thin films.

Macromolecules 38: 3395-3405.

Lee, B., Park, I., Yoon, J., Park, S., Kim, J., Kim, K-W, Chang, T., and Ree, M. (2005). Structural analysis of block copolymer thin films with grazing incidence small-angle X-ray scattering. **Macromolecules** 38: 4311-4323.

Lee, B., Oh, W., Yoon, J., Hwang, Y., Kim, J., Landes, B. G., Quintana, J. P. and Ree, M. (2005). Scattering Studies of Nanoporous Organosilicate Thin Films Imprinted with Reactive Star Porogens. **Macromolecules** 38: 8991-8995.

Lee, B., Park, Y.-H., Hwang, Y.-T., Oh, W., Yoon, J., and Ree, M. (2005). Ultralow- k nanoporous organosilicate dielectric films imprinted with dendritic spheres. **Nat. Mater.** 4: 147-150.

Lazzari, R. (2002). IsGISAXS: a program for grazing-incidence small-angle X-ray scattering analysis of supported islands. **J. Appl. Crystallogr.** 35: 406-421.

Levine, J. R., Cohen, J. B., Chung, Y. W., and Georgopoulos, P. (1989). Grazing-incidence small-angle X-ray scattering: new tool for studying thin film growth. **J. Appl. Cryst.** 22: 528-532.

Meyer, R., Lemire C., Shaikhutdinov S. K., and Freund, H. J. (2004). Surface chemistry of catalysis by gold. **Gold Bull.** 37: 72-124.

Müller-Buschbaum, P. (2009). A basic introduction to grazing incidence small-angle X-ray scattering. **Lect. Notes Phys.** 776: 61-89.

Müller-Buschbaum, P. (2003). Grazing incidence small-angle X-ray scattering: an advanced scattering technique for the investigation of nanostructured polymer films. **Anal. Bioanal. Chem.** 376: 3-10.

- Montes De Oca, H., and Ward, I. M. (2007). Structure and Mechanical Properties of Poly(L-lactic acid) Crystals and Fibers. **J. Polym. Sci. Part B Polym. Phys.** 45: 892-902.
- Nakamura, S., and Fujiki, S. (1968). Comparative Studies on the Glucose Oxidases of *Aspergillus niger* and *Penicillium amagasakiense*. **J. Biochem.** 63: 51-58.
- Niebuhr, M. (2004). **Readout system for delay line detectors with a time stamp TDC and a small angle scattering study of intermolecular interactions in protein solutions.** PhD thesis. University of Hamburg. Germany.
- O'Malley, J. J. and Weaver, J. L. (1972). Subunit Structure of Glucose Oxidase from *Aspergillus niger*. **Biochemistry** 11: 3527-3532.
- Omote, K., Ito, Y., and Kawamura, S. (2003). Small angle x-ray scattering for measuring pore-size distributions in porous low- κ films. **Appl. Phys. Lett.** 82: 544-546.
- Putnam, C. D., Hammel, M., Hura, G. L., and Tainer, J. A. (2007). X-ray solution scattering (SAXS) combined with crystallography and computation: defining accurate macromolecular structures, conformations and assemblies in solution. **Q. Rev. Biophys.** 40(3): 191-285.
- Parpinello, G., Chinnici, F., Versari, A., and Riponi C. (2002). Preliminary study on glucose oxidase–catalase enzyme system to control the browning of apple and pear purées. **Lebenson Wiss Technol.** 35: 239-243.
- Petoukhov, M. V., Konarev, P. V., Kikhney, A. G., and Svergun D. I. (2007). ATSAS 2.1 – towards automated and web-supported small-angle scattering data analysis. **J. Appl. Cryst.** 40: s223-s228.

- Pazur, J. H., Kleppe, K., and Cepure, A. (1965). A glycoprotein structure for glucose oxidase from *Aspergillus niger*. **Arch. Biochem. Biophys.** 111: 3517-3527.
- Pazur, J. H., and Kleppe, K. (1964). The Oxidation of Glucose and Related Compounds by Glucose Oxidase from *Aspergillus niger*. **Biochemistry** 3: 578-583.
- Park, I., Lee, B., Ryu, J., Im, K., Yoon, J., Ree, M., and Chang, T. (2005). Epitaxial Phase Transition of Polystyrene-*b*-Polyisoprene from Hexagonally Perforated Layer to Gyroid Phase in Thin Film. **Macromolecules** 38: 10532-10536.
- Pitsikalis, M., Pispas, S., Maysi, J. W., and Hadjichristidis, N. (1998). Synthesis of well-defined star-branched polymers by stepwise iterative methodology using living anionic polymerization. **Adv. Polym. Sci.** 135: 1-137.
- Pan, P., Zhu, B., Kai, W., Dong, T., and Inoue, Y. (2008). Polymorphic transition in disordered poly(L-lactide) crystals induced by annealing at elevated temperatures. **Macromolecules** 41: 4296-4304.
- Renaud, G., Lazzari, R., and Leroy, F. (2009). Probing surface and interface morphology with grazing incidence small angle X-ray scattering. **Surf. Sci. Rep.** 64: 255-380.
- Rho, Y., Kim, C., Higashihara, T., Jin, S., Jung, J., Shin, T. J., Hirao, A., and Ree, M. (2013). Complex self-assembled morphologies of thin films of an asymmetric $A_3B_3C_3$ star polymer. **ACS. Macro. Lett.** 2: 849-855.
- Xu, T., Goldbach, J. T., Misner, M. J., Kim, S., Gibaud, A., Gang, O., Ocko, B., Guarini, K. W., Black, C. T., Hawker, C. J., and Russell, T. P. (2004). Scattering study on the selective solvent swelling induced surface reconstruction. **Macromolecules** 37: 2972-2977.

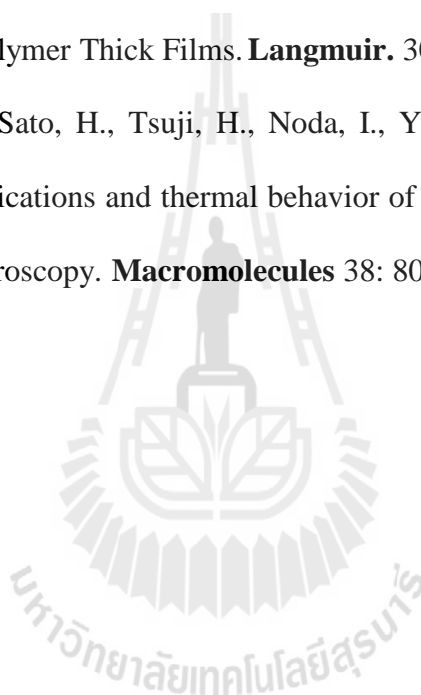
- Ramachandran S., Fontanille P., Pandey A., and Larroche C. (2006). Gluconic Acid: Properties, Applications and Microbial Production. **Food Technol. Biotech.** 44: 185-195.
- Rauscher, M., Paniago, R., and Metzger, H. (1999). Grazing incidence small angle X-ray scattering from free-standing nanostructures. **J. Appl. Phys.** 86: 6763-6769.
- Rauscher, M., Salditt, T., and Spohn, H. (1995). Small-angle x-ray scattering under grazing incidence: The cross section in the distorted-wave Born approximation. **Phys. Rev. B.** 52: 16855.
- Rahman, M. S., Changez, M., Yoo, J. W., Lee, C. H., Samal, S., and Lee, J. S. (2008). Synthesis of Amphiphilic Miktoarm Star Copolymers of Poly(*n*-hexyl isocyanate) and Poly(ethylene glycol) through Reaction with the Active Methylene Group. **Macromolecules** 41: 7029-7032.
- Rho, Y., Min, J., Yoon, J., Ahn, B., Jung, S., Kim, K., Shah, P., Lee, J.-S., and Ree, M. (2012). Reversible conformation-driven order–order transition of peptide-mimic poly(*n*-alkyl isocyanate) in thin films via selective solvent-annealing. **NPG Asia Mater.** 4: e29.
- Rho, Y., Ahn, B, Yoon, J., and Ree, M. (2014). Comprehensive synchrotron grazing-incidence X-ray scattering analysis of nanostructures in porous polymethylsilsesquioxane dielectric thin films. **J. Appl. Crystallogr.** 46: 466-475.
- Svergun, D. I. (2007). Small-angle scattering studies of macromolecular solutions. **J. Appl. Cryst.** 40: s10-s17.

- Svergun, D. I., and Koch M. H. J. (2003). Small-angle scattering studies of biological macromolecules in solution. **Rep. Prog. Phys.** 66: 1735-1782.
- Sohail Akhtar, Md., and Bhakuni V. (2003). Alkaline treatment has contrasting effects on the structure of deglycosylated and glycosylated forms of glucose oxidase **Arch. Biochem. Biophys.** 413: 221-228.
- Svergun, D. I., Barberato C. and Koch, M. H. J. (1995). CRY SOL - a Program to evaluate X-ray solution scattering of biological macromolecules from atomic coordinates. **J. Appl. Cryst.** 28: 768-773.
- Svergun, D. I. (1999). Determination of the regularization parameter in indirect-transform methods using perceptual criteria. **J. Appl. Cryst.** 25: 495-503.
- Svergun, D. I. (1999). Restoring Low Resolution Structure of Biological Macromolecules from Solution Scattering Using Simulated Annealing. **Biophys. J.:** 2879-2886.
- Svergun, D. I., Barberato C., and Koch, M. H. J. (1995). CRY SOL – a program to evaluate X-ray solution scattering of biological macromolecules from atomic coordinates. **J. Appl. Cryst.** 28: 768-773.
- Sinha, S. K., Sirota, E. B., Garoff. S., and Stanley, H. B. (1988). X-ray and neutron scattering from rough surfaces. **Phys. Rev. B.** 38: 2297.
- Satoh, T., Nishikawa, N., Kawato, D., Suemasa, D., Jung, S., Kim, Y. Y., and Ree, M., and Kakuchi, T. (2014). Precise synthesis of a rod-coil type miktoarm star copolymer containing poly(n-hexyl isocyanate) and aliphatic polyester. **Polymer. Chem.** 5: 588-599.
- Sasaki, S., and Asakura, T. (2003). Helix Distortion and Crystal Structure of the α -Form of Poly(L-lactide). **Macromolecules** 36: 8385-8390.

- Sun S. H., Murray C. B., Weller D., Folks L., and Moser A. (2000). Monodisperse FePt nanoparticles and ferromagnetic FePt nanocrystal superlattices. **Science**. 287: 1989-1992.
- Touris, A., Kostakis, K., Mourmouris, S., Kotzabasaki, V., Pitsikalis, M., Hadjichristidis, N. (2008). Complex macromolecular architectures based on *n*-Hexyl Isocyanate and ϵ -Caprolactone using Titanium-mediated coordination polymerization. **Macromolecules** 41: 2426-2438.
- Tsuge, H. J., Natsuaki O., and Ohashi, K. (1975). Purification, Properties, and Molecular Features of Glucose Oxidase from *Aspergillus niger*. **J. Biochem.** 78: 835-843.
- Teichert, C. (2002). Self-organization of nanostructures in semiconductor heteroepitaxy. **Surf. Sci. Rep.** 365: 335-342.
- Volkov, V. V., and Svergun, D. I. (2003). Uniqueness of ab initio shape determination in small-angle scattering. **J. Appl. Cryst.** 36: 860-864.
- Wignall G. D., and Bates F. S. (1987). Absolute calibration of small-angle neutron scattering data. **J. Appl. Cryst.** 20: 28-40.
- Wilson, R., and Turner, A. P. F. (1992). Glucose oxidase: an ideal enzyme. **Biosens. Bioelectr.** 7: 165-185.
- Wohlfahrt, G., Witt, S., Hendle, J., Schomburg, D., Kalisz, H. M., and Hacht, H. J. (1999). 1.8 and 1.9 Å resolution structures of the *Penicillium amagasakiense* and *Aspergillus niger* glucose oxidases as a basis for modeling substrate complexes. **Acta Crystallogr. D: Biol. Crystallogr.** 55: 969-977.
- Woodruff, M. A., and Hutmacher, D. W. (2010). The return of a forgotten polymer- Polycaprolactone in the 21st century. **Prog. Polym. Sci.** 35: 1217-1256.

- Xu, T., Goldbach, J. T., Misner, M. J., Kim, S., Gibaud, A., Gang, O., Ocko, B., Guarini, K. W., Black, C. T., Hawker, C. J., and Russell, T. P. (2004). Scattering Study on the Selective Solvent Swelling Induced Surface Reconstruction. **Macromolecules** 37: 2972-2977.
- Yang, J., and Liang, S. C. (2005). α -Cyclodextrin-modified infrared chemical sensing system that utilizes enzymatic reactions for the determination of glucose. **Anal. Chim. Acta.** 537: 385-392.
- Yoon, J., Jin, S., Ahn, B., Rho, Y., Hirai, T., Maeda, R., Hayakawa, T., Kim, J., Kim, K.-W., and Ree, M. (2008). Phase transitions in thin films of a diblock copolymer composed of a linear polymer block and a brush polymer Block with mesogenic oligothiophenyl bristles. **Macromolecules** 41: 8778-8784.
- 5, J., Jin, S. K., Kim, H. C., Kim, G., Heo, K., Jin, S., Kim, J., Kim, K.-W., and Ree, M. (2007). Quantitative analysis of lamellar structures in brush polymer thin films by synchrotron grazing-incidence X-ray scattering. **J. Appl. Cryst.** 40: 476-488.
- Yoon, J., Kim, K.-W., Kim, J., Heo, K., Jin, K. S., Jin. S., Shin, T. J., Lee, B., Rho, Y., Ahn, B., and Ree, M. (2008). Small-angle X-ray scattering station 4C2 BL of Pohang accelerator laboratory for advance in Korean polymer science. **Macromol. Res.** 16: 575-585.
- Yoon, J., Lee, S. W., Choi, S., Heo, K., Jin, K. S., Jin, S., Kim, G., Kim, J., Kim, K.-W., Kim, H., and Ree, M. (2008). Two-Dimensionally well-ordered multilayer structures in thin films of a brush polypeptide. **J. Phys. Chem. B.** 112: 5338-5349.

- Yasuniwa, M., Tsubakihara, S., Iura, K., Ono, Y., Dan, Y., and Takahashi, K. (2006). Crystallization behavior of poly(L-lactic acid). **Polymer**. 47: 7554-7563.
- Yasuniwa, M., Iura, K., and Dan, Y. (2007). Melting behavior of poly(L-lactic acid): Effects of crystallization temperature and time. **Polymer**. 48: 5398-5407.
- Yang, J., Liang, Y., and Han, C. C. (2014). Crystallization-Driven Surface Segregation and Surface Structures in Poly(L-lactide)-block-Poly(ethylene glycol) Copolymer Thick Films. **Langmuir**. 30: 394–401.
- Zhang, J., Duan, Y., Sato, H., Tsuji, H., Noda, I., Yan, S., and Ozaki, Y. (2005). Crystal modifications and thermal behavior of poly(L-lactic acid) revealed by infrared spectroscopy. **Macromolecules** 38: 8012-8021.





APPENDIX

APPENDIX

Abstract published in Science of Advanced Materials

Grazing Incidence Small-Angle X-ray Scattering Studies of the Thin Film Morphologies of Miktoarm Crystalline Star Polymers

Authors: Phinjaroenphan, Rarm; Kim, Young Yong; Jung, Sungmin; Isono, Takuya; Satoh, Yusuke; Maensiri, Santi; Rugmai, Supagorn; Kakuchi, Toyoji; Satoh, Toshifumi; Ree, Moonhor

Source: [Science of Advanced Materials](#), Volume 6, Number 11, November 2014, pp.2526-2531(6)

Publisher: [American Scientific Publishers](#)

Abstract:

The nanoscale thin film morphologies of a series of interesting miktoarm star polymers composed of a highly rigid and crystallizable poly(*n*-hexyl isocyanate) (PHIC) arm and one to three flexible and crystallizable poly(ϵ -caprolactone) (PCL) arms were investigated using synchrotron grazing incidence X-ray scattering methods. Nanoscale thin films of a PHIC and a PCL homopolymer were also characterized for comparison. The PCL homopolymer and star polymers formed horizontally oriented lamellar structures in toluene-annealed films. The horizontal lamellar structures formed in the miktoarm star polymer films were quite different from those observed in common flexible block copolymer specimens. Interestingly, the structural parameters associated with the star polymer films were significantly influenced by the exceptional rigidity of the PHIC arm chain and by the number and length of the PCL arms. This study demonstrated that a miktoarm star polymer system consisting of rigid and crystallizable arms could form thin films with a morphology that is suitable for specific target applications.

Keywords: CRYSTALLIZATION; LAMELLAR NANOSTRUCTURES; MIKTOARM STAR POLYMER THIN FILMS; PHASE-SEPARATION; SOLVENT-ANNEALING; SYNCHROTRON GRAZING INCIDENCE X-RAY SCATTERING

Document Type: Research Article

DOI: <http://dx.doi.org/10.1166/sam.2014.2232>

Publication date: November 1, 2014

Manuscript submitted in the Macromolecules

Complex thin film morphologies of poly(*n*-hexyl isocyanate)(5k,10k)–poly(ϵ caprolactone)_{1–3}(10k,17k) miktoarm star polymers[†]

Rarm Phinjaroenphan,^{+abc} Young Yong Kim,^{+c} Brian J. Ree,^c Takuya Isono,^d Jinseok Lee,^c Heesoo Kim,^e Santi Maensiri,^{*ab} Supagorn Rugmai,^{*ab} Toyoji Kakuchi,^{*d} Toshifumi Satoh,^{*d} and Moonhor Ree^{*c}

^aSchool of Physics, Suranaree University of Technology, Nakhon Ratchasima 30000, Thailand. E-mail: santimaensiri@g.sut.ac.th (SM), supagorn@slri.or.th (SR); Fax: +66-44-22-4651 (SM), +66-44- 21-7047 (SR); Tel: + 66-44-22-4293 (SM), +66-44-21-7040 (SR)

^bSynchrotron Light Research Institute, Nakhon Ratchasima 30000, Thailand. E-mail: santimaensiri@g.sut.ac.th (SM), supagorn@slri.or.th (SR); Fax: +66-44-22-4651 (SM), +66-44- 21-7047 (SR); Tel: + 66-44-22-4293 (SM), +66-44-21-7040 (SR)

^cDepartment of Chemistry, Division of Advanced Materials Science, Pohang Accelerator Laboratory, Polymer Research Institute, and BK School of Molecular Science, Pohang University of Science & Technology, Pohang 790-784, Korea. E-mail: ree@postech.edu; Fax: +82-54-279-2120; Tel: +82-54-279-3399

^dDivision of Biotechnology and Macromolecular Chemistry, Faculty of Engineering, Hokkaido University, Sapporo 060-8628, Japan. E-mail: kakuchi@poly-bm.eng.hokudai.ac.jp (TK), satoh@poly-bm.eng.hokudai.ac.jp (TS); Fax: (TK), +82-11-706-6603(TS); Tel: (TK), +82-11-706-6603 (TS)

^eDepartment of Microbiology, Dongguk University College of Medicine, Gyeongju 780-350, Korea

[†]Electronic supplementary information (ESI) available: Synthesis and Fig. S1-S3.

⁺R. Phinjaroenphan and Y. Y. Kim contributed equally to this work.

Abstract

Two series of crystalline-crystalline miktoarm star polymers were prepared and their thin film morphologies were investigated in detail by synchrotron grazing incidence X-ray scattering (GIXS): poly(*n*-hexyl isocyanate)(5000)–poly(ϵ -caprolactone)₁₋₃(17000) (PHIC(5k)-PCL₁₋₃(17k)) and poly(*n*-hexyl isocyanate)(10000)–poly(ϵ -caprolactone)₁₋₃(10000) (PHIC(10k)-PCL₁₋₃(10k)). In addition, their thermal properties were examined. All miktoarm star polymers revealed a two-step thermal degradation behavior where the PHIC arm was degraded first, followed by the PCL arm underwent degradation. Interestingly, all miktoarms were found to show a highly enhanced thermal stability, regardless of their molecular weight over 3k to 17k, which might be attributed to their one-end group capped with the counterpart arm(s) via arm-joint formation. Surprisingly, all miktoarm star polymers always developed only lamellar structure in toluene- and chloroform-annealed films via phase-separation, regardless of the length of PHIC arm as well as the length and number of PCL arm. Despite having highly imbalanced volume fractions, lamellar structure was constructed in the films of miktoarm star polymers through the override of volume fraction rule based on the rigid chain properties, self-assembling characteristics, conformational asymmetry, and compressibilities of PHIC and PCL arms. Furthermore, the orientation of such lamellar structures was controlled by the selection of either toluene or chloroform in the solvent-annealing process. The PHIC arm phases in the lamellar structures favorably formed a mixture of edge-on and face-on structures with fully extended backbone and bristle conformations even under the confined lamellar geometry and arm-jointer. The PCL arm phases still crystallized, forming fringed-micelle like structures in which orthorhombic crystals were laterally grown along the in-plane direction of lamellae although their crystallization was somewhat suppressed by the confined lamellar geometry and arm-jointer. Overall, crystalline-crystalline PHIC-PCL₁₋₃ miktoarm polymers demonstrated very interesting but unusual, very complex hierarchical structures in the solvent-annealed thin films.

Keywords: crystalline-crystalline miktoarm star polymers, synchrotron grazing incidence X-ray scattering, nanoscale thin film, phase separation, self-assembly,

hierarchical structure, lamellar nanostructure, multibilayer structure, edge-on structure, face-on structure, folded lamella, fringed-micelle like structure, orthorhombic crystal, confinement effect

Introduction

Miktoarm star polymer is composed of chemically different (i.e., asymmetric) arms and can indeed undergo microphase separation between immiscible arms, very often producing distinctive morphological structures and properties. The resulting structures and properties have the potentials to be applied to various fields. Thus, much effort has been made on the development of miktoarm star polymers and various types of miktoarm star polymers have been reported for the last two decades.¹⁻¹¹ They can be classified into two families, namely coil-coil¹⁻⁶ and rod-coil miktoarm star polymers,⁷⁻¹¹ according to the chain characteristics of the arm components. While the morphological structures and properties in the bulk or solution state have been reported numerous times,¹⁻¹⁶ nanoscale thin film morphologies and properties have rarely been examined¹⁷ despite the potential applications in advanced microelectronic, optical, and optoelectronic devices.

Recently we have reported the synthesis and basic characterization of a new family of miktoarm star polymers which consist of a fully rigid but self-assemble poly(*n*-hexylisocyanate) (PHIC) arm and fully flexible but crystallizable poly(ϵ -caprolactone) (PCL) or poly(*L*-lactide) (PLLA) arms.^{18,19} Among several series of these miktoarm star polymers, only one set of PHIC(12k $M_{n,NMR}$)-PCL₁₋₃(5k $M_{n,NMR}$) miktoarm star polymers has been investigated in detail in the aspect of nanoscale thin film morphology using synchrotron grazing incidence X-ray scattering (GIXS), atomic force microscopy (AFM) and differential scanning calorimetry (DSC);²⁰ here $M_{n,NMR}$ is the number-average molecular weight determined by nuclear magnetic resonance (NMR) spectroscopy analysis. Surprisingly, this set of the miktoarm star polymers always demonstrated only vertical lamellar structure in toluene-annealed thin films even though the PCL arm number varied from one to three and the PCL arm component had a volume fraction of 27–29%. The vertical lamellae formation is a very distinct feature compared to the structures observed in common coil-coil miktoarm star polymers including flexible diblock copolymers of comparable volume

fractions. In the vertical lamellar structures, the PHIC phases formed a mixture of horizontal and vertical multilayer structures with a fully extended chain conformation while the PCL phases formed fringed micelle-like crystals and/or highly imperfect folded crystals that are significantly different from typical folded lamellar crystals formed in PCL homopolymer films. Overall, the PHIC(12k)-PCL₁₋₃(5k) miktoarm star polymers revealed exceptionally unique but very complex thin film morphologies. Now there is raised a question: what interesting morphological features can be generated in nanoscale thin films of PHIC-PCL₁₋₃ miktoarm star polymers having other compositions and arm lengths?

In this study we attempted to investigate structural details of PHIC(5k $M_{n,NMR}$)-PCL₁₋₃(17k $M_{n,NMR}$) and PHIC(10k $M_{n,NMR}$)-PCL₁₋₃(10k $M_{n,NMR}$) miktoarm star polymers in nanoscale thin films using synchrotron GIXS and DSC. Very interestingly, all miktoarm polymers always developed only horizontal lamellar structure in toluene-annealed films via phase-separation, regardless of the length of PHIC arm as well as the length and number of PCL arm. In addition, PHIC(10k)-PCL₂(10k) and PHIC(10k)-PCL₃(10k) miktoarm star polymers always developed vertical lamellar structure in the films annealed with chloroform (CHCl₃) solvent vapor. These unusual lamellar structure formations might be driven by factors overriding the volume fraction imbalance such as cooperative efforts of the rigid chain properties, self-assembling characteristics, conformational asymmetry, and compressibilities of PHIC and PCL arms. In the horizontal/vertical lamellar structures the PHIC arm phases were found to maintain strong self-assembling characteristics even in the confined situation originating from the lamellar structure and the arm-jointer; the self-assembly power seemed to be comparable to the homopolymer molecules in thin films. The PCL arm phases were also found to still reveal crystallization ability and, however, their crystallization was significantly suppressed, which might be caused by the confinement effects due to the lamellar structure and the arm-jointer. Overall, crystalline-crystalline PHIC(5k)-PCL₁₋₃(17k) and PHIC(10k)-PCL₁₋₃(10k) miktoarm polymers demonstrated very interesting but unusually complex hierarchical structures in solvent-annealed thin films.

Experimental

Materials and measurements

Two series of PHIC-PCL_m star polymers ($m = 1\sim 3$) were prepared according to the synthetic methods reported previously:¹⁸ PHIC(5k)-PCL_{1~3}(17k) and PHIC(10k)-PCL_{1~3}(10k) (Fig. 1). PHIC and PCL homopolymers were additionally synthesized. Details of the syntheses were given in the Electronic Supplementary Information (ESI) including Fig. S1.[†] The fundamental characteristics of the synthesized polymer products were summarized in Table 1 and 2. In particular, it is noted here that the volume fraction f_{PHIC} of a single PHIC arm ranged in 24.6–26.1% for PHIC(5k)-PCL_{1~3}(17k) and in 50.0–52.8% for PHIC(10k)-PCL_{1~3}(10k).

Thermal stabilities of the polymers were investigated at a rate of 10.0 °C/min in nitrogen atmosphere using a thermogravimeter (model TG/DTA 6200, Seiko Instruments, Tokyo, Japan). Phase transition characteristics of the polymers were examined at a rate of 10.0 °C/min in nitrogen atmosphere using a calorimeter (model DSC 6200, Seiko Instruments).

Each polymer product was dissolved in CHCl₃ and filtered using a disposable syringe equipped with polytetrafluoroethylene filter of pore size 0.2 μm, producing a 1.0 wt% solution. The obtained polymer solutions were spin-coated onto pre-cleaned silicon substrates and dried in vacuum at room temperature for 24 h. The obtained polymer thin films were determined to have a thickness between 80 to 120 nm by using a spectroscopic ellipsometer (model M2000, J. A. Woollam, Lincoln, NE, USA). The as-cast polymer films were further thermally annealed at various temperatures over room temperature to 100 °C or annealed at room temperature under vapors of various solvents including toluene, CHCl₃, carbon disulfide (CS₂) and tetrahydrofuran (THF).

GIXS measurements were conducted at the 3C and 9A beamlines²¹⁻²³ of the Pohang Accelerator Laboratory (PAL). Grazing incidence wide-angle X-ray scattering (GIWAXS) measurements were carried out at a sample-to-detector distances (SDD) of 229 mm while grazing incidence small-angle X-ray scattering (GISAXS) measurements were performed at SDD = 992 and 2922 mm, using an X-ray radiation source with a wavelength λ of 0.1120 nm or 0.1180 nm. Scattering data

were collected for 30–60 s with a two-dimensional (2D) charge-coupled detector (CCD) (model Rayonix 2D MAR, Evanston, IL, USA). The incidence angle α_i of the X-ray beam was set in the range 0.110–0.140°, which was between the critical angle of the polymer thin film and the silicon substrate ($\alpha_{c,f}$ and $\alpha_{c,s}$). Scattering angles were corrected according to the method reported previously.²¹⁻²³

GIXS data analysis

The intensity of GIXS (I_{GIXS}) from structures in a thin film can be expressed by a scattering formula:^{22,23}

$$I_{\text{GIXS}}(\alpha_f, 2\theta_f) \cong \frac{1}{16\pi^2} \cdot \frac{1 - e^{-2\text{Im}(q_z)t}}{2\text{Im}(q_z)} \cdot \left[\begin{array}{l} |T_i T_f|^2 I_1(q_{\parallel}, \text{Re}(q_{1,z})) + \\ |T_i R_f|^2 I_1(q_{\parallel}, \text{Re}(q_{2,z})) + \\ |T_f R_i|^2 I_1(q_{\parallel}, \text{Re}(q_{3,z})) + \\ |R_i R_f|^2 I_1(q_{\parallel}, \text{Re}(q_{4,z})) \end{array} \right] \quad (1)$$

where α_f and $2\theta_f$ are the out-of-plane and in-plane exit angle of the out-going X-ray beam respectively, $\text{Im}(q_z) = |\text{Im}(k_{z,f})| + |\text{Im}(k_{z,i})|$, $\text{Re}(x)$ is the real part of x , t is the film thickness, R_i and T_i are the reflected and transmitted amplitudes of the incoming X-ray beam respectively, and R_f and T_f are the reflected and transmitted amplitudes of the outgoing X-ray beam respectively. In addition, $q_{\parallel} = \sqrt{q_x^2 + q_y^2}$, $q_{1,z} = k_{z,f} - k_{z,i}$, $q_{2,z} = -k_{z,f} - k_{z,i}$, $q_{3,z} = k_{z,f} + k_{z,i}$, and $q_{4,z} = -k_{z,f} + k_{z,i}$; here, $k_{z,i}$ is the z -component of the wave vector of the incoming X-ray beam, which is given by $k_{z,i} = k_o \sqrt{n_R^2 - \cos^2 \alpha_i}$, and $k_{z,f}$ is the z -component of the wave vector of the outgoing X-ray beam, which is given by $k_{z,f} = k_o \sqrt{n_R^2 - \cos^2 \alpha_f}$, where $k_o = 2\pi/\lambda$, λ is the wavelength of the X-ray beam, n_R is the refractive index of the film given by $n_R = 1 - \delta + i\zeta$ with dispersion δ and absorption ζ , and α_i is the out-of-plane grazing incident angle of the incoming X-ray beam. q_x , q_y , and q_z are the components of the scattering vector \mathbf{q} . I_1 is the scattering intensity of the structure in the film, which can be calculated kinematically.

In eq 1, I_1 is the scattered intensity from morphological structures in the film and, thus, can be expressed by the following equation:²²⁻²⁵

$$I_1(\mathbf{q}) = P(\mathbf{q}) \cdot S(\mathbf{q}) \quad (2)$$

where $P(\mathbf{q})$ is the form factor that describes the shape, size, and orientation of scatterers in a thin film, and $S(\mathbf{q})$ is the structure factor which provides information on the relative positions of the group of scatterers, such as the crystal lattice parameters, orientation, dimension, and symmetry in an ordered structure and the interdistance of domains.

The lamellar structure formed in a film can be handled by using either a three or a two layer model. The lamellar structure with the presence of interfacial layers formed in a polymer thin film may be appropriately handled by using a three layer model with a long period L that is composed of a dense layer (thickness: ℓ_1 or ℓ_c ; electron density: ρ_1 or ρ_c), a less dense layer (thickness: ℓ_2 or ℓ_a ; electron density: ρ_2 or ρ_a), and their interfacial layer (thickness: ℓ_i ; electron density: ρ_i) (Fig. 2a). The form factor $P(\mathbf{q})$ of such lamellar structure can be expressed by the following equation:²⁰

$$P(\mathbf{q}) = \left[\begin{aligned} &4L_x L_y \ell_1 (\rho_1 - \rho_i) \cdot \frac{\sin(q_x L_x)}{q_x L_x} \cdot \frac{\sin(q_y L_y)}{q_y L_y} \cdot \frac{\sin(q_z \ell_1)}{q_z \ell_1} + \\ &4L_x L_y H_o (\rho_1 - \rho_2) \cdot \frac{\sin(q_x L_x)}{q_x L_x} \cdot \frac{\sin(q_y L_y)}{q_y L_y} \cdot \frac{\sin(q_z H_o)}{q_z H_o} \end{aligned} \right]^2 \quad (3)$$

where L_x and L_y are the length and width of lamellar structure respectively and $H_o = \ell_1$ (or ℓ_c) + $2\ell_i$ (Fig. 2a). Using the H_o parameter, the thickness (ℓ_2 or ℓ_a) of less dense layer is obtained from the long period L that can be extracted from the structure factor $S(\mathbf{q})$: ℓ_1 (or ℓ_a) = $L - 2\ell_i - \ell_1$ (or ℓ_c).

On the other hand, the lamellar structure with sharp, narrow interfacial layers in a polymer thin film can be expressed by using a two layer model with a long period d_L that is composed of a dense layer (thickness: ℓ_1 or h ; electron density: ρ_H) and a less

dense layer (thickness: ℓ_2 or ℓ_a ; electron density: ρ_L) (Fig. 2b). Its form factor $P(\mathbf{q})$ can be given as below,^{26,27}

$$P(\mathbf{q}) = \exp\left[\frac{1}{4\pi}(l_x^2 q_x^2 + l_y^2 q_y^2 + h^2 q_z^2)\right] \quad (4)$$

where l_x and l_y are the length and width of lamellar structure respectively; the less dense layer thickness ℓ_2 (or ℓ_a) can be obtained from the long period d_L that is extracted from the structure factor $S(\mathbf{q})$: ℓ_2 (or ℓ_a) = $d_L - \ell_1$ (or h).

For the lamellar structures above, the dense layers are generally composed of the laterally ordered polymer chain segments (or alkyl bristles) in fully-extended conformation. The extended chain segments can be considered as molecular cylinders. For such molecular cylindrical scatterers, the form factor $P(\mathbf{q})$ can be expressed by the following equation:^{26,27}

$$P(\mathbf{q}) = \left[2\pi R^2 H \cdot \frac{J_1(q_{\parallel} R)}{q_{\parallel} R} \cdot \frac{\sin(q_z H / 2)}{q_z H / 2}\right]^2 \quad (5)$$

where R and H are the radius and length of cylindrical scatterer.

For the form factors considered above, all structural parameters are further assumed to follow a Gaussian distribution $G(A)$:

$$G(A) = \frac{1}{\sqrt{2\pi}\sigma_A} \exp\left[-\frac{(A - \bar{A})^2}{2\sigma_A^2}\right] \quad (6)$$

where A can be one of the parameters, \bar{A} is the mean value, and σ_A is the standard deviation of A from \bar{A} .

For the nanostructures (i.e., lamellar structures and cylinder assemblies) described above, we have considered all possible structural models and then found that paracrystal model is most appropriate. For a paracrystalline lattice consisting of

the three layers or two layers or cylinders described above, the structure factor $S(\mathbf{q})$ (the so-called interference function or lattice factor) can be determined from the Fourier transform of a complete set of lattice points.^{20,22,26,27} In a paracrystal with distortion of the second kind, the positions of the lattice points can only be described with a positional distribution function (i.e., g -factor). In the simple case where the autocorrelation function of the crystal lattice is given by the convolution product of the distributions of the lattice points along three axes, and the distribution function is a Gaussian, $S(\mathbf{q})$ can be expressed by the following equation:²⁶

$$S(\mathbf{q}) = \prod_{k=1}^3 Z_k(\mathbf{q}) \quad (7)$$

$$Z_k(\mathbf{q}) = 1 + \frac{F_k(\mathbf{q})}{1 - F_k(\mathbf{q})} + \frac{F_k^*(\mathbf{q})}{1 - F_k^*(\mathbf{q})} \quad (8)$$

$$F_k(\mathbf{q}) = |F_k(\mathbf{q})| e^{-i\mathbf{q}\cdot\mathbf{a}_k} \quad (9)$$

$$|F_k(\mathbf{q})| = \exp\left[-\frac{1}{2}(q_1^2 g_1^2 + q_2^2 g_2^2 + q_3^2 g_3^2)\right]. \quad (10)$$

Here g_1 , g_2 , and g_3 are the components of the g -factor defined as

$$g_1 = \Delta\mathbf{a}_1/\mathbf{a}_1 \quad (11a)$$

$$g_2 = \Delta\mathbf{a}_2/\mathbf{a}_2 \quad (11b)$$

$$g_3 = \Delta\mathbf{a}_3/\mathbf{a}_3 \quad (11c)$$

where \mathbf{a}_k is the component of the fundamental vector \mathbf{a} of the domain structure and $\Delta\mathbf{a}_k$ is the displacement of the vector \mathbf{a}_k . And q_1 , q_2 , and q_3 are the components of the scattering vector \mathbf{q} .

For the lamellar structure composed of three layers, the components of \mathbf{q} in eq 10 are defined by

$$q_1 = \mathbf{a}_1 \cdot \mathbf{q}_x = |d_x \times \mathbf{q}_x| \quad (12a)$$

$$q_2 = \mathbf{a}_2 \cdot \mathbf{q}_y = |d_y \times \mathbf{q}_y| \quad (12b)$$

$$q_3 = \mathbf{a}_3 \cdot \mathbf{q}_z = |L \times \mathbf{q}_z| \quad (12c)$$

where d_x and d_y are the lattice dimension parameters (i.e., d -spacing values) along the q_x - and q_y -direction respectively, and L is the long period along the q_z -direction. In case of the lamellar structure composed of two layers, the components of \mathbf{q} in eq 10 are defined by

$$q_1 = \mathbf{a}_1 \cdot \mathbf{q}_x = |d_x \times \mathbf{q}_x| \quad (13a)$$

$$q_2 = \mathbf{a}_2 \cdot \mathbf{q}_y = |d_y \times \mathbf{q}_y| \quad (13b)$$

$$q_3 = \mathbf{a}_3 \cdot \mathbf{q}_z = |d_L \times \mathbf{q}_z| \quad (13c)$$

where d_x and d_y are the lattice dimension parameters (i.e., d -spacing values) along the q_x - and q_y -direction respectively, and d_L is the long period along the q_z -direction.

For the laterally-ordered n -hexyl bristles in the PHIC homopolymer films as well as in the PHIC phase domains of the PHIC-PCL_{*m*} films, the components of \mathbf{q} can be defined by

$$q_1 = \mathbf{a}_1 \cdot \mathbf{q}_x + \mathbf{a}_1 \cdot \mathbf{q}_y = |d_3 \sin\beta \times \mathbf{q}_x + d_3 \cos\beta \times \mathbf{q}_y| \quad (14a)$$

$$q_2 = \mathbf{a}_2 \cdot \mathbf{q}_x + \mathbf{a}_2 \cdot \mathbf{q}_y = |0 \times \mathbf{q}_x + d_2 \times \mathbf{q}_y| \quad (14b)$$

$$q_3 = \mathbf{a}_3 \cdot \mathbf{q}_x + \mathbf{a}_3 \cdot \mathbf{q}_y = |d_1 \times \mathbf{q}_x + 0 \times \mathbf{q}_y| \quad (14c)$$

where d_1 is the interdistance between the n -hexyl bristles of the neighboring polymer chains whose repeat units are matched in position along their backbones, d_2 is the interdistance between the nearest n -hexyl bristles along the polymer backbone, d_3 is the interdistance between the n -hexyl bristles of the nearest neighboring polymer chains, and β is the angle between the d_3 - and d_2 -direction (Fig. S2a).[†]

In case of the orthorhombic assembly of the extended chain segments in the PCL crystals in the PCL homopolymer film as well as in the PCL phases of the PHIC-PCL_{*m*} films, the components of \mathbf{q} can be defined by

$$q_1 = \mathbf{a}_1 \cdot \mathbf{q}_x + \mathbf{a}_1 \cdot \mathbf{q}_y = |d_{020} \times \mathbf{q}_x + d_{200} \times \mathbf{q}_y| \quad (15a)$$

$$q_2 = \mathbf{a}_2 \cdot \mathbf{q}_x + \mathbf{a}_2 \cdot \mathbf{q}_y = |0 \times \mathbf{q}_x + (2 \cdot d_{200}) \times \mathbf{q}_y| \quad (15b)$$

$$q_3 = \mathbf{a}_3 \cdot \mathbf{q}_z = |d_{002} \times \mathbf{q}_z| \quad (15c)$$

where d_{020} and d_{200} are the lattice dimension parameters (i.e., d -spacing values) of orthorhombic lattice as shown in Fig. S2b.[†]

Furthermore, information on orientations of the lamellar structures and/or the laterally-ordered structures can be obtained from GIXS data. An orientation vector \mathbf{n}_i is defined for the structure as shown in Fig. 2 and S2b.[†] The orientation distribution of the structure with \mathbf{n}_i is given by a function $D(\varphi)$, where φ is the polar angle between the \mathbf{n}_i vector and the out-of-plane of the film. In relation to the distribution of the structure orientation, $D(\varphi)$ can generally be considered as a Gaussian distribution:

$$D(\varphi) = \frac{1}{\sqrt{2\pi}\sigma_\varphi} \exp\left[-\frac{(\varphi - \bar{\varphi})^2}{2\sigma_\varphi^2}\right] \quad (16)$$

where $\bar{\varphi}$ and σ_φ are the mean angle of φ and the standard deviation of φ from $\bar{\varphi}$, respectively. The observed scattering intensity $I_{\text{GIXS},\varphi}(\mathbf{q})$ is obtained by integrating $I_{\text{GIXS}}(\mathbf{q})$ over possible orientations of the structure:

$$I_{\text{GIXS},\varphi}(\mathbf{q}) = \int_{-\pi}^{\pi} I_{\text{GIXS}}(\mathbf{q}) D(\varphi) d\varphi \quad (17)$$

The second order orientation factor O_s can be defined as the following equation:^{20,26,27}

$$O_s = \int D(\varphi) \frac{(3\cos^2\varphi - 1)}{2} d\varphi \quad (18)$$

When $D(\varphi)$ is strongly peaked around $\varphi = 0^\circ$ (i.e. horizontal alignment), $\cos\varphi = 1$ and $O_s = 1$. On the other hand, when $\varphi = 90^\circ$ (i.e., vertical alignment), $\cos\varphi = 0$ and $O_s = -0.5$. If the orientation is entirely random, $\langle \cos^2\varphi \rangle = 1/3$ and $O_s = 0$. Therefore, O_s is a measure of the orientation of structures.

Results and Discussions

Thermal properties

Thermal properties of PHIC(5k, 10k) and PCL(10k, 15k) homopolymers and their miktoarm star polymers (PHIC(5k)-PCL₁₋₃(17k) and PHIC(10k)-PCL₁₋₃(10k)) were studied in nitrogen atmosphere by thermogravimetry (TGA) and DSC. The PHIC(5k) polymer was found to begin its degradation at 179 °C ($= T_{d,PHIC}$); the PHIC(10k) polymer revealed $T_{d,PHIC} = 180$ °C (Fig. 3d and S3d[†]). In comparison, degradation was started at 260 °C ($= T_{d,PCL}$) for the PCL(10k) polymer and 260 °C for the PCL(15k) polymer (Fig. 3e and S3e[†]). For both the PHIC and PCL homopolymers, higher molecular weight polymer exhibited slightly higher thermal stabilities. Overall, the PHIC homopolymers revealed relatively lower thermal stability than did the PCL homopolymers. Furthermore, all the homopolymers showed a single-step degradation behavior.

In contrast, all the PHIC-PCL_m miktoarm star polymers were found to undergo a two-step degradation process, regardless of the number of arms present (Fig. 3a-3c and S3a-S3c[†]). Considering the thermal stabilities of the homopolymers, the first step of degradation in the low temperature region was originated from the PHIC arm, whereas the second step of degradation in the high temperature region was attributed to the PCL arm(s). The PHIC(5k) and PHIC(10k) arms revealed $T_{d,PHIC} = 197$ °C and 200 °C respectively, regardless of the number of PCL arms present. The PCL₁₋₃(17k) arms, as well as the PCL₁₋₃(10k) arms showed $T_{d,PCL} = ca. 280$ °C, regardless of the significant reduction of molecular weight in the arms due to the variation of PCL arm number from one to three. Interestingly, the $T_{d,PHIC}$ values are 18–20 °C higher than those of the corresponding homopolymers. Moreover, the $T_{d,PCL}$ values are 20 °C higher than those of the PCL(10k) and PCL(15k) homopolymers. In general, it is known that the thermal stability of a polymer is negatively affected by the presence of chain end-groups. Taking into consideration this fact, the significantly enhanced stabilities of PHIC and PCL arms in the PHIC-PCL_m miktoarm star polymers might be attributed to their one-end group capped with the other jointed arm(s).

Considering the thermal stability results above, DSC runs were carried out over the temperature range –50 °C to 150 °C (Fig. 3f-3j and S3f-S3j[†]; Table 1). The PHIC

homo polymers, as well as the PHIC arms in the PHIC-PCL_m miktoarm star polymers did not reveal any discernible phase transitions. In contrast, the PCL homo polymers and arms in the miktoarm polymers always showed an exothermic crystallization peak in cooling run from the melt state and an endothermic crystal melting peak in heating run. The PCL(15k) homo polymer exhibited a crystallization temperature $T_{c,PCL}$ of 23.2 °C, a crystal melting temperature $T_{m,PCL}$ of 54.6 °C, and a heat of fusion $\Delta H_{f,PCL}$, 72.05 J/g for the crystal melting. From the $\Delta H_{f,PCL}$ value, the crystallinity $X_{c,PCL}$ was estimated to be 53.0%, using that (136 J/g) of a perfect PCL crystal.²⁸ Similar results were measured for the PCL(10k) homo polymer. These parameter values, however, were found to be lowered for the PCL arm(s) in the miktoarm polymers. Such suppressions were relatively more severe with increasing the PCL arm number, which may be caused by the reduction in the molecular weight of the individual PCL arms and the geometrical confinement effect of the PCL arm phases generated in the miktoarm polymer samples via phase-separation. The results further suggest that, in the miktoarm polymer samples, higher number of PCL arms result in smaller and more imperfect crystals.

GISAXS analysis

Morphological structures of the miktoarm star polymers in thin films were investigated using synchrotron GIXS analysis. The as-cast films of the miktoarm star polymers were found to comprise of highly disordered structures in random orientation. Thus, the as-cast films were subjected to post treatments, including thermal-annealing under various conditions and solvent annealing in various solvents, to induce the formation of nanostructures via phase-separation. As a result, the miktoarm star polymer thin films could develop ordered nanostructures via toluene- or CHCl₃-annealing, rather than any other post-treatments. The PHIC(5k)-PCL₁₋₃(17k) films were found to develop ordered nanostructures under toluene-annealing at room temperature for 2.5 h. The PHIC(10k)-PCL₁₋₃(10k) films formed nanostructures under toluene-annealing at room temperature for 2.0–4.0 h or CHCl₃-annealing at room temperature for 45 min to 3.0 h.

Fig. 4 shows representative 2D GISAXS patterns of the toluene-annealed films (110–120 nm thick) of PHIC(5k)-PCL₁₋₃(17k) polymers. From the 2D scattering

patterns, the out-of-plane scattering profiles were extracted along the α_f direction at $2\theta_f = 0.140^\circ$ or 0.160° , whereas the in-plane scattering profiles were extracted along the $2\theta_f$ direction at $\alpha_f = 0.190^\circ$ (Fig. 5a-1 and 5a-2). The PHIC(5k)-PCL(17k) films presented two peaks around $\alpha_f = 0.39^\circ$ and 1.16° in the out-of-plane scattering profile. Their relative scattering vector lengths from the specular reflection position were 1 and 2, respectively, indicating that they are the first- and second-order scattering peaks arising from the same structural origin. These out-of-plane scattering characteristics inform that horizontally-oriented lamellar structures were formed in the films. In addition, the in-plane scattering profile revealed a very weak peak around $2\theta_f = 0.26^\circ$, which was not related to the two peaks in the out-of-plane scattering profile. The appearance of the in-plane scattering peak suggests that vertically-oriented lamellar structures were present as a very minor component in the films. These scattering results collectively inform that there was formed a mixture of horizontal lamellar structure (major structural component) and vertical lamellar structure (very minor component) in the PHIC(5k)-PCL(17k) films. In contrast, the PHIC(5k)-PCL₂(17k) and PHIC(5k)-PCL₃(17k) films showed such two peaks only in the out-of-plane scattering profile, indicating that only horizontal lamellar structures were formed in the PHIC(5k)-PCL₂(17k) and PHIC(5k)-PCL₃(17k) films. All out-of-plane and in-plane scattering profiles could be satisfactorily fitted using the GIXS formula derived for a lamellar structure model with three layers rather than two layers, as shown in Fig. 5a-1 and 5a-2. The obtained structural parameters are summarized in Table 2.

The horizontal lamellar structures formed in the toluene-annealed PHIC(5k)-PCL₁₋₃(17k) films were characterized by $L = 16.0\sim 16.4$ nm, $l_1 = 7.7\sim 8.3$ nm, $l_2 = 2.0\sim 2.2$ nm, $l_3 = 3.9\sim 4.1$ nm, $O_{s,1} = 0.916\sim 0.926$ ($\bar{\varphi}_1 = 0^\circ$ and $\sigma_{\varphi_1} = 13.1\sim 14.0^\circ$), and $g = 0.27\sim 0.31$ (Table 2). The l_1 values were always larger than the l_2 values. Considering the volume fractions of the PHIC(5k) and PCL(17k) arms and their phase-separation nature, the l_1 and l_3 could be assigned as the PCL arm layer thickness ($= l_{\text{PCL}}$) and the PHIC arm layer thickness ($= l_{\text{PHIC}}$) respectively, while the l_2 could be assigned as the thickness of interfacial layer ($= l_i$) between the PCL and PHIC arm layers. As the PCL arm number was increased, L , l_{PCL} and l_{PHIC} were

slightly shortened with a minor thickening of ℓ_i . Nevertheless, both the g and O_s values were interestingly improved somewhat. The vertical lamellar structure additionally formed in the PHIC(5k)-PCL(17k) films was identified by $L = 21.8$ nm, $\ell_{\text{PCL}} = 8.9$ nm, $\ell_i = 3.2$ nm, $\ell_{\text{PHIC}} = 6.5$ nm, $\bar{\varphi}_1 = 90^\circ$, and $g = 0.38$ (Table 2). Overall, the GISAXS analysis results confirm that all PHIC(5k)-PCL₁₋₃(17k) polymers developed mainly horizontal lamellar structure in thin films, regardless of the number of arms, via phase-separation with the aid of toluene-annealing, but the structural parameters including the positional ordering and orientation were influenced slightly by the number and length of PCL arm. Furthermore, the determined structural parameters were used to reconstruct the 2D GISAXS images. The reconstructed scattering images were confirmed to be in good agreement with the experimental data (Fig. 4a-3, 4b-3, and 4c-3).

Fig. 6 presents representative 2D GISAXS patterns of the toluene-annealed PHIC(10k)-PCL₁₋₃(10k) films (80–90 nm thick). The out-of-plane scattering profiles were extracted along the α_f direction at $2\theta_f = 0.100^\circ$, whereas the in-plane scattering profiles were extracted along the $2\theta_f$ direction at $\alpha_f = 0.160^\circ$ (Fig. 5b-1 and 5b-2). The miktoarm star polymer films showed featured scattering patterns, which apparently resembled those of the toluene-annealed PHIC(5k)-PCL₂(17k) and PHIC(5k)-PCL₃(17k) films. The out-of-plane and in-plane and out-of-plane scattering profiles could be successfully fitted using the GIXS formula derived for a lamellar structure model with three layers. The obtained structural parameters are listed in Table 2.

The horizontal lamellar structures developed in the toluene-annealed PHIC(10k)-PCL₁₋₃(10k) films were characterized by $L = 18.5\sim 22.9$ nm, $\ell_{\text{PCL}} = 5.6\sim 7.1$ nm, $\ell_i = 2.2\sim 2.4$ nm, $\ell_{\text{PHIC}} = 8.1\sim 11.2$ nm, $O_{s,1} = 0.919\sim 0.970$ ($\bar{\varphi}_1 = 0^\circ$ and $\sigma_{\varphi_1} = 8.2\sim 13.7^\circ$), and $g = 0.31\sim 0.34$ (Table 2). The number and length of PCL arm were found to affect somewhat the structural parameters. It is remarkable that the ℓ_{PHIC} values were larger than the ℓ_{PCL} values even though the volume fractions of PHIC arm were comparable to those of PCL arms. Moreover, the L values were always larger than those of the horizontal lamellar structures formed in the toluene-annealed films of PHIC(5k)-PCL₁₋₃(17k) although their overall molecular weights were comparable each other. The GISAXS analysis results collectively indicate that

the PHIC(10k)-PCL₁₋₃(10k) miktoarm star polymers also developed only horizontal lamellar structure in the toluene-annealed thin films, regardless of the number and length of PCL arm. The scattering images reconstructed with determined structural parameters showed good agreement with the experimental patterns (Fig. 6a-3, 6b-3, and 6c-3).

Fig. 7 presents representative 2D GISAXS patterns of the CHCl₃-annealed PHIC(10k)-PCL₁₋₃(10k) films (80–90 nm thick). The out-of-plane scattering profiles were extracted along the α_f direction at $2\theta_f = 0.060^\circ$ or 0.080° , whereas the in-plane scattering profiles were extracted along the $2\theta_f$ direction at $\alpha_f = 0.140^\circ$ (Fig. 5c-1 and 5c-2). The PHIC(10k)-PCL(10k) films revealed featured scattering patterns, which apparently resembled those of the toluene-annealed films. These results indicate that only horizontal lamellar structure was formed in the PHIC(10k)-PCL(10k) films. The PHIC(10k)-PCL₂(10k) and PHIC(10k)-PCL₃(10k) films, however, showed different scattering patterns. The in-plane scattering profiles revealed two scattering peaks in which the relative scattering vector lengths from the specular reflection position were 1 and 2, respectively. Such scattering peaks could not be discernible in the out-of-plane scattering profiles. These scattering characteristics inform that only vertical lamellar structures were formed in the PHIC(10k)-PCL₂(10k) and PHIC(10k)-PCL₃(10k) films. The in-plane and/or out-of-plane scattering profiles could be satisfactorily fitted using the GIXS formula derived for a lamellar structure model with three layers. The determined structural parameters are listed in Table 2.

The CHCl₃-annealed PHIC(10k)-PCL₁₋₃(10k) films formed relatively larger dimensions of lamellar structures, compared to those developed in the toluene-annealed films. Furthermore, the positional disorder (i.e., g value) of lamellar structure was increased by CHCl₃-annealing. More interestingly, the orientation of the lamellar structures formed in the CHCl₃-annealed films was significantly affected by the number and length of PCL arm. Namely, a horizontal lamellar structure was developed in the PHIC(10k)-PCL(10k) films while a vertical lamellar structure was generated in the PHIC(10k)-PCL₂(10k) and PHIC(10k)-PCL₃(10k) films. Overall, the scattering analysis results indicate that the PHIC(10k)-PCL₁₋₃(10k) miktoarm star polymers also developed a lamellar structure in the CHCl₃-annealed thin films and, however, their main orientation director was significantly changed towards either the

in-plane direction or the out-of-plane direction of the film by increasing the PCL arm number and shortening the PCL arm length. The scattering images reconstructed with determined structural parameters were in good agreement with the experimental patterns (Fig. 7a-3, 7b-3, and 7c-3). Furthermore, taking into account the morphologies in the toluene-annealed films, these results indicate that both PHIC(10k)-PCL₂(10k) and PHIC(10k)-PCL₃(10k) in thin films could simply demonstrate either horizontal lamellar structure or vertical lamellar structure by changing solvent-annealing conditions, namely, toluene-annealing versus CHCl₃-annealing.

As discussed above, surprisingly the two series of PHIC-PCL₁₋₃ miktoarm star polymers in the present study demonstrated only lamellar structures (horizontal or vertical lamellae) in the toluene- and CHCl₃-annealed films, regardless of the volume fractions of PHIC and PCL arm components as well as of the number and length of PCL arm. In addition, another series of PHIC(12k)-PCL₁₋₃(5k) miktoarm star polymers was previously reported to form only vertical lamellar structures in toluene-annealed films in regardless of the volume fractions of PHIC and PCL arm components as well as of the number and length of PCL arm.²⁰ These results collectively confirmed that PHIC-PCL₁₋₃ miktoarm star polymers with $f_{\text{PHIC}} = 24\sim 73\%$ own a strong tendency to build up lamellar structure in thin films via phase-separation with an aid of either toluene- or CHCl₃-annealing. In particular, the horizontal lamellar structures formed in the PHIC(5k)-PCL₁₋₃(17k) and PHIC(12k)-PCL₁₋₃(5k) films are quite far from the hexagonally-packed cylinder structures commonly observed in the same or similar volume fractions of amorphous-amorphous diblock copolymers^{22,29} crystalline-amorphous diblock copolymers,^{30,31} crystalline-crystalline diblock copolymers,³² and rigid-rigid diblock copolymers.³³

Here a big question is arising: How come the nanostructure formations of PHIC-PCL₁₋₃ miktoarm star polymers based on phase-separation could not follow any predictions from a simple rule of volume fractions? Recently, the phase diagram of diblock copolymer has been proposed to be influenced by a number of factors such conformational asymmetry, chain stiffness, compressibility, and modifications to the enthalpic interactions, in addition to the volume fractions.³⁴ PHIC has recently been discovered to reveal 2₁ or 8₃ helical conformation in solid state thin films and

therefore behave like a highly rigid polymer chain, favorably self-assembling into molecular multilayer structure in toluene-annealed films or hexagonal cylinder structure in CS₂-annealed films.²⁷ PCL, however, can be classified as a flexible polymer and is known to undergo very rapid crystallization, thereby showing high crystallinity in thin and bulk states.²⁰ Due to such high crystallinity, PCL may behave like a rigid polymer rather than a flexible polymer in temperatures below $T_{m,PCL}$. Taking these facts into account, the formation of such the interesting, exceptional lamellar structures in the PHIC(5k)-PCL₁₋₃(17k) and PHIC(12k)-PCL₁₋₃(5k) films may be attributed to cooperative works of the rigid chain properties, self-assembling characteristics, conformational asymmetry, and compressibilities of PHIC and PCL arms which can override the volume fraction rule. These factors may further drive to develop lamellar structures in case of the PHIC(10k)-PCL₁₋₃(10k) films, which are under getting a positive assistance from the volume fraction rule. Among such the factors, the rigid chain properties, self-assembling characteristics, and conformational asymmetry are speculated to make significant contributions to the formation of unusual lamellar structure in the toluene- or CHCl₃-annealed PHIC-PCL₁₋₃ films.

The toluene- and CHCl₃-annealed films of PHIC and PCL homopolymers were also characterized by GISAXS analysis. The measured 2D scattering patterns are shown in Fig. 4d-1, 4d-2, 5d-1, 5d-2, 7d-1, and 7d-2. The out-of-plane scattering profiles were extracted along the α_f direction at $2\theta_f = 0.090^\circ$ or 0.100° , whereas the in-plane scattering profiles were extracted along the $2\theta_f$ direction at $\alpha_f = 0.140^\circ$ or 0.170° (Fig. 5). All PHIC(5k) and PHIC(10k) homopolymer films revealed a featureless scattering pattern, regardless of the solvent-annealing history. In contrast, the PCL(10k) and PCL(15k) homopolymer films presented a featured scattering pattern. The out-of-plane scattering profiles displayed a broad weak peak at $0.30\text{--}0.80^\circ$. The broad nature of this scattering peak was attributed to the heavy overlap between the scattering features along the α_f direction from the reflected and transmitted X-ray beams. Such the scattering peak could not be discerned in the in-plane scattering profile of the PCL(10k) films (Fig. 5b-2). A very weak, broad peak was, however, observed around $2\theta_f = 0.50^\circ$ in the in-plane scattering profile of the PCL(15k) films (Fig. 5a-2). These scattering characteristics informed that a horizontal lamellar structure was predominantly formed in the PCL films. In case of the

PCL(15k) film, a vertical lamellar structure was present as a very minor structural component, in addition to the horizontal lamellar structures. The out-of-plane and in-plane scattering profiles could be satisfactorily fitted using the GIXS formula derived for a lamellar structure model with three layers. The obtained structural parameters are listed in Table 2.

The horizontal lamellar structure formed in the toluene-annealed PCL(15k) films was characterized by $L = 12.6$ nm, $\ell_c = 3.3$ nm, $\ell_i = 1.6$ nm, $\ell_a = 6.1$ nm, $O_{s,1} = 0.982$ ($\bar{\varphi}_1 = 0^\circ$ and $\sigma_{\varphi_1} = 6.3^\circ$), and $g = 0.35$. The crystal layer thickness ℓ_c was almost a half of the amorphous layer thickness ℓ_a . Similar structural parameters were determined for the horizontal lamellar structures formed in the PCL(10k) films, regardless of the toluene- and CHCl_3 -annealing. The vertical lamellar structure additionally formed as a very minor component in the PHIC(15k) films was characterized by $L = 21.8$ nm, $\ell_{\text{PCL}} = 8.9$ nm, $\ell_i = 3.2$ nm, $\ell_{\text{PHIC}} = 6.5$ nm, $\bar{\varphi}_1 = 90^\circ$, and $g = 0.38$. Overall, the lamellar structures had relatively higher in-plane orientation order, compared to those of the miktoarm star polymer films. Moreover, the scattering images reconstructed with determined structural parameters were confirmed to have good agreement with the experimental data (Fig. 4d-3, 6d-3, and 7d-3). Taking into account the $T_{c,\text{PCL}} = 23.2$ °C and $T_{m,\text{PCL}} = 54.6$ °C of PCL(15k) measured in the DSC runs above, the formation of horizontal lamellar crystal structures in the PCL films might be induced mainly by thermal-annealing (which was carried out during kept at room temperature after the solvent-annealing), rather than toluene- or CHCl_3 -annealing.

Considering the lamellar crystal structure formation nature of PCL homopolymers, one may expect that the PCL arm layers in the lamellar structured PHIC-PCL₁₋₃ films can undergo crystallization, forming lamellar crystals. If such nanostructure formation is possible, lamellar crystals can undergo lateral growth using the whole spaces in the PCL arm layers but have stack growth being allowed only along the in-plane direction of the PCL arm layers because of the very limited thickness (5.6–11.4 nm) of the PCL arm layers. The CHCl_3 -annealed PHIC(10k)-PCL₂(10k) films additionally revealed a very broad, weak scattering peak around 1.02° (6.6 nm d -spacing) in the out-of-plane scattering profile, as shown in Fig. 5c-1.

Similar scattering peak was observed around 1.22° (5.5 nm d -spacing) in the out-of-plane scattering profile of the CHCl_3 -annealed PHIC(10k)-PCL₃(10k) films. The d -spacing values are almost a half of the L value of the lamellar structure formed in the PCL(10k) homopolymer films. They are comparable with the ℓ_a of the PCL(10k) films but almost twice the ℓ_c value of the PCL(10k) films. Thus, the observation of such the additional scattering peaks suggests that a regular type of lamellar crystals could not be formed even along the in-plane direction of the PCL arm layers. Instead, a heterogeneous semicrystalline morphology consisting of highly imperfect or micelle-like crystals might be developed in the PCL arm layers; in such heterogeneous morphology, the crystals were distributed over a mean distance of 5.5–6.6 nm. Except these two film cases, the other miktoarm star polymer films could not show any scattering signals about either such heterogeneous semicrystalline morphology formation or typical lamellar crystal stack formation in the PCL arm layers. These results collectively concluded that nanostructures like typical lamellar crystals could not be developed within the PCL arm layers. Instead, there might be formed highly defected crystals or fringed micelle-like crystals in the PCL arm layer phases. Such imperfect crystal formation might result from the confinement effects caused by the thin PCL arm layer geometry and the arm-jointer.

The details of nanostructures (i.e., lamellar structures), which were determined for the solvent-annealed thin films above, are schematically illustrated in Fig. 8-10. No nanostructure could be identified for the PHIC(5k) and PHIC(10k) films (Fig. 8). In contrast, the PCL(10k) and PCL(17k) polymers revealed a lamellar structure via thermodynamically favorable crystallization (Fig. 9A and B). Moreover, their miktoarm polymers nicely demonstrated lamellar structures in thin films, regardless of the number and length of arms and of the volume ratio, via phase-separations. Instead, the preferential orientation of lamellar structures in the miktoarm polymer films was controlled by the solvent used in the annealing process and further influenced by the number and length of PCL arm (Fig. 10A and B).

GIWAXS analysis

The toluene- and CHCl_3 -annealed PHIC(5k)-PCL₁₋₃(17k) and PHIC(10k)-PCL₁₋₃(10k) films were further investigated by GIWAXS analysis, in order to get

more structural information on the PHIC arm layers as well as the PCL arm layers in the horizontal or vertical lamellar structure. The measured 2D scattering patterns are shown in Fig. 11. The PHIC and PCL homopolymer films were also examined by GIWAXS, in order to get structural information as references. From the 2D scattering patterns, the out-of-plane scattering profiles were extracted along the α_f direction at $2\theta_f = 0.000^\circ$, whereas the in-plane scattering profiles were extracted along the $2\theta_f$ direction at $\alpha_f = 0.260^\circ, 0.300^\circ$ or 0.390° (Fig. 12).

The PHIC(5k) and PHIC(10k) films showed a clearly featured GIWAXS pattern, as shown in Fig. 11a-1, 11b-1, 11c-1, and 12. The toluene-annealed PHIC(5k) films revealed characteristic peaks at $3.85^\circ, 7.69^\circ$, and 11.52° along the α_f direction at $2\theta_f = 0^\circ$ as well as along the $2\theta_f$ direction at $\alpha_f = 0^\circ$, which were periodic arc peaks with a regular spacing (Fig. 11a-1). These periodic arc peaks had much stronger intensity in the out-of-plane profile than in the in-plane scattering profile (Fig. 12a-1 and 12a-2). Similar periodic arc peaks were observed for the toluene-annealed PHIC(10k) films (Fig. 11b-1, 12b-1 and 12b-2). These scattering characteristics indicate that both horizontal and vertical lamellar structures were present in the toluene-annealed PHIC(5k) and PHIC(10k) films. Unlike the toluene-annealed films, the CHCl_3 -annealed films showed such the periodic arc peaks only along the α_f direction at $2\theta_f = 0^\circ$ (Fig. 11c-1, 12c-1 and 12c-2), indicating that only horizontal lamellar structure was developed in the CHCl_3 -annealed films. All scattering profiles were attempted to be analyzed using the GIXS formulas derived for lamellar structure models with two and three layers. Then it was found that both the lamellar models could be suitable to analyze the scattering profiles, indicating that the lamellar structures in the PHIC films were composed of more ordered layers sharply interfaced with less ordered layers. Fig. 12 showed the out-of-plane and in-plane scattering profiles fitted satisfactorily with the GIXS formula derived for a lamellar structure model with two layers (Fig. 2b and S2a[†]). The obtained structural parameters are summarized in Tables 3, 4, and 5.

The structural parameters of the toluene-annealed PHIC(5k) and PHIC(10k) in this study are in good agreement with those reported previously for the toluene-annealed PHIC(10k) films.²⁰ These results confirm that both horizontal and vertical lamellar (i.e., multibilayer) structures with a fully extended conformation of the

backbone and bristle were highly reproduced with a volume fraction $\phi_{h,2}/\phi_{v,2}$ of ca. 80/20 in PHIC thin films over the molecular weight range 5400 to 10400 via toluene-annealing. Moreover, the structural parameters of the CHCl_3 -annealed PHIC(10k) film, except for orientation factor, are well matched with those of the toluene-annealed films. Excitingly, the CHCl_3 -annealing process, however, produced only horizontal multibilayer structure (i.e., edge-on structure) in the PHIC films. This is the first successful demonstration that PHIC can favorably self-assemble in thin films as a well-defined edge-on structure via CHCl_3 -annealing. Overall, this study confirms again that PHIC homopolymer owns a strong tendency to favorably self-assemble in thin films as multibilayer structure with the backbone in 2_1 conformation and the bristles in fully extended conformation via toluene- or CHCl_3 -annealing.

In view of the orientation control of multibilayer structure formation, the results of the present study are surprisingly different from those previously reported for the PHIC(61k) polymer bearing benzaldehyde group (which originated from the sodium benzaldehyde initiator used in solution anionic polymerization in THF at $-98\text{ }^\circ\text{C}$) at one end of the backbone chain.²⁷ In toluene-annealed films the PHIC(61k) polymer formed only edge-on structure rather than a mixture of edge-on structure and vertical multibilayer structure (i.e., face-on structure); in CHCl_3 -annealed films PHIC(61k) polymer, however, built a mixture of edge-on and face-on structures rather than edge-on structure only.²⁷ Here, it is noteworthy that the CHCl_3 -annealed PHIC(10k) film made edge-on structure with much higher degree of structural and orientational orders, compared to that formed in the toluene-annealed PHIC(61k) film. These significant differences might be associated with their polymerization histories (bulk polymerization at $0\text{ }^\circ\text{C}$ versus solution polymerization at THF at $-98\text{ }^\circ\text{C}$), initiator-originated one-end groups (benzyloxy versus benzaldehyde), molecular weight (5400 and 10400 versus 61000), and polydispersity (1.05 and 1.11 versus 1.20). In particular, the difference in the backbone end groups, as well as in the polydispersities may play a key role to cause such the significant differences in the multibilayer structure formation and orientation control.

In conjunction with the mixed edge-on and face-on structures in the toluene-annealed PHIC(5k) and PHIC(10k) films, one may imagine that orientational domains are developed in the toluene-annealed films. No scattering signals about such

orientational domains could be discernible in the GISAXS patterns, however, as discussed in an earlier section. Perhaps, no detection of such orientational domains may be caused either by no or very small electron density difference between the edge-on and face-on structural domains occupied fully through the whole film or by their sizes larger than the resolution limit of the GISAXS setup used.

The toluene-annealed PCL(15k) films revealed a featured GIWAXS pattern. They clearly showed characteristic reflections such as {002}, {004}, {101}, {102}, {110}, and {200}, which were originated from PCL crystals with orthorhombic lattice (Fig. 11a-2). Similar GIWAXS patterns were measured for the toluene- and CHCl₃-annealed PCL(10k) films (Fig. 11b-2 and 11c-2). The out-of-plane and in-plane scattering profiles could successfully analyzed (Fig. 12), using the GIXS formula derived for an orthorhombic crystal lattice model (Fig. S2b[†]). The determined structural parameters were summarized in Table 3, 4 and 5. The orthorhombic lattices of lamellar crystals formed in all PCL films were characterized by the dimensional parameters, such as $a = 0.80$ nm, $b = 0.53$ nm, and $c = 1.78$ nm, and the high positional order ($g = 0.060\sim 0.065$). The c value corresponds to the length of two repeat units plus one carbonyl carbon atom in a fully extended PCL conformation. Furthermore, the orthorhombic crystals were present in two different orientations, which related directly to the mixture of horizontal and vertical lamellar structures formed in the PCL films. The volume fraction ratio ($\phi_{v,3}/\phi_{h,3}$) in the vertical and horizontal orthorhombic crystals was 71/29 for the toluene-annealed PCL(15k) films, 93/7 for the toluene-annealed PCL(10k) films, and 79/21 for the CHCl₃-annealed PCL(10k) films.

All PHIC(5k)-PCL₁₋₃(17k) and PHIC(10k)-PCL₁₋₃(10k) films revealed a complex featured GIWAXS pattern, as shown in Fig. 11 and 12. Such complex scattering features were found to originate from the scattering peaks of multilayer structured PHIC and orthorhombic PCL crystals. For each scattering pattern, the origin of each scattering peak was thus identified with aids of the scattering characteristics of PHIC and PCL homopolymer films. Then, the out-of-plane and in-plane scattering profiles were successfully analyzed with using the GIXS formulas derived for a lamellar model with two layers and an orthorhombic lattice (Fig. 12). The GIWAXS analysis results are listed in Table 3, 4 and 5. For all the lamellar

structured miktoarm polymer films, the structural dimensions of multilayer structures formed in the PHIC layers were comparable with that those of the multilayer structured PHIC homopolymer films, regardless of the number and length of PCL arm. The structural dimensions of orthorhombic crystals formed in the PCL layers were also comparable with that those of the crystal lattice formed in the PCL homopolymer films, regardless of the number and length of PCL arm.

In the miktoarm star polymer films, however, the population (i.e., $\phi_{h,2}/\phi_{v,2}$) of edge-on and face-on PHIC structures was significantly influenced in a negative way (Table 3, 4 and 5). The $\phi_{h,2}/\phi_{v,2}$ value was varied in the range 60/40 to 23/77 depending on the number and length of arm as well as the solvent used in the annealing process. These changes in the structural orientation were quite far from the edge-on structure ($\phi_{h,2} = 78\sim 100\%$) predominantly formed in the solvent-annealed PHIC homopolymer films. These orientation variations in the multilayer structure might result from a smart self-assembling behavior of PHIC arm with a fully extended chain conformation under the confinement effects due to the lamellar geometry and the arm-jointer.

In comparison, in the miktoarm polymer films the population ($\phi_{v,3}/\phi_{h,3}$) of vertical and horizontal orthorhombic PCL crystals was significantly influenced in a positive way (Table 3, 4 and 5). In case of the horizontal lamellar structure formed in the toluene-annealed PHIC(5k)-PCL(17k) and PHIC(5k)-PCL₂(17k) films, surprisingly the PCL layers were found to form only vertically-oriented orthorhombic crystals ($\phi_{v,3} = 100\%$) in which the *c*-axis (i.e., the extended chain segment axis) aligned in the out-of-plane of the PCL layer. The formation of only vertically-oriented orthorhombic crystals was also observed for the PCL layers of the horizontal lamellar structure formed in the toluene-annealed PHIC(10k)-PCL₂(10k) and PHIC(10k)-PCL₃(10k) films. These epitaxial orientations of PCL crystals are quite different from the mixed orientations of PCL crystals in the PCL homopolymer films. Instead, for the other toluene-annealed miktoarm star polymer films, the $\phi_{v,3}/\phi_{h,3}$ values were slightly increased, compared to those observed for the corresponding PCL homopolymer films. In contrast, the formation of only horizontally-oriented orthorhombic crystals ($\phi_{h,3} = 100\%$) was observed for the PCL layers of the vertical lamellar structure formed in the CHCl₃-annealed PHIC(10k)-PCL₃(10k) films; here it

is noted that the *c*-axis of orthorhombic PCL crystals aligned in the out-of-plane of the PCL layer. Horizontally-oriented orthorhombic PCL crystals were further formed predominantly in the PCL layers of the vertical lamellar structure formed in the CHCl₃-annealed PHIC(10k)-PCL₂(10k) films. Surprisingly, horizontal orthorhombic PCL crystals were predominantly formed even in the PCL layers of the horizontal lamellar structure formed in the CHCl₃-annealed PHIC(10k)-PCL(10k) films. Overall, the orientations of orthorhombic PCL crystals in the CHCl₃-annealed PHIC(10k)-PCL₁₋₃(10k) films were significantly different from those of PCL crystals in the PCL(10k) homopolymer films. Collectively, in the miktoarm polymer films the enhanced orientation of orthorhombic PCL crystals with respect to the out-of-plane of PCL arm layer might result from the crystallization behavior of PCL arm(s) that took place in a manner adjusted kinetically and thermodynamically to the confinement effects due to the thin PCL arm layer and arm-jointer. From the view of these senses, the predominant horizontal orientation of PCL crystals in the CHCl₃-annealed PHIC(10k)-PCL(10k) films (that formed a horizontal lamellar structure) could yet be understood at this moment.

The details of molecular self-assemblies formed in the PHIC and PCL arm phases of the miktoarm star polymer films as well as in the PHIC and PCL homopolymer films, which were determined for the solvent-annealed thin films above, are schematically illustrated in Fig. 8-10. The PHIC arm phases in the miktoarm polymer films, as well as the PHIC molecules in the homopolymer films always formed a mixture of edge-on and face-on structures. The PHIC molecules in the films formed the edge-on structure with a major population and the face-on structure with a minor population (Fig. 8A-E). In contrast, in the PHIC arm layer phases of the miktoarm polymer films, the populations of edge-on and face-on structures were sensitively changed depending on the molecular weight of PHIC arm, the solvent-annealing, the orientation of lamellar structure, and the number of PCL arm (Fig. 10C-F,J,K). On the other hand, the PCL arm phases in the miktoarm polymer films, as well as the PCL molecules in the homopolymer films mainly formed a mixture of horizontal and vertical orthorhombic crystals. The PCL molecules formed predominantly vertical orthorhombic crystals in the homopolymer films with horizontal lamellar structure (Fig. 9A,C,D). The PCL arms also formed

predominantly vertical orthorhombic crystals in the miktoarm star polymer films with horizontal lamellar structure (Fig. 10A,G,H,I). In contrast, the PCL arms formed predominantly horizontal orthorhombic crystals in the miktoarm star polymer films with vertical lamellar structure (Fig. 10B,L,M,N). Overall, the PCL molecules, as well as the PCL arms were restricted to develop orthorhombic crystals whose the *c*-axis was aligned to a direction normal to the in-plane of lamellae because of the geometrical confinement.

Conclusions

Two series of crystalline-crystalline miktoarm star polymers, PHIC(5k)-PCL₁₋₃(17k) and PHIC(10k)-PCL₁₋₃(10k), were investigated in aspects of thermal property and thin film morphology. In addition, their homopolymers were examined.

All the miktoarm star polymers were found to reveal a two-step thermal degradation behavior. The PHIC arm degraded in the first step; PCL arm degraded in the second step even though its molecular weight was lower than that of the PHIC arm. Furthermore, the PHIC(5k) and PHIC(10k) arms in the miktoarm star polymers revealed a significant enhancement in the thermal stability over the corresponding homopolymers. The PCL arms in the miktoarm polymers also showed a highly enhanced thermal stability. Overall, the enhanced thermal stabilities of arms in the miktoarm star polymers were originated by the capping effect of their one-end group with the counterpart arm(s) via arm-joint formation. In contrast, the crystallization of PCL arm in the miktoarm star polymers was found to be somewhat suppressed, based on lower T_c and T_m than that of its homopolymer. The suppressed crystallization might be caused by the presence of the arm-jointer as well as the geometrical confinement due to the phase-separation. In comparison, the PHIC arm, as well as its homopolymer could not show any discernible phase transition over the temperature range considered.

Toluene- and CHCl₃-annealing processes were suitable to develop nanostructures in the miktoarm polymer thin films via phase-separation between the miktoarm components. The quantitative GIXS analysis successfully provided details on the nanostructures formed in the films. Surprisingly, all the miktoarm polymers always formed a lamellar structure, regardless of the length of PHIC arm as well as

the length and number of PCL arm. In particular, the PHIC(5k)-PCL₁₋₃(17k) miktoarm polymers constructed a lamellar structure even though the miktoarm components had highly imbalanced volume fractions ($f_{\text{PHIC}} = 24.6\sim 26.1\%$), which was remarkably different from the nanostructures reported for conventional diblock copolymer systems. Moreover, the preferential orientation of lamellar structure, namely horizontal versus vertical lamellar structure formation, was well controlled by the selection of solvent in the solvent-annealing process. The formation of a horizontal lamellar structure in films of all miktoarm polymers was successfully demonstrated by toluene-annealing process. The formation of a vertical lamellar structure was succeeded in films of only PHIC(10k)-PCL₂(10k) and PHIC(10k)-PCL₃(10k) by CHCl₃-annealing process.

The PHIC arm phases in the lamellar structures favorably self-assembled to form a multibilayer structure with fully extended backbone and bristle conformations even under the confined PHIC lamellar geometry and arm-jointer. The multibilayer structure was always formed as a mixture of edge-on and face-on structure. Their populations were varied depending on the molecular weight of PHIC arm, the solvent-annealing, the orientation of lamellar structure, and the number of PCL arm. On the other hand, the PCL arm phases in the lamellar structures still revealed a certain level of ability to crystallize although their crystallization was somewhat suppressed by the confined lamellar geometry and arm-jointer. The PCL arms were found to form fringed-micelle like crystals (whose defect level was relatively high), rather than typical folded lamellar crystals observed in their homopolymer films. As a result, the PCL arm phases had relatively lower overall crystallinity, compared to the homopolymer film. The crystals in the PCL arm phases, however, were confirmed to have an orthorhombic lattice, which was same with that of the regular folded lamellar crystals in the homopolymer films. Interestingly the *c*-axis of the orthorhombic crystals was always aligned to a direction normal to the in-plane of the PCL arm layers in the lamellar structure, regardless of the length and number of arm. Such the preferential alignment of orthorhombic crystals might be driven by the crystallization of PCL arms with a certain level of restriction under the geometrical confinement caused by the lamellar structure.

Taking into account these molecular self-assembly behaviors, the formation of only lamellar structures in the solvent-annealed films of all miktoarm polymers with $f_{\text{PHIC}} = 24.6\sim 52.8\%$ might be driven by a collection of factors overriding the volume fraction rule such as the rigid chain properties, self-assembling characteristics, conformational asymmetry, and compressibilities of PHIC and PCL arms.

Acknowledgments

This study was supported by the National Research Foundation (NRF) of Korea (Doyak Program 2011-0028678 and Center for Electro-Photo Behaviors in Advanced Molecular Systems (2010-0001784)) and the Ministry of Science, ICT & Future Planning (MSIP) and the Ministry of Education (BK21 Plus Program and Global Excel Program). This work was also supported by the Japan Society for the Promotion of Science (JSPS) Grant-in-Aid for Scientific Research (B): No. 25288093. R.P. appreciates the financial supports from Suranaree University of Science & Technology and Synchrotron Light Research Institute of Thailand. The synchrotron X-ray scattering measurements at the Pohang Accelerator Laboratory were supported by MSIP, POSTECH Foundation, and POSCO Company. The synchrotron X-ray scattering measurements at the Synchrotron Light Research Institute were supported by the Ministry of Science and Technology, Thailand.

References

- 1 (a) N. Hadjichristidis, M. Pitsikalis, H. Iatrou, *Adv. Polym. Sci.*, 2005, **189**, 1-124; (b) H. Iatrou, N. Hadjichristidis, *Macromolecules*, 1992, **25**, 4649-4651.
- 2 (a) G. Ungar, C. Tschierske, V. Abetz, R. Holyst, M. A. Bates, F. Liu, M. Prehm, R. Kieffer, X. Zeng, M. Walker, B. Glettner, A. Zywockinski, *Adv. Funct. Mater.*, 2011, **21**, 1296-1323; (b) K. Khanna, S. Varshney, A. Kakkar, *Polym. Chem.*, 2010, **1**, 1171-1185.
- 3 (a) S. Ito, R. Goseki, T. Ishizone, A. Hirao, *European Polym. J.*, 2013, **49**, 2545-2566; (b) T. Higashihara, M. Hayashi, A. Hirao, *Prog. Polym. Sci.*, 2011, **36**, 323-375.
- 4 (a) P. G. Fragouli, H. Iatrou, N. Hadjichristidis, T. Sakurai, A. Hirao, *J. Polym. Sci., Part A: Polym. Chem.*, 2006, **44**, 614-619; (b) A. Mavroudis, A.

- Avgeropoulos, N. Hadjichristidis, E. L. Thomas, D. J. Lohse, *Chem. Mater.*, 2003, **15**, 1976-1983; (c) D. Cho, S. Park, T. Chang, A. Avgeropoulos, N. Hadjichristidis, *Eur. Polym. J.*, 2003, **39**, 2155-2160.
- 5 (a) S. Ito, R. Goseki, T. Ishizone, S. Senda, A. Hirao, *Macromolecules*, 2013, **46**, 819-827; (b) Y. L. Zhao, T. Higashihara, K. Sugiyama, A. Hirao, *J. Am. Chem. Soc.*, 2005, **127**, 14158-14159.
- 6 (a) K. Khanna, S. Varshney, A. Kakkar, *Macromolecules*, 2010, **43**, 5688- 5698; (b) M. R. Whittaker, C. N. Urbani, M. J. Monteiro, *J. Am. Chem. Soc.*, 2006, **128**, 11360-11361; (c) Y. Cai, Y. Tang, S. P. Armes, *Macromolecules*, 2004, **37**, 9728-9737; (d) R. Francis, B. Lepoittevin, D. Taton, Y. Gnanou, *Macromolecules*, 2002, **35**, 9001-9008.
- 7 (a) J. Babin, D. Taton, M. Brinkmann, S. Lecommandoux *Macromolecules*, 2008, **41**, 1384-1392; (b) A. Gitsas, G. Floudas, M. Mondeshki, I. Lieberwirth, H. W. Spiess, H. Iatrou, N. Hadjichristidis, A. Hirao, *Macromolecules*, 2010, **43**, 1874-1881.
- 8 S. Junnila, N. Houbenov, A. Karatzas, N. Hadjichristidis, A. Hirao, H. Iatrou, O. Ikkala, *Macromolecules*, 2012, **45**, 2850-2856.
- 9 A. Touris, K. Kostakis, S. Mourmouris, V. Kotzabasakis, M. Pitsikalis, N. Hadjichristidis, *Macromolecules*, 2008, **41**, 2426-2438.
- 10 M. S. Rahman, M. Changez, J.-W. Yoo, C. H. Lee, S. Samal, J.-S. Lee, *Macromolecules*, 2008, **41**, 7029-7032.
- 11 J. Chen, X. Wang, X. Liao, H. Zhang, X. Wang, Q. Zhou, *Macromol. Rapid Commun.*, 2006, **27**, 51-56.
- 12 Y. Yamazaki, N. Ajioka, A. Yokoyama, T. Yokozawa, *Macromolecules*, 2009, **42**, 606-611.
- 13 (a) J. G. Ray, A. J. Johnson, D. A. Savin, *J. Polym. Sci., Part B: Polym. Phys.*, 2013, **51**, 508-523; (b) Z. Ge, S. Liu, *Macromol. Rapid Commun.*, 2009, **30**, 1523-1532.
- 14 (a) K. Hayashida, N. Saito, S. Arai, A. Takano, N. Tanaka, Y. Matsushita, *Macromolecules*, 2007, **40**, 3695-3699; (b) A. Takano, S. Wada, S. Sato, T. Araki, K. Hirahara, T. Kazama, S. Kawahara, Y. Isono, A. Ohono, N. Tanaka, Y. Matsushita, *Macromolecules*, 2004, **37**, 9941-9946; (c) K. Yamaguchi, K. Takahashi, H. Hasegawa, H. Iatrou, N. Hadjichristidis, T. Kaneko, Y.

- Nishikawa, H. Jinnai, T. Matsui, H. Nishioka, M. Shimizu, H. Furukawa, *Macromolecules*, 2003, **36**, 6962-6966; (d) S. Sioula, N. Hadjichristidis, E. L. Thomas, *Macromolecules*, 1998, **31**, 5272-5277.
- 15 (a) X. He, L. Huang, H. Liang, C. Pan, *J. Chem. Phys.*, 2003, **118**, 9861-9863; (b) T. Gemma, A. Hatano, T. Dotera, *Macromolecules*, 2002, **35**, 3225-3237; (c) H. Huckstadt, A. Gopfert, V. Abetz, *Macromol. Chem. Phys.*, 2000, **201**, 296-307.
- 16 (a) K. S. Lyakhova, A. Horvat, A. V. Zvelindovsky, G. J. Sevink, *Langmuir*, 2006, **22**, 5848-5855; (b) P. F. Green, R. Limary, *Adv. Colloid Interface Sci.*, 2001, **94**, 53-81; (c) P. Mansky, P. Chaikin, E. L. Thomas, *J. Mater. Sci.*, 1995, **30**, 1987-1992; (d) S. H. Anastasiadis, T. P. Russell, S. K. Satija, C. F. Majkrzak, *Phys. Rev. Lett.*, 1989, **62**, 1852-1855; (e) C. S. Henkee, E. L. Thomas, L. J. Fetters, *J. Mater. Sci.*, 1988, **23**, 1685-1694.
- 17 Y. Rho, C. Kim, T. Higashihara, S. Jin, J. Jung, T. J. Shin, A. Hirao, M. Ree, *ACS Macro Lett.*, 2013, **2**, 849-855.
- 18 T. Satoh, N. Nishikawa, D. Kawato, D. Suemasa, S. Jung, Y. Y. Kim, M. Ree, T. Kakuchi, *Polym. Chem.*, 2014, **5**, 588-599.
- 19 R. Phinjaroenphan, Y. Y. Kim, S. Jung, T. Isono, Y. Sato, S. Maensiri, S. Rugmai, T. Kakuchi, T. Satoh, M. Ree, *Sci. Adv. Mater.*, 2014, **6**, 2526-2531.
- 20 Y. Y. Kim, S. Jung, C. Kim, B. J. Ree, D. Kawato, N. Nishikawa, D. Suemasa, T. Isono, T. Kakuchi, T. Satoh, M. Ree, *Macromolecules*, 2014, **47**, 7510-7524.
- 21 (a) J. Yoon, K.-W. Kim, J. Kim, K. Heo, K. S. Jin, S. Jin, T. J. Shin, B. Lee, Y. Rho, B. Ahn, M. Ree, *Macromol. Res.*, 2008, **16**, 575-585; (b) M. Ree, *Macromol. Rapid Commun.*, 2014, **35**, 930-959.
- 22 (a) B. Lee, I. Park, J. Yoon, S. Park, J. Kim, K.-W. Kim, T. Chang, M. Ree, *Macromolecules*, 2005, **38**, 4311-4323; (b) S. Jin, J. Yoon, K. Heo, H.-W. Park, T. J. Shin, T. Chang, M. Ree, *J. Appl. Crystallogr.*, 2007, **40**, 950-958; (c) K. Heo, J. Yoon, S. Jin, J. Kim, K.-W. Kim, T. J. Shin, B. Chung, T. Chang, M. Ree, *J. Appl. Cryst.*, 2008, **41**, 281-291; (d) J. Yoon, S. Y. Yang, K. Heo, B. Lee, W. Joo, J. K. Kim, M. Ree, *J. Appl. Crystallogr.*, 2007, **40**, 305-312; (e) K. Kim, Y. Y. Kim, S. Park, Y.-G. Ko, Y. Rho, W. Kwon, T. J. Shin, J. Kim, M. Ree, *Macromolecules*, 2014, **47**, 4397-4407.

- 23 (a) Y. Rho, B. Ahn, J. Yoon, M. Ree, *J. Appl. Crystallogr.*, 2013, **46**, 466-475; (b) B. Lee, J. Yoon, W. Oh, Y. Hwang, K. Heo, K. S. Jin, J. Kim, K.-W. Kim, M. Ree, *Macromolecules*, 2005, **38**, 3395-3405; (c) B. Lee, W. Oh, J. Yoon, Y. Hwang, J. Kim, B. G. Landes, J. P. Quintana, M. Ree, *Macromolecules*, 2005, **38**, 8991-8995; (d) B. Lee, Y.-H. Park, Y. Hwang, W. Oh, J. Yoon, M. Ree, *Nat. Mater.*, 2005, **4**, 147-150; (e) B. Lee, W. Oh, Y. Hwang, Y.-H. Park, J. Yoon, K. S. Jin, K. Heo, J. Kim, K.-W. Kim, M. Ree, *Adv. Mater.*, 2005, **17**, 696-701.
- 24 (a) Y. J. Roe, *Methods of X-ray and Neutron Scattering in Polymer Science*, Oxford University Press, New York, 2000; (b) R. Lazzari, *J. Appl. Crystallogr.*, 2002, **35**, 406-421; (c) G. Renaud, R. Lazzari, F. Leroy, *Surf. Sci. Rep.*, 2009, **64**, 255-380.
- 25 (a) J. S. Pedersen, *J. Appl. Crystallogr.*, 1994, **27**, 595-608; (b) R. Hosemann, S. N. Bagchi, *Direct analysis of diffraction by matter*, North-Holland, Amsterdam, 1962.
- 26 (a) J. Yoon, S. K. Jin, H. C. Kim, G. Kim, K. Heo, S. Jin, J. Kim, K.-W. Kim, M. Ree, *J. Appl. Crystallogr.*, 2007, **40**, 476-488; (b) S. G. Hahm, Y. Rho, J. Jung, S. H. Kim, T. Sajoto, F. S. Kim, S. Barlow, C. E. Park, S. A. Jenekhe, S. R. Marder, M. Ree, *Adv. Funct. Mater.*, 2013, **23**, 2060-2071.
- 27 Y. Rho, J. Min, J. Yoon, B. Ahn, S. Jung, K. Kim, P. Shah, J.-S. Lee, M. Ree, *NPG Asia Mater.*, 2012, **4**, e29.
- 28 Q. Guo, G. Groeninckx, *Polymer*, 2001, **42**, 8647-8655.
- 29 (a) F. S. Bates, M. F. Schulz, A. K. Khandpur, S. Foerster, J. H. Rosedale, *Faraday Discussions*, 1994, **98**, 7-18; (b) T. Hashimoto, *Macromol. Symp.*, 2001, **174**, 69-84; (c) L. Leibler, *Macromolecules*, 1980, **13**, 1602-1617; (d) T. P. Lodge, B. Pudil, K. J. Hanley, *Macromolecules*, 2002, **35**, 4707-4717; (e) M. W. Matsen, M. Schick, *Macromolecules*, 1994, **27**, 4014-4015.
- 30 Y. Y. Kim, B. Ahn, S. Sa, M. Jeon, S. V. Roth, S. Y. Kim, M. Ree, *Macromolecules*, 2013, **46**, 8235-8244.
- 31 J. Yoon, S. Jin, B. Ahn, Y. Rho, T. Hirai, R. Maeda, T. Hayakawa, J. Kim, K.-W. Kim, M. Ree, *Macromolecules*, 2008, **41**, 8778-8784.
- 32 J. Yoon, S. Y. Jung, B. Ahn, K. Heo, S. Jin, T. Iyoda, H. Yoshida, M. Ree, *J. Phys. Chem. B.*, 2008, **112**, 8486-8495.
- 33 B. Ahn, W. Kwon, H. Kim, M. Ree, *Polym. Chem.*, 2014, **5**, 1912-1922.

34 M. W. Matsen, *Eur. Phys. J. E*, 2009, **30**, 361-369.



Table 1 Fundamental, thermal, and crystallinity properties of PHIC-PCL_{1~3} miktoarm polymers and their homopolymers used in the study

Polymer	PHIC-(OH) _m ^a		M _{n,NMR} ^b	PDI ^c	f _{PHIC} ^d (%)	T _{c,PCL} ^e (°C)	T _{m,PCL} ^f (°C)	ΔH _{f,PCL} ^g (J/g)	X _{c,PCL} ^h (%)
	M _{n,NMR} ^b	PDI ^c							
PHIC(5k)			5400	1.05					
PCL(15k)			15000	1.10		23.2	54.6	72.1	53.0
PHIC(5k)– PCL(17k)	5100	1.06	21700	1.04	26.1	14.2	54.0	65.9	48.5
PHIC(5k)– PCL ₂ (17k)	5100	1.06	22700	1.08	25.0	13.5	50.9	64.9	47.7
PHIC(5k)– PCL ₃ (17k)	5200	1.06	23500	1.05	24.6	13.0	50.5	64.4	47.4
PHIC(10k)			10,400	1.11					
PCL(10k)			10,500	1.04		23.3	55.5	76.1	56.0
PHIC(10k)– PCL(10k)	10300	1.13	20,900	1.07	52.8	19.5	53.3	65.6	48.2
PHIC(10k)– PCL ₂ (10k)	10900	1.13	22,200	1.17	52.6	17.2	52.5	64.1	47.1
PHIC(10k)– PCL ₃ (10k)	9600	1.16	20,600	1.09	50.0	12.5	47.9	58.7	43.2

^a Macroinitiator ($m = 1\sim 3$) used in the polymerization of ϵ -caprolactone. ^b Number-average molecular weight determined in CDCl₃ by ¹H NMR spectroscopy analysis. ^c Polydispersity index ($= M_{w,GPC}/M_{n,GPC}$) determined by gel permeation chromatography (GPC) in THF using polystyrene standards; here $M_{w,GPC}$ and $M_{n,GPC}$ are the weight- and number-average molecular weights respectively which were determined by GPC analysis.

^d Volume fraction of PHIC arm: $f_{PHIC} = (M_{n,NMR,PHIC}/d_{PHIC}) / (M_{n,NMR,PHIC}/d_{PHIC} + M_{n,NMR,PCL}/d_{PCL})$; $d_{PHIC} = 1.00$ g/cm³ and $d_{PCL} = 1.15$ g/cm³.

^e Crystallization temperature of PCL, which corresponds to the temperature at the peak maximum of the exothermic crystallization transition measured by DSC analysis with a rate of 10.0 °C/min. ^f Melting temperature of PCL crystals, which corresponds to the temperature at the peak maximum of the endothermic melting transition measured by DSC analysis with a rate of 10.0 °C/min. ^g Heat of fusion of PCL crystals, which was measured by DSC analysis with a rate of 10.0 °C/min. ^h Overall crystallinity of PCL homopolymer or PCL arms, which was determined by DSC analysis; $X_{c,PCL}$ (%) was estimated from the heat of fusion of PCL crystals with respect to that (136.0 J/g) of perfect PCL crystals (Ref. 28).

Table 2 Nanostructural parameters of the toluene- and CHCl_3 -annealed thin films (115-120 nm thick) of PHIC-PCL₁₋₃ miktoarm polymers and their homopolymers, which were determined by GISAXS analysis

Polymer thin film	Nanostructure (observed)	L^a (nm)	ℓ_1^b (nm)	ℓ_2^c (nm)	ℓ_3^d (nm)	σ_1^e (nm)	σ_2^f (nm)	g^g	$\bar{\varphi}_1^h$ (deg.)	$\sigma_{\varphi_1}^i$ (deg.)	O_s^j	ℓ^k (nm)
Toluene-annealed films												
PHIC(5k)	not identified											
PCL(15k)	Horizontal lamellae	12.6	3.3	1.6	6.1	0.6	0.4	0.35	0	6.3	0.982	
	Vertical Lamellae ^l	10.6	2.5	1.3	5.5	0.8	0.5	0.40	90			
PHIC(5k)-PCL(17k)	Horizontal lamellae	16.4	8.3	2.0	4.1	1.3	0.7	0.31	0	14.0	0.916	
	Vertical lamellae ^l	21.8	8.9	3.2	6.5	2.1	1.8	0.38	90			
PHIC(5k)-PCL ₂ (17k)	Horizontal lamellae	16.2	8.0	2.1	4.0	1.6	0.7	0.27	0	13.1	0.926	
PHIC(5k)-PCL ₃ (17k)	Horizontal lamellae	16.0	7.7	2.2	3.9	1.8	0.9	0.27	0	13.4	0.923	
Toluene-annealed films												
PHIC(10k)	not identified											
PCL(10k)	Horizontal lamellae	12.4	3.6	1.5	5.8	0.5	0.5	0.36	0	6.3	0.982	
PHIC(10k)-PCL(10k)	Horizontal lamellae	19.2	6.2	2.2	8.6	1.7	0.7	0.32	0	10.3	0.953	
PHIC(10k)-PCL ₂ (10k)	Horizontal lamellae	22.9	7.1	2.3	11.2	2.3	0.7	0.34	0	8.2	0.970	3.7-5.1
PHIC(10k)-PCL ₃ (10k)	Horizontal lamellae	18.5	5.6	2.4	8.1	1.5	0.8	0.31	0	13.7	0.919	
CHCl_3-annealed films												
PHIC(10k)	not identified											
PCL(10k)	Horizontal lamellae	12.5	3.6	1.4	6.1	0.5	0.6	0.36	0	5.8	0.985	
PHIC(10k)-PCL(10k)	Horizontal lamellae	22.6	6.8	2.2	11.4	2.7	0.8	0.32	0	9.0	0.964	
PHIC(10k)-PCL ₂ (10k)	Vertical lamellae	29.1	11.4	2.3	13.1	3.5	1.1	0.19	90	12.7	-0.430	6.6
PHIC(10k)-PCL ₃ (10k)	Vertical lamellae	24.0	8.6	2.4	10.6	2.4	0.6	0.20	90	10.8	-0.448	5.5

^a Long period of lamellar structure. ^b Thickness of more dense (i.e., crystalline) layer ($=\ell_c$) in the lamellar structure formed in PCL homopolymer films; thickness of more dense layer (i.e., PCL arm phase: ℓ_{PCL}) in the lamellar structured PHIC-PCL_m films. ^c Thickness of interfacial layer (ℓ_i) between the highly dense and less dense layers in lamellar structure. ^d Thickness of less dense (i.e., amorphous) layer ($=\ell_a$) in the lamellar structure formed in PCL homopolymer films; thickness of less dense layer (i.e., PHIC arm phase: ℓ_{PHIC}) in the lamellar structured PHIC-PCL_m films.

^e Standard deviation for the more dense layer in lamellar structure. ^f Standard deviation for the interfacial layer in lamellar structure. ^g Paracrystal distortion factor along the direction parallel to the long period of lamellar structure. ^h Mean value of the polar angle φ_1 (i.e., orientation angle) between the orientation vector \mathbf{n}_1 (which is set along the direction parallel to the long period of lamellar structure) and the out-of-plane of the film.

ⁱ Standard deviation for the orientation angle ϕ_1 of lamellar structure. ^j Second order orientation factor. ^k Mean interdistance of the crystals formed in the PCL arm phase layers along the out-of-plane of the film. ^l Vertical lamellar structure was formed in a very minor fraction.

Table 3 Structural parameters of the toluene-annealed thin films (115-120 nm thick) of PHIC(5k)-PCL₁₋₃(17k) miktoarm polymers and their homopolymers, which were determined by GIWAXS analysis

Structural parameter	PHIC(5k)	PCL(15k)	PHIC(5k)-PCL(17k)	PHIC(5k)-PCL ₂ (17k)	PHIC(5k)-PCL ₃ (17k)
d_L^a (nm)	1		1.67	1.67	1.67
	.67				
ℓ_1^b (nm)	0		0.77	0.77	0.77
	.77				
ℓ_2^c (nm)	0		0.90	0.90	0.90
	.90				
d_1^d (nm)	0		0.67	0.67	0.67
	.67				
d_2^e (nm)	0		0.50	0.50	0.50
	.50				
d_3^f (nm)	0		0.45	0.45	0.45
	.45				
g_{dL}^g (nm)	0		0.078	0.065	0.065
	.056				
g_{d1}^h (nm)	0		0.170	0.140	0.160
	.140				
g_{d2}^i (nm)	0		0.140	0.150	0.160
	.120				
g_{d3}^j (nm)	0		0.110	0.110	0.110
	.160				
$\overline{\varphi_2}^k$ (deg.)	0		0	0	0
$\sigma_{\varphi_2,0}^l$ (deg)	4		4.20	5.10	6.30
	.70				
$O_{s,2,0}^m$	0		0.992	0.988	0.982
	.990				
$\overline{\varphi_2}$ (deg.)	90		90	90	90
$\sigma_{\varphi_2,90}$ (deg)	20		18.60	17.90	21.8
	.10				
$O_{s,2,90}$	-0.		-0.357	-0.367	-0.311
	.336				
$\phi_{h,2}/\phi_{v,2}^n$ (v/v)	80 /20		41/59	46/54	38/62
a^o (nm)		0.80	0.80	0.80	0.80
b^p (nm)		0.53	0.53	0.53	0.53
c^q (nm)		1.76	1.76	1.76	1.76
g^r		0.060	0.064	0.064	0.064
$\overline{\varphi_3}^s$ (deg.)		0			0
$\sigma_{\varphi_3,0}^t$ (deg)		10.6			10.10
$O_{s,3,0}^u$		0.9			0.955
	50				
$\overline{\varphi_3}$ (deg.)		90	90	90	90
$\sigma_{\varphi_3,90}$ (deg)		14.3	18.70	17.80	18.50
	0				
$O_{s,3,90}$		-0.4	-0.356	-0.368	-0.359
	12				

$\phi_{v,3}/\phi_{h,3}$ ^v (v/v)	71/2 9	100/0	100/0	85/15
---	-----------	-------	-------	-------

^a Long period of the molecular multilayer PHIC structure. ^b Thickness of more dense layer in the molecular multilayer PHIC structure.

^c Thickness of less dense layer in the molecular multilayer PHIC structure. ^d Mean interdistance between the *n*-hexyl bristles of the neighboring polymer chains whose repeat units are matched in position along their backbones. ^e Mean interdistance between the nearest *n*-hexyl bristles along the polymer backbone. ^f Mean interdistance between the *n*-hexyl bristles of the nearest neighboring polymer chains. ^g Paracrystal distortion factor along the direction parallel to the long period of molecular multilayer structure. ^h Paracrystal distortion factor along *n*-hexyl bristles of the neighboring polymer chains whose repeat units are matched in position along their backbones. ⁱ Paracrystal distortion factor along the nearest *n*-hexyl bristles along the polymer backbone. ^j Paracrystal distortion factor along the *n*-hexyl bristles of the nearest neighboring polymer chains. ^k Mean value of the polar angle φ_2 (i.e., orientation angle) between the orientation vector \mathbf{n}_2 (which is set along the direction parallel to the long period of molecular multilayer PHIC structure) and the out-of-plane of the film. ^l Standard deviation for the orientation angle φ_2 of molecular multilayer PHIC structure. ^m Second order orientation factor of the molecular multilayer PHIC structure. ⁿ Volume fraction ratio of the horizontal and vertical multilayer PHIC structures. ^o A unit cell dimension along the *a*-axis of orthorhombic PCL crystals. ^p A unit cell dimension along the *b*-axis of orthorhombic PCL crystals. ^q A unit cell dimension along the *c*-axis of orthorhombic PCL crystals. ^r Paracrystal distortion factor of the PCL crystal.

^s Mean value of the polar angle φ_3 (i.e., orientation angle) between the orientation vector \mathbf{n}_3 (which is set along the direction parallel to the long period of lamellar structure) and the out-of-plane of the film. ^t Standard deviation for the orientation angle φ_3 of lamellar structure. ^u Second order orientation factor of lamellar PCL crystal structure. ^v Volume fraction ratio of the horizontal and vertical lamellar PCL crystal structures.

Table 4 Structural parameters of the toluene-annealed thin films (115-120 nm thick) of PHIC(10k)-PCL_{1~3}(10k) miktoarm polymers and their homopolymers, which were determined by GIWAXS analysis

Structural parameter	PHIC(10k)	PCL(10k)	PHIC(10k)- PCL(10k)	PHIC(10k)- PCL ₂ (10k)	PHIC(10k)- PCL ₃ (10k)
d_L^a (nm)	1.66		1.66	1.66	1.66
ℓ_1^b (nm)	0.76		0.76	0.76	0.76
ℓ_2^c (nm)	0.90		0.90	0.90	0.90
d_1^d (nm)	0.67		0.67	0.67	0.67
d_2^e (nm)	0.50		0.50	0.50	0.50
d_3^f (nm)	0.45		0.45	0.45	0.45
g_{dL}^g (nm)	0.067		0.069	0.069	0.089
g_{d1}^h (nm)	0.140		0.160	0.160	0.155
g_{d2}^i (nm)	0.110		0.110	0.110	0.140
g_{d3}^j (nm)	0.130		0.130	0.130	0.150
φ_2^k (deg.)	0		0	0	0
$\sigma_{\varphi_2,0}^l$ (deg)	5.10		7.90	8.50	7.70
$O_{s,2,0}^m$	0.988		0.972	0.968	0.974
φ_2 (deg.)	90		90	90	90
$\sigma_{\varphi_2,90}$ (deg)	14.40		17.80	22.30	20.1
$O_{s,2,90}$	-0.411		-0.368	-0.304	-0.336
$\phi_{h,2}/\phi_{v,2}^n$ (v/v)	78/22		32/68	23/77	28/72
a^o (nm)		0.80	0.80	0.80	0.80
b^p (nm)		0.53	0.53	0.53	0.53
c^q (nm)		1.74	1.74	1.74	1.74
g^r		0.060	0.065	0.070	0.070
φ_3^s (deg.)		0	0		

$\sigma_{\varphi_3,0}^t$	8.8	7.8		
(deg)				
$O_{s,3,0}^u$	0.966	0.973		
φ_3 (deg.)	90	90	90	90
$\sigma_{\varphi_3,90}$ (deg)	17.30	18.80	20.40	23.00
$O_{s,3,90}$	-0.375	-0.355	-0.332	-0.293
$\phi_{v,3}/\phi_{h,3}^v$	93/7	95/5	100/0	100/0
(v/v)				

^a Long period of the molecular multibilayer PHIC structure. ^b Thickness of more dense layer in the molecular multibilayer PHIC structure. ^c Thickness of less dense layer in the molecular multibilayer PHIC structure. ^d Mean interdistance between the *n*-hexyl bristles of the neighboring polymer chains whose repeat units are matched in position along their backbones. ^e Mean interdistance between the nearest *n*-hexyl bristles along the polymer backbone. ^f Mean interdistance between the *n*-hexyl bristles of the nearest neighboring polymer chains. ^g Paracrystal distortion factor along the direction parallel to the long period of molecular multibilayer structure. ^h Paracrystal distortion factor along *n*-hexyl bristles of the neighboring polymer chains whose repeat units are matched in position along their backbones. ⁱ Paracrystal distortion factor along the nearest *n*-hexyl bristles along the polymer backbone. ^j Paracrystal distortion factor along the *n*-hexyl bristles of the nearest neighboring polymer chains. ^k Mean value of the polar angle φ_2 (i.e., orientation angle) between the orientation vector \mathbf{n}_2 (which is set along the direction parallel to the long period of molecular multibilayer PHIC structure) and the out-of-plane of the film. ^l Standard deviation for the orientation angle φ_2 of molecular multibilayer PHIC structure. ^m Second order orientation factor of the molecular multibilayer PHIC structure. ⁿ Volume fraction ratio of the horizontal and vertical multibilayer PHIC structures. ^o A unit cell dimension along the *a*-axis of orthorhombic PCL crystals. ^p A unit cell dimension along the *b*-axis of orthorhombic PCL crystals. ^q A unit cell dimension along the *c*-axis of orthorhombic PCL crystals. ^r Paracrystal distortion factor of the PCL crystal.

^s Mean value of the polar angle φ_3 (i.e., orientation angle) between the orientation vector \mathbf{n}_3 (which is set along the direction parallel to the long period of lamellar structure) and the out-of-plane of the film. ^t Standard deviation for the orientation angle φ_3 of lamellar structure. ^u Second order orientation factor of lamellar PCL crystal structure. ^v Volume fraction ratio of the horizontal and vertical lamellar PCL crystal structures.

Table 5 Structural parameters of the CHCl₃-annealed thin films (115-120 nm thick) of PHIC(10k)-PCL_{1~3}(10k) miktoarm polymers and their homopolymers, which were determined by GIWAXS analysis

Structural parameter	PHIC(10k)	PCL(10k)	PHIC(10k)-PCL(10k)	PHIC(10k)-PCL ₂ (10k)	PHIC(10k)-PCL ₃ (10k)
d_L^a (nm)	1.65		1.65	1.65	1.65
ℓ_1^b (nm)	0.76		0.76	0.76	0.76
ℓ_2^c (nm)	0.89		0.89	0.89	0.89
d_1^d (nm)	0.67		0.67	0.67	0.67
d_2^e (nm)	0.50		0.50	0.50	0.50
d_3^f (nm)	0.45		0.45	0.45	0.45
g_{dL}^g (nm)	0.048		0.056	0.069	0.089
g_{d1}^h (nm)	0.100		0.140	0.130	0.130
g_{d2}^i (nm)	0.100		0.150	0.150	0.150
g_{d3}^j (nm)	0.110		0.150	0.150	0.145
φ_2^k (deg.)	0		0	0	0
$\sigma_{\varphi_2,0}^l$	3.70		8.70	7.40	5.40
(deg)					
$O_{s,2,0}^m$	0.994		0.966	0.975	0.987
φ_2 (deg.)			90	90	90
$\sigma_{\varphi_2,90}$ (deg)			18.30	18.60	13.40
$O_{s,2,90}$			-0.362	-0.357	-0.422
$\phi_{h,2}/\phi_{v,2}^n$	100/0		60/40	48/52	37/63

(v/v)				
a^o (nm)	0.80	0.80	0.80	0.80
b^p (nm)	0.53	0.53	0.53	0.53
c^q (nm)	1.74	1.74	1.74	1.74
g^r	0.065	0.072	0.075	0.075
$\overline{\varphi_3^s}$ (deg.)	0	0	0	0
$\sigma_{\varphi_3,0}^t$	8.1	12.2	14.9	8.2
(deg)				
$O_{s,3,0}^u$	0.971	0.935	0.905	0.970
$\overline{\varphi_3}$ (deg.)	90	90	90	
$\sigma_{\varphi_3,90}$ (deg)	7.2	9.30	9.90	
$O_{s,3,90}$	-0.477	-0.462	-0.457	
$\phi_{v,3}/\phi_{h,3}^v$	79/21	22/78	29/71	0/100
(v/v)				

^a Long period of the molecular multibilayer PHIC structure. ^b Thickness of more dense layer in the molecular multibilayer PHIC structure. ^c Thickness of less dense layer in the molecular multibilayer PHIC structure. ^d Mean interdistance between the *n*-hexyl bristles of the neighboring polymer chains whose repeat units are matched in position along their backbones. ^e Mean interdistance between the nearest *n*-hexyl bristles along the polymer backbone. ^f Mean interdistance between the *n*-hexyl bristles of the nearest neighboring polymer chains. ^g Paracrystal distortion factor along the direction parallel to the long period of molecular multibilayer structure. ^h Paracrystal distortion factor along *n*-hexyl bristles of the neighboring polymer chains whose repeat units are matched in position along their backbones. ⁱ Paracrystal distortion factor along the nearest *n*-hexyl bristles along the polymer backbone. ^j Paracrystal distortion factor along the *n*-hexyl bristles of the nearest neighboring polymer chains. ^k Mean value of the polar angle φ_2 (i.e., orientation angle) between the orientation vector \mathbf{n}_2 (which is set along the direction parallel to the long period of molecular multibilayer PHIC structure) and the out-of-plane of the film. ^l Standard deviation for the orientation angle φ_2 of molecular multibilayer PHIC structure. ^m Second order orientation factor of the molecular multibilayer PHIC structure. ⁿ Volume fraction ratio of the horizontal and vertical multibilayer PHIC structures. ^o A unit cell dimension along the *a*-axis of orthorhombic PCL crystals. ^p A unit cell dimension along the *b*-axis of orthorhombic PCL crystals. ^q A unit cell dimension along the *c*-axis of orthorhombic PCL crystals. ^r Paracrystal distortion factor of the PCL crystal.

^s Mean value of the polar angle φ_3 (i.e., orientation angle) between the orientation vector \mathbf{n}_3 (which is set along the direction parallel to the long period of lamellar structure) and the out-of-plane of the film. ^t Standard deviation for the orientation angle φ_3 of lamellar structure. ^u Second order orientation factor of lamellar PCL crystal structure. ^v Volume fraction ratio of the horizontal and vertical lamellar PCL crystal structures.

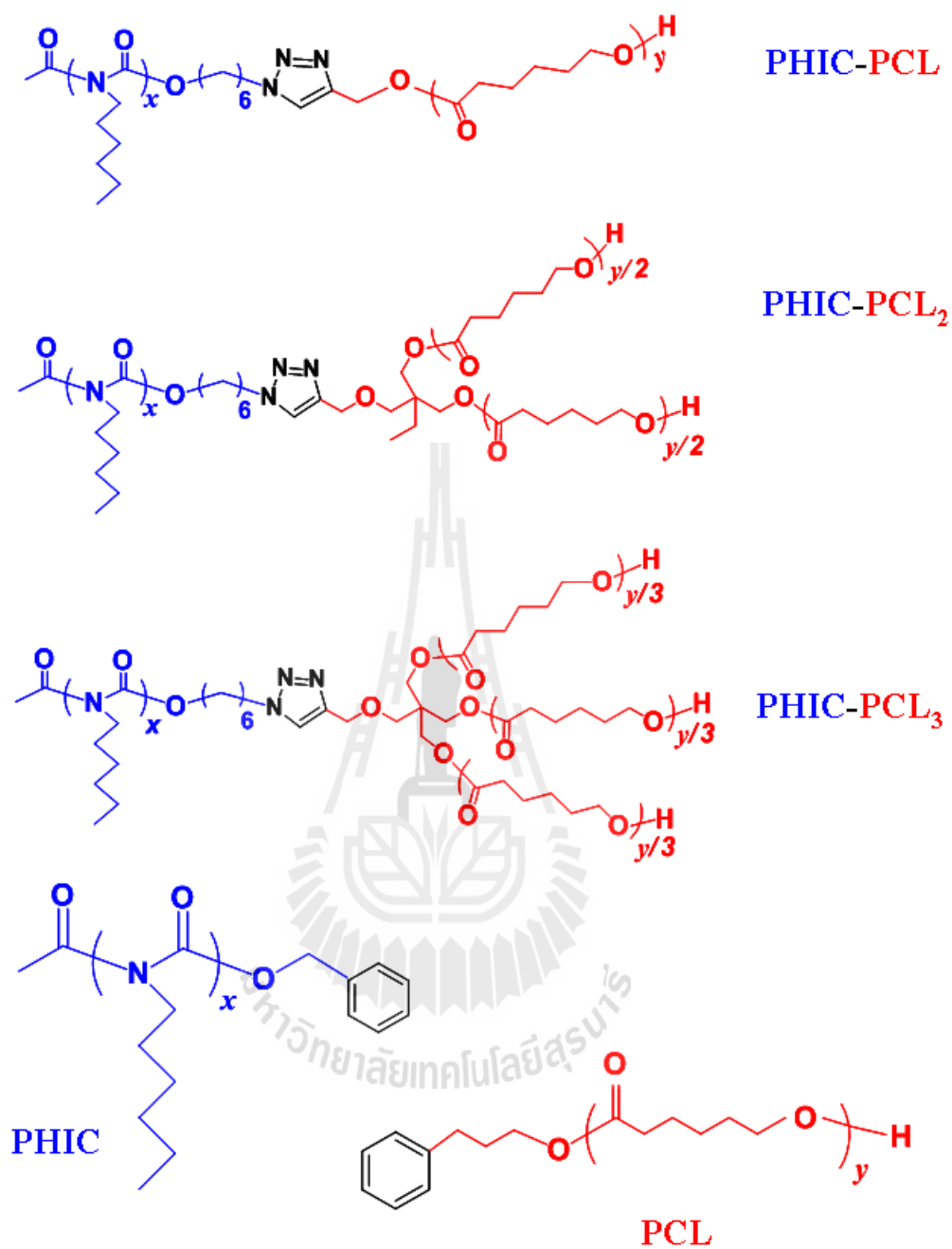


Fig. 1 Chemical structures of PHIC-PCL₁₋₃ miktoarm polymers and their homopolymers.

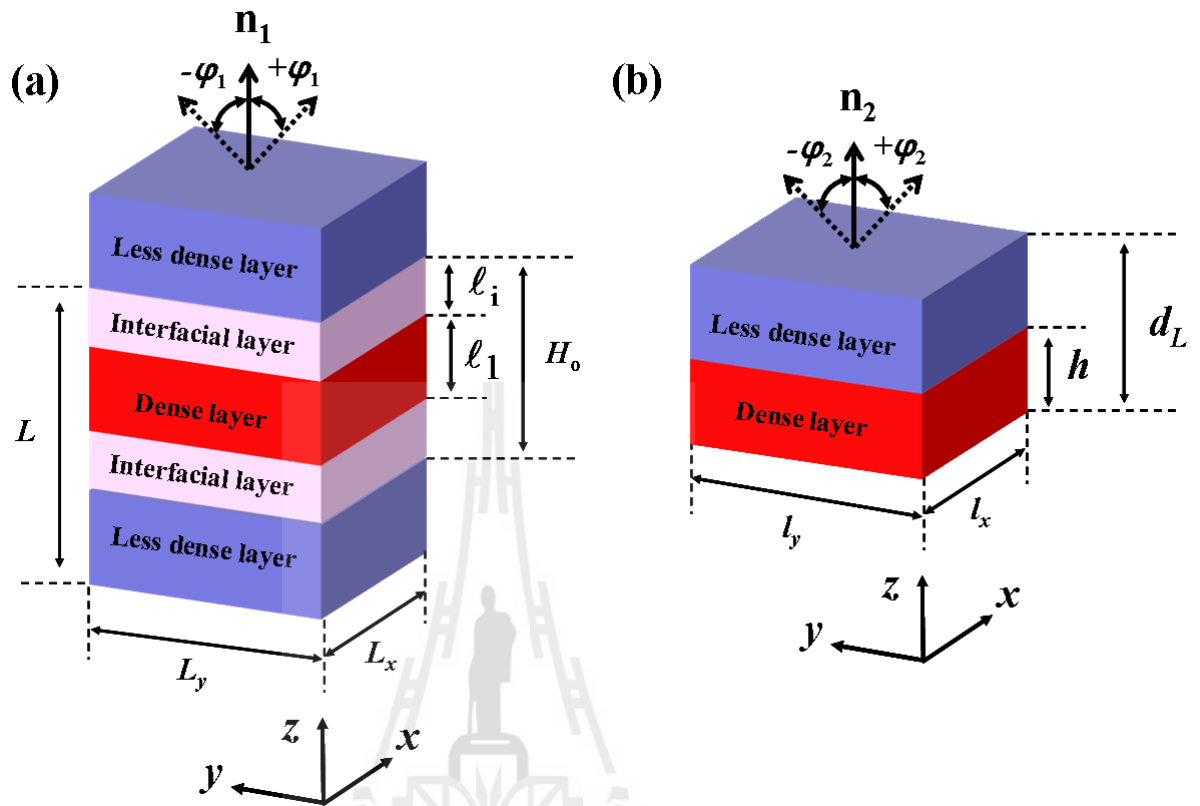


Fig. 2 Three-dimensional (3D) lamellar structure models: (a) a model composed of three layers, which is defined by a set of structural parameters, long period L , dense layer thickness ℓ_1 , interfacial layer thickness ℓ_i , $H_o = \ell_1 + 2\ell_i$, less dense layer thickness $\ell_2 (= L - H_o)$, L_x (dimension along the x -axis), L_y (dimension along the y -axis), orientation vector \mathbf{n}_1 (which is parallel to a normal direction to the in-plane of lamellar structure), and polar angle φ_1 between the \mathbf{n}_1 vector and the out-of-plane of the film; (a) a model composed of two layers, which is defined by a set of structural parameters, long period d_L , dense layer thickness h , l_x (dimension along the x -axis), l_y (dimension along the y -axis), orientation vector \mathbf{n}_2 (which is parallel to a normal direction to the in-plane of lamellar structure), and polar angle φ_2 between the \mathbf{n}_2 vector and the out-of-plane of the film.

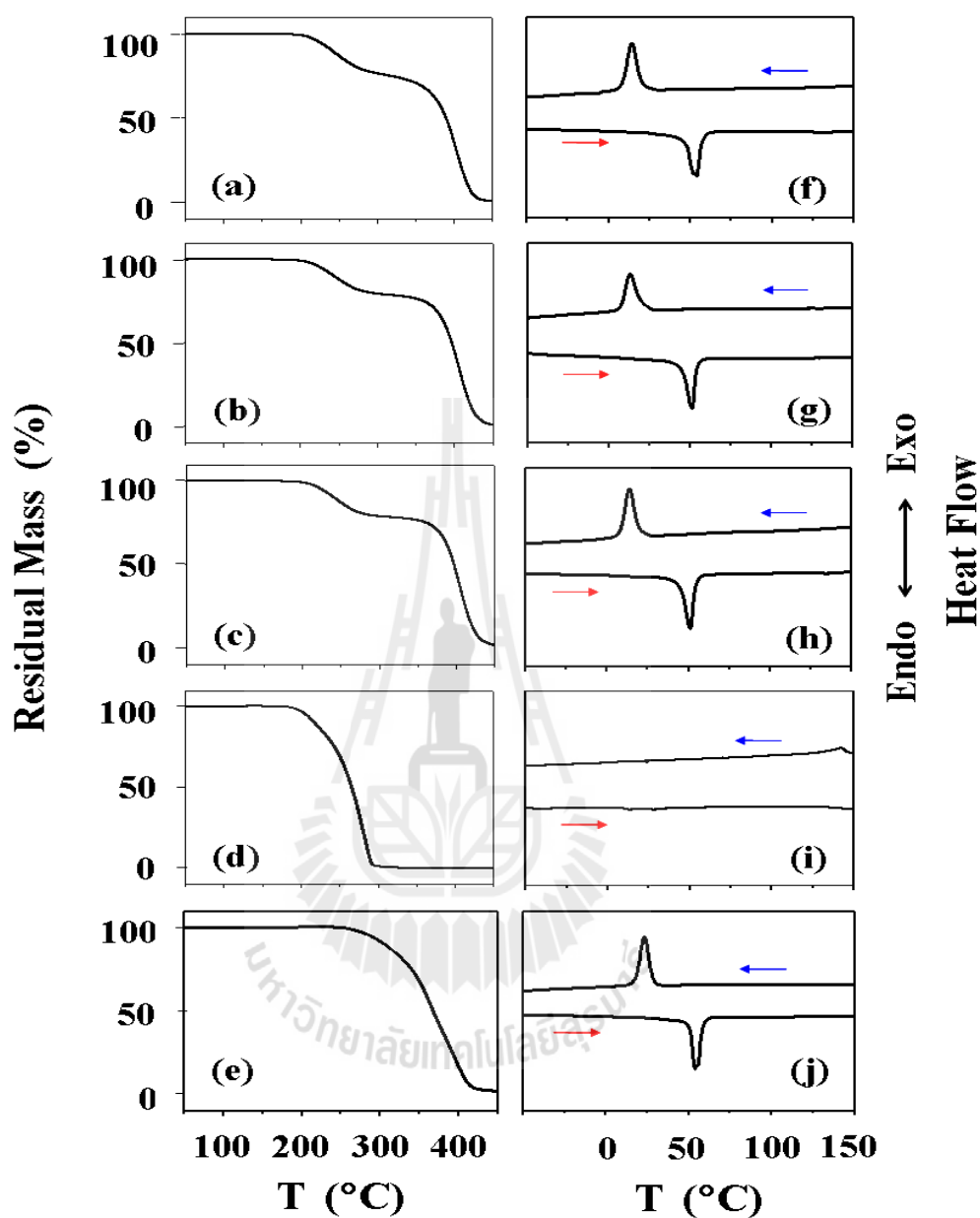


Fig. 3 TGA and DSC thermograms of the PHIC-PCL₁₋₃ miktoarm polymers and their homopolymers: (a,f) PHIC-PCL; (b,g) PHIC-PCL₂; (c,h) PHIC-PCL₃; (d,i) PHIC; (e,j) PCL. The measurements were conducted with a rate of 10.0 °C/min in nitrogen atmosphere.

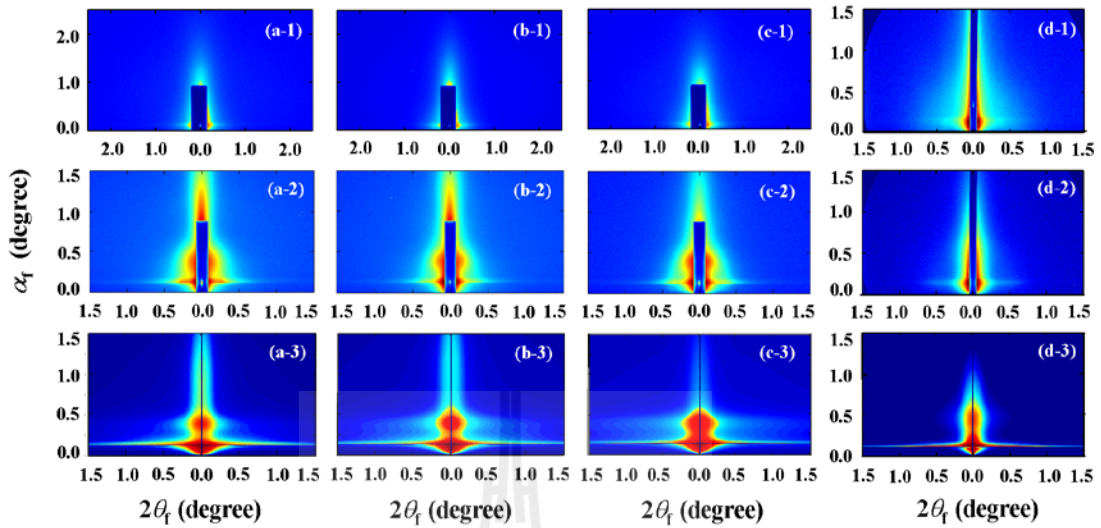


Fig. 4 Two-dimensional (2D) GISAXS patterns of the toluene-annealed thin films of PHIC(5k)-PCL₁₋₃(17k) miktoarm polymers and their homopolymers; PHIC(5k)-PCL(17k): (a-1) measured at $\alpha_i = 0.110^\circ$ and SDD = 992 mm, (a-2) measured at $\alpha_i = 0.140^\circ$ and SDD = 2922 mm, and (a-3) reconstructed with the structural parameters in Table 2 using the GIXS formula; PHIC(5k)-PCL₂(17k): (b-1) measured at $\alpha_i = 0.110^\circ$ and SDD = 992 mm, (b-2) measured at $\alpha_i = 0.140^\circ$ and SDD = 2922 mm, and (b-3) reconstructed with the structural parameters in Table 2 using the GIXS formula; PHIC(5k)-PCL₃(17k): (c-1) measured at $\alpha_i = 0.110^\circ$ and SDD = 992 mm, (c-2) measured at $\alpha_i = 0.140^\circ$ and SDD = 2922 mm, and (c-3) reconstructed with the structural parameters in Table 2 using the GIXS formula; PHIC(5k): (d-1) measured at $\alpha_i = 0.140^\circ$ and SDD = 2922 mm; PCL(15k): (d-2) measured at $\alpha_i = 0.140^\circ$ and SDD = 2922 mm and (d-3) reconstructed with the structural parameters in Table 2 using the GIXS formula. A synchrotron X-ray source with a wavelength λ of 0.1180 nm was used.

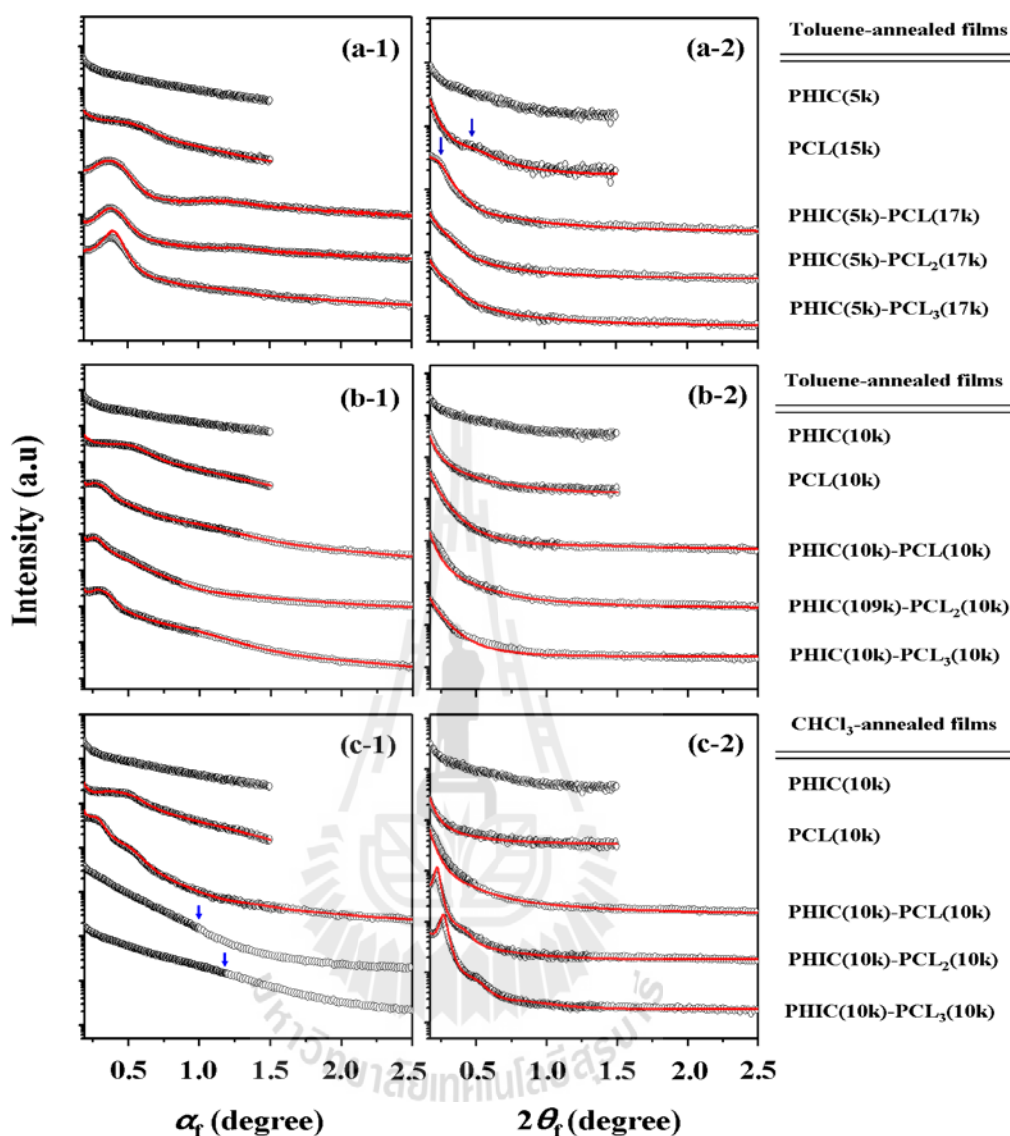


Fig. 5 Out-of-plane and in-plane scattering profiles extracted from the 2D GISAXS patterns in Fig. 4, 6 and 7. Toluene-annealed PHIC(5k)-PCL₁₋₃(17k) and homopolymer films: (a-1) extracted from the data in Figure 4 along the α_f direction at $2\theta_f = 0.100^\circ, 0.140^\circ$ or 0.160° and (a-2) extracted the data in Figure 4 along the $2\theta_f$ direction at $\alpha_f = 0.170^\circ$ or 0.190° . Toluene-annealed PHIC(10k)-PCL₁₋₃(10k) and homopolymer films: (b-1) extracted from the data in Figure 6 along the α_f direction at $2\theta_f = 0.090^\circ$ or 0.100° and (b-2) extracted the data in Figure 6 along the $2\theta_f$ direction at $\alpha_f = 0.140^\circ$ or 0.160° . CHCl₃-annealed PHIC(10k)-PCL₁₋₃(10k) and homopolymer films: (c-1) extracted from the data in Figure 7 along the α_f direction at $2\theta_f = 0.060^\circ, 0.080^\circ$ or 0.090° and (c-2) extracted the data in Figure 7 along the $2\theta_f$ direction at $\alpha_f = 0.140^\circ$.

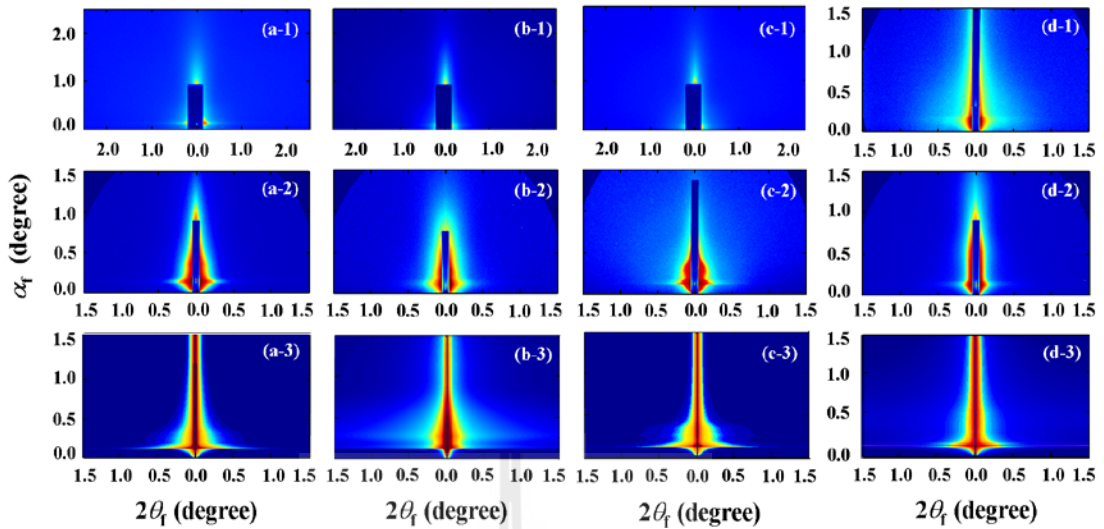


Fig. 6 2D GISAXS patterns of the toluene-annealed thin films of PHIC(10k)-PCL_{1~3}(10k) miktoarm polymers and their homopolymers; PHIC(10k)-PCL(10k): (a-1, a-2) measured with an X-ray beam ($\lambda = 0.1170$ nm) and $\alpha_i = 0.130^\circ$ at SDD = 992 and 2922 mm respectively and (a-3) reconstructed with the structural parameters in Table 2 using the GIXS formula; PHIC(10k)-PCL₂(10k): (b-1, b-2) measured with an X-ray beam ($\lambda = 0.1210$ nm) and $\alpha_i = 0.110^\circ$ at SDD = 992 and 2922 mm respectively and (b-3) reconstructed with the structural parameters in Table 2 using the GIXS formula; PHIC(10k)-PCL₃(10k): (c-1, c-2) measured with an X-ray beam ($\lambda = 0.1170$ nm) and $\alpha_i = 0.130^\circ$ at SDD = 992 and 2922 mm respectively and (c-3) reconstructed with the structural parameters in Table 2 using the GIXS formula; PHIC(10k): (d-1) measured with an X-ray beam ($\lambda = 0.1170$ nm) and $\alpha_i = 0.130^\circ$ at SDD = 2922 mm; PCL(10k): (d-2) measured with an X-ray beam ($\lambda = 0.1170$ nm) and $\alpha_i = 0.130^\circ$ at SDD 2922 mm and (d-3) reconstructed with the structural parameters in Table 2 using the GIXS formula.

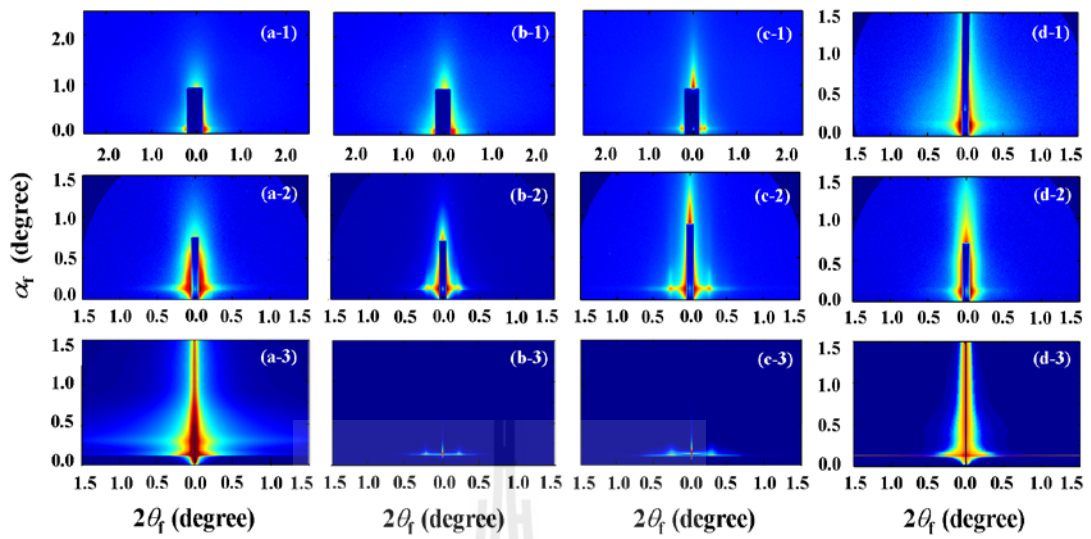


Fig. 7 2D GISAXS patterns of the CHCl_3 -annealed thin films of PHIC(10k)-PCL₁₋₃(10k) miktoarm polymers and their homopolymers; PHIC(10k)-PCL(10k): (a-1, a-2) measured with an X-ray beam ($\lambda = 0.1210$ nm) and $\alpha_i = 0.120^\circ$ at SDD = 992 and 2922 mm respectively and (a-3) reconstructed with the structural parameters in Table 2 using the GIXS formula; PHIC(10k)-PCL₂(10k): (b-1, b-2) measured with an X-ray beam ($\lambda = 0.1170$ nm) and $\alpha_i = 0.140^\circ$ at SDD = 992 and 2922 mm respectively and (b-3) reconstructed with the structural parameters in Table 2 using the GIXS formula; PHIC(10k)-PCL₃(10k): (c-1, c-2) measured with an X-ray beam ($\lambda = 0.1170$ nm) and $\alpha_i = 0.140^\circ$ at SDD = 992 and 2922 mm respectively and (c-3) reconstructed with the structural parameters in Table 2 using the GIXS formula; PHIC(10k): (d-1) measured with an X-ray beam ($\lambda = 0.1170$ nm) and $\alpha_i = 0.130^\circ$ at SDD = 2922 mm; PCL(10k): (d-2) measured with an X-ray beam ($\lambda = 0.1170$ nm) and $\alpha_i = 0.130^\circ$ at SDD 2922 mm and (d-3) reconstructed with the structural parameters in Table 2 using the GIXS formula.

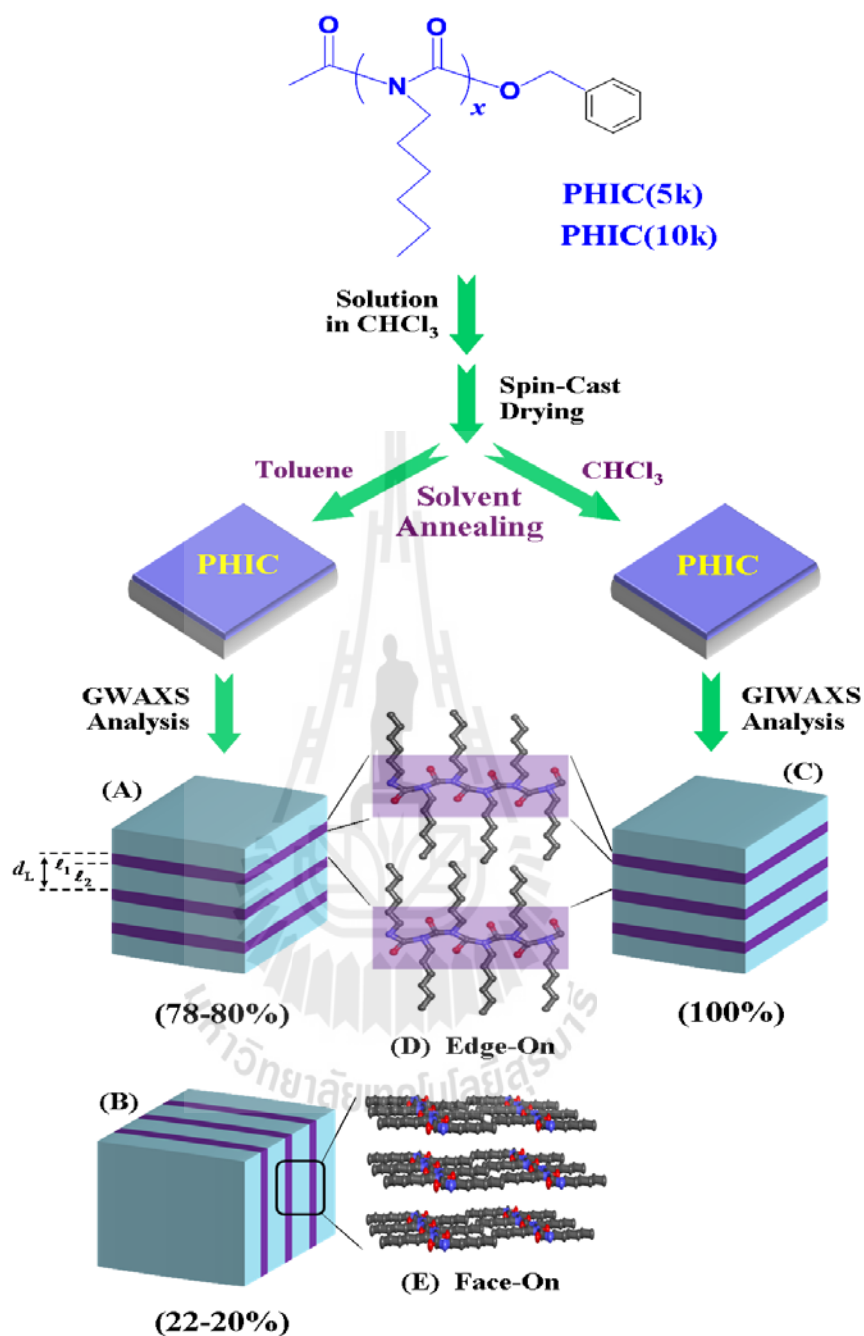


Fig. 8 Schematic representations of molecular chain conformation and self-assembly in PHIC(5k) and PHIC(10k) thin films; toluene-annealed films: A mixture of (A) horizontal multilayer structure (edge-on structure (D)) and (B) vertical multilayer structure (face-on structure (E)); CHCl₃-annealed films: (C) vertical multilayer structure (face-on structure (E)).

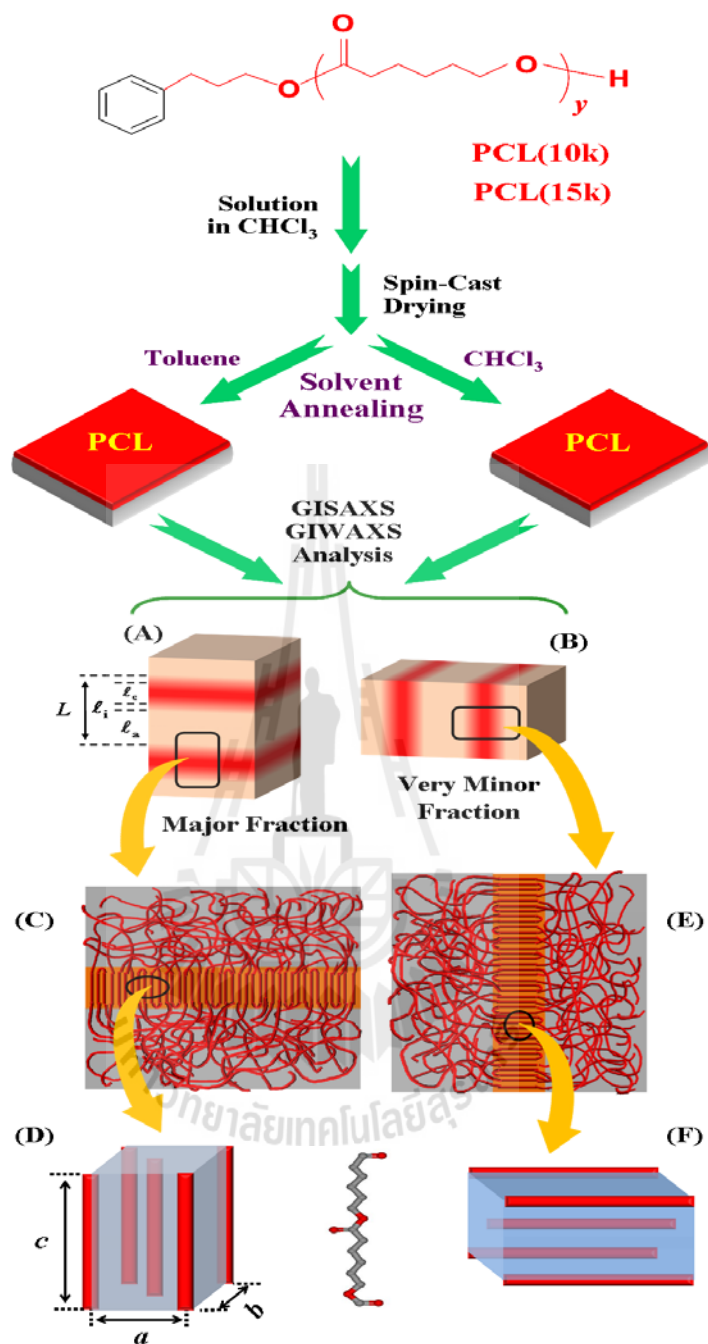


Fig. 9 Schematic representations of molecular chain conformation and self-assembly in toluene- and CHCl_3 -annealed PCL(10k) and PCL(15k) thin films: (A) horizontal lamellar structure composed of amorphous layers and (B) folded crystal layers with (C) vertical orthorhombic crystals; (B) vertical lamellar structure composed of amorphous layers and (E) folded crystal layers with (F) horizontal orthorhombic crystals.

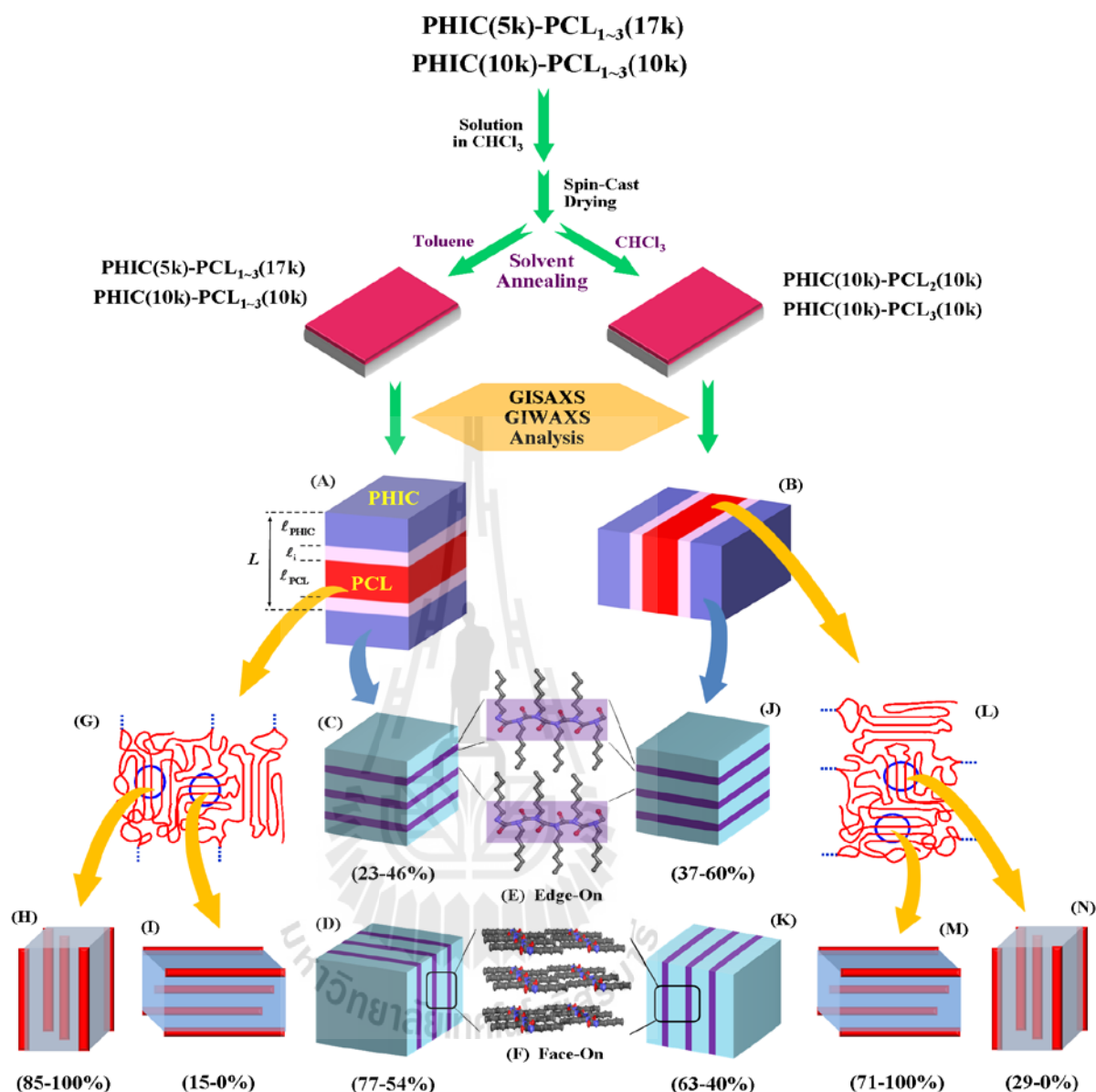


Fig. 10 Schematic representations of molecular chain conformations and self-assemblies in PHIC-PCL₁₋₃ thin films; toluene-annealed PHIC(5k)-PCL₁₋₃(17k) and PHIC(10k)-PCL₁₋₃(10k) films and CHCl₃-annealed PHIC(10k)-PCL(10k) films: (A) phase-separated horizontal lamellar structure where the PHIC layer is composed of a mixture of (C) horizontal multibilayer structure (edge-on structure (E)) and (E) vertical multibilayer structure (face-on structure (F)) and the PCL layer contains (G) fringed-micelle like crystal layers with (H) vertical and (I) horizontal orthorhombic crystals; CHCl₃-annealed PHIC(10k)-PCL₂(10k) and PHIC(10k)-PCL₃(10k) films: (B) phase-separated vertical lamellar structure where the PHIC layer is composed of a mixture of (J) horizontal multibilayer structure (edge-on structure (E)) and (K) vertical multibilayer structure (face-on structure (F)) and the PCL layer contains (L) fringed-micelle like crystal layers with (M) horizontal and (N) vertical orthorhombic crystals.

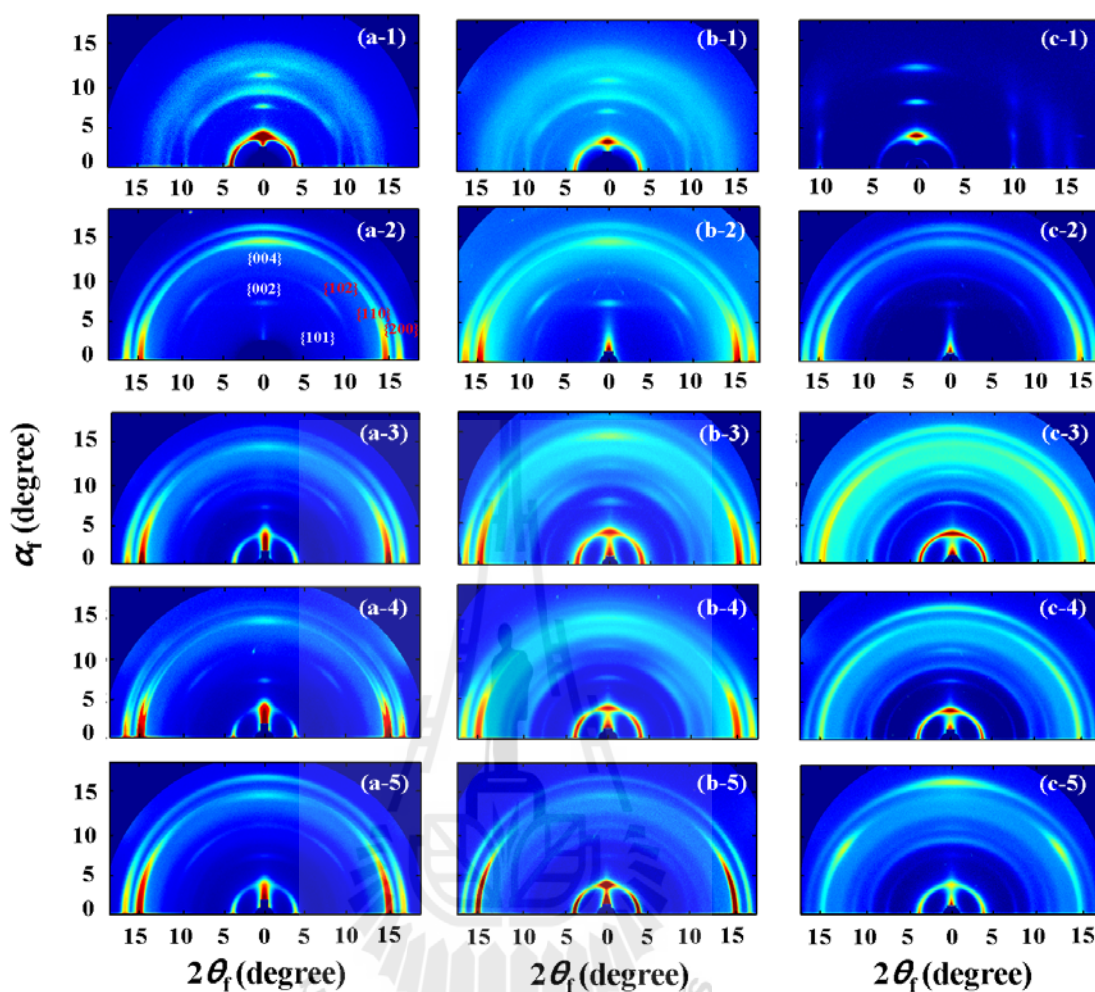


Fig. 11 2D GIWAXS patterns of the thin films (115-120 nm thick) of PHIC-PCL₁₋₃ miktoarm polymers and their homopolymers, measured with an X-ray beam ($\lambda = 0.1120$ nm or 0.1180 nm) at $\alpha_f = 0.130^\circ$ or 0.140° . Toluene-annealed films: (a-1) PHIC(5k); (a-2) PCL(15k); (a-3) PHIC(5k)-PCL(17k); (a-4) PHIC(5k)-PCL₂(17k); (a-5) PHIC(5k)-PCL₃(17k); (b-1) PHIC(10k); (b-2) PCL(10k); (b-3) PHIC(10k)-PCL(10k); (b-4) PHIC(10k)-PCL₂(10k); (b-5) PHIC(10k)-PCL₃(10k). CHCl₃-annealed films: (c-1) PHIC(10k); (c-2) PCL(10k); (c-3) PHIC(10k)-PCL(10k); (c-4) PHIC(10k)-PCL₂(10k); (c-5) PHIC(10k)-PCL₃(10k).

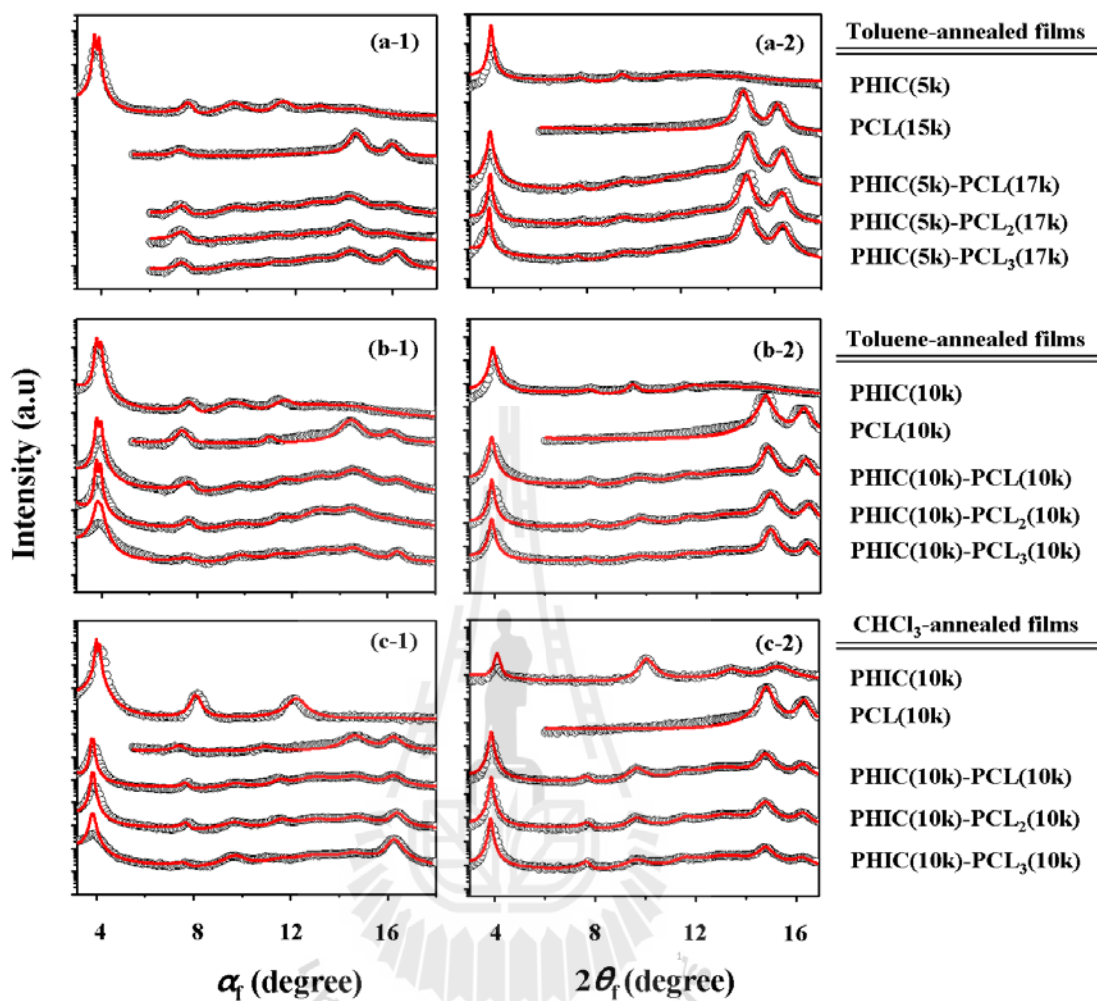


Fig. 12 Out-of-plane and in-plane scattering profiles extracted from the 2D GIWAXS patterns in Fig. 10 along the α_f direction at $2\theta_f = 0^\circ$ and the $2\theta_f$ direction at $\alpha_f = 0.260^\circ$, 0.300° or 0.390° , respectively: (a-1, a-2) toluene-annealed PHIC(5k)-PCL₁₋₃(17k) and homopolymer films; (b-1, b-2) toluene-annealed PHIC(10k)-PCL₁₋₃(10k) and homopolymer films; (c-1, c-2) CHCl₃-annealed PHIC(10k)-PCL₁₋₃(10k) and homopolymer films.

CURRICULUM VITAE

Name	Mr. Rarm Phinjaroenphan
Date of Birth	29 July 1981
Place of Birth	Nakhon Ratchasima, Thailand
Nationality	Thai
Education	
1999-2003	Kasetsart University, Bangkok, Thailand Bachelor of Science (Physics)
2004-2007	Suranaree University of Technology, Nakhon Ratchasima, Thailand Master of Science (Physics)
2010-present	Suranaree University of Technology, Nakhon Ratchasima, Thailand Ph.D. candidate in Physics
Experience	
2011-2013	Research assistant at Synchrotron Light Research Institute, Nakhon Ratchasima, Thailand
2013-2014	Exchange student (Prof. Moonhor Ree at Pohang University of Science and Technology, Pohang, South Korea)